The Stability of Multiple Wing-tip Vortices

Edward James Whitehead

Thesis submitted for the degree of

Doctor of Philosophy

in

Applied Mathematics

at

The University of Adelaide

(School of Mathematical Sciences)

July, 2009

Contents

Signed Statement

NAME: ..... PROGRAM: .....

This work contains no material which has been accepted for the award of any other degree or diploma in any university or other tertiary institution and, to the best of my knowledge and belief, contains no material previously published or written by another person, except where due reference has been made in the text.

I give consent to this copy of my thesis, when deposited in the University Library, being made available for loan and photocopying, subject to the provisions of the Copyright Act 1968.

I also give permission for the digital version of my thesis to be made available on the web, via the University's digital research repository, the Library catalogue, the Australasian Digital Theses Program (ADTP) and also through web search engines, unless permission has been granted by the University to restrict access for a period of time.

SIGNED: ..... DATE: .....

Acknowledgements

I would like to acknowledge the help and support of my supervisor Associate Professor Jim Denier throughout the duration of my PhD who despite a very large workload as head of school and overseeing the relocation of the mathematics department, still managed to provide quality feedback and guidance. I would also like to acknowledge my co-supervisor, Associate Professor Steve Cox, now at the University of Nottingham and Dr Trent Mattner with whom I had useful discussions regarding this work. This work was also supported by a grant from the Sir Ross and Sir Keith Smith Fund and an Australian Postgraduate Award.

I would like to dedicate this thesis to Petrina Rohrlach, for without her encouragement and support my time at the University of Adelaide may never had happened.

Abstract

Over the last forty or so years interest in the study of wing-tip vortices has increased, primarily due to the introduction of larger passenger aircraft and their subsequent interaction with smaller aircraft. The vortices generated by these larger aircraft present a problem in two main areas; the wake hazard problem, where other aircraft can be subjected to the large tangential velocities of the vortex, and the interaction with ground based features of vortices created during landing and take-off. The first of these is particularly dangerous close to the ground when aircraft are in a high lift configuration at take-off and landing. As the vortices effectively scale with aircraft wing span, significant encounters between large vortices and smaller aircraft have been documented over the years. An example of one such documented wake vortex interaction incident can be found in Ogawa [45].

In this study, the system of vortices are described as classical Batchelor vortices (or linear superpositions thereof) which are then subjected to small perturbations. By discretising the domain and solving for the eigenvalues of the system it is possible to ascertain the stability characteristics of the flow as a function of the system parameters which include the axial wave-number, the spacing of the vortices, their cross-flow decay rate and their axial strength.

We first consider the inviscid instability of multiple tip vortices, an approximation which is valid in the limit of large Reynolds numbers. In this limit the stability of the flow is dominated by the axial component of the basic vortex flow. The governing equations of continuity and momentum are reduced to a second order partial differential equation (PDE). This equation is solved numerically to determine which vortex configurations produce the greatest instability growth rate. These results are extended to consider the effect of compressibility on the inviscid instability. Finally

we consider the effects of viscosity on the stability of the full Batchelor similarity solution which results in a second order PDE in four dependent variables.

The stability equations are solved both globally (for the entire eigenspectra) and locally (for a single eigenvalue in a pre-determined region) using codes that run in both serial and parallel form. The numerical methods are based on pseudo-spectral discretisation (Chebyshev polynomials for Cartesian and radial directions and Fourier for azimuthal) in the global scheme, the eigenvalues being recovered either with a QZ algorithm or a shift-and-invert Arnoldi algorithm. For the local scheme, fourth order centred finite-diffences are used in conjunction with an iterative eigenvalue recovery method.

Chapter 1

Literature Review

1.1 Introduction

Lifting surfaces by their very nature produce tip vortices. For a surface to produce lift it must create a pressure differential between the top and bottom surfaces. In a standard lifting surface such as an aircraft wing, a high pressure zone is created beneath the wing and low pressure above. The air surrounding the wing will always try to equalise the pressure; the high pressure air flowing around the path of least resistance, the wing-tips, to the low pressure region. The circular motion of this flow, combined with free stream flow created by the aircraft's forward motion produces what is known as a *wing-tip vortex*. An aircraft produces two counter-rotating wing-tip vortices, one for each wing (figure 1.1). Secondary vortices may be produced by other features of the aircraft including (primarily) the inboard flaps, the engines, landing gear and any other protruding features.

Wing-tip vortices pose a considerable hazard. In a condition of high lift (large pressure differential), usually found during landing or take-off, vortices are at their largest being of a scale proportional to the aircraft's wingspan and hence the size of the aircraft [22]. The nature of modern international airports result in situations in which many aircraft are usually found in close proximity. If a following aircraft were to interact with these trailing vortices, depending on the relative size of the two aircraft, it could experience large and sudden rolling moments. Experiments documented by Condit and Tracy [7] showed that the encountering aircraft was

quickly expelled from the wake and that steady flight was recoverable with little effort. Whilst this would seem to diminish the hazard associated with wake vortex interaction, it should be pointed out that this is particularly dangerous when the aircraft is close to the ground as is the case during landing and take-off where the following aircraft cannot tolerate large excursions from its flight path. An example of one such documented wake vortex interaction incident can be found in Ogawa [45].

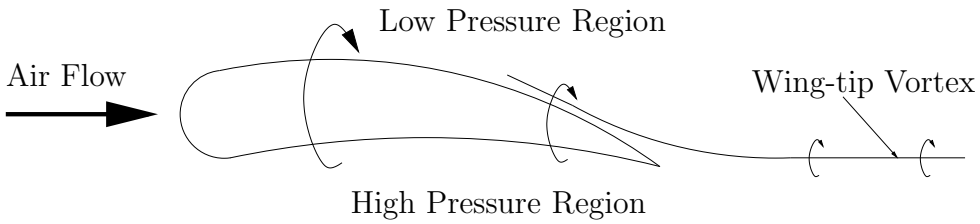

Figure 1.1: Wing-tip vortex creation on a lifting surface [22].

A further problem associated with wing-tip vortices is induced drag. Induced drag, which is essentially the result of the energy required to create the tip vortices, counts for approximately 35% of the total drag on an aircraft [22, 26]. The most obvious result of increased drag, apart from the aerodynamic effects, is greater fuel consumption. The benefits of reducing the size and strength of wing-tip vortices are therefore obvious.

At present, airports around the world require specific spacing between aircraft landing and taking off to allow trailing vortices to dissipate to a safe level [7, 55], an example of which can be found in the Civil Aviation Authority Circular [2] which details the requirements at Heathrow Airport, one of the world's busiest. Being able to manage the vortices from aircraft would allow the spacing to be optimised or reduced, thus potentially giving the airport greater traffic handling capabilities, saving both time and money. By controlling the creation of vortices, drag could be reduced, which would result in significant fuel savings resulting in cheaper operating costs which could in turn be passed on to the consumer or increase airline profits. A reduction in fuel consumption by aircraft would also be beneficial in terms of environmental impact and would allow longer distances to be travelled between re-fueling stops. The ability to manage aircraft trailing vortices could also significantly

reduce the occurrence of roof and ground damage in areas directly beneath the landing path.

Many possible methods of managing wing-tip vortices have been proposed. These include the reduction of the amount of slip around the wing-tip by wing modifications such as winglets or wing fences as discussed by Nosenchuck *et al.* [44]. Crouch [9] describes several methods in detail including both passive and active control. Crow [11] discussed a method of active control during landing whereby front flaps (or flaperons) in conjunction with the ailerons would be used to excite an instability by oscillating at the wavelength of the fastest growing unstable mode. This was seen as a more preferable alternative so far as passenger comfort is concerned than a 'porpoising' motion of the entire plane! Luffsey [40] describes further potential methods for wake vortex dissipation such as bleeding compressed air from the engines into the vortex cores and various wing modifications along with several possible methods of wake control by ground based processes.

Savaş [50] details tow tank experiments using triangular shaped outboard flaps to generate a region of high lift and hence the standard form of a counter-rotating vortex pair on the same side of the aircraft but also notes that significant structural modifications are required to implement this scheme. One of the more unorthodox suggestions was by Menkes and Abernathy [42] which involves removal of the wake vortex itself close to the ground by means of placing suction blowers in ditches around the runway to draw the vortices down more rapidly.

Rennich and Lele [48] examined the careful manipulation of vortex placement into configurations of high strain in order to excite the Crow [10] instability to promote a faster vortex breakdown than would naturally occur. Over the last few decades this has been the most popular method of approaching the trailing-vortex problem. Vortices that are more unstable dissipate quicker than those that are stable and so lend themselves to this type of approach. Implementing methods that induce instabilities (by means of a small perturbation into the trailing vortices) and hence accelerate their transition to turbulence, would effectively accelerate their decay [44]. Orlandi *et al.* [46] have suggested that one such method of introducing these perturbations is through heating within or between the vortices which could be achieved via redirection of some portion of exhaust gas. Vortex interaction has

also been shown as an effective way to amplify instabilities which result in faster dissipation rates [8]. In order to benefit from this, careful placement of wing structures could promote the required vortex interaction.

The aim of this research is to investigate the type of trailing vortices and the various mechanisms by which they become unstable. The research will aim to build upon current knowledge, whilst examining avenues to alternative approaches. Due to the nature of the problem, the work will be carried out using mathematical, numerical and computational techniques utilising the perturbation theory alluded to earlier. It should be noted at this stage that throughout the literature the terms wing-tip vortex, trailing vortex and wake-vortex are all used to describe the swirling flow produced by the interaction of a finite lifting surface moving through a fluid and are used interchangeably throughout this study.

1.2 General Outline

Research has been performed on lift producing bodies and their associated vortices since they were first discovered and used for practical purpose. Since the pioneering work of Kelvin, Lamb and Prandtl there has been much interest in the field of vortex stability and many researchers have analysed the theoretical aspects of vortices and the causes of transition to turbulence. Over the years there has appeared a vast array of literature covering almost all feasible aspects of vortex behaviour. It is therefore essential for this particular study to identify those areas that are of importance to the particular problem at hand.

In the literature there are two preferred methods of developing the equations with which to analyse trailing line vortices. The first of these is the linearisation and simplification of the general governing equations in their primitive form with the introduction of small perturbations as pioneered by Batchelor [3] and subsequently used by many researchers such as Brown [6], Lessen *et al.* [38], Mayer and Powell [41] and Duck and Foster [15] to name but a few. The general form of the perturbations introduced throughout the literature for a single vortex with a dependance on the azimuthal wave-number can be written as follows (1.2.1),

$$(U_p, V_p, W_p) = \{U_p(r),\ V_p(r),\ W_p(r)\}\mathrm{e}^{\mathrm{i}\alpha(x-ct)-\mathrm{i}n\theta}, \tag{1.2.1}$$

with α, n, c being the axial and azimuthal wave-numbers and the complex phase velocity (the eigenvalue) respectively. The form used in this study for application to multiple vortices is detailed in section 2.2.1 where the vortices are perturbed by disturbances of the same axial wave-number.

The second method is to use the vorticity equations to develop a system for analysis as used by Crow [10] and the vortex filament approach applied to a pair of vortices by Widnal *et al.* [66], Jimenez [29] and Crouch [8] and for a four vortex system by Fabre *et al.* [20]. A comprehensive review of these methods can be found in Theofilis [62]. Further computational tools include Direct Numerical Simulation (DNS) as used by Orlandi *et al.* [46], Abid *et al.* [1] and Laporte and Corjon [33], Large Eddy Simulations (LES) performed by Gerz and Holzäpfel [21], Sipp *et al.* [53] and Lewellen and Lewellen [39] to examine how turbulence affects the decay of trailing vortices, Computational Fluid Dynamics (CFD) as found in Czech *et al.* [12] and of course, experiments such as Singh and Uberoi [52], Nosenchuck *et al.* [44] and Devenport *et al.* [14].

Further to this perturbation method is the representation of the multiple vortex configuration by introduction of a single vortex into a strain field analysed asymptotically by Le Dizés [34] and using DNS by Jacquin and Pantano [28] and Ryan and Sheard [49]. In essence, a second vortex (or multiple vortices) applies a strain field on the original, or primary vortex, which can be used to examine the destabilising effect on the vortex due to a variety of external parameters.

Also, different mathematical models of vortices are used, the most prevalent (but not limited to) are the Rankine (constant vorticity), Lamb-Oseen or Batchelor (essentially a Lamb-Oseen vortex with a Gaussian axial field) type vortices. Whilst the Batchelor vortex is most commonly used, several authors, including Fabre *et al.* [17] and Sipp *et al.* [53] build their analysis around Rankine vortices. Spalart [55] states that the Rankine vortex is a poor approximation of a realistic flow and whilst the classic Batchelor similarity solution is far from perfect in its approximation of a real flow, from a mathematical stand-point it is still a useful tool for the study of the physics (linear stability) of three-dimensional slender vortices [19].

Whilst much work has gone into understanding the mechanism behind the generation and stability of trailing line vortices, there appears to be a shortfall when it

comes to describing a global solution for the problem of controlling these vortices. Solutions obtained to date are specific to certain vortex placements and initial conditions and whilst the analytical results do occasionally align themselves with those obtained experimentally, this is only when stringent control conditions are met, conditions which are inappropriate for an inter-continental aircraft which may experience a wide range of conditions in a single flight. More recent work sets out to identify further causes and types of instabilities and how these can be generated by vortex manipulation. Considerable effort is now being placed on the use of increased computing power to solve large-scale eigenvalue problems both in two and three dimensions to the degrees of accuracy required in such complex systems [25, 55, 62].

As computing power has increased, the study of trailing line vortices has been extended from a single vortex to multiple vortex systems (and allowing larger scale DNS, LES), better describing the physics of real-life situations. From the work of Crow [10] in which a pair of counter-rotating vortices (representing the outer wing-tip vortices) were analysed, Crouch [8] looked at the case of two co-rotating vortices, thus simulating vortices created by a wing-tip and an inboard flap (for example) on the same side of the aircraft. To further this, Fabre and Jacquin [18] and Fabre *et al.* [20] analysed a system of four vortices, two opposing sides of the Crouch [8] analysis using a vortex filament approach, better still representing a complete aircraft trailing vortex system.

1.3 Findings To Date

The work of Batchelor [3] on the axial flow of trailing line vortices could be described as the first modern work detailing wing-tip vortices. Batchelor developed a similarity solution for the full Navier-Stokes equations leading to a set of equations which describe the axial and azimuthal components of a basic vortex flow in a system of cylindrical polar co-ordinates (known colloquially as the Batchelor or q-vortex). The Batchelor vortex has since been almost universally used in the linear stability analysis of trailing vortex problems.

Crow [10] described a mechanism by which a pair of counter-rotating tip vortices

interact and how this leads to long wave-length instabilities. Crow showed that after formation, a pair of vortices oscillate sinusoidally in a plane $\approx 45°$ to the horizontal. These oscillations amplify until, at various points, the two vortices interact to form a series of individual vortex rings. Since referred to as the Crow instability, this long wave-length instability has been further studied by Rennich and Lele [48] and Fabre and Jacquin [18] in an effort to identify ways in which to further excite the instability to promote a more rapid transition to turbulence. Importantly though, whilst the Crow instability will on its own cause vortex break-down [48], the time-frame over which this instability grows is too long for it to be an efficient mechanism for trailing-vortex dissipation [18]. An interesting point to note from the article by Rennich and Lele [48] is the so-called Rennich and Lele Criterion which states that, for a four-vortex system of span ratio $x = b_2/b_1$ and circulation ratio $y = \Gamma_2/\Gamma_1$, an expression for determining a vortex system with a rigidly translating mean system is given by

$$x^3 + 3yx^2 + 3x + y = 0, \tag{1.3.1}$$

which, for the majority of multiple-vortex studies since, has been used to describe the relative strength and spacing of a four-vortex system. It is interesting to note that Rennich and Lele [48] show that only a small percentage of aircraft meet this criterion when the relative spacing of the wing-tips and inboard flaps are considered. This spacing is also comparable to the spacing of the wing-tips and rear horizontal stabilisers (elevators) but these authors do not specify a criterion for circumstances when vortex configurations are not co-linear.

1.3.1 Inviscid Stability Analysis

Whilst not directly applicable to a vortex flow problem, the work of Batchelor and Gill [4] on the inviscid stability of jets is an early example of a stability anaylsis for a complex flow. It is also the basis of the boundary conditions for all studies implementing equation (1.2.1). Furthermore, asymptotic analysis of the governing equations when substituted with the basic flow of Batchelor [3] shows that for an inviscid problem at leading order, the vortex essentially behaves as a jet with a Gaussian axial profile [64].

As has already been discussed, both Crow [10] and Widnal [66] used vorticity methods to examine the stability of a pair of counter-rotating vortices. However, the work of Lessen *et al.* [38] is more pertinent to the present study. By linearising the governing equations and applying Batchelor's similarity solution, the stability characteristics of a single vortex were analysed with respect to varying axial and azimuthal wave-numbers and it was found that negative azimuthal wave-numbers were, in general, more unstable than their positive counterparts for small values of swirl. Duck and Foster [15] examined a similar flow using an iterative numerical method and found that in addition to those modes cited by Lessen *et al.* [38], a further spectrum of unstable modes existed including several modes at higher azimuthal wave-numbers (for a given swirl value) that exhibited greater growth rates than the most unstable modes at the previously analysed lower azimuthal wave-numbers.

The asymptotic expansion of the linear inviscid stability problem by Leibovich and Stewartson [36] aimed to derive a sufficient condition for the instability of columnar vortices through comparison of their asymptotic theory to numerically derived results for positive n using a Batchelor vortex as the basis. They state that the most dangerous modes are those with a positive azimuthal wave-number. Whilst this may seem to contradict the earlier statement regarding the work of Lessen *et al.* [38] and negative azimuthal wave-numbers being dominant, due to these authors' translation and inversion of the axial velocity profile (see section 4.3.1), their negative azimuthal wave-numbers are equivalent to the positive wave-numbers of Leibovich and Stewartson [36]. Their asymptotic results yield a value of swirl above which all modes are stabilised as $q \approx 1.6$ (where q is the swirl parameter defined in detail in section 4.3.1), which matched those of the primary mode of Lessen *et al.* [38] and their own numerical results. Like Duck and Foster [15], Leibovich and Stewartson [36] encountered problems with their numerical schemes near the neutral curve due to 'mode jumping' [31]. That is, for very small values of imaginary component of the eigenvalue (defined more specifically in section 2.4.3) c_i, it is not possible to consistently track an individual mode whose eigenvalue may only differ marginally to that of its structurally different counterpart.

The inviscid near-neutral stability of a trailing vortex was investigated by Stew-

artson and Capell [58] and Stewartson and Brown [57], with the former looking at ring-modes (moderate n-values) and the latter at centre-modes (high n-values). This led them to find a dependance of the eigenvalues on the axial wave-number normalised with respect to the azimuthal wave-number and also a dependance on the swirl parameter (q), where instabilities were found at higher than previously reported values of q, up to $q \approx 2.31$. Khorrami [30] reported that the higher inviscid modes found by Duck and Foster [15] persist to much lower Reynolds numbers. The inviscid work of Mayer and Powell [41] follows much the same lines as previous work concentrating on the non-negative azimuthal wave-numbers for a large variation in q. Using a spectral collocation technique they reported that $n = 1$ has the largest unstable region and surmised that the location and region of the previously reported maximum disturbance growth rate was incorrect.

More recent work by Heaton [24] applied a Batchelor vortex to a theory of inviscid centre-modes using a localised numerical scheme and stated that most previous instabilities found either through numerical work or asymptotically can be loosely described as centre-modes. Heaton [24] also numerically verified Stewartson and Brown's [57] asymptotic assertion that the upper neutral point is at a higher swirl ($q \approx 2.31$) than previously stated and made the claim that previous numerical results surrounding the neutral curve at this point are in error. Essentially, the majority of inviscid work over the last forty or so years revolves around the stability of a single Batchelor-style trailing vortex aiming to establish a set of values for swirl (q), axial and azimuthal wave-numbers (α, n) for which various modes of differing degrees of instability can be identified.

1.3.2 Viscous Stability Analysis

In the follow-up paper to [38], Lessen and Paillet [37] expanded their research to include viscous effects on a single Batchelor vortex. The basic flow remained unchanged, only the governing equations differed to include the relevant parameters in order to examine the effect of the Reynolds number on the stability of several modes. The location of the points of neutral stability were found and the assertion that increased swirl has a stabilising effect was made. Whilst these results were sig-

nificant in the field of vortex stability and have been used to verify many subsequent works, it has been shown that some of the results lack the degree of accuracy that might be expected from today's researchers [19, 32, 41]. Stewartson [56] presented an asymptotic theory to describe the stability of a vortex at large Reynolds numbers and large azimuthal wave-numbers in order to link the results of the viscous work of Lessen and Paillet [37], that indicated the most unstable modes can be found at low azimuthal wave-numbers, to the inviscid case of Lessen *et al.* [38], where the most unstable modes were found to occur at $n \gg 1$. Stewartson found that viscosity has a stabilising role by reducing the critical swirl value from which a vortex is stable and predicts a finite azimuthal wave-number to provide the most unstable mode.

Khorrami [32] presented an informative study of the application of spectral collocation techniques to the stability of swirling flows; among other flows the Batchelor vortex was explored and results were given that showed good agreement with previously published work. What is useful about this paper however, is that it demonstrates the applicability of spectral methods to the problem of viscous linear stability. In a follow-up paper Khorrami [30] used these spectral techniques to study the viscous stability of a Batchelor vortex at moderate to high Reynolds numbers. Khorrami [30] found two long-wave viscous modes of instability at $n = 0, 1$ with growth rates an order of magnitude smaller than inviscid modes, thus contradicting earlier work which stated viscosity has a purely stabilising effect. Mayer and Powell [41] in the second part of their paper discussed the viscous instabilities of the Batchelor vortex where the existence of destabilising viscous modes was examined further and documented in more detail with a critical Reynolds number for the axisymmetric mode ($n = 0$) found to be close to that of Khorrami [30]. Duck and Khorrami [16] discussed these viscous modes further and presented an asymptotic analysis that agreed with the viscous modes found by Khorrami [30]. Further work by Khorrami [31] traced the behaviour of the asymmetric ($n = 1$) viscous mode near the upper neutral curve. Several more recent papers discuss these viscous instabilities further and examine them with variations in one or more of the dependent parameters (Fabre and Jacquin [19] for example), essentially building a more thorough picture of the results initially presented by Khorrami [30].

One of the first studies to introduce the concept of a linear stability analysis

of a multiple wake-vortex system (where equation (1.2.1) was replaced by equation (2.2.25) of chapter 2) using an Euler equation approach (as opposed to a vorticity method) was Jacquin *et al.* [27] whose results were further detailed in Hein and Theofilis [25]. A linear superposition of the Batchelor vortex profile was used to build the basic flow which was then iterated numerically to produce a flow that satisfies the steady Navier-Stokes equations. A Chebyshev discretisation scheme was used with a clustering modification algorithm that aims to re-cluster the grid points about the origin. A shift-and-invert Arnoldi algorithm was used to extract the eigenvalue spectrum for one, two and four vortex configurations and used to show that the stability characteristics of the Batchelor vortex are significantly altered by the addition of extra, counter-rotating vortices (or vortex pairs). A similar approach to that used by Hein and Theofilis [25] is used in this study. Denier and Stott [13] provided an asymptotic analysis of the dominant wave mode finding the critical Reynolds number, azimuthal wave-number and swirl number for short wave disturbances in a trailing vortex. They found that the most unstable mode has an azimuthal wave-number of $\mathcal{O}(Re^{\frac{2}{5}})$ and axial wave-number of $\mathcal{O}(Re^{\frac{2}{5}})$.

1.3.3 Compressible Stability Analysis

As speeds approach the supersonic realm ($1 \leq M \leq 5$) and increase further into the hypersonic region ($M > 5$) it is unrealistic to assume in our model that the density remains constant and hence the flow is incompressible. Therefore, for a more accurate representation of a real flow, compressibility should be re-introduced to the governing equations.

Compressible boundary-layers have been shown to be unstable to both inviscid and viscous perturbations [54]. As we are in effect utilising a boundary-layer type approximation in the formation of our basic flow it is appropriate to include some review of previous compressible boundary-layer stability work before discussing vortex flows directly. Smith and Brown [54] investigated the stability of an inviscid Blasius boundary-layer at large Mach numbers. They observed a vorticity mode where the wave-number becomes a continuous function of the Mach number as $M \to \infty$, hence giving a compressibility dependent mode that is the most dominant mode at high

Mach numbers.

Stott and Duck [59] were one of the first to examine the stability of a compressible vortex flow whereby compressibility was added via the inclusion of two further equations; namely the energy equation and an ideal gas law. Stott and Duck [59] showed that Batchelor's similarity solution for a swirling incompressible vortex flow was also a viable solution for a compressible flow. They examined the inviscid case and found that, as the Mach number is increased the growth rates generally decrease and predicted that the original family of modes will stabilise when $M = \mathcal{O}(|n|^{\frac{1}{2}})$ where n is the azimuthal wave-number. They also pointed out the possible existence of dominant unstable modes that are purely a result of fluid compressibility and which don't exist at lower Mach numbers.

Stott and Duck [60] extended their previous work to include viscous effects in which they find that the key Mach number for maximum instability growth rate is dependent on the wave-number and that, to the Reynolds numbers that their computations were performed, the effect of increasing the Mach number is generally a stabilising one.

1.4 Research Objectives

Trailing vortices are ubiquitous in all areas of aeronautics and present considerable challenges from both a design and management perspective. By exploring the stability of multiple trailing vortex systems, the dominant forms of instability can potentially be identified and the critical parameters (such as vortex strength and relative spacing) for the onset of instability can be examined. These results can be used to develop techniques for alleviation of the wake-vortex hazard through active promotion of transition to turbulence within the flow.

Even with the advancements in the understanding of trailing vortices and the improvement in mathematical and numerical tools, it would be naive to think that any single piece of research in this particular field would lead directly to a solution (or at least alleviation) of the wake-vortex problem. Whilst most researchers begin their studies with some reference to applying their methods to the alleviation of the wake-vortex hazard, this is somewhat tempered by the understanding that due to

the range of variable parameters and modelling assumptions required, the work is contributing to the wider picture; to build a complete knowledge base with which to tackle the problem. As such the over-riding aim of this thesis is to further advance the understanding of the fundamental fluid dynamical behaviour of trailing vortices.

Unlike most previous work however, the current study will aim to analyse the multiple vortex stability problem through manipulation of the primitive governing equations of motions and not the more common vortex filament method. Initailly an inviscid two-dimensional flow in the form of an asymptotic representation of the Batchelor similarity solution [3] and linear super-positions thereof will be examined where we show that for high Reynolds numbers (inviscid flow), the amount of swirl in the cross-flow components of our basic flow is negligible in terms of a leading-order stability analysis. This enables us to simplify the governing equations to a single, linear elliptic partial differential equation for the perturbation pressure. The resulting equation is solved as a generalised eigenvalue problem where the eigenvalues determine the stability characteristics of the system. This work is then extended to include the effects of compressibility and so to investigate what effect a variation in density (in terms of the dimensionless Mach number) has on the growth rates of the dominant unstable modes. The incompressible analysis is then extended to include viscous effects where the critical Reynolds number for neutral stability (for a particular set of parameters) is sought.

A large portion of the following research is devoted to developing and characterising the various numerical methods and tools used in the analysis, it seemed only appropriate to do so considering the large percentage of time devoted to developing and implementing these methods. The building blocks of the following research are the numerical methods, mathematical models, assumptions and computer modelling tools for without these, it would not be possible to further this research. The time taken for the computer to produce the numerical results pales when considered along side the time spent developing the methods by which to obtain these results.

Chapter 2

Stability Equations

2.1 Introduction

In order to perform a linear stability analysis on a system consisting of one or more vortices, the governing equations are chosen to be the Navier-Stokes equations for the three spatial directions with the fourth equation being that of continuity. For the analysis that follows it is desirable to have these equations documented in both a Cartesian (x, y, z) and cylindrical polar (r, θ, x) co-ordinate basis as both co-ordinate systems are used in this study. It is worth noting here that in all cases, x is the axial direction and y, z in Cartesian co-ordinates or r, θ in polar co-ordinates, form the cross-flow directions. For this analysis buoyancy and other 'body' forces can be neglected as it is assumed that the fluid density is constant.

2.2 Cartesian Co-ordinates

The governing equations in Cartesian co-ordinates are the three-dimensional continuity equation and the (x^*, y^*, z^*) momentum equations

$$\frac{\partial u^*}{\partial x^*} + \frac{\partial v^*}{\partial y^*} + \frac{\partial w^*}{\partial z^*} = 0, \tag{2.2.1}$$

$$\frac{Du^*}{Dt^*} = -\frac{1}{\rho^*}\frac{\partial p^*}{\partial x^*} + \nu^*\nabla^2 u^*, \tag{2.2.2}$$

$$\frac{Dv^*}{Dt^*} = -\frac{1}{\rho^*}\frac{\partial p^*}{\partial y^*} + \nu^*\nabla^2 v^*, \tag{2.2.3}$$

$$\frac{Dw^*}{Dt^*} = -\frac{1}{\rho^*}\frac{\partial p^*}{\partial z^*} + \nu^*\nabla^2 w^*, \tag{2.2.4}$$

where

$$\frac{D^*}{Dt^*} = \frac{\partial}{\partial t^*} + u^*\frac{\partial}{\partial x^*} + v^*\frac{\partial}{\partial y^*} + w^*\frac{\partial}{\partial z^*}, \tag{2.2.5}$$

and $(u^*, v^*, w^*), p^*, (x^*, y^*, z^*), t^*$ are the dimensional units of velocity, pressure, distance and time respectively, ν^* is the kinematic viscosity and ρ^* is the fluid density.

2.2.1 Derivation of the Disturbance Equations

In order to assess the stability characteristics of the flow we introduce disturbances to the steady-state flow that are significantly smaller in magnitude relative to the basic flow quantities and examine whether they will grow or decay. The disturbances whose specific form will be defined later can be written as,

$$u^* = \hat{u} + u'(x^*, y^*, z^*, t^*), \tag{2.2.6}$$

$$v^* = \hat{v} + v'(x^*, y^*, z^*, t^*), \tag{2.2.7}$$

$$w^* = \hat{w} + w'(x^*, y^*, z^*, t^*), \tag{2.2.8}$$

$$p^* = \hat{p} + p'(x^*, y^*, z^*, t^*), \tag{2.2.9}$$

where $(\hat{u}, \hat{v}, \hat{w}, \hat{p})$ is the undisturbed basic flow and pressure and u', v', w', p' are the dimensional disturbances. We can substitute equations (2.2.6) – (2.2.9) into equations (2.2.1) – (2.2.4) and write the equation for the axial component (the cross-sectional components are derived in the same manner) such that

$$\begin{aligned}\frac{\partial}{\partial t^*}(\hat{u}+u') \quad &+ \quad (\hat{u}+u')\frac{\partial}{\partial x^*}(\hat{u}+u') + (\hat{v}+v')\frac{\partial}{\partial y^*}(\hat{u}+u') \\ &+(\hat{w}+w')\frac{\partial}{\partial z^*}(\hat{u}+u') = -\frac{1}{\rho^*}\frac{\partial}{\partial x^*}(\hat{p}+p') + \nu^*\nabla^2(\hat{u}+u'),\end{aligned}$$

$$\begin{aligned}\frac{\partial \hat{u}}{\partial t^*} \quad &+ \quad \frac{\partial u'}{\partial t^*} + \left[\hat{u}\frac{\partial \hat{u}}{\partial x^*} + \hat{u}\frac{\partial u'}{\partial x^*} + u'\frac{\partial \hat{u}}{\partial x^*} + u'\frac{\partial u'}{\partial x^*}\right] + \left[\hat{v}\frac{\partial \hat{u}}{\partial y^*}\right. \\ &+ \quad \left.\hat{v}\frac{\partial u'}{\partial y^*} + v'\frac{\partial \hat{u}}{\partial y^*} + v'\frac{\partial u'}{\partial y^*}\right] + \left[\hat{w}\frac{\partial \hat{u}}{\partial z^*} + \hat{w}\frac{\partial u'}{\partial z^*} + w'\frac{\partial \hat{u}}{\partial z^*}\right. \\ &+ \quad \left.w'\frac{\partial u'}{\partial z^*}\right] = -\frac{1}{\rho^*}\left[\frac{\partial \hat{p}}{\partial x^*} + \frac{\partial p'}{\partial x^*}\right] + \nu^*\left[\nabla^2\hat{u} + \nabla^2 u'\right].\end{aligned} \tag{2.2.10}$$

It is assumed that the steady state basic flow is already a solution of the governing equations and as such this can be removed from our disturbed system so that we are left with

$$\begin{aligned}\frac{\partial u'}{\partial t^*} &+ \hat{u}\frac{\partial u'}{\partial x^*} + u'\frac{\partial \hat{u}}{\partial x^*} + u'\frac{\partial u'}{\partial x^*} + \hat{v}\frac{\partial u'}{\partial y^*} + v'\frac{\partial \hat{u}}{\partial y^*} \\ &+ v'\frac{\partial u'}{\partial y^*} + \hat{w}\frac{\partial u'}{\partial z^*} + w'\frac{\partial \hat{u}}{\partial z^*} + w'\frac{\partial u'}{\partial z^*} = -\frac{1}{\rho^*}\frac{\partial p'}{\partial x^*} + \nu^*\nabla^2 u'. \end{aligned} \tag{2.2.11}$$

By defining L_s, a cross-sectional length scale and U_s, an axial component of velocity and using them to scale the respective dimensional variables such that

$$\begin{aligned}(u^*, v^*, w^*) &= U_s^*(\hat{u} + u', \hat{v} + v', \hat{w} + w') \\ &= U_s^*(U + U_p, V + V_p, W + W_p), \end{aligned} \tag{2.2.12}$$

and

$$(x^*, y^*, z^*) = L_s^*(x, y, z), \tag{2.2.13}$$

with the following non-dimensional expressions for time, perturbation pressure and the Reynolds Number,

$$t^* = \frac{L_s^* t}{U_s^*}, \qquad p^* = \rho^* U_s^{*2}(P + P_p), \qquad Re = \frac{U_s^* L_s^*}{\nu^*}, \tag{2.2.14}$$

equation (2.2.11) can be written as

$$\begin{aligned}\frac{\partial U_p}{\partial t} &+ U\frac{\partial U_p}{\partial x} + U_p\frac{\partial U}{\partial x} + U_p\frac{\partial U_p}{\partial x} + V\frac{\partial U_p}{\partial y} \\ &+ V_p\frac{\partial U}{\partial y} + V_p\frac{\partial U_p}{\partial y} + W\frac{\partial U_p}{\partial z} + W_p\frac{\partial U}{\partial z} + W_p\frac{\partial U_p}{\partial z} \\ &= -\frac{\partial P_p}{\partial x} + \frac{1}{Re}\left(\frac{\partial^2 U_p}{\partial x^2} + \frac{\partial^2 U_p}{\partial y^2} + \frac{\partial^2 U_p}{\partial z^2}\right). \end{aligned} \tag{2.2.15}$$

Equation (2.2.15) is now a dimensionless form of (2.2.2) and equations (2.2.3) and (2.2.4) can be treated similarly resulting in our non-dimensional system of equations for the perturbation quantities

$$\frac{\partial U_p}{\partial x} + \frac{\partial V_p}{\partial y} + \frac{\partial W_p}{\partial z} = 0, \tag{2.2.16}$$

$$\begin{aligned}\frac{\partial U_p}{\partial t} &+ U\frac{\partial U_p}{\partial x} + U_p\frac{\partial U}{\partial x} + U_p\frac{\partial U_p}{\partial x} + V\frac{\partial U_p}{\partial y} + V_p\frac{\partial U}{\partial y} + V_p\frac{\partial U_p}{\partial y} \\ &+ W\frac{\partial U_p}{\partial z} + W_p\frac{\partial U}{\partial z} + W_p\frac{\partial U_p}{\partial z} = -\frac{\partial P_p}{\partial x} + \frac{1}{Re}\nabla^2 U_p, \end{aligned} \tag{2.2.17}$$

$$\frac{\partial V_p}{\partial t} + U\frac{\partial V_p}{\partial x} + U_p\frac{\partial V}{\partial x} + U_p\frac{\partial V_p}{\partial x} + V\frac{\partial V_p}{\partial y} + V_p\frac{\partial V}{\partial y} + V_p\frac{\partial V_p}{\partial y} + W\frac{\partial V_p}{\partial z} + W_p\frac{\partial V}{\partial z} + W_p\frac{\partial V_p}{\partial z} = -\frac{\partial P_p}{\partial y} + \frac{1}{Re}\nabla^2 V_p, \tag{2.2.18}$$

$$\frac{\partial W_p}{\partial t} + U\frac{\partial W_p}{\partial x} + U_p\frac{\partial W}{\partial x} + U_p\frac{\partial W_p}{\partial x} + V\frac{\partial W_p}{\partial y} + V_p\frac{\partial W}{\partial y} + V_p\frac{\partial W_p}{\partial y} + W\frac{\partial W_p}{\partial z} + W_p\frac{\partial W}{\partial z} + W_p\frac{\partial W_p}{\partial z} = -\frac{\partial P_p}{\partial z} + \frac{1}{Re}\nabla^2 W_p. \tag{2.2.19}$$

We have already stated that the disturbances are significantly smaller in magnitude than the basic flow and as such, to leading order, we can neglect multiples of these quantities (or derivatives thereof). The fact that the streamwise length scale of the vortex is long such that $x \gg 1$ compared to $(y, z) = \mathcal{O}(1)$ allows us to employ a boundary-layer type approximation. For our basic flow components (U, V, W), we therefore assume that

$$\frac{\partial}{\partial x} \ll \frac{\partial}{\partial y}, \frac{\partial}{\partial z}. \tag{2.2.20}$$

Equations (2.2.16) – (2.2.19) reduce to

$$\frac{\partial U_p}{\partial x} + \frac{\partial V_p}{\partial y} + \frac{\partial W_p}{\partial z} = 0, \tag{2.2.21}$$

$$\frac{\partial U_p}{\partial t} + U\frac{\partial U_p}{\partial x} + V_p\frac{\partial U}{\partial y} + W_p\frac{\partial U}{\partial z} + V\frac{\partial U_p}{\partial y} + W\frac{\partial U_p}{\partial z} = -\frac{\partial P_p}{\partial x} + \frac{1}{Re}\nabla^2 U_p, \tag{2.2.22}$$

$$\frac{\partial V_p}{\partial t} + U\frac{\partial V_p}{\partial x} + V\frac{\partial V_p}{\partial y} + W\frac{\partial V_p}{\partial z} + V_p\frac{\partial V}{\partial y} + W_p\frac{\partial V}{\partial z} = -\frac{\partial P_p}{\partial y} + \frac{1}{Re}\nabla^2 V_p, \tag{2.2.23}$$

$$\frac{\partial W_p}{\partial t} + U\frac{\partial W_p}{\partial x} + V\frac{\partial W_p}{\partial y} + W\frac{\partial W_p}{\partial z} + V_p\frac{\partial W}{\partial y} + W_p\frac{\partial W}{\partial z} = -\frac{\partial P_p}{\partial z} + \frac{1}{Re}\nabla^2 W_p. \tag{2.2.24}$$

Following Hall and Horseman [23] (see also Tatsumi and Yoshimura [61] and Hein and Theofilis [25]), we consider disturbances with axial and temporal dependence proportional to $\exp[\mathrm{i}\alpha(x - ct)]$ such that

$$(U_p, V_p, W_p, P_p) = \{U_p(y, z),\ V_p(y, z),\ W_p(y, z),\ P_p(y, z)\}\mathrm{e}^{\mathrm{i}\alpha(x-ct)}, \tag{2.2.25}$$

where α = streamwise (or axial, real) wavenumber, c = the corresponding (complex) phase speed of the disturbance and hence the frequency, $\omega = \alpha c$. Equations (2.2.21) – (2.2.24) can now be written as

$$\mathrm{i}\alpha U_p + \frac{\partial V_p}{\partial y} + \frac{\partial W_p}{\partial z} = 0, \tag{2.2.26}$$

$$\begin{aligned}\mathrm{i}\alpha(U-c)U_p \quad + \quad & V_p\frac{\partial U}{\partial y} + W_p\frac{\partial U}{\partial z} + V\frac{\partial U_p}{\partial y} + W\frac{\partial U_p}{\partial z} \\ & = -\mathrm{i}\alpha P_p + \frac{1}{Re}\left(-\alpha^2 U_p + \frac{\partial^2 U_p}{\partial y^2} + \frac{\partial U_p}{\partial z^2}\right),\end{aligned} \tag{2.2.27}$$

and similarly for y and z momentum equations

$$\begin{aligned}\mathrm{i}\alpha(U-c)V_p + V_p\frac{\partial V}{\partial y} \quad + \quad & W_p\frac{\partial V}{\partial z} + V\frac{\partial V_p}{\partial y} + W\frac{\partial V_p}{\partial z} \\ = \quad & -\frac{\partial P_p}{\partial y} + \frac{1}{Re}\left(-\alpha^2 V_p + \frac{\partial^2 V_p}{\partial y^2} + \frac{\partial V_p}{\partial z^2}\right),\end{aligned} \tag{2.2.28}$$

$$\begin{aligned}\mathrm{i}\alpha(U-c)W_p + V_p\frac{\partial W}{\partial y} \quad + \quad & W_p\frac{\partial W}{\partial z} + V\frac{\partial W_p}{\partial y} + W\frac{\partial W_p}{\partial z} \\ = \quad & -\frac{\partial P_p}{\partial z} + \frac{1}{Re}\left(-\alpha^2 W_p + \frac{\partial^2 W_p}{\partial y^2} + \frac{\partial W_p}{\partial z^2}\right).\end{aligned} \tag{2.2.29}$$

Equations (2.2.26) – (2.2.29) are the reduced, dimensionless viscous stability equations. It is worth noting that in most single vortex stability analyses, the (real) azimuthal wave-number n is incorporated into the disturbance as a parameter to further specify the mode being sought; for example through disturbances of the form $\exp[\mathrm{i}\alpha(x-ct)+\mathrm{i}n\theta]$. With a single vortex the perturbations have a distinct θ-dependence, however when further vortices are superimposed onto the original (or the original vortex is moved away from the co-ordinate origin) this θ-dependence is lost and as such the basic flow is written as a function of θ; $U(y,z;\theta)$. The result of this is that eigenvalues and corresponding modes are found for all values of n and with no specific method of identifying a particular azimuthal wave-number, subsequent comparisons to previously published work on a single vortex is left to visual methods or comparing individual eigenvalues.

2.3 Cylindrical Polar Co-ordinates

The governing equations in polar co-ordinates consist of the three-dimensional continuity equation and the polar momentum equations, where (v^*, w^*, u^*) are the (di-

mensional) velocity components in the cylindrical polar coordinates (r^*, θ, x^*), t^*, p^* again denote dimensional time and pressure and ρ^* and ν^* the fluid density and kinematic viscosity respectively. Again, with body forces neglected, the governing equations are

$$\frac{1}{r^*}\frac{\partial(r^*v^*)}{\partial r^*} + \frac{1}{r^*}\frac{\partial w^*}{\partial \theta} + \frac{\partial u^*}{\partial x^*} = 0, \tag{2.3.1}$$

$$\begin{aligned}\frac{\partial u^*}{\partial t^*} &+ v^*\frac{\partial u^*}{\partial r^*} + \frac{w^*}{r^*}\frac{\partial u^*}{\partial \theta} + u^*\frac{\partial u^*}{\partial x^*} = -\frac{\partial p^*}{\partial x^*} \\ &+ \nu^*\left[\frac{1}{r^*}\frac{\partial}{\partial r^*}\left(r^*\frac{\partial u^*}{\partial r^*}\right) + \frac{1}{r^{*2}}\frac{\partial^2 u^*}{\partial \theta^{*2}} + \frac{\partial^2 u^*}{\partial x^{*2}}\right],\end{aligned} \tag{2.3.2}$$

$$\begin{aligned}\frac{\partial v^*}{\partial t^*} &+ v^*\frac{\partial v^*}{\partial r^*} + \frac{w^*}{r^*}\frac{\partial v^*}{\partial \theta} - \frac{w^{*2}}{r^*} + u^*\frac{\partial v^*}{\partial x^*} = -\frac{\partial p^*}{\partial r^*} + \nu^*\left[\frac{1}{r^*}\frac{\partial}{\partial r^*}\left(r^*\frac{\partial v^*}{\partial r^*}\right)\right. \\ &- \left.\frac{v^*}{r^{*2}} + \frac{1}{r^{*2}}\frac{\partial^2 v^*}{\partial \theta^{*2}} - \frac{2}{r*^2}\frac{\partial w^*}{\partial \theta} + \frac{\partial^2 v^*}{\partial x^{*2}}\right],\end{aligned} \tag{2.3.3}$$

$$\begin{aligned}\frac{\partial w^*}{\partial t^*} &+ v^*\frac{\partial w^*}{\partial r^*} + \frac{w^*}{r^*}\frac{\partial w^*}{\partial \theta} - \frac{v^*w^*}{r^*} + u^*\frac{\partial w^*}{\partial x^*} = -\frac{1}{r^*}\frac{\partial p^*}{\partial \theta} \\ &+ \nu^*\left[\frac{1}{r^*}\frac{\partial}{\partial r^*}\left(r^*\frac{\partial w^*}{\partial r^*}\right) - \frac{w^*}{r^{*2}} + \frac{1}{r^{*2}}\frac{\partial^2 w^*}{\partial \theta^{*2}} + \frac{2}{r^{*2}}\frac{\partial v^*}{\partial \theta} + \frac{\partial^2 w^*}{\partial x^{*2}}\right].\end{aligned} \tag{2.3.4}$$

2.3.1 Derivation of the Disturbance Equations

As with the derivation of the equations in a Cartesian frame, disturbances of the form $u^* = \hat{u} + u'(r^*, \theta, x^*, t^*), etc$ are considered. Again, the steady-state basic flow can be eliminated from the governing equations as it is assumed to be a solution, leaving only the disturbed flow (v', w', u'). Defining characteristic scales r_s^*, a typical radial length scale and U_s^*, a typical axial speed, we can then define non-dimensional variables

$$(r^*, \theta, x^*) = r_s^*(r, \theta, x), \tag{2.3.5}$$

and

$$\begin{aligned}(v^*, w^*, u^*) &= U_s^*(\hat{v} + v', \hat{w} + w', \hat{u} + u') \\ &= U_s^*(V + V_p, W + W_p, U + U_p).\end{aligned} \tag{2.3.6}$$

As before, the non-dimensional time, perturbation pressure and the non-dimensional variable, the Reynolds Number are given by

$$t^* = \frac{r_s^* t}{U_s^*}, \qquad p^* = \rho^* U_s^{*2}(P + P_p), \qquad Re = \frac{U_s^* r_s^*}{\nu^*}. \tag{2.3.7}$$

Substitution into (2.3.1) – (2.3.4) and retaining only those terms that are of first order in the disturbance quantities yields

$$\frac{V_p}{r} + \frac{\partial V_p}{\partial r} + \frac{1}{r}\frac{\partial W_p}{\partial \theta} + \frac{\partial U_p}{\partial x} = 0, \tag{2.3.8}$$

$$\begin{aligned}\frac{\partial V_p}{\partial t} + U\frac{\partial V_p}{\partial x} + \frac{W}{r}\frac{\partial V_p}{\partial \theta} &= -\frac{\partial P_p}{\partial r} + \frac{1}{Re}\left[\frac{1}{r}\frac{\partial V_p}{\partial r} + \frac{\partial^2 V_p}{\partial r^2} - \frac{V_p}{r^2}\right. \\ &+ \left.\frac{1}{r^2}\frac{\partial^2 V_p}{\partial \theta^2} - \frac{2}{r^2}\frac{\partial W_p}{\partial \theta} + \frac{\partial^2 V_p}{\partial x^2}\right],\end{aligned} \tag{2.3.9}$$

$$\begin{aligned}\frac{\partial W_p}{\partial t} &+ U\frac{\partial W_p}{\partial x} + \frac{W}{r}\frac{\partial W_p}{\partial \theta} + V_p\frac{\partial W}{\partial r} + \frac{W_p}{r}\frac{\partial W}{\partial \theta} + \frac{WV_P}{r} = -\frac{1}{r}\frac{\partial P_p}{\partial \theta} \\ &+ \frac{1}{Re}\left[\frac{1}{r}\frac{\partial W_p}{\partial r} + \frac{\partial^2 W_p}{\partial r^2} - \frac{W_p}{r^2} + \frac{1}{r^2}\frac{\partial^2 W_p}{\partial \theta^2} + \frac{2}{r^2}\frac{\partial V_p}{\partial \theta} + \frac{\partial^2 W_p}{\partial x^2}\right],\end{aligned} \tag{2.3.10}$$

$$\begin{aligned}\frac{\partial U_p}{\partial t} + V_p\frac{\partial U}{\partial r} &+ \frac{W}{r}\frac{\partial U_p}{\partial \theta} + \frac{W_p}{r}\frac{\partial U}{\partial \theta} + U\frac{\partial U_p}{\partial x} \\ &= -\frac{\partial P_p}{\partial x} + \frac{1}{Re}\left[\frac{1}{r}\frac{\partial U_p}{\partial r} + \frac{\partial^2 U_p}{\partial r^2} + \frac{1}{r^2}\frac{\partial^2 U_p}{\partial \theta^2} + \frac{\partial^2 U_p}{\partial x^2}\right],\end{aligned} \tag{2.3.11}$$

where we have denoted the basic flow by $(V, W, U) = (0, W_B, U_B)$. As with the Cartesian case, we consider perturbations of the form

$$(V_p, W_p, U_p, P_p) = (V_p, W_p, U_p, P_p)\mathrm{e}^{\mathrm{i}\alpha(x-ct)}.$$

In what follows it proves convenient to define

$$\mathcal{L} = \left[\frac{1}{r}\frac{\partial}{\partial r} + \frac{\partial^2}{\partial r^2} + \frac{1}{r^2}\frac{\partial^2}{\partial \theta^2} - \alpha^2\right].$$

Equations (2.3.8) – (2.3.11) can then be written as

$$\frac{V_p}{r} + \frac{\partial V_p}{\partial r} + \frac{1}{r}\frac{\partial W_p}{\partial \theta} + \mathrm{i}\alpha U_p = 0, \tag{2.3.12}$$

$$\mathrm{i}\alpha(U_B - c)V_p + \frac{W_B}{r}\frac{\partial V_p}{\partial \theta} = -\frac{\partial P_p}{\partial r} + \frac{1}{Re}\mathcal{L}(V_p) - \frac{V_p}{r^2 Re} - \frac{2}{r^2 Re}\frac{\partial W_p}{\partial \theta}, \tag{2.3.13}$$

$$\begin{aligned} \mathrm{i}\alpha(U_B - c)W_p &+ \frac{W_B}{r}\frac{\partial W_p}{\partial \theta} + V_p\frac{\partial W_B}{\partial r} + \frac{W_p}{r}\frac{\partial W_B}{\partial \theta} + \frac{W_B V_P}{r} \\ &= -\frac{1}{r}\frac{\partial P_p}{\partial \theta} + \frac{1}{Re}\mathcal{L}(W_p) - \frac{W_p}{r^2 Re} + \frac{2}{r^2 Re}\frac{\partial V_p}{\partial \theta}, \end{aligned} \tag{2.3.14}$$

$$\mathrm{i}\alpha(U_B - c)U_p + \frac{W_B}{r}\frac{\partial U_p}{\partial \theta} + V_p\frac{\partial U_B}{\partial r} + \frac{W_p}{r}\frac{\partial U_B}{\partial \theta} = -\mathrm{i}\alpha P_p + \frac{1}{Re}\mathcal{L}(U_p), \tag{2.3.15}$$

which are the non-dimensional system of equations governing the linearised stability of our trailing line vortex base flow.

2.4 Constructing the Eigenvalue Problem

2.4.1 Inviscid (Rayleigh) Instability

For the inviscid problem it proves convenient to derive the equation in its Cartesian form and then convert to polar co-ordinates. In the inviscid limit, Re formally approaches infinity and hence the components of the governing equations that are multiplied by Re^{-1} can be neglected at leading order. It will be shown in section 4.3 that for this inviscid stability analysis it is acceptable to disregard the azimuthal components of the basic flow. Re-writing equations (2.2.26) – (2.2.29) in this inviscid form gives

$$\mathrm{i}\alpha U_p + \frac{\partial V_p}{\partial y} + \frac{\partial W_p}{\partial z} = 0, \tag{2.4.1}$$

$$\mathrm{i}\alpha(U - c)U_p + V_p\frac{\partial U}{\partial y} + W_p\frac{\partial U}{\partial z} = -\mathrm{i}\alpha P_p, \tag{2.4.2}$$

$$\mathrm{i}\alpha(U - c)V_p = -\frac{\partial P_p}{\partial y}, \tag{2.4.3}$$

$$\mathrm{i}\alpha(U - c)W_p = -\frac{\partial P_p}{\partial z}. \tag{2.4.4}$$

Differentiating (2.4.3) with respect to y and (2.4.4) with respect to z and combining the results gives

$$(U - c)\left[\frac{\partial^2}{\partial y^2} + \frac{\partial^2}{\partial z^2} - \alpha^2\right]P_p - 2\left[\frac{\partial U}{\partial y}\frac{\partial}{\partial y} + \frac{\partial U}{\partial z}\frac{\partial}{\partial z}\right]P_p = 0. \tag{2.4.5}$$

Equation (2.4.5) is often referred to as the two-dimensional Rayleigh equation in Cartesian co-ordinates. By defining

$$\mathcal{J} = \left[\frac{\partial^2}{\partial y^2} + \frac{\partial^2}{\partial z^2} - \alpha^2\right] \quad \text{and} \quad \mathcal{H} = \left[\frac{\partial U}{\partial y}\frac{\partial}{\partial y} + \frac{\partial U}{\partial z}\frac{\partial}{\partial z}\right],$$

we can re-write (2.4.5) in the form

$$(U\mathcal{J} - 2\mathcal{H})P_p = c\mathcal{J}P_p. \tag{2.4.6}$$

This is now a generalised eigenvalue problem in the form $\mathbf{Ax} = c\mathbf{Bx}$. The eigenfunctions, $\mathbf{x}$ (or equivalently $[P_p]$) can only exist if α and ω are constrained to satisfy the dispersion relation, $\mathbf{D}[\alpha, \omega] = 0$. It is more convenient for our subsequent two-dimensional analysis to convert the governing equation into cylindrical polar co-ordinates. This can be achieved by setting

$$r^2 = y^2 + z^2, \qquad y = r\cos\theta, \qquad z = r\sin\theta. \tag{2.4.7}$$

Equation (2.4.5) can be re-written as the two-dimensional Rayleigh equation in cylindrical polar co-ordinates

$$(U_B - c)\left[\frac{\partial^2}{\partial r^2} + \frac{1}{r}\frac{\partial}{\partial r} + \frac{1}{r^2}\frac{\partial^2}{\partial\theta^2} - \alpha^2\right]P_p - 2\left[\frac{\partial U_B}{\partial r}\frac{\partial}{\partial r} + \frac{1}{r^2}\frac{\partial U_B}{\partial\theta}\frac{\partial}{\partial\theta}\right]P_p = 0. \tag{2.4.8}$$

As for the Cartesian case, we define

$$\mathcal{K} = \left[\frac{\partial^2}{\partial r^2} + \frac{1}{r}\frac{\partial}{\partial r} + \frac{1}{r^2}\frac{\partial^2}{\partial\theta^2} - \alpha^2\right] \quad \text{and} \quad \mathcal{R} = \left[\frac{\partial U_B}{\partial r}\frac{\partial}{\partial r} + \frac{1}{r^2}\frac{\partial U_B}{\partial\theta}\frac{\partial}{\partial\theta}\right],$$

and can re-write (2.4.8) as

$$(U\mathcal{K} - 2\mathcal{R})P_p = c\mathcal{K}P_p. \tag{2.4.9}$$

Again, this is now a Generalised eigenvalue problem in the form $\mathbf{Ax} = c\mathbf{Bx}$, subject to $\mathbf{D}[\alpha, \omega] = 0$.

2.4.2 Viscous Problem

We note that to derive our eigenvalue problem for the viscous instability, equations (2.2.26) – (2.2.29) require no further reduction and represent an eigenvalue problem $\mathbf{Ax} = \lambda\mathbf{Bx}$ with the eigenfunctions, $\mathbf{x}$ in terms of the four perturbation quantities (U_p, V_p, W_p, P_p) and an eigenvalue $\lambda = \omega = \alpha c$. In this case the eigenvalue problem can be written as

$$\begin{bmatrix} \mathcal{Q} & \frac{\partial U}{\partial y} & \frac{\partial U}{\partial z} & \mathrm{i}\alpha \\ 0 & \mathcal{Q}+\frac{\partial V}{\partial y} & \frac{\partial V}{\partial z} & \frac{\partial}{\partial y} \\ 0 & \frac{\partial W}{\partial y} & \mathcal{Q}+\frac{\partial W}{\partial z} & \frac{\partial}{\partial z} \\ \mathrm{i}\alpha & \frac{\partial}{\partial y} & \frac{\partial}{\partial z} & 0 \end{bmatrix} \begin{bmatrix} U_p \\ V_p \\ W_p \\ P_p \end{bmatrix} = \omega \begin{bmatrix} \mathrm{i} & 0 & 0 & 0 \\ 0 & \mathrm{i} & 0 & 0 \\ 0 & 0 & \mathrm{i} & 0 \\ 0 & 0 & 0 & 0 \end{bmatrix} \begin{bmatrix} U_p \\ V_p \\ W_p \\ P_p \end{bmatrix},$$

where

$$\mathcal{Q} = \mathrm{i}\alpha U + V\frac{\partial}{\partial y} + W\frac{\partial}{\partial z} - \frac{1}{Re}\left(-\alpha^2 + \frac{\partial^2}{\partial y^2} + \frac{\partial^2}{\partial z^2}\right). \tag{2.4.10}$$

Unlike the inviscid case where the stability equation in Cartesian co-ordinates can be easily transformed to cylindrical polar form by applying the relevant relationships, in the viscous case it proves far more involved and as such a derivation of the equations from the full equations of motion in cylindrical polar co-ordinates is preferred. As in the Cartesian case, equations (2.3.12) – (2.3.15) represent an eigenvalue problem in terms of the four perturbation quantities (U_p, V_p, W_p, P_p) and an eigenvalue ω such that it can be written in the generalised form $\mathbf{Ax} = \lambda\mathbf{Bx}$ with the eigenfunctions $\mathbf{x}$ as

$$\begin{bmatrix} \mathcal{Q} & \frac{\partial U_B}{\partial r} & \frac{1}{r}\frac{\partial U_B}{\partial \theta} & \mathrm{i}\alpha \\ 0 & \mathcal{Q}+\frac{1}{r^2 Re} & \frac{2}{r^2 Re}\frac{\partial}{\partial \theta} & \frac{\partial}{\partial r} \\ 0 & \mathcal{M} & \mathcal{Q}+\mathcal{N} & \frac{1}{r}\frac{\partial}{\partial \theta} \\ \mathrm{i}\alpha & \frac{1}{r}+\frac{\partial}{\partial r} & \frac{1}{r}\frac{\partial}{\partial \theta} & 0 \end{bmatrix} \begin{bmatrix} U_p \\ V_p \\ W_p \\ P_p \end{bmatrix} = \omega \begin{bmatrix} \mathrm{i} & 0 & 0 & 0 \\ 0 & \mathrm{i} & 0 & 0 \\ 0 & 0 & \mathrm{i} & 0 \\ 0 & 0 & 0 & 0 \end{bmatrix} \begin{bmatrix} U_p \\ V_p \\ W_p \\ P_p \end{bmatrix},$$

where

$$\mathcal{Q} = \mathrm{i}\alpha U_B + \frac{W_B}{r}\frac{\partial}{\partial \theta} - \frac{1}{Re}\left(\frac{1}{r}\frac{\partial}{\partial r} + \frac{\partial^2}{\partial r^2} + \frac{1}{r^2}\frac{\partial^2}{\partial \theta^2} - \alpha^2\right), \tag{2.4.11}$$

and

$$\mathcal{M} = \frac{\partial W_B}{\partial r} + \frac{W_B}{r} - \frac{2}{r^2 Re}\frac{\partial}{\partial \theta}, \quad \mathcal{N} = \frac{1}{r}\frac{\partial W_B}{\partial \theta} + \frac{1}{r^2 Re}. \tag{2.4.12}$$

An alternative method of producing an eigenvalue problem from the governing equations is to rearrange them to form two equations in two unknowns, namely the cross-flow perturbation quantities $[V_p, W_p]$. The resulting equations are effectively a two-dimensional version of the Orr-Sommerfeld and Squire equations [62] which

were first solved numerically by Tatsumi and Yoshimura [61] for Plane Poiseuille flow through a rectangular duct. The derivation of the Cartesian version of these equations can be found in Appendix B along with the final equation in polar co-ordinates. Whilst this system produces a smaller eigenvalue problem in terms of the size of the corresponding matrices, the presence of fourth order derivatives will usually require a larger domain to ensure the higher derivatives of the perturbation cross-flow components decay to zero. This will undoubtedly also require the use of significantly more grid resolution to accurately resolve the flow and hence the savings made in using this formulation are likely to be lost by the increased problem size resulting from more discretised grid points [62].

2.4.3 Characterisation of the Flow Instability

It is useful to define the terms used to categorise whether a flow is stable or unstable. We have stated that, in the inviscid case, the eigenvalue is the complex phase velocity, $c = c_r + c_i$, where c_r is the wave speed and c_i describes the amplification or damping of the oscillation. For the viscous case, the complex frequency, $\omega = \omega_r + \omega_i$ is the eigenvalue where $\omega = \alpha c \equiv \alpha c_r + \alpha c_i$. We define αc_r as being the wave frequency and αc_i as the temporal growth rate of the oscillation. It is the sign of the temporal growth rate that determines the flow stability characteristics. As, for this analysis, the axial wave-number α is always considered to be positive, the stability characteristics of the flow can be defined as follows;

$c_i < 0$ The flow is **stable**,

$c_i > 0$ The flow is **unstable**,

$c_i = 0$ The flow is **neutrally stable**.

Chapter 3

Numerical Methods

3.1 Introduction

Due to their complexity, the set of equations derived in chapter 2 are unable to be solved analytically and whilst asymptotic solutions based, for example, on a short-wave or long-wave approximation can provide a leading order behaviour of the system, the most appropriate method of obtaining detailed information about the stability characteristics of this complex system is through some form of numerical analysis. The particular methods employed here involve discretising the governing equations over a closed domain to produce differentiation matrices which describe the components of the final generalised eigenvalue problem $\mathbf{Ax} = c\mathbf{Bx}$ or linear equation $\mathbf{Ax} = \mathbf{b}$.

3.1.1 Inviscid Disturbances

The governing equations for an inviscid analysis, derived in section 2.4.1, become a second order partial differential equation (PDE) written in cylindrical polar co-ordinates (r, θ, x) (or in Cartesian co-ordinates (y, z, x)) in terms of the perturbed pressure, P_p, the basic flow and respective eigenvalue such that $\mathcal{L}(y, z; U, c)P_p = 0$ where $\mathcal{L}$ is a second order linear operator.

Two distinct numerical methods are employed for the inviscid case; a global pseudo-spectral eigenvalue solver, where in this sense global means that it solves for all eigenvalues and corresponding eigenfunctions over the entire domain, and a local

finite-difference iterative solver which converges onto a single eigenvalue targeted from an intial guess.

The first incarnation of the global code was written using the commercial matrix algebra software, MATLAB™ based on the pseudo-spectral methods of Trefethen [65] and refined to our particular problem utilising the inbuilt MATLAB™ function `eig.m` which employs a QZ algorithm to obtain the eigenvalues/functions. A subsequent version was written in Fortran 90 to allow portability to larger capacity machines for higher resolution runs without the need for an individual MATLAB™ licence. LAPACK (Linear Algebra PACKage) fortran routines obtained from *Netlib* were used to compute the eigenvalues. Both 'global' codes were tested and shown to produce the same results for a variety of parameters thus providing a useful test of the integrity of these codes.

Computational expense in terms of both processor time and memory play a large part in determining the effectiveness and viability of global solvers to large scale eigenvalue problems. This particular case is no different and whilst the global solver is sufficient in the inviscid regime to give stability results to an acceptable accuracy, an iterative local solver is used to verify the integrity of these results and improve the converged accuracy without exceeding machine memory or experiencing excessive run times. An iterative solver based on the work of Otto and Denier [47] using finite-differences was written in Fortran 90 for this purpose. Results from the 'global' codes were used to test the integrity of the 'local' code.

3.1.2 Viscous Disturbances

The viscous eigenvalue problem, derived in section 2.4.2, consists of a set of four equations with the frequency ω being the eigenvalue and the perturbation quantity $[U_p, V_p, W_p, P_p]$ the corresponding eigenfunction. The resulting problem remains second order in terms of the size of the largest derivative but has a leading matrix dimension of $[4(N_y - 1)(N_z - 1)]$.

The viscous code has been written in both Cartesian and cylindrical polar coordinates to allow for a variety of verification methods to be utilised and for cross-checking of results. Although it is beyond the scope of this particular study, it is

worth noting that the two different co-ordinate basis codes allow for most regular (and infinite domain) stability geometries to be studied, especially when considered with some form of grid transformation.

Problems with machine memory arose when the resolution was increased towards an acceptable level. The discretisation employed for the viscous problem uses substantially more memory than is required in the inviscid problem as all four perturbed quantities are used in the eigenvalue problem rather than the single perturbed pressure as in the inviscid case. With typical matrices consisting of 10^6 double-precision complex variables, allocated processor memory is quickly used up. Parallel Fortran 90 versions of both codes were written to not only save on processor memory by distributing data across multiple processors but in doing so, also speed up the computation time. As will be explained later, ScaLAPACK, PBLAS and ARPACK (an implementation of the implicitly restarted Arnoldi algorithm) were used to solve the eigenvalue problem in parallel. Further to the Cartesian and polar global codes, by combining the finite-difference iterative scheme and the parallelisation methods of the global code, a large scale iterative local solver was developed that allows greater accuracy and speed without the need for a parallel global (eigenvalue) solution routine.

3.2 Spectral Discretisation

The pseudo-spectral discretisation scheme used and discussed in detail below is based on the work of Trefethen [65] whereby the domain is divided up using a number of distinct polynomials. The discussion of the differentiation process which follows is in reference to the radial direction in cylindrical polar co-ordinates. The same methodology is applied to the (y, z)-plane (x being the axial or streamwise direction) when discretising in Cartesian co-ordinates.

3.2.1 Radial Discretisation

The radial domain is the bounded and non-periodic region, $r \in [-1, 1]$. Algebraic polynomials which produce an irregular grid (preferably clustered at the boundaries;

we approximate our infinite domain by a semi-infinite bounded domain) are used for the discretisation. Of these, Chebyshev polynomials are the simplest and given by

$$r_j = \cos\left(\frac{j\pi}{N}\right), \qquad j = 0, 1, \cdots, N. \tag{3.2.1}$$

These are the equi-spaced points on one half-circle, projected down onto a horizontal plane (figure 3.1). Following Trefethen [65], the Chebyshev spectral differentiation matrix is, for $N \geqslant 1$, a two-dimensional matrix, D_N, of size $(N+1) \times (N+1)$. D_N is indexed from 0 to N by the differentiation matrix row/column indices (i, j) as follows

$$(D_N)_{ij} = \frac{c_i}{c_j}\frac{(-1)^{i+j}}{(r_i - r_j)}, \qquad i \neq j, \qquad i, j = 0, \cdots, N, \tag{3.2.2}$$

$$(D_N)_{ii} = -\sum_{\substack{j=0 \\ j\neq 1}}^{N} (D_N)_{ij}, \tag{3.2.3}$$

$$c_{i/j} = \begin{cases} 2 & , \quad i/j = 0 \text{ or } N \\ 1 & , \quad \text{otherwise,} \end{cases} \tag{3.2.4}$$

with the resulting differentiation matrices have no specific order except for the antisymmetry condition [65],

$$(D_N)_{ij} = -(D_N)_{N-i,N-j}. \tag{3.2.5}$$

As an example, a Chebyshev spectral differentiation matrix for $N = 5$ is given below,

$$D_5 = \begin{bmatrix} 8.5000 & -10.4721 & 2.8944 & -1.5279 & 1.1056 & -0.5000 \\ 2.6180 & -1.1708 & -2.0000 & 0.8944 & -0.6180 & 0.2764 \\ -0.7236 & 2.0000 & -0.1708 & -1.6180 & 0.8944 & -0.3820 \\ 0.3820 & -0.8944 & 1.6180 & 0.1708 & -2.0000 & 0.7236 \\ -0.2764 & 0.6180 & -0.8944 & 2.0000 & 1.1708 & -2.6180 \\ 0.5000 & -1.1056 & 1.5279 & -2.8944 & 10.4721 & -8.5000 \end{bmatrix}.$$

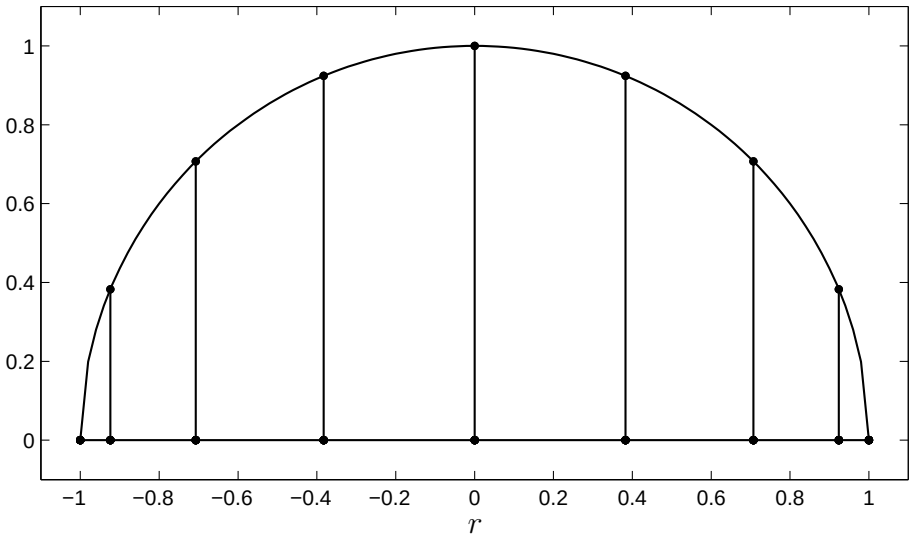

Figure 3.1: Chebyshev points, r_j, $j = 1, \cdots, N$ [65].

3.2.2 Azimuthal Differentiation

The domain is discretised in the azimuthal direction using trigonometric polynomials, the periodic nature of the computational space (the interval $[0, 2\pi]$ corresponds to the computational domain) is particularly suited to this type of disretisation. The interval h, representing the discretisation of the domain $[0, 2\pi]$ over N points, can be described as $h = 2\pi/N$ which can be visualised as the projection of the points at the crests of the basis function onto the horizontal (θ) axis as shown in figure 3.2.

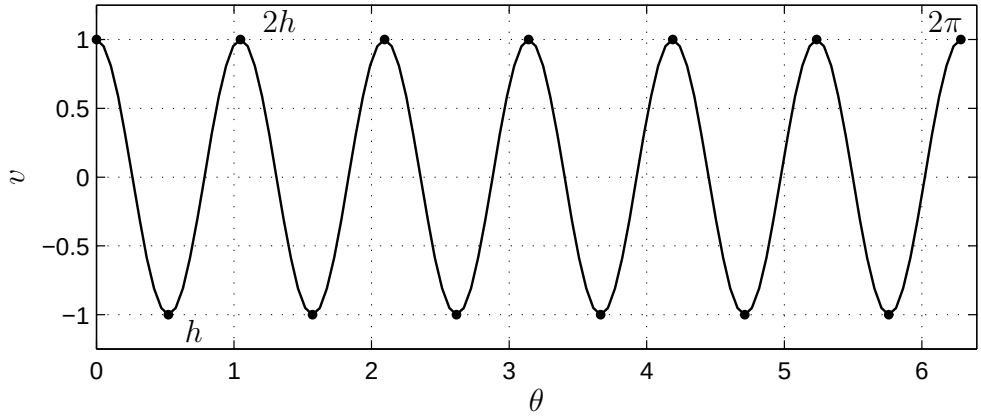

Figure 3.2: The periodic grid function $e^{iN\theta/2}$, $N = 6$ [65].

Now, following Trefethen [65], the Discrete Fourier Transform (DFT) is written as

$$\hat{v}_k = h\sum_{j=1}^{N} e^{-ik\theta_j} v_j, \qquad k = -\frac{N}{2}, \cdots, \frac{N}{2}, \tag{3.2.6}$$

and accordingly, the inverse Discrete Fourier Transform (iDFT) is

$$v_j = \frac{1}{2\pi}\sum_{k=-N/2+1}^{N/2} e^{ik\theta_j}\hat{v}_k, \qquad j = 1, \cdots, N, \tag{3.2.7}$$

where we can say, $\hat{v}_{-N/2} = \hat{v}_{N/2}$ so that

$$v_j = \frac{1}{2\pi}\sum_{k=-N/2}^{N/2}{}' e^{ik\theta_j}\hat{v}_k, \qquad j = 1, \cdots, N, \tag{3.2.8}$$

where the prime indicates $k = \pm N/2$ are multiplied by $1/2$. We therefore have

$$p(\theta) = \frac{1}{2\pi}\sum_{k=-N/2}^{N/2}{}' e^{ik\theta}\hat{v}_k, \qquad \theta \in [0, 2\pi]. \tag{3.2.9}$$

Following Trefethen [65] we can interpolate the grid function v by expressing it as a linear combination of translated delta functions obtained through expansion of (3.2.9) such that,

$$\delta_j = \begin{cases} 1 & , \quad j = 0 \\ 0 & , \quad j \neq 0. \end{cases} \tag{3.2.10}$$

From the DFT, $\hat{\delta}_k = h$ for each k,

$$p(\theta) = \frac{h}{2\pi}\sum_{k=-N/2}^{N/2}{}' e^{ik\theta} = \frac{h}{2\pi}\cos\left(\frac{\theta}{2}\right)\frac{\sin\left(\frac{N\theta}{2}\right)}{\sin\left(\frac{\theta}{2}\right)}. \tag{3.2.11}$$

Therefore, if we set

$$S_N = \frac{h}{2\pi}\frac{\sin\left(\frac{\pi\theta}{h}\right)}{\tan\left(\frac{\theta}{2}\right)}, \tag{3.2.12}$$

which can also be written in terms of a series expansion

$$S_N = 1 + \left(-\frac{\pi^2}{6h^2} - \frac{1}{12}\right)\theta^2 \quad + \quad \left(\frac{\pi^4}{120h^4} - \frac{1}{120} + \frac{2\pi^2 + h^2}{144h^2}\right)\theta^4 + \mathcal{O}(\theta^5), \tag{3.2.13}$$

we obtain an expression for the interpolant at each position, θ. Now, if we take the derivatives of S_N and employ the substitution $\theta = jh$ we can derive the entries of the differentiation matrices for any position θ_j. Also we note the trigonometric relationship, $\sec^2\theta = 1 + \tan^2\theta$. For the first derivative

$$S'_N(\theta_j) = \frac{1}{2}\frac{\cos(\pi j)}{\tan\left(\frac{jh}{2}\right)}, \tag{3.2.14}$$

with the respective series expansion being

$$S'_N(\theta_j) = 2\left(-\frac{\pi^2}{6h^2} - \frac{1}{12}\right)\theta \quad + \quad 4\left(\frac{\pi^4}{120h^4} - \frac{1}{120} + \frac{2\pi^2 + h^2}{144h^2}\right)\theta^3 + \mathcal{O}(\theta^4),$$

$$S'_N(\theta_j) = \begin{cases} \frac{1}{2}(-1)^j \cot\left(\frac{jh}{2}\right) & , \quad j \neq 0 \\ \\ 0 & , \quad j = 0, \end{cases}$$

and similarly for subsequent derivatives.

The second derivative;

$$S''_N(\theta_j) = -\frac{1}{2}(-1)^j \frac{\sec^2\left(\frac{jh}{2}\right)}{\tan^2\left(\frac{jh}{2}\right)}, \tag{3.2.15}$$

$$S''_N(\theta_j) = 2\left(-\frac{\pi^2}{6h^2} - \frac{1}{12}\right) \quad + \quad 12\left(\frac{\pi^4}{120h^4} - \frac{1}{120} + \frac{2\pi^2 + h^2}{144h^2}\right)\theta^2 + \mathcal{O}(\theta^3),$$

$$S''_N(\theta_j) = \begin{cases} -\frac{1}{2}\frac{(-1)^j}{\sin^2\left(\frac{jh}{2}\right)} & , \quad j \neq 0 \\ \\ -\frac{\pi^2}{3h^2} - \frac{1}{6} & , \quad j = 0. \end{cases}$$

The third derivative;

$$S'''_N(\theta_j) = -\left(\frac{\pi^2}{2h^2}\right)\frac{(-1)^j}{\tan\left(\frac{jh}{2}\right)} + \frac{3(-1)^j}{4}\left[\frac{\sec^4\left(\frac{jh}{2}\right)}{\tan^3\left(\frac{jh}{2}\right)} - \frac{\sec^2\left(\frac{jh}{2}\right)}{\tan\left(\frac{jh}{2}\right)}\right], \tag{3.2.16}$$

$$S'''_N(\theta_j) = 24\left(\frac{\pi^4}{120h^4} - \frac{1}{120} + \frac{2\pi^2 + h^2}{144h^2}\right)\theta + \mathcal{O}(\theta^2),$$

$$S'''_N(\theta_j) = \begin{cases} -\left(\frac{\pi^2}{2h^2}\right)\frac{(-1)^j}{\tan\left(\frac{jh}{2}\right)} + \frac{3(-1)^j}{4\cos\left(\frac{jh}{2}\right)}\left[\frac{1}{\sin^3\left(\frac{jh}{2}\right)} - \frac{1}{\sin\left(\frac{jh}{2}\right)}\right] & , \quad j \neq 0 \\ \\ 0 & , \quad j = 0. \end{cases}$$

The fourth derivative;

$$S_N^{(IV)}(\theta_j) = \left(\frac{\pi}{h}\right)^2 \frac{(-1)^j}{\sin^2\left(\frac{jh}{2}\right)} - \frac{3}{2}\frac{(-1)^j}{\sin^4\left(\frac{jh}{2}\right)\cos^2\left(\frac{jh}{2}\right)} + \frac{5}{2}\frac{(-1)^j}{\sin^2\left(\frac{jh}{2}\right)\cos^2\left(\frac{jh}{2}\right)} - \frac{(-1)^j}{\cos^2\left(\frac{jh}{2}\right)}, \tag{3.2.17}$$

$$S_N^{(IV)}(\theta_j) = 24\left(\frac{\pi^4}{120h^4} - \frac{1}{120} + \frac{2\pi^2+h^2}{144h^2}\right) + \mathcal{O}(\theta),$$

$$S_N^{(IV)}(\theta_j) = \begin{cases} \left(\frac{\pi}{h}\right)^2 \frac{(-1)^j}{\sin^2\left(\frac{jh}{2}\right)} - \frac{(-1)^j}{2\cos^2\left(\frac{jh}{2}\right)}\left[\frac{3}{\sin^4\left(\frac{jh}{2}\right)} - \frac{5}{\sin^2\left(\frac{jh}{2}\right)} + 2\right] & , \quad j \neq 0 \\ \frac{\pi^4}{5h^4} - \frac{1}{5} + \frac{2\pi^2+h^2}{6h^2} & , \quad j = 0. \end{cases}$$

The values of $S_N(\theta_j)$ (and its derivatives) are the entries of one column of the differentiation matrix. They form the N^{th} column of the $N \times N$ differentiation matrix. The other entries are the same as the N^{th} column but on corresponding diagonals. It should be noted that for the odd derivatives there is a loss of symmetry about the diagonal of the differentiation matrix

$$D_N^{(odd)}(i,j) = -D_N^{(odd)}(j,i). \tag{3.2.18}$$

The Fourier spectral differentiation matrices for the first and second derivatives can be written as follows

$$D_\theta = \begin{bmatrix} 0 & \ddots & -\frac{1}{2}\cot\frac{1h}{2} \\ -\frac{1}{2}\cot\frac{1h}{2} & \ddots & \frac{1}{2}\cot\frac{2h}{2} \\ \frac{1}{2}\cot\frac{2h}{2} & \ddots & -\frac{1}{2}\cot\frac{3h}{2} \\ -\frac{1}{2}\cot\frac{3h}{2} & \ddots & \vdots \\ \vdots & \ddots & \frac{1}{2}\cot\frac{1h}{2} \\ \frac{1}{2}\cot\frac{1h}{2} & \ddots & 0 \end{bmatrix}, \qquad D_\theta^2 = \begin{bmatrix} \ddots & \vdots & \ddots \\ \ddots & -\frac{1}{2}\csc^2\left(\frac{2h}{2}\right) & \ddots \\ \ddots & \frac{1}{2}\csc^2\left(\frac{1h}{2}\right) & \ddots \\ \ddots & -\frac{\pi^2}{3h^2} - \frac{1}{6} & \ddots \\ \ddots & \frac{1}{2}\csc^2\left(\frac{1h}{2}\right) & \ddots \\ \ddots & \vdots & \ddots \end{bmatrix}.$$

3.2.3 Grid Clustering

Whilst one of the main advantages to using pseudo-spectral numerical methods is undoubtedly the higher degree of accuracy for a lower number of collocation points (and hence, decreased computational expense), the scale of the eigenvalue problem considered here results in regular exhaustion of computational resources. This is amplified by the fact that Chebyshev collocation method concentrates grid points

about the outer regions of our domain, whereas for the vortex problem we ideally want the grid points concentrated near the centre (or close to the vortices). For this reason it was found necessary to include some form of grid clustering in the algorithm. Several methods were investigated, a logarithmic algorithm

$$r_c = \frac{\log(1 + s_1(1 + r)) - \log(1 + s_1(1 - r))}{\log(s_2)}, \qquad s > 1, \tag{3.2.19}$$

where $s_1 = 2(s - 1)$ and $s_2 = 1 + 2s_1$, and a trigonometric algorithm similar to that used by [25],

$$r_c = \frac{\tan\left(\frac{s\pi r}{2}\right)}{\tan\left(\frac{\pi r}{2}\right)}, \qquad 0 < s < 1. \tag{3.2.20}$$

In both cases r_c is the new set of clustered grid points and s is the clustering parameter, with range as shown. The respective derivatives of the clustering functions are used to adjust the differentiation matrices accordingly. Of the two methods outlined above, the trigonometric algorithm of Hein and Theofilis [25] (3.2.20) proved to be the most effective in terms of delivering a good degree of points clustered about the origin whilst maintaining adequate resolution in the domain extremities. Figure 3.3 illustrates the degree by which the clustering parameter, s changes the positioning of the Chebyshev points using equation (3.2.20). It can be seen from this figure that relatively high values of s are required to 'pull' the points away from the boundaries.

The validity of the clustering routine is illustrated in figures 3.4 – 3.6, which show the eigenspectra for the stability of plane Poiseuille flow (PPF) in a pipe which was used to verify the axial component of the viscous polar code (see section 3.7.3). Whilst there are some small differences in the results, in general, the structure of the spectrum is unchanged. It is worth noting that pseudo-spectral clustering is not required for plane Poiseuille flow as the grid points are naturally clustered about the regions of interest, namely the boundaries. The differences seen in figure 3.4 can be attributed to the progressive relocation of grid points away from the boundaries which in turn results in a decreased resolution of, what are, viscous wave modes (stable). Despite this however, the well documented PPF results used in this case illustrate that the clustering algorithm does not alter the structure of the eigenspectra. The number of grid points used was $(N_r, N_\theta) = (61, 32)$.

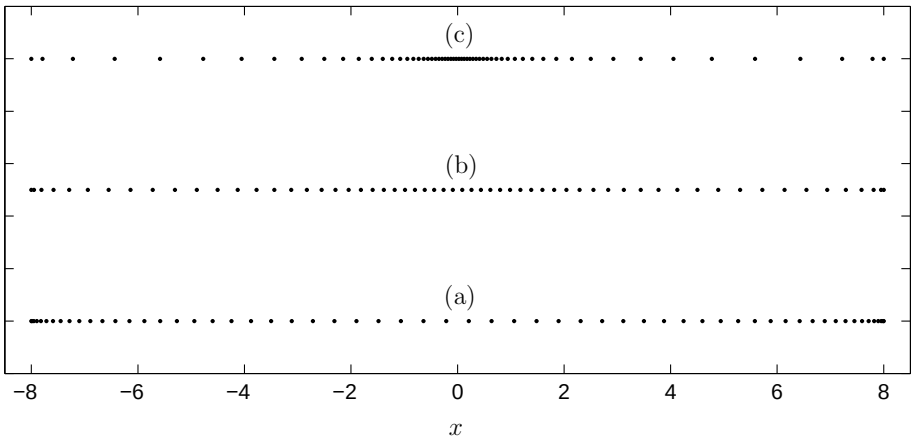

Figure 3.3: Different rates of grid clustering Chebyshev points using equation (3.2.20). (a) No clustering. (b) $s = 0.8$. (c) $s = 0.95$.

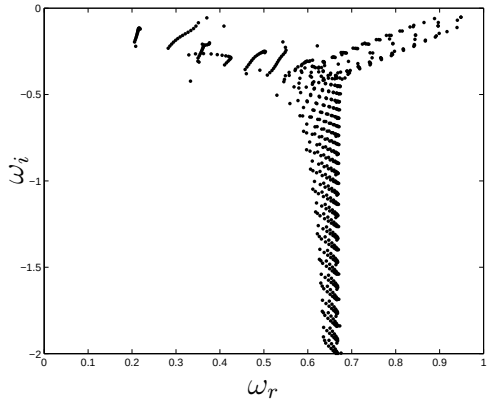

Figure 3.4: Plane Poiseuille flow in a pipe obtained using a pseudo-spectral numerical code with no grid clustering.

Due in part to the success of the clustering mechanism, which is effectively a mapping algorithm, it is possible to further hypothesise future developments utilising this technique. The most interesting, and perhaps useful of these is the application to linear stability analysis within domains of non-uniform (or irregular) boundaries. Rather than move the existing Chebyshev grid points within the existing domain it should be possible to transpose them to an altogether different domain via a mapping algorithm. This is beyond the scope of this study but is worthwhile considering for future applications.

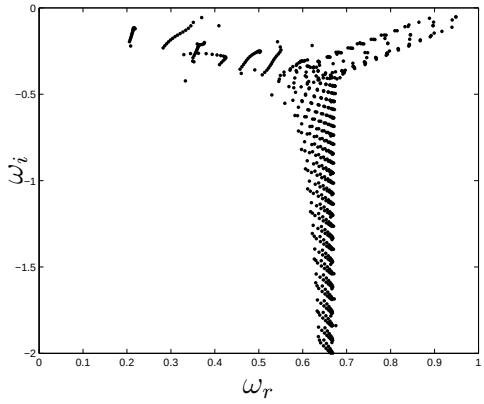

Figure 3.5: Psuedo-spectral grid clustering in Plane Poiseuille pipe flow, $s = 0.2$.

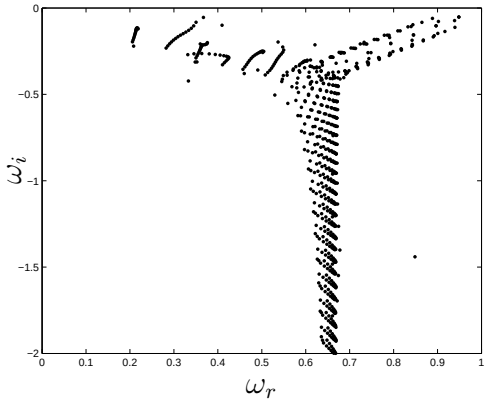

Figure 3.6: Psuedo-spectral grid clustering in Plane Poiseuille pipe flow, $s = 0.5$.

3.3 Finite-Difference Discrestisation

For the local problem, a finite-difference method based on the work of Otto and Denier [47] was developed to be used over the bounded Cartesian domain shown in figure 3.7.

3.3.1 Finite-Difference Scheme

A five point finite-difference stencil in both the horizontal (y) and vertical (z) directions is used to create a nine point, two-dimensional stencil (figure 3.8) which is used to discretize the governing equations resulting in fourth-order accuracy. The number of intervals is $N_{y,z}$, whilst the number of grid points is $N_{y,z} + 1$. Figure 3.9

illustrates a five point stencil in the y-direction (and similarly for the z-direction).

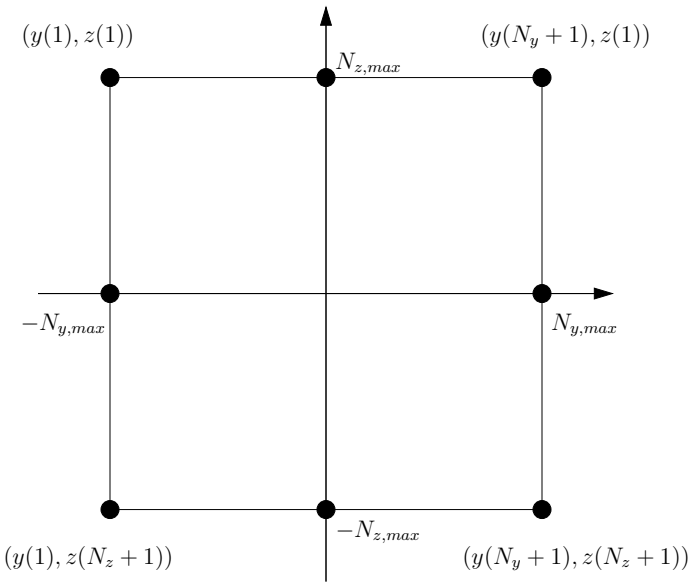

Figure 3.7: Computational domain of the vortex system in Cartesian co-ordinates.

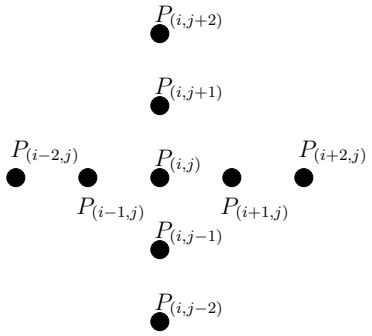

Figure 3.8: Computational stencil of the finite-difference scheme used herein.

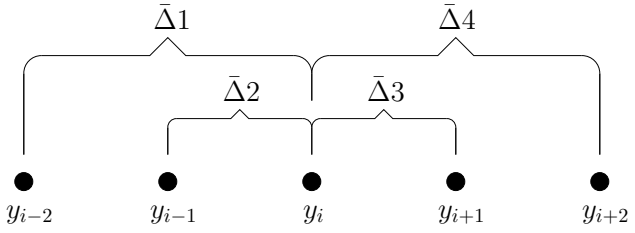

Figure 3.9: A one-dimensional, five point finite-difference stencil.

From figure 3.9 we can define

$$\bar{\Delta}1 = y_{i-2} - y_i, \tag{3.3.1}$$

$$\bar{\Delta}2 = y_{i-1} - y_i, \tag{3.3.2}$$

$$\bar{\Delta}3 = y_{i+1} - y_i, \tag{3.3.3}$$

$$\bar{\Delta}4 = y_{i+2} - y_i. \tag{3.3.4}$$

Now, if we expand about the point y_i using a Taylor series expansion, we can write the function at each of the four surrounding points in terms of y_i such that

$$f_{i-2} = f_i + (y_{i-2} - y_i)f_i' + (y_{i-2} - y_i)^2 \frac{f_i''}{2!} + \ldots, \tag{3.3.5}$$

$$f_{i-1} = f_i + (y_{i-1} - y_i)f_i' + (y_{i-1} - y_i)^2 \frac{f_i''}{2!} + \ldots, \tag{3.3.6}$$

$$f_i = f_i, \tag{3.3.7}$$

$$f_{i+1} = f_i + (y_{i+1} - y_i)f_i' + (y_{i+1} - y_i)^2 \frac{f_i''}{2!} + \ldots, \tag{3.3.8}$$

$$f_{i+2} = f_i + (y_{i+2} - y_i)f_i' + (y_{i+2} - y_i)^2 \frac{f_i''}{2!} + \ldots. \tag{3.3.9}$$

The function at a particular point can be expressed in terms of the five point stencil (figure 3.9) with the function values of the surrounding points being multiplied by weighting functions depending on their proximity to the grid point of interest. The function can be written as

$$F = a_i f_{i-2} + b_i f_{i-1} + c_i f_i + d_i f_{i+1} + e_i f_{i+2}, \tag{3.3.10}$$

where the f's can be substituted with equations (3.3.5) – (3.3.9). Truncating at $f^{(iv)}$ for fourth-order accuracy gives

$$\begin{aligned} F &= [a_i + b_i + c_i + d_i + e_i]f_i \\ &+ [a_i(\bar{\Delta}1) + b_i(\bar{\Delta}2) + d_i(\bar{\Delta}3) + e_i(\bar{\Delta}4)]f_i' \\ &+ \tfrac{1}{2}[a_i(\bar{\Delta}1)^2 + b_i(\bar{\Delta}2)^2 + d_i(\bar{\Delta}3)^2 + e_i(\bar{\Delta}4)^2]f_i'' \\ &+ \tfrac{1}{6}[a_i(\bar{\Delta}1)^3 + b_i(\bar{\Delta}2)^3 + d_i(\bar{\Delta}3)^3 + e_i(\bar{\Delta}4)^3]f_i''' \\ &+ \tfrac{1}{24}[a_i(\bar{\Delta}1)^4 + b_i(\bar{\Delta}2)^4 + d_i(\bar{\Delta}3)^4 + e_i(\bar{\Delta}4)^4]f_i^{(iv)}, \end{aligned} \tag{3.3.11}$$

which can be written in the matrix form

$$\begin{bmatrix} 1 & 1 & 1 & 1 & 1 \\ (\bar{\Delta}1) & (\bar{\Delta}2) & 0 & (\bar{\Delta}3) & (\bar{\Delta}4) \\ \frac{1}{2}(\bar{\Delta}1)^2 & \frac{1}{2}(\bar{\Delta}2)^2 & 0 & \frac{1}{2}(\bar{\Delta}3)^2 & \frac{1}{2}(\bar{\Delta}4)^2 \\ \frac{1}{6}(\bar{\Delta}1)^3 & \frac{1}{6}(\bar{\Delta}2)^3 & 0 & \frac{1}{6}(\bar{\Delta}3)^3 & \frac{1}{6}(\bar{\Delta}4)^3 \\ \frac{1}{24}(\bar{\Delta}1)^4 & \frac{1}{24}(\bar{\Delta}2)^4 & 0 & \frac{1}{24}(\bar{\Delta}3)^4 & \frac{1}{24}(\bar{\Delta}4)^4 \end{bmatrix} \begin{bmatrix} a_i \\ b_i \\ c_i \\ d_i \\ e_i \end{bmatrix} = V, \tag{3.3.12}$$

where

$$V = [0,1,0,0,0]^T \quad \text{for first derivative,} \tag{3.3.13}$$

$$V = [0,0,1,0,0]^T \quad \text{for second derivative,} \tag{3.3.14}$$

$$V = [0,0,0,1,0]^T \quad \text{for third derivative,} \tag{3.3.15}$$

$$V = [0,0,0,0,1]^T \quad \text{for fourth derivative.} \tag{3.3.16}$$

The stencil weightings, a_i, b_i, c_i, d_i, e_i can be found for each point in the discretised domain by solving the linear system (3.3.12). The points at (and near) the boundaries require special attention due to the lack of defined grid points external to the boundary. In order to calculate $\bar{\Delta}$ at these points it is useful to situate 'imaginary' points external to the domain that are the internal near-boundary points mirrored about the boundary and hence have the same spacing as their counterparts within the boundary (figure 3.10).

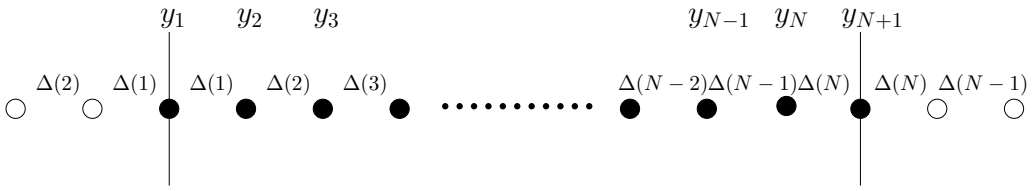

Figure 3.10: A one-dimensional stencil including 'imaginary' points (non-filled circles) external to the computational domain.

From figure 3.10 we can state the relationship between the grid points relevant

to the boundaries in the usual way as,

$$\Delta(1) = y_3 - y_2,$$
$$\Delta(2) = y_2 - y_1,$$
$$\Delta(N-1) = y_N - y_{N-1},$$
$$\Delta(N) = y_{N+1} - y_N.$$

$\bar{\Delta}$ at all grid points can be defined by

$\bar{\Delta}$	y_1	y_2	y_N	y_{N+1}
$\bar{\Delta}1$	$-\Delta(2) - \Delta(1)$	$-\Delta(1) - \Delta(1)$	$-\Delta$(N-2) $- \Delta$(N-1)	$-\Delta$(N-1) $- \Delta(N)$
$\bar{\Delta}2$	$-\Delta(1)$	$-\Delta(1)$	$-\Delta$(N-1)	$-\Delta(N)$
$\bar{\Delta}3$	$\Delta(1)$	$\Delta(2)$	$\Delta(N)$	$\Delta(N)$
$\bar{\Delta}4$	$\Delta(1) + \Delta(2)$	$\Delta(2) + \Delta(3)$	$\Delta(N) + \Delta(N)$	$\Delta(N) + \Delta$(N-1)

with all other grid points being calculated as follows;

$\bar{\Delta}$	$y_i \rightarrow y_{i-2} \quad i = 3, \cdots, N$
$\bar{\Delta}1$	$-\Delta(i$-2$) - \Delta(i$-1$)$
$\bar{\Delta}2$	$-\Delta(i$-1$)$
$\bar{\Delta}3$	$\Delta(i)$
$\bar{\Delta}4$	$\Delta(i) + \Delta(i$+1$)$

Therefore, for the points on or near the boundaries the function F can be written

$$F = c_1 f_1 + d_1 f_2 + e_1 f_3, \qquad i = 1, \tag{3.3.17}$$
$$F = b_2 f_1 + c_2 f_2 + d_2 f_3 + e_2 f_4, \qquad i = 2, \tag{3.3.18}$$
$$F = a_N f_{n-2} + b_N f_{N-1} + c_N f_N + d_N f_{N+1}, \qquad i = N, \tag{3.3.19}$$
$$F = a_{N+1} f_{N-1} + b_{N+1} f_N + c_{N+1} f_{N+1}, \qquad i = N+1, \tag{3.3.20}$$

where
$$a_1 = a_2 = b_1 = d_{N+1} = e_N = e_{N+1} = 0.$$

The stencil weightings can be ordered in matrix form to produce a differentiation matrix for the one-dimensional stencil, $y_1, \cdots, y_{N+1}$ that when multiplied by the

vector containing y grid points will produce a vector of derivatives, the order of which depends on the choice of V. The differentiation matrix, D, is constructed from the stencil weighting as,

$$\begin{bmatrix} c_1 & d_1 & e_1 & 0 & 0 & 0 & \cdots & \cdots & \cdots & \cdots & 0 \\ b_2 & c_2 & d_2 & e_2 & 0 & 0 & \cdots & \cdots & \cdots & \cdots & 0 \\ a_3 & b_3 & c_3 & d_3 & e_3 & 0 & \cdots & \cdots & \cdots & \cdots & 0 \\ 0 & a_4 & b_4 & c_4 & d_4 & e_4 & 0 & \cdots & \cdots & \cdots & 0 \\ \vdots & & \ddots & & \ddots & & \ddots & & \ddots & & \vdots \\ 0 & \cdots & \cdots & \cdots & 0 & a_{N-2} & b_{N-2} & c_{N-2} & d_{N-2} & e_{N-2} & 0 \\ 0 & \cdots & \cdots & \cdots & \cdots & 0 & a_{N-1} & b_{N-1} & c_{N-1} & d_{N-1} & e_{N-1} \\ 0 & \cdots & \cdots & \cdots & \cdots & 0 & 0 & a_N & b_N & c_N & d_N \\ 0 & \cdots & \cdots & \cdots & \cdots & 0 & 0 & 0 & a_{N+1} & b_{N+1} & c_{N+1} \end{bmatrix} \begin{bmatrix} y_1 \\ y_2 \\ y_3 \\ y_4 \\ \vdots \\ y_{N-2} \\ y_{N-1} \\ y_N \\ y_{N+1} \end{bmatrix},$$

resulting in a classical penta-diagonal matrix. Similarly there exists a matrix for each of the higher order derivatives. These can also be calculated by $(D^{'})^n$ but is less preferable than the method outlined above as the resulting matrix is in general non-sparse and therefore will require substantially more computational effort to solve the resulting linear system. For the two-dimensional domain there will be

$$\begin{aligned} y-direction &\Rightarrow \text{first derivative}, && D_y(N_y{+}1,N_y{+}1), \\ &\Rightarrow \text{second derivative}, && D_{yy}(N_y{+}1,N_y{+}1). \\ z-direction &\Rightarrow \text{first derivative}, && D_z(N_z{+}1,N_z{+}1), \\ &\Rightarrow \text{second derivative}, && D_{zz}(N_z{+}1,N_z{+}1). \end{aligned}$$

and similarly for higher order derivatives. The process of constructing two-dimensional differentiation matrices from the one-dimensional matrices derived above is detailed in Appendix A.

3.3.2 Boundary Conditions

In our formulation of the stability equation we are forcing the value of the function P at the boundary to zero (ie, Dirichlet boundary conditions) and as such the derivative $\frac{\partial P}{\partial y}\,|_{y=b'dry} = \frac{\partial P}{\partial y}\,|_{y=b'dry} = 0$. Therefore, we can employ a pseudo-Neumann boundary condition which can be implemented directly by setting the correspond-

ing entries in the differentiation matrices equal to zero. Figure 3.11 shows a one-dimensional discretised domain, where to employ the boundary conditions we set $P_1 = P_{N+1} = 0$.

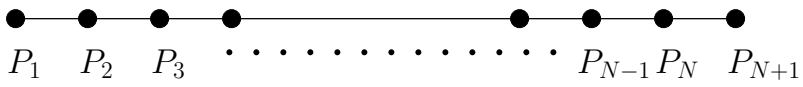

Figure 3.11: Discretized one-dimensional grid.

Therefore, the columns of A (in the linear system $AP = B$) associated with P_1 and P_{N+1} can also be set to zero and as we are now only interested in $P_2 - P_N$, the solutions, B_1 and B_{N+1} can also be ignored. We now only need examine a system that is $(N-1) \times (N-1)$ in size. This is of particular advantage in the two-dimensionial case where due to the use of the Kronecker tensor product to construct the two-dimensional differentiation matrices, the final computational domain is reduced by $2(N_z + N_y)$ points which can make a significant difference in terms of computational expense for very large systems. The final system of equations is then (still using one-dimensional notation)

$$\begin{array}{ccccccccccccc}
A_{(2,2)}P_2 & + & A_{(2,3)}P_3 & + & \cdots & + & A_{(2,\mathrm{N}-1)}P_{\mathrm{N}-1} & + & A_{(2,\mathrm{N})}P_{\mathrm{N}} & = & B_2 \\
A_{(3,2)}P_2 & + & A_{(3,3)}P_3 & + & \cdots & + & A_{(3,\mathrm{N}-1)}P_{\mathrm{N}-1} & + & A_{(3,\mathrm{N})}P_{\mathrm{N}} & = & B_3 \\
\vdots & & \vdots & & & & \vdots & & \vdots & & \vdots \\
A_{(\mathrm{N}-1,2)}P_2 & + & A_{(\mathrm{N}-1,3)}P_3 & + & \cdots & + & A_{(\mathrm{N}-1,\mathrm{N}-1)}P_{\mathrm{N}-1} & + & A_{(\mathrm{N}-1,\mathrm{N})}P_{\mathrm{N}} & = & B_{\mathrm{N}-1} \\
A_{(\mathrm{N},2)}P_2 & + & A_{(\mathrm{N},3)}P_3 & + & \cdots & + & A_{(\mathrm{N},\mathrm{N}-1)}P_{\mathrm{N}-1} & + & A_{(\mathrm{N},\mathrm{N})}P_{\mathrm{N}} & = & B_{\mathrm{N}}.
\end{array}$$

3.3.3 Grid Clustering

Most simple finite-difference schemes consist of evenly spaced grid points. Often in such situations, computational time can be wasted by performing calculations of unnecessarily high accuracy to ensure adequate resolution about the regions of interest. To overcome this, the derivation of the finite-difference scheme is such that a variation in the grid-point spacing can easily be implemented. There are many ways of clustering grid points in desired locations, but for the problem at hand, clustering about the origin in both the y and z axes (to varying degrees) is sufficient.

Let the set of grid points be, $y = y_1, y_2, \cdots, y_N, y_{N+1}$ where, $y_1 = -N_{y,max}$ and $y_{N+1} = N_{y,max}$ and for an evenly spaced grid, the spacing, $\delta = (2N_{y,max})/N_y$. Therefore, we can write

$$y_i = -N_{y,max} - (i\text{-}1)\delta, \qquad i = 1, \cdots, N_y{+}1, \tag{3.3.21}$$

which, for the grid clustering function being used, must be scaled from $-N_{y,max} \leq y_i \leq N_{y,max}$ to $-1 \leq y_i \leq 1$ so that y_i can be written

$$y_i = \frac{-N_{y,max} - (i\text{-}1)\delta}{N_{y,max}}, \qquad i = 1, \cdots, N_y{+}1. \tag{3.3.22}$$

Therefore, the set of clustered grid points ($\bar{y}_i$) are calculated as

$$\bar{y}_i = \frac{s^{|y_i|} - 1}{s - 1}, \qquad i = 1, \cdots, N_y{+}1, \tag{3.3.23}$$

where s is the stretching (or clustering) parameter and yields $\bar{y}_i = 1, \cdots, 0, \cdots, 1$.

Finally, all values $\bar{y}_i = 1, \cdots, \bar{y}_i = 0$ are multiplied by -1 to restore the set of grid points on the negative side of the origin and the resulting vector $\bar{y}_i$ is multiplied by $N_{y,max}$ to restore the set of values to cover the full domain. The results of applying the clustering technique to an evenly spaced grid are shown in figure 3.12. Here a stretching factor $s = 5$ is used to illustrate the degree of clustering that is attainable and how it concentrates the grid points in the regions inhabited by a typical four-vortex configuration with the primary ($z = 0$) vortices at the extremities of their placement for computational purposes. It should be remembered that if the clustering is too severe there will be insufficient points in the outer regions of the domain to accurately resolve the disturbance field and so the degree of clustering should be chosen specific to the individual problem being examined.

3.3.4 Basic Flow

The basic flow components (these can be U, V, W and derivatives thereof) are also organised into column vectors consisting of $N_y - 1$ blocks with $N_z - 1$ entries. Each entry is placed on the corresponding main diagonal of an $(N_y - 1)(N_z - 1)$ square matrix. For example, the non-dimensional axial velocity U is given by

$$U = \begin{bmatrix}
U_{(1,1)} & 0 & \cdots & \cdots & \cdots & \cdots & \cdots & \cdots & \cdots & \cdots & 0 \\
0 & U_{(1,2)} & 0 & & & & & & & & \vdots \\
\vdots & \ddots & \ddots & \ddots & & & & & & & \vdots \\
\vdots & & 0 & U_{(1,N_z\text{-}1)} & 0 & & & & & & \vdots \\
\vdots & & & 0 & U_{(2,1)} & 0 & & & & & \vdots \\
\vdots & & & & \ddots & \ddots & \ddots & & & & \vdots \\
\vdots & & & & & 0 & U_{(2,N_z\text{-}1)} & 0 & & & \vdots \\
\vdots & & & & & & \ddots & \ddots & \ddots & & \vdots \\
\vdots & & & & & & & 0 & U_{(N_y\text{-}1,1)} & 0 & \vdots \\
\vdots & & & & & & & & \ddots & \ddots & \vdots \\
0 & \cdots & \cdots & \cdots & \cdots & \cdots & \cdots & \cdots & \cdots & 0 & U_{(N_y\text{-}1,N_z\text{-}1)}
\end{bmatrix}.$$

It should also be noted that the component α^2 (which has the constant value on each diagonal) is dealt with in the same way. Note that the subscripts are representative of the position of the individual basic flow component in the one-dimensional grid in (y, z) co-ordinate notation and not traditional vector notation $(row, column)$.

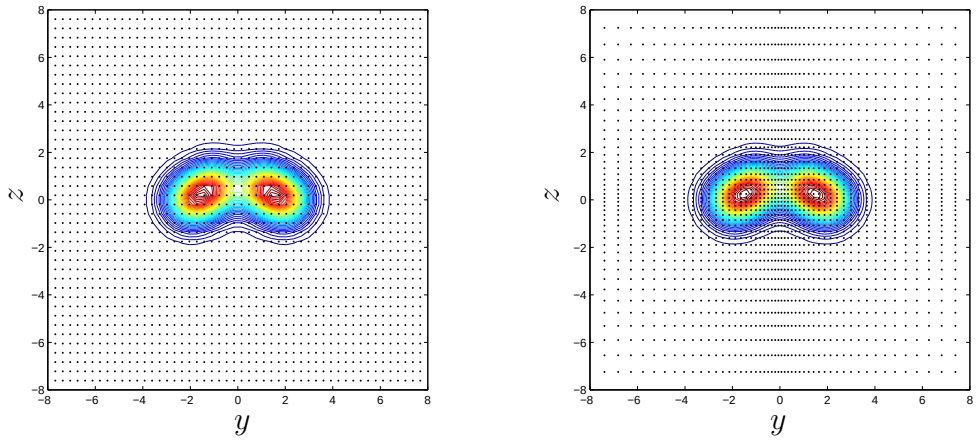

(a) (b)

Figure 3.12: Comparison of concentration of grid points with four-vortex system. (a) No clustering, (b) $s = 5$.

3.3.5 Governing Equation

The discretisation of the governing equation is treated the same for both the inviscid (compressible and incompressible) and viscous models used in this study. The generalised eigenvalue problem is rearranged to form a linear system. For the inviscid

case this is

$$\left[(U-c)\left(\frac{\partial^2}{\partial y^2}+\frac{\partial^2}{\partial z^2}-\alpha^2\right)-2\left(\frac{\partial U}{\partial y}\frac{\partial}{\partial y}+\frac{\partial U}{\partial z}\frac{\partial}{\partial z}\right)\right]P_p=0, \tag{3.3.24}$$

and for the viscous case,

$$\left\{\begin{bmatrix} \mathcal{Q} & \frac{\partial U}{\partial y} & \frac{\partial U}{\partial z} & \mathrm{i}\alpha \\ 0 & \mathcal{Q}+\frac{\partial V}{\partial y} & \frac{\partial V}{\partial z} & \frac{\partial}{\partial y} \\ 0 & \frac{\partial W}{\partial y} & \mathcal{Q}+\frac{\partial W}{\partial z} & \frac{\partial}{\partial z} \\ \mathrm{i}\alpha & \frac{\partial}{\partial y} & \frac{\partial}{\partial z} & 0 \end{bmatrix}-\omega\begin{bmatrix} \mathrm{i} & 0 & 0 & 0 \\ 0 & \mathrm{i} & 0 & 0 \\ 0 & 0 & \mathrm{i} & 0 \\ 0 & 0 & 0 & 0 \end{bmatrix}\right\}\begin{bmatrix} U_p \\ V_p \\ W_p \\ P_p \end{bmatrix}=0,$$

where

$$\mathcal{Q}=\mathrm{i}\alpha U+V\frac{\partial}{\partial y}+W\frac{\partial}{\partial z}-\frac{1}{Re}\left(-\alpha^2+\frac{\partial^2}{\partial y^2}+\frac{\partial^2}{\partial z^2}\right). \tag{3.3.25}$$

The homogeneous discretised equation results in a square matrix of the form

$$AP=0. \tag{3.3.26}$$

3.3.6 Iterative Procedure

The iterative technique used to recover the eigenvalues and eigenfunctions follows the work of Otto and Denier [47] for the solution of a non-separable elliptic, linear partial differential equation. Essentially the algorithm normalises at a point in the representing linear matrix, internal to the domain, and aims to exploit the fact that the differential equation has not been satisfied at this point. A simple iterative procedure is then used to converge on the eigenvalue at this point which leads to the solution of the entire system. The non-homogeneous matrix equation $AP=B$ represents a system of linear equations

$$\begin{array}{ccccccccccccccc}
A_{(1,1)}P_1 & + & A_{(1,2)}P_2 & + & \cdots & + & A_{(1,k)}P_k & + & \cdots & + & A_{(1,\mathrm{N}-1)}P_{\mathrm{N}-1} & + & A_{(1,N)}P_N & = & B_1 \\
A_{(2,1)}P_1 & + & A_{(2,2)}P_2 & + & \cdots & + & A_{(2,k)}P_k & + & \cdots & + & A_{(2,\mathrm{N}-1)}P_{\mathrm{N}-1} & + & A_{(2,N)}P_N & = & B_2 \\
\vdots & & \vdots & & & & \vdots & & & & \vdots & & \vdots & & \vdots \\
A_{(k,1)}P_1 & + & A_{(k,2)}P_2 & + & \cdots & + & A_{(k,k)}P_i & + & \cdots & + & A_{(k,\mathrm{N}-1)}P_{\mathrm{N}-1} & + & A_{(k,N)}P_N & = & B_k \\
\vdots & & \vdots & & & & \vdots & & & & \vdots & & \vdots & & \vdots \\
A_{(N,1)}P_1 & + & A_{(N,2)}P_2 & + & \cdots & + & A_{(N,k)}P_k & + & \cdots & + & A_{(N,\mathrm{N}-1)}P_{\mathrm{N}-1} & + & A_{(N,N)}P_N & = & B_N,
\end{array}$$

where $B_1,\cdots,B_N=0$ for the homogeneous solution. Note that in this case N represents a matrix dimension of $(N_y-1)\times(N_z-1)$.

At a particular point, we set $P_k = 1$ and replace the disretised equation at this point with this condition. This is the normalisation of the equation at P_k. A suitable choice for this point is typically where the pressure field attains its maximum absolute value ($\max\{|P_k|\}$). As this is generally not known *a priori* either an educated guess can be made as to the location or, more preferably, a low resolution study can be performed using a suitable global solver. This will provide both an initial estimate of the eigenvalue sought and a good indication of the location of ($\max\{|P_k|\}$). Note that in this sense, the point P_k in the vector P is representative of the point P_{kj} in the two-dimensional computational domain. We write

$$\begin{array}{ccccccccccccccc}
A_{(1,1)}P_1 & + & A_{(1,2)}P_2 & + & \cdots & + & A_{(1,k)}P_k & + & \cdots & + & A_{(1,\mathrm{N}\text{-}1)}P_{\mathrm{N}\text{-}1} & + & A_{(1,N)}P_N & = & 0 \\
A_{(2,1)}P_1 & + & A_{(2,2)}P_2 & + & \cdots & + & A_{(2,k)}P_k & + & \cdots & + & A_{(2,\mathrm{N}\text{-}1)}P_{\mathrm{N}\text{-}1} & + & A_{(2,N)}P_N & = & 0 \\
\vdots & & \vdots & & & & \vdots & & & & \vdots & & \vdots & & \vdots \\
A_{(k-1,1)}P_1 & + & A_{(k-1,2)}P_2 & + & \cdots & + & A_{(k-1,k)}P_k & + & \cdots & + & A_{(k-1,\mathrm{N}\text{-}1)}P_{\mathrm{N}\text{-}1} & + & A_{(k-1,N)}P_N & = & 0 \\
0 & + & 0 & + & \cdots & + & P_k & + & \cdots & + & 0 & + & 0 & = & 1 \\
A_{(k+1,1)}P_1 & + & A_{(k+1,2)}P_2 & + & \cdots & + & A_{(k+1,k)}P_k & + & \cdots & + & A_{(k+1,\mathrm{N}\text{-}1)}P_{\mathrm{N}\text{-}1} & + & A_{(k+1,N)}P_N & = & 0 \\
\vdots & & \vdots & & & & \vdots & & & & \vdots & & \vdots & & \vdots \\
A_{(N,1)}P_1 & + & A_{(N,2)}P_2 & + & \cdots & + & A_{(N,k)}P_k & + & \cdots & + & A_{(N,\mathrm{N}\text{-}1)}P_{\mathrm{N}\text{-}1} & + & A_{(N,N)}P_N & = & 0.
\end{array}$$

We now let the 'normalised' A matrix $= \bar{A}$, and $\bar{P}$ and $\bar{B}$ be the modified P and B matrices respectively, therefore

$$\bar{A}\,\bar{P} = \bar{B}. \tag{3.3.27}$$

The new (normalised) function matrix $\bar{P}$ is obtained by solving the linear system (3.3.27). We want to satisfy the discretised equation at the point k such that

$$A_{(k,1)}P_1 + \cdots + A_{(k,k)}P_k + \cdots + A_{(k,N)}P_N = B_k = 0. \tag{3.3.28}$$

To obtain B_k we use the original matrix A so that

$$A\,\bar{P} = B, \tag{3.3.29}$$

where $B_k \neq 0$ unless the initial eigenvalue guess is exactly an eigenvalue of the system

$$A_{(k,1)}\bar{P}_1 + \cdots + A_{(k,k)}\bar{P}_k + \cdots + A_{(k,N)}\bar{P}_N \neq 0. \tag{3.3.30}$$

Now, in order to find an eigenvalue and corresponding eigenfunction of the system we iterate on c (eigenvalue) for $\mathcal{L}(c, P_k) = B_k = 0$ to within some desired tolerance.

A simple method of performing the iteration is a secant method which requires two initial guesses (c_{-1} and c_{-2}) to start the procedure

$$c_k = c_{k-1} - \frac{\mathcal{L}(c_{k-1})(c_{k-1} - c_{k-2})}{\mathcal{L}(c_{k-1}) - \mathcal{L}(c_{k-2})}, \qquad k = 1, 2, \cdots, N. \tag{3.3.31}$$

3.3.7 Parameter Variation

One particularly useful aspect of an iterative local solver is its ability to track a specific eigenvalue over a range of parameters. If a parameter study is to be performed, such as a variation in α, it is advantageous (if the parameter steps are sufficiently small) to re-set the point of normalisation to the maximum absolute value of the previous parameter's function. This reduces the number of iterations required to achieve eigenvalue convergence and scales the maximum function value to unity.

One such application is the tracking of the curve of neutral stability for a set of parameters (done specifically in the viscous case, chapter 6) from a starting eigenvalue found using the global method. Some subtle additions are required to be made to the iterative process in order to successfully track around the neutral curve, specifically a second iterative process is needed after each eigenvalue convergence iteration to ensure that the value then converges onto the neutral curve. Further details are given in section 3.6.5. In chapter 5, parameter stepping is used to examine the effects of compressibility on the stability of particular configurations by using the Mach number as the stepping parameter.

The global code, whilst being computationally expensive is quite efficient at finding the whole spectra of values for a low resolution grid. The particular value of interest (and some small variation thereof to act as the second required starting value) can be iterated upon in the local solver and the parametric variable initially can be the number of grid points thus enabling the eigenvalue of interest to be tracked up to a grid resolution that will provide adequate numerical convergence for the study being undertaken. Then, as the desired resolution is reached, the number of grid points is fixed and other parameters of interest can be varied. It should be noted however, that care needs to be taken when deciding upon the resolution of the global solver to produce the starting values as spurious or inaccurate eigenvalues may be found that may not converge as the resolution increases. A balance between

adequate (lower) resolution and computational time must, as always, be found.

3.4 Implementation of Serial Codes

All the eigenvalue solvers used in this study are written in either MATLAB™ or Fortran 90 and are designed to produce a single or set of eigenvalues and their respective eigenfunctions. All the computer codes used have been written specifically for the analysis of this study with the exception of the intrinsic Fortran, MATLAB™ and LAPACK subroutine libraries. The serial codes have been run on several machines of varying capacity including an Apple G4 laptop, G5 dual quad-core and in multiple serial form on the South Australian Partnership for Advanced Computing (SAPAC) Linux cluster 'Hydra' with up to 2Gb of main memory. Computation times for a single set of parameters vary from 1 hour to 8 or more hours depending on the machine load and problem size.

3.4.1 Global Solvers

In section 3.7.3 it is shown that the viscous model in both pseudo-spectral and finite-difference forms produced numerically correct values, however, the number of grid points required for accurate convergence increases substantially when an azimuthal component is added into the basic flow. Significant grid clustering ($0.8 < s < 0.975$ in the Chebyshev discretised domains) was used in order to produce results of sufficient starting accuracy with acceptable computational expense. This enabled the solvers to be run in serial mode on many processors on the SAPAC supercomputers representing various parameter adjustments, producing results that would have been unobtainable (due to time constraints) on a single processor.

3.4.2 Local Solvers

The iterative local solvers (inviscid and viscous) are implemented in serial form in the same way as the global code, the difference being in the solution of a linear system as opposed to the eigenvalue problem (as mentioned earlier).

3.5 Implementation of Parallel Codes

Parallel implementation of both the global spectral solver and the local finite-difference solver for the viscous case is developed so as to overcome problems such as lack of local memory for large grid resolutions and excessive run times. The basis of the code remains the same as the serial form except parallel BLAS (Basic Linear Algebra Subprograms) routines are used in place of the serial versions. Whilst the method of obtaining the relevant eigenvalues and eigenfunctions may differ (the QZ algorithm is not used, Arnoldi iteration is used exclusively for the global case), the basics of distribution remain consistent. All parallel codes are run on the SAPAC Linux cluster 'Hydra' using 8 dual processor nodes each with 2Gb main memory. Whilst the number of processors is 16, actual computational scalability is around 10 times greater (in terms of global problem size) than the fastest available serial machine due mainly to the external memory requirements of the numerous parallel subroutines. The computational time scale varies with increased problem size but at $(N_r, N_\theta) = (80, 32)$, which is the maximum achievable serially in polar co-ordinates, the parallel code is approximately 12 times faster in terms of computational time, the loss (as intuitively we might expect the computational time to scale with the number of processors) being due to the inherent cost associated with communication over a large number of nodes.

3.5.1 Global Spectral Solver

The distribution of information is fixed over the 16 processors in a 4×4 block cyclic distributed processor grid. The numerical details are distributed evenly across the processor grid and the program makes use of routines that distribute the information in the problem construction stage to avoid having to store large global matrices on all processors. The parallel routines used are from the ScaLAPCK and PARPACK libraries. In polar co-ordinates, N_r is the number of points in the radial direction, N_θ is the number of points in the azimuthal (or angular) direction. It is important to note that in order to maintain even data distribution across all 16 processors distributed in a 4×4 processor grid the global size of the problem must be divisible by four. To ensure this, the requirements set out below must be met.

Cartesian:

Global problem size $= 2(N_y - 1)(N_z - 1) \times 2(N_y - 1)(N_z - 1))$.

Local problem size (largest) $= (N_y + 1) \times (N_y + 1)$ for N_y larger than N_z.

- Both N_y and N_z must be odd.
- The product $(N_y - 1) \times (N_z - 1)$ must be divisible by 8.

Polar:

Global problem size $= 2(N_r - 1)N_\theta \times 2(N_r - 1)N_\theta$.

Local problem size (largest) $= 2N_r \times 2N_r$.

- N_r must be odd.
- The product $(N_r - 1) \times N_\theta$ must be divisible by 8.

The code is set up to accommodate a variety of basic flows, the details of these can be found in section 6.3. Further basic flows can be added as required. Implementation of the parallel routines is identical for codes of both co-ordinate bases and as such, for clarity, further reference is made only to the Cartesian problem.

3.6 Parallel Code Details

The parallel discretisation of the governing equations uses the PBLACS (Parallel Basic Linear Algebra Communication Subprograms) which arrange the processor grid into as much of a square formation as is possible depending on the number of processors being used. In this particular case, 16 processors are used to ensure a block-cyclic processor grid of 4×4 (figure 3.13).

By ensuring that the number of collocation points nominated at the call of the routine meets the requirements set out previously, each processor in the grid will receive the same amount of evenly distributed data making for a more intuitive problem lay-out.

0	1	2	3
4	5	6	7
8	9	10	11
12	13	14	15

Figure 3.13: PBLACS 16 node processor grid.

3.6.1 Two-dimensional Differentiation Matrices

In order to produce two-dimensional differentiation matrices, a Kronecker tensor product is used (see Appendix A). Essentially, an algorithm was written to take the one dimensional differentiation matrices and convert them into a two dimensional, fully distributed format. That is, the global two-dimensional matrix does not exist on any one processor, rather the individual processor reads which element it is in the processor grid and computes only its portion of the two-dimensional matrix. In this way the storage requirements for each individual processor are kept to a minimum. The two-dimensional array of grid points is restructured into a one-dimensional vector of size $(N_y - 1)(N_z - 1)$ in $(N_y - 1)$ block form.

3.6.2 Basic Flow

The description and types of basic flow employed in this study are detailed in section 6.3. The basic flow computed by all of these routines produces axial U, horizontal V and vertical W components of velocity as a vector of size $(N_y - 1)(N_z - 1)$. The ScaLAPACK PBLAS routine PZGEMV (matrix – vector) is used to produce velocity derivatives by multiplication of the velocity vector by the respective differentiation matrix. In the processor grid, only the first column of processors 0, 4, 8 and 12 are used to store vector information, all other entries are zero.

The vectors representing the velocity derivatives are then transformed into two-dimensional matrices with the entries of the vector placed on the diagonals of the matrix. The ScaLAPACK redistribution routine PZGEMR2D is used to redistribute the data found in localised diagonal form on processors 0, 4, 8 and 12 to global diagonal form on processors 0, 5, 10 and 15. Figure 3.14 illustrates this process. The following sections are included to finalise the parallel distribution and solution of the viscous stability equation and to also highlight the work that went into the final development stage of the parallel global solver.

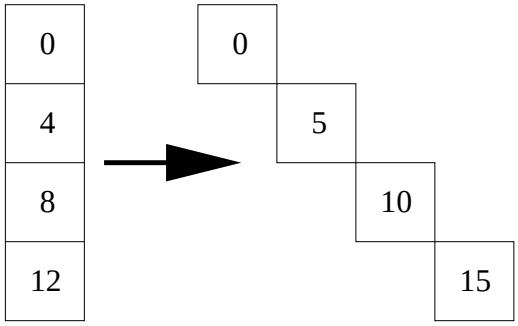

Figure 3.14: Processor redistribution of velocity vectors.

3.6.3 Redistribution of data to full dimensions

Whilst the processor grid remains the same, namely 16 processors, the way which the data is transfered to each processor is now different. Unlike previously where every distributed matrix had a portion on each of the 16 processors, now each of the previously built matrices will be described by only one processor. This enables the full problem to be built on the same 16 processor grid as has already been established. The processor grid as passed to the full problem is shown in figure 3.15.

3.6.4 Solving the Eigenvalue Problem

Whilst the equation is formed as a generalised eigenvalue problem, the fact that the governing matrices are (usually) neither symmetric or Hermitian positive-definite (as prescribed by the ARPACK routine for the solution of a generalised problem)

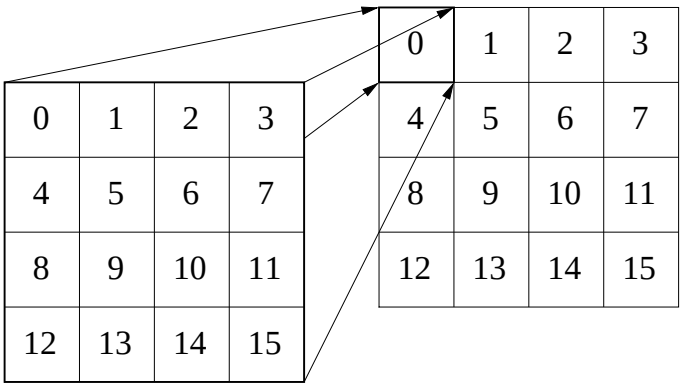

Figure 3.15: Redistribution of already distributed data to full dimensions as passed to processor 0. Similarly for all other processors.

results in a necessary conversion to standard form. This is done most simply by inverting the **B** matrix and multiplying by **A**, an operation that is achieved with little computational over-head using parallel ScaLAPACK algorithms (it is acceptable to do this due to the existing 'full' nature of the matrices; we are not taking a sparse set of matrices and creating a 'full' matrix through this process). For the problem at hand however, the **B** matrix is singular and as such has no inverse. For singular or ill-conditioned matrices a slightly different approach is required to convert the generalised eigenvalue problem to a standard one. The process is a spectral transformation [35] as follows. Starting with our generalised form

$$\mathbf{A}\mathbf{x} = \lambda\mathbf{B}\mathbf{x}, \tag{3.6.1}$$

subtracting $\sigma\mathbf{B}\mathbf{x}$ from both sides gives

$$\mathbf{A}\mathbf{x} - \sigma\mathbf{B}\mathbf{x} = \lambda\mathbf{B}\mathbf{x} - \sigma\mathbf{B}\mathbf{x},$$

or

$$(\mathbf{A} - \sigma\mathbf{B})^{-1}\mathbf{B}\mathbf{x} = \frac{1}{\lambda - \sigma}\mathbf{x},$$

which can be written as

$$\hat{\mathbf{A}}\mathbf{x} = \mu\mathbf{x}, \tag{3.6.2}$$

where

$$\hat{\mathbf{A}} = (\mathbf{A} - \sigma\mathbf{B})^{-1}\mathbf{B} \quad \text{and} \quad \mu = \frac{1}{\lambda - \sigma}.$$

Equation (3.6.2) can be solved as a standard eigenvalue problem for the eigenvalues μ using a regular interface, reverse-communication routine. A shift-and-invert interface is not required as the shift parameter, σ, is already included in the derivation of (3.6.2). The eigenvalues can then be transformed to those of (3.6.1) using the relationship

$$\lambda_j = \sigma + \frac{1}{\mu_j}. \tag{3.6.3}$$

The spectral transformation ensures that the eigenvalues μ of the standard problem (3.6.2), when transformed to the eigenvalues, λ, of the original problem (3.6.1), converge most rapidly near the shift value σ [35]. By setting the parameter 'which' to 'LM', the ARPACK routine focusses on eigenvalues of the standard problem that are of largest magnitude and when substituted into (3.6.3), produce eigenvalues of the original system that are closest to σ. There are several other user-defined properties that can be set to enhance the prospect of finding eigenvalues in the desired region, all of which are listed in the ARPACK manual [35].

An alternative method of dealing with the singular nature of the $\mathbf{B}$ matrix is to introduce a small, artificial perturbation pressure $\epsilon\omega P_p$ (where $\epsilon \ll 1$) into the continuity equation which serves to remove, or eliminate, the matrix singularity. We have shown this to produce identical eigenvalues to those produced by the previous method, however, this artificial term does tend to produce more spurious eigenvalues generally characterised by their large values [32].

3.6.5 Local Finite Difference Solver

The parallel version of the local iterative solver is built from a combination of the serial iteration scheme and the parallel distribution of differentiation matrices. The matrices are constructed using the same five-point FD stencil and reformed into two-dimensions by the algorithm outlined in section 3.6.1. The advantage of this method is that the process remains purely parallel as no specific eigenvalue solver is required; the iteration takes place over the distributed processor grid allowing for fast computational times.

A further use of this method is to track a neutral stability curve, or more specifically, a particular mode over a range of parameters. This is achieved with the

addition of a second iteration step for each parameter iteration. The selected parameter, say the Reynolds number, will be stepped until the desired location is reached, in this case close proximity to the neutral stability curve. Then there will be an iteration on the Reynolds number (by searching for the purely real eigenvalue) and the subsequent convergence iterations to find the appropriate eigenvalue. This continues until the point on the neutral curve is found. A further parameter step can then be made to find an adjacent point on the curve, and so forth.

3.7 Testing of Numerical Methods

As is always the case with a new numerical computer algorithm, it is necessary to test it against published (and credible) results to establish the degree by which the accuracy of the results produced can be verified and trusted. Considerable weight is placed on ensuring both the numerical stability and accuracy of the pseudo-spectral methods used in the inviscid analysis as these methods transfer directly to the more complicated viscous problem, thus we can be sure that the theory behind our numerical schemes is sound and concentrate on verifying the coding of the complex mathematical derivations that form the eigenvalue problem. It is worth stating that when we talk about the available resolution, we are refering to the amount of computing resources allocated to the program. In the inviscid case this is a single processor, however in the viscous case the available resolution refers to the size of the problem achievable on sixteen processors (being the limit reliably accessible at the time). Should greater resolutions be required for future work, the code would need to be re-written to accommodate this.

3.7.1 Testing Inviscid Global Solver

The inviscid version of the global eigenvalue solver is written in polar co-ordinates and aims to compute a set of eigenvalues and corresponding eigenfunctions, satisfying the two-dimensional Rayleigh equation,

$$(U-c)\left[\frac{\partial^2}{\partial r^2}+\frac{1}{r}\frac{\partial}{\partial r}+\frac{1}{r^2}\frac{\partial^2}{\partial \theta^2}-\alpha^2\right]P_p-2\left[\frac{\partial U}{\partial r}\frac{\partial}{\partial r}+\frac{1}{r^2}\frac{\partial U}{\partial \theta}\frac{\partial}{\partial \theta}\right]P_p=0. \quad (3.7.1)$$

Code symmetry

The code was run with a reduced number of collocation points (to restrict the time of the study to a manageable length) at various positions in order to ascertain the stability of the numerics and any inherent symmetries. Initially outputs were compared from vortex located in positions mirrored across either the y or z-axis. Then, diagonal symmetry was examined, with results compared as mirrored across a diagonal (ie; $(3,1)$ and $(-3,-1)$). These results showed that the code exhibited symmetry for vortex placement either side of the $z = 0$ axis (as expected) and as such we only need examine vortex placement in either the $+z$ or $-z$ domains.

Evaluating Numerical Stability

To test the numerical stability of the code, a single Batchelor type vortex which has an axial component of velocity

$$U = e^{-ar^2}, \tag{3.7.2}$$

is placed at the origin. This is consistent with the axial velocity profile used by Lessen and Paillet [38] when computing similar eigenvalues (with $a = 1$). The values published therein will be used to evaluate the legitimacy and accuracy of the global eigenvalue solver. The code is to be tested initially by artificially introducing an eigenfunction P and an eigenvalue c into equation (3.7.1) and running the code, ensuring that one of the eigenvalues produced is the artificial eigenvalue used. The degree of spectral collocation required to achieve this to a satisfactory accuracy will determine the numerical stability of the code. The artificial eigenfunctions can be produced by letting

$$P_p(r,\theta) = P_p(r)e^{ik\theta}, \tag{3.7.3}$$

where

$$P_p(r) = r^4 e^{-ar^2}, \qquad r^2 = y^2 + z^2, \qquad y = r\sin\theta, \qquad z = r\cos\theta,$$

therefore

$$P_p(r,\theta) = P_p(y,z) = ((y-y_0)^2 + z^2)^2 e^{-a((y-y_0)^2+z^2)} e^{ik\theta},$$

$$P_p(r,\theta) = (r^2 - 2y_0 r\sin\theta + y_0^2)^2 e^{-a(r^2-2y_0 r\sin\theta+y_0^2)} e^{ik\theta}. \tag{3.7.4}$$

For convenience we set

$$B = r^2 - 2y_0 r\sin\theta + y_0^2,$$

therefore (3.7.4) can be written as

$$P_p(r,\theta) = B^2 e^{-aB} e^{ik\theta}, \tag{3.7.5}$$

and the subsequent derivatives with respect to r and θ are

$$P_{p,r}(r,\theta) = [(2r - 2y_0\sin\theta)(2B - aB^2)]e^{-aB}e^{ik\theta},$$

$$\begin{aligned} P_{p,rr}(r,\theta) &= [(2r - 2y_0\sin\theta)^2(a^2B^2 - 4aB + 2) \\ &+ 2(2B - aB^2)]e^{-aB}e^{ik\theta}, \end{aligned}$$

$$P_{p,\theta}(r,\theta) = [2By_0 r\cos\theta(aB - 2) + ikB^2]e^{-aB}e^{ik\theta},$$

$$\begin{aligned} P_{p,\theta\theta}(r,\theta) &= [4y_0^2 r^2\cos^2\theta(2 - 4aB + a^2B^2) + 4Biky_0 r\cos\theta(aB - 2) \\ &+ 2By_0 r\sin\theta(2 - aB) - B^2k^2]e^{-aB}e^{ik\theta}. \end{aligned}$$

For clarity, let

$$L_P = P_{p,rr}(r,\theta) + \frac{1}{r}P_{p,r}(r,\theta) + \frac{1}{r^2}P_{p,\theta\theta}(r,\theta) - \alpha^2 P_p(r,\theta), \tag{3.7.6}$$

and substituting (3.7.6) into (3.7.1) gives us

$$(U - c)L_P - 2(U_r P_{p,r} + \frac{1}{r^2}U_\theta P_{p,\theta}) = 0, \tag{3.7.7}$$

where $c = c_r + ic_i$. Equation (3.7.7) can be satisfied by choosing

$$(UL_P - 2U_r P_{p,r}) - \frac{2}{r^2}U_\theta P_{p,\theta} = c_r L_P + ic_i L_P, \tag{3.7.8}$$

with one possible solution of (3.7.8) being

$$U_r = \frac{UL_P - c_r L_P}{2P_{p,r}} = \frac{(U - c_r)L_P}{2P_{p,r}}, \tag{3.7.9}$$

$$U_\theta = -\frac{ic_i r^2 L_P}{2P_{p,\theta}}, \tag{3.7.10}$$

where an appropriate expression for U is equation (3.7.2) and c is an arbitrary, user defined eigenvalue, either real or complex.

The results showed good (and remarkably quick) convergence for $k = 1$ and $k = 2$ with a completely real eigenvalue c, whilst for odd values of k the convergence was somewhat slower. For these tests the number of collocation points in the radial direction (N_r) was varied and the number of collocation points in the azimuthal direction (N_θ) was kept at 4. Further tests, varying N_θ as well as N_r revealed convergence for a reduced N_r when N_θ was increased.

Tests using complex eigenvalues were also performed and seemed to marginally increase the convergence rate of the odd integer k runs. Finally, slower decay rates, represented by the parameter a, were used and it was found that the rate of convergence was increased substantially with a slower decay rate. The computational domain is over a radial distance of $r_{max} = 10$. It was noted that as the vortex was moved away from the origin, the number of collocation points required to achieve satisfactory convergence increased due mainly to the removal of the inherent symmetry of the problem. The results of this exercise prove that the code converges and can be expected to produce correct and consistent eigenvalues.

Comparison to Published Data

The final part of the verification process was to reproduce published values that have been confirmed through independent studies. As outlined earlier, a range of eigenvalues for a single vortex located at the origin can be found in Lessen and Paillet [38]. Figure 3.16 displays the results obtained from running the modified test code with $(N_r, N_\theta) = (80, 32)$ and $r_{max} = 3$ as in Lessen and Paillet [38], and $q = 0$ over a range of α. The eigenvalues used for comparison are those of $n = \pm 1$. For $\alpha = 1$, a high resolution run was performed to ensure convergence of the code when reproducing the eigenvalues published by Lessen and Paillet [38]. These results are given in table 3.1.

It can be seen from the figures and the corresponding tabulated eigenvalues that the global pseudo-spectral code does find eigenvalues that match those obtained by Lessen and Paillet [38] to an acceptable accuracy. These results allow further analysis of more complex vortex systems to proceed with confidence that the code

will produce accurate results. It should be noted however, that whilst the results of Lessen and Paillet [38] are reproduced here, their inherent accuracy remains suspect due to their particularly small value of r_{max}. This has also been pointed out by subsequent authors such as Khorrami *et al.* [32], Mayer and Powell [41] and Fabre and Jacquin [19] but despite this, many authors have used the results of Lessen and Paillet [38] as a benchmark for showcasing the integrity of their numerical schemes.

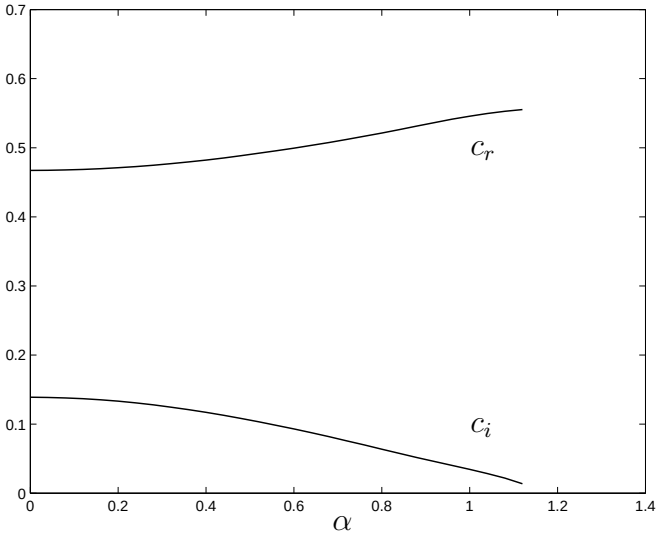

Figure 3.16: Eigenvalues from the global pseudo-spectral code equivalent to $q = 0$.

Source	Eigenvalue
Lessen and Paillet	0.55+0.03i
Matlab code	0.5456+0.0344i
Fortran code	0.54565+0.0344i

Table 3.1: A comparison of the present results to those of Lessen & Paillet [38].

3.7.2 Testing Numerical Algorithms

As part of the verification process the various numerical algorithms used, both those written specifically for this study and those obtained through other means and adapted, had to be checked to ensure correct operation. As a result of the successful

reproduction of published results by the inviscid code (section 3.7.1), the LAPACK QZ eigenvalue routine ZGGEV.f became the basis for comparison. The validity of higher order differentiation matrices was proven by accurate reproduction of both plane Poiseuille duct and Hagen-Poiseuille pipe flow results. The algorithms that were checked either directly or indirectly by this process were grid clustering routines and the serial and parallel eigenvalues solvers ARPACK and P_ARPACK.

Clustering

Duct flow results obtained using ZGGEV.f were reproduced using trigonometric clustering of pseudo-spectral Chebyshev points, section 3.2.3.

ARPACK

For the same **A** and **B** matrices in the generalised eigenvalue problem, the ARPACK shift-and-invert routines produced a set of values, all of which could be found in the entire spectrum as produced by ZGGEV.f.

P_ARPACK

Using the same parameter variables and grid sizing, the parallel code produced eigenvalues identical to those produced by the serial form of ARPACK. As there is no compatible distinctly parallel 'full-spectrum' solver, the code was modified to pass the distributed matrices and solve on a single processor thus producing a full set of values using distributed matrices. All results from these two parallel methods correlated, the set of values found by the Arnoldi algorithm being found in the entire spectra recovered by the QZ algorithm. Figure 3.17 is a comparison between the results recovered by the QZ algorithm (dots) and the Arnoldi method (circles) from which it can be seen there is complete agreement.

3.7.3 Testing Viscous Global Solver

The accuracy of the viscous solver is tested first in its serial form for the ease of which the results of the full-spectrum eigenvalue solver can be compared to published values and then in parallel form to examine the convergence behaviour of the eigenvalues as the resolution is increased beyond that which is achievable on a single processor.

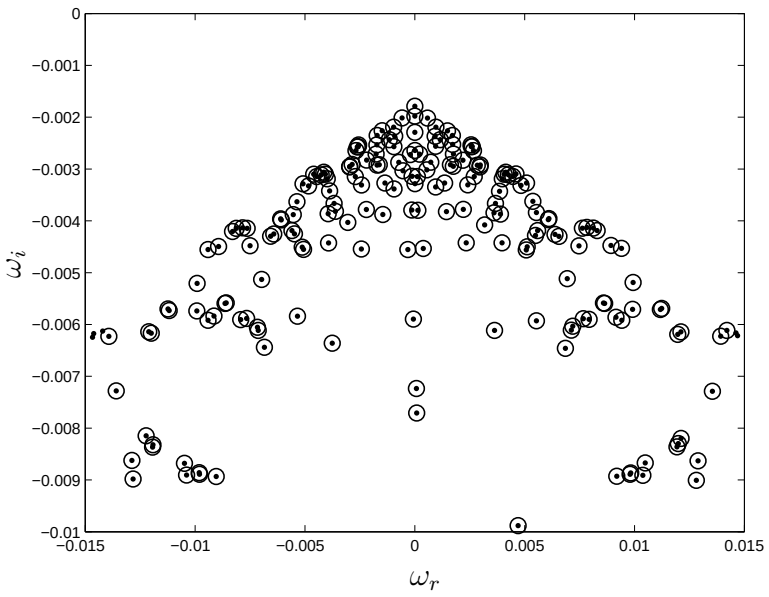

Figure 3.17: Comparison between QZ (dots) and Arnoldi (circles) methods for a single vortex using spectral transformation to standard form in the Arnoldi case.

Axial flow in a Rectangular Duct

One method used to test the accuracy of the discretisation process and the derivation of the axial component of the stability equations was to reproduce published results for stability in a rectangular duct. A duct flow was chosen to validate the Cartesian discretisation (a pipe flow was selected for polar co-ordinates) where there exists sufficient results with which to verify our numerical process.

The results for plane Poiseuille flow (PPF) in a duct are widely known and provide an adequate benchmark for comparison. For our analysis, the work of Theofilis *et al.* [63] reproduces the classic PPF form for a large aspect ratio duct using a pressure gradient driven flow and solves similar governing equations in a similar fashion, also using ARPACK's shift-and-invert routines. The basic flow used satisfies the Poisson equation

$$\frac{\partial^2 U(y,z)}{\partial y^2} + \frac{\partial^2 U(y,z)}{\partial z^2} = -\frac{\partial p}{\partial x} = c, \tag{3.7.11}$$

where, as in Theofilis *et al.* [63] the axial pressure gradient is taken to be constant and set to $c = -2$. The Poisson equation must be solved subject to the boundary conditions $U(y = -N_{max}, z) = U(y = N_{max}, z) = U(y, z = 1) = U(y, z = -1) = 0$.

As is pointed out by Theofilis *et al.* [63], the Poisson equation may also be solved in a series form such that

$$U(y,z) = 1 - z^2 - 4\left(\frac{2}{\pi}\right)\sum_{n=0}^{\infty}\frac{(-1)^n}{(2n+1)^3}\frac{\cosh[(2n+1)\pi y/2]\cos[(2n+1)\pi z/2]}{\cosh[(2n+1)\pi N_{max}/2]}. \tag{3.7.12}$$

The plane Poiseuille basic flow when $N_{max} \to \infty$ is $U(z) = 1 - z^2$. As with Theofilis *et al.* [63] however, in this analysis the numerical discretisation matrices produced firstly with the pseudo-spectral numerical scheme and then secondly with the finite-difference numerical scheme are used to solve equation (3.7.11) and produce our basic axial duct flow. It is obvious that the pseudo-spectral numerical scheme is more suited to this type of flow due to the clustering of grid points around the boundaries, the duct walls, where the no-slip boundary condition is applied. The derivatives of the basic flow are obtained through multiplication by the respective differentiation matrices. It is important to note that whilst this is acceptable for the numerically derived duct flow it isn't always safe to do so. Care should be taken to ensure that the derivatives of the basic flow do in-fact decay to zero over the domain otherwise numerical inaccuracies may occur. For a base flow prescribed by an analytic function it is best, if possible, to prescribe the analytic derivatives rather than using multiplication by the differentiation matrices.

In order to replicate the results of Theofilis *et al.* [63] for $Re = 1000$, the duct aspect ratio was set at 100 by setting N_{max} in the y-direction to 100 and N_{max} in the z-direction to be 1. Figure 3.18 shows the eigenvalue spectra recovered by the two equation fourth order derivative model using pseudo-spectral discretisation. Further plots showing the eigenvalue spectra produced using the four-parameter pseudo-spectral code and two-parameter finite-difference code can be found in Appendix D.

Figure 3.18 can be seen to exhibit the classical profile of PPF with the spectra forming a 45° band for the first mode with $\omega_i \approx -0.3$ and then forming a distinctive band of eigenvalues for varying growth rates at $\omega_r \approx 0.67$. Figure 3.18 corresponds well to those presented in Theofilis *et al.* [63]. The fact that the general form of the PPF spectra is produced however, demonstrates that the viscous global code is effective at producing results relating to the axial component of a basic flow.

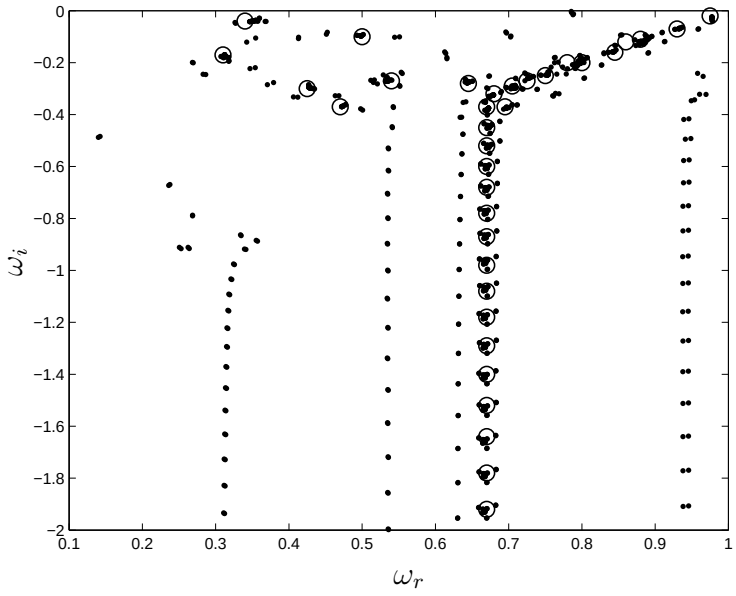

Figure 3.18: Plane Poiseuille flow in a large aspect ratio duct using a pseudo-spectral numerical scheme with dependent parameters $[V, W]$. Circles represent the results of Theofilis *et al.* [63].

Axial flow in a Circular Pipe

Similar to the duct problem, the axial flow in a circular pipe can be used to check the integrity of the viscous polar code. There has been much work over the years into this area with more recent papers producing increasingly more accurate results. In the same vein as before, the two-dimensional polar pseudo-spectral codes (two and four parameter versions) written for this study are used to find the entire spectra of eigenvalues (encompassing all azimuthal wave-numbers n) which can be compared to the one-dimensional results for nominated n-values published previously by Schmid and Henningson [51] and Meseguer and Mellibovsky [43] and also recovered using a one-dimensional code written from the same set of governing equations as the two-dimensional code being tested. For these examples we chose $Re = 3000$ which corresponds to the results of Schmid and Henningson [51] and Meseguer and Mellibovsky [43]. The basic flow is written as

$$U(r) = 1 - r^2, \tag{3.7.13}$$

with the flow in the azimuthal direction being zero, noting the similarity to the plane Poiseuille flow for a large aspect ratio duct. Figure 3.19 shows the eigenvalue spectra generated using the four parameter code, (a), with those values produced by the one-dimensional code for $n = 0, 1, \cdots, 25$, (b).

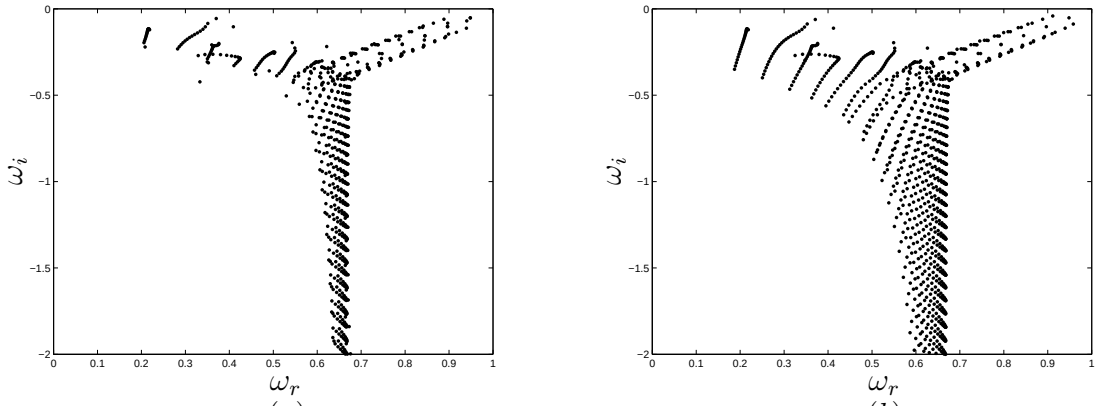

Figure 3.19: Hagen-Poiseuille flow in a pipe of radius 1, found using a two-dimensional pseudo-spectral numerical scheme implementing the four equation method (a) and a quasi one-dimensional code based on the same set of equations (b).

Again, as with the duct flow we can see that figure 3.19 exhibits the expected eigenvalue spectra with the eigenvalues more resolved about the $\omega_r = 0.67$ than in most other regions, however, the classic 45^o form of the PPF profile can still be seen. Exact recovery of this portion of the spectra suffers from a lack of available grid resolution in the two-dimensional global version of the code but the fact that the expected form is achieved suggests the numerical methods behind the scheme are correct.

Single Batchelor Vortex Located at the Origin

Whilst the results previously presented in section 3.7.3 demonstrate the numerical integrity of the discretisation scheme, they only illustrated the solution accuracy with respect to the axial component of basic flow. Whilst we are confident that the numerical discretisation is correct (as the same approach is used as with the

axial components) it is desirable to finalise the verification process by ensuring the cross-flow components themselves are correct. This is done using the Batchelor (or q) vortex, as derived in detail in section 5.3, situated at the co-ordinate origin. Equations (6.3.11) – (6.3.13) with $n = 1$, and with γ and a normalised to unity with the vortex situated at the co-ordinate origin read

$$U = e^{-(y^2+z^2)}, \tag{3.7.14}$$

$$V = \frac{qz}{(y^2+z^2)}[1 - e^{-(y^2+z^2)}], \tag{3.7.15}$$

$$W = \frac{-qy}{(y^2+z^2)}[1 - e^{-(y^2+z^2)}]. \tag{3.7.16}$$

To illustrate the effectiveness of our numerical scheme we present in figure 3.20 the eigenspectra for those values of axial wave-number α, swirl q and Reynolds number Re used by Hein and Theofilis [25]. It should be noted that these authors do not provide specific values for their results and some aspects of their numerical method is omitted (such as the exact number of spectral collocation points or the parameters of the Arnoldi method). However, as an illustrative tool it is useful to compare results. We can see that the general form and magnitude of the eigenvalue spectra produced herein (figure 3.20) is similar to that presented by Hein and Theofilis [25] except that we produce a more defined and dense structure close to the neutral axis (shown to be correct by comparison to our quasi one-dimensional code). This could be attributed to the aforementioned authors selectively presenting results at specific locations using a targeted Arnoldi approach and only recovering a few eigenvalues at a time. The two unstable modes ($\omega_{n=1} = 0.02855 + 0.11854i$ and $\omega_{n=-1} = 0.02835 + 0.00962i$) found in [25] can be seen although as will be explained later, these have not converged to the exact values at the available resolution. Differences in numerical techniques notwithstanding, the results display significant similarity. A comparison with the Cartesian results can be found in Appendix D.

Finally, we present in tables 3.2 – 3.5 a comparison of the first ten least-stable eigenvalues recovered by our four-parameter, two-dimensional (parallel) 'global' code ($(N_r, N_\theta) = (77, 56)$), with those recovered using a quasi one-dimensional code (N_r sufficient for a minimum of 8 decimal place convergence) derived from the same set

of governing equations for $n = 0, 1, 2, 3$ respectively. The latter code has reproduced all listed values of Schmid and Henningson [51] and Meseguer and Mellibovsky [43] for Hagen-Poiseuille flow, all values published in Khorrami *et al.* [32] pertaining to the flow in a swirling pipe and the single Batchelor vortex results of Mayer and Powell [41], Khorrami [30] and Fabre and Jacquin [19] to name but a few. We see that for the axisymmetric case, the comparative results are very good and that those for the higher, non-axisymmetric modes $n \neq \pm 1$ are also very good. For $n = \pm 1$ there is poor correlation in all but the first few modes. The difference is due to the number of extra grid points required in the azimuthal direction to resolve these significantly more complex modes. Figure 3.21 illustrates the compatibility for $n = -10, \cdots, 0, \cdots, 10$.

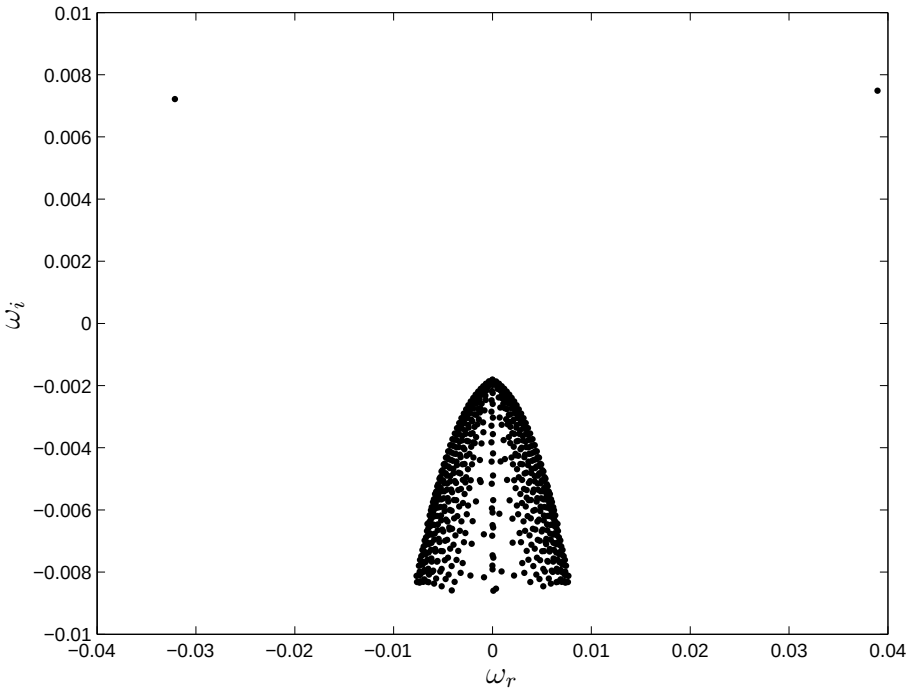

Figure 3.20: Eigenvalue spectra recovered using parameters matching those of Hein and Theofilis [25] for an isolated Batchelor vortex at the co-ordinate origin.

We can conclude from this that the components that make up our numerical scheme are correct and will produce correct and consistent results if, with the available resolution, we restrict our analysis to regions about the neutral axis where we

can safely say the solution has converged. We can however, look further away from the neutral axis to gain an insight into the behaviour of the stability of the system providing we qualify the results by stating that, for the available resolution, convergence to the level of accuracy prescribed above, is not guaranteed nor can it be obtained with the existing computational resources at our disposal. Preference is to be given to the code written in cylindrical polar co-ordinates due to the greater accuracy achievable per number of grid points.

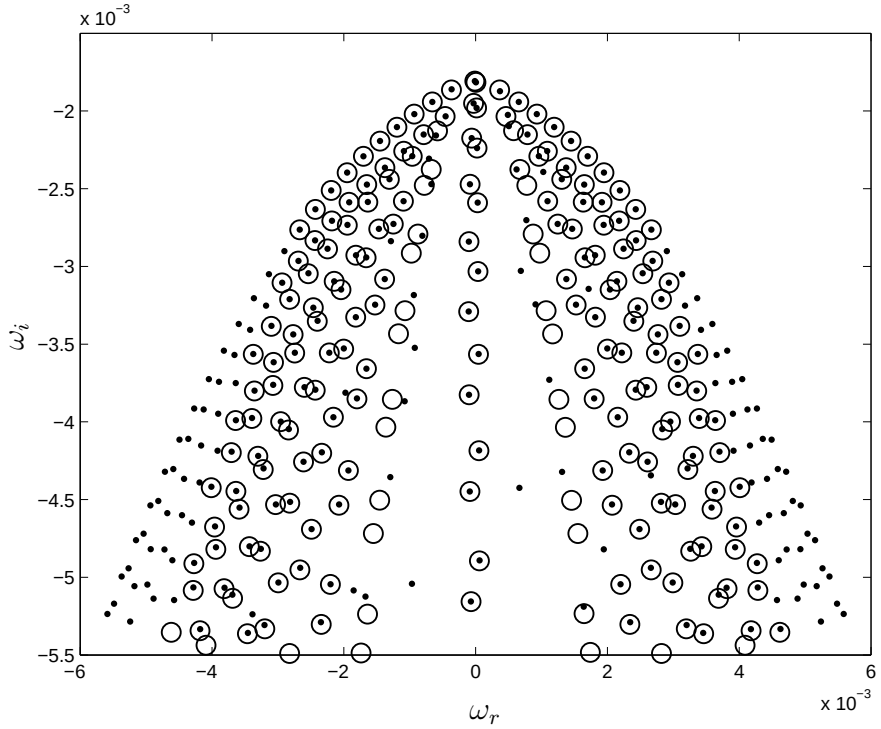

Figure 3.21: A comparison of the eigenvalue spectra recovered by the two-dimensional polar 'global' code (dots) and quasi one-dimensional code (circles) using parameters matching those of Hein and Theofilis [25] for a single Batchelor vortex.

quasi one-dimensional	'global'
-0.0000097601061 - 0.0018073663994i	-0.0000097681697 - 0.0018073430540i
0.0000057931427 - 0.0018160673396i	0.0000058045524 - 0.0018160241657i
-0.0000307171987 - 0.0019514013397i	-0.0000307583673 - 0.0019513231622i
0.0000145711035 - 0.0019801685084i	0.0000146269489 - 0.0019800123366i
-0.0000576961447 - 0.0021747588783i	-0.0000578162757 - 0.0021746200423i
0.0000232584361 - 0.0022385985425i	0.0000234152938 - 0.0022382386180i
-0.0000838939477 - 0.0024713158204i	-0.0000841352478 - 0.0024711103692i
0.0000309890677 - 0.0025900561352i	0.0000313056215 - 0.0025893880027i
-0.0001004100881 - 0.0028409007174i	-0.0001008400659 - 0.0028406599847i
0.0000379834519 - 0.0030328982167i	0.0000385338431 - 0.0030318015657i

Table 3.2: Comparison between the results of the two-dimensional 'global' and quasi one-dimensional codes for the axisymmetric case, $n = 0$.

quasi one-dimensional	'global'
0.0003659888983 - 0.0018647230811i	0.0003697537209 - 0.0018693280591i
0.0004619340702 - 0.0020351257915i	0.0004768027079 - 0.0020293675699i
0.0005756284228 - 0.0021273501976i	0.0005245838722 - 0.0021089946745i
0.0006734145521 - 0.0023757943842i	0.0006321610689 - 0.0023797195791i
0.0007772053144 - 0.0024782625586i	-
0.0008738472024 - 0.0027918770828i	-
0.0009747736306 - 0.0029145997323i	-
0.0010702535461 - 0.0032850412409i	-
0.0011697442095 - 0.0034340908272i	-
0.0012644088854 - 0.0038558679541i	-

Table 3.3: Comparison between the results of the two-dimensional 'global' and quasi one-dimensional codes for the non-axisymmetric case, $n = 1$.

quasi one-dimensional	'global'
0.0006569692230 - 0.0019421161736i	0.0006566921083 - 0.0019419875015i
0.0007886904969 - 0.0021518674196i	0.0007883603212 - 0.0021517552552i
0.0009608422734 - 0.0022913262340i	0.0009603360072 - 0.0022909628257i
0.0010939604118 - 0.0025805519182i	0.0010935762032 - 0.0025803925144i
0.0012474791130 - 0.0027274561778i	0.0012467050082 - 0.0027267212507i
0.0013790358329 - 0.0030813353793i	0.0013786108659 - 0.0030811684979i
0.0015262853783 - 0.0032482802941i	0.0015252009204 - 0.0032470480841i
0.0016565082516 - 0.0036584022009i	0.0016560500030 - 0.0036582490426i
0.0018007046982 - 0.0038519012824i	0.0017992180150 - 0.0038500729030i
0.0019302237827 - 0.0043130647754i	0.0019297318539 - 0.0043129437666i

Table 3.4: Comparison between the results of the two-dimensional 'global' and quasi one-dimensional codes for the non-axisymmetric case, $n = 2$.

quasi one-dimensional	'global'
0.0009306332149 - 0.0020205036875i	0.0009299620041 - 0.0020200165297i
0.0010893405533 - 0.0022586812718i	0.0010885797319 - 0.0022582543419i
0.0013082184227 - 0.0024401761855i	0.0013071197876 - 0.0024390632441i
0.0014676960048 - 0.0027587869462i	0.0014668558088 - 0.0027582379669i
0.0016602600793 - 0.0029442424159i	0.0016587290895 - 0.0029422482551i
0.0018178852488 - 0.0033271464471i	0.0018169722417 - 0.0033265550087i
0.0020009612790 - 0.0035318547525i	0.0019989828689 - 0.0035287713088i
0.0021572011033 - 0.0039706385120i	0.0021562281324 - 0.0039700510385i
0.0023354749277 - 0.0042016684248i	0.0023329207270 - 0.0041974072179i
0.0024910221247 - 0.0046913258821i	0.0024900034831 - 0.0046908358087i

Table 3.5: Comparison between the results of the two-dimensional 'global' and quasi one-dimensional codes for the non-axisymmetric case, $n = 3$.

Chapter 4

Inviscid Flow

4.1 Introduction

Now that we have defined the governing equations and the numerical methods by which we are going to solve them in the previous two chapters, we turn our attention to an incompressible, inviscid stability analysis of several common vortex configurations.

Although no practical flow is inviscid, the study of inviscid flows allows us to solve simplified problems that lead to a basic understanding of the dynamics of the system at hand. It is possible to justify the use of inviscid theory for high Reynolds number flows near a boundary by noting that the boundary layer is thin compared to the axial length scale of the instability. Whilst a vortex flow does not interact with a boundary, we show in section 4.3.2 that, to leading order, the equations governing the flow in the inviscid limit reduce to a simple diffusion equation for which boundary layer approximations are valid.

For this particular study, as the dynamic viscosity of the fluid is small and the speeds and defining length scales are quite large, the use of the inviscid model to approximate the stability characteristics of the flow is entirely acceptable. However, it shouldn't be forgotten that it is an approximation and that whilst the Reynolds number may be high, it is never infinite and as such viscosity will play some small role be it stabilising or otherwise. The adoption of inviscid theory allows the governing equations to be simplified down to a single equation, the two-dimensional Rayleigh

equation, in terms of the perturbation pressure (the dependent variable) and c, the eigenvalue.

4.2 Governing Equations

For our inviscid stability analysis, the governing perturbation equation derived in section 2.4.1 is equation (2.4.8), which we reproduce here for convenience,

$$(U-c)\left[\frac{\partial^2}{\partial r^2}+\frac{1}{r}\frac{\partial}{\partial r}+\frac{1}{r^2}\frac{\partial^2}{\partial \theta^2}-\alpha^2\right]P_p-2\left[\frac{\partial U}{\partial r}\frac{\partial}{\partial r}+\frac{1}{r^2}\frac{\partial U}{\partial \theta}\frac{\partial}{\partial \theta}\right]P_p=0. \quad (4.2.1)$$

4.3 Basic Flow

Whilst the governing equations are relatively standard across many aspects of fluid dynamical stability problems, it is the choice of the basic flow that makes the problem specific. For this study the Batchelor [3] vortex (or multiples thereof) is chosen to represent the trailing vortex flow from an aircraft wing-tip (or tips in the case of multiple vortices). Throughout the literature, the Batchelor vortex is used almost exclusively for studies involving wing-tip vortex stability. In what follows we provide a derivation of the Batchelor vortex resulting in the axial and cross-flow components together with an asymptotic analysis that shows only the axial component is relevant to leading order in this inviscid stability study (which is similar to the method used by Timoshin and Smith [64]). An analytical derivation of the axial basic flow component based on the results of the asymptotic theory is developed by first deriving Batchelor's similarity solution for a single vortex and then expanding this to a multiple vortex solution.

4.3.1 Batchelor's Similarity Solution

The (dimensional) equations governing a steady axis-symmetric flow in cylindrical polar co-ordinates (from equations (2.3.2) – (2.3.4)) are

$$u^*\frac{\partial u^*}{\partial x^*}+v^*\frac{\partial u^*}{\partial r^*}=-\frac{1}{\rho^*}\frac{\partial p^*}{\partial x^*}+\nu^*\nabla^{*2}u^*, \quad (4.3.1)$$

$$u^*\frac{\partial v^*}{\partial x^*} + v^*\frac{\partial v^*}{\partial r^*} - \frac{w^{*2}}{r^*} = -\frac{1}{\rho^*}\frac{\partial p^*}{\partial r^*} + \nu^*\left(\nabla^{*2}v^* - \frac{v^*}{r^{*2}}\right), \tag{4.3.2}$$

$$u^*\frac{\partial w^*}{\partial x^*} + v^*\frac{\partial w^*}{\partial r^*} - \frac{v^*w^*}{r^*} = \nu^*\left(\nabla^{*2}w^* - \frac{w^*}{r^{*2}}\right), \tag{4.3.3}$$

where

$$\nabla^{*2} = \frac{\partial^2}{\partial x^{*2}} + \frac{\partial^2}{\partial r^{*2}} + \frac{1}{r^*}\frac{\partial}{\partial r^*}. \tag{4.3.4}$$

Following Batchelor [3], we consider flow fields where axial gradients are significantly smaller in magnitude than those found in the radial direction which suggests the following boundary-layer type approximation

$$\frac{\partial}{\partial x^*} \ll \frac{\partial}{\partial r^*}, \qquad v^* \ll u^*. \tag{4.3.5}$$

The two-dimensional Laplacian reduces to

$$\nabla^{*2} = \frac{\partial^2}{\partial r^{*2}} + \frac{1}{r^*}\frac{\partial}{\partial r^*}, \tag{4.3.6}$$

and from (4.3.2) we have

$$\frac{1}{\rho^*}\frac{\partial p^*}{\partial r^*} = \frac{w^{*2}}{r^*}. \tag{4.3.7}$$

As the pressure is uniform (p_∞) some distance from the axis (far from the vortex), equation (4.3.7) can be integrated to give

$$\frac{p_\infty - p^*}{p_\infty} = \int_{r^*}^{\infty}\frac{C^{*2}}{r^{*3}}\mathrm{d}r^*, \tag{4.3.8}$$

where $C^* = r^*w^*$. Now, for the solution far downstream of the trailing edge (the focus of our study), Batchelor notes that $|u^* - U_\infty| \ll U_\infty$. The equations of motion (4.3.1) – (4.3.3) are now, with the implementation of these approximations, reduced to the equations that Batchelor [3] derived in his similarity solution for an incompressible flow, namely

$$U_\infty\frac{\partial u^*}{\partial x^*} = -\frac{1}{\rho_\infty}\frac{\partial p^*}{\partial x^*} + \nu_\infty\left(\frac{\partial^2 u^*}{\partial r^{*2}} + \frac{1}{r^*}\frac{\partial u^*}{\partial r^*}\right), \tag{4.3.9}$$

$$\frac{p_\infty - p^*}{p_\infty} = \int_{r^*}^{\infty}\frac{C^{*2}}{r^{*3}}\mathrm{d}r^*, \tag{4.3.10}$$

$$U_\infty \frac{\partial w^*}{\partial x^*} = \nu_\infty \left(\frac{\partial^2 w^*}{\partial r^{*2}} + \frac{1}{r^*}\frac{\partial w^*}{\partial r^*} - \frac{w^*}{r^{*2}} \right). \tag{4.3.11}$$

Batchelor demonstrated that these have the solution

$$u^* = U_\infty - \frac{C_\infty^2}{8\mu_\infty x^*} \log\left(\frac{x^* U_\infty}{\nu_\infty}\right) \mathrm{e}^{-\eta} + \frac{C_\infty^2}{8\nu_\infty x^*} Q(\eta) - \frac{L U_\infty^2}{8\nu_\infty x^*} \mathrm{e}^{-\eta}, \tag{4.3.12}$$

$$v^* = 0, \tag{4.3.13}$$

$$w^* = \frac{C_\infty}{r^*}(1 - \mathrm{e}^{-\eta}). \tag{4.3.14}$$

Here, C_∞ is the value of C^* at large r^*, L is a constant with the dimensions of area and representing the characteristic area of the object being studied, the similarity variable η is given by

$$\eta = \frac{U_\infty r^{*2}}{4\nu_\infty x^*}, \tag{4.3.15}$$

and

$$Q(\eta) = \mathrm{e}^{-\eta}(\log(\eta) + \mathrm{ei}(\eta) - 0.807) + 2\mathrm{ei}(\eta) - 2\mathrm{ei}(2\eta), \tag{4.3.16}$$

with

$$\mathrm{ei}(\eta) = \int_\eta^\infty \frac{\mathrm{e}^{-\xi}}{\xi} \mathrm{d}\xi, \tag{4.3.17}$$

where $\xi = 2\eta^{\frac{1}{2}}$. If we now follow the non-dimensionalisation of Lessen *et al.* [38] we can show that the term involving $Q(\eta)$ in (4.3.12) is significantly smaller than the other term involving C_∞^2 for large Re and as such the velocity scales by

$$U_s = \frac{C_\infty^2}{8\mu_\infty x^*} \log\left(\frac{x^* U_\infty}{\nu_\infty}\right) \mathrm{e}^{-\eta} + \frac{L U_\infty^2}{8\nu_\infty x^*} \mathrm{e}^{-\eta}, \tag{4.3.18}$$

and the length by

$$r_s = \left(\frac{4\nu_\infty x^*}{U_\infty}\right)^{\frac{1}{2}}. \tag{4.3.19}$$

The non-dimensional basic flow can be written as

$$(U, V, W) = \left(\frac{U_\infty}{U_s} - \mathrm{e}^{-r^2}, 0, \frac{q}{r}(1 - \mathrm{e}^{-r^2}) \right), \tag{4.3.20}$$

where the swirl parameter, q is the inverse of the Rossby number such that

$$q = \frac{C_\infty}{2\pi U_s r_s}, \tag{4.3.21}$$

and

$$r = \frac{r^*}{r_s} = \eta^{\frac{1}{2}}. \tag{4.3.22}$$

It is important to note that Batchelor's similarity solution is valid *"...for the flow in a trailing vortex far downstream."* Thus, by this statement we can assume $x^* \gg 1$ which from (4.3.19) implies that $r_s \gg 1$ ($r_s \propto x^{*\frac{1}{2}}$) and as such, from (4.3.21) the swirl parameter q is found to be small ($q \ll 1$) for this inviscid analysis.

As was initially shown by Lessen and Paillet [38], and later by Fabre and Jacquin [19], and for the compressible case by Stott and Duck [59], only the real component of the eigenvalue in (4.2.1) is affected by the translation and inversion of the axial velocity profile. We therefore set

$$U = \mathrm{e}^{-r^2}. \tag{4.3.23}$$

It should be noted however, that whilst many authors use this simplification (and it is justifiably correct to do so), Khorrami [30] also points out that the removal of the quantity U_∞/U_s and subsequent inversion of the axial velocity profile causes the sign of the unstable azimuthal wave-number to change. Whilst this is important to keep this in mind it has no bearing on the present analysis due to the global nature of our analysis, we solve the disturbance equation for the entire spectra of n values and do not stipulate our unstable modes by their azimuthal wave-numbers. For comparative purposes, in studies that set $U_\infty/U_s = 1$, a factor of α is added to the real component of the complex phase velocity, c.

In what follows we present an alternative derivation of the basic flow that will show that the derivation and subsequent simplification of the Batchelor similarity solution to a one-dimensional flow in terms of the axial component for our far-field analysis at high Reynolds numbers (as encountered in an inviscid analysis) is a valid one.

4.3.2 Leading Order Asymptotic Analysis

If we assume that the flow far from the wing-tip is uniform and given by $(u^*, v^*, w^*) = U_s(U, V, W)$ which can be normalised at some distance far from the vortices by $(u^*, v^*, w^*) = U_\infty(1, 0, 0)$, we can define a Reynolds number as $Re = U_\infty L_s/\nu$, where L_s is a typical length scale in the cross-section and ν is, as before, the kinematic viscosity. The long streamwise length scale of Batchelor can then be formalised by defining non-dimensional variables via $(x^*, y^*, z^*) = L_s(Re\ x, y, z)$ where Re is used as the axial length scale where the dimensional variations occur at $\mathcal{O}(Re)$ as opposed to $\mathcal{O}(1)$ in the cross-section. We also define time and pressure in terms of the free-stream velocity as non-dimensional variables, $t^* = L_s t/U_\infty$ and $p^* = \rho^* U_\infty^2 P$ respectively. With this non-dimensionalisation, the continuity equation becomes

$$\frac{1}{Re}\frac{\partial U}{\partial x} + \frac{\partial V}{\partial y} + \frac{\partial W}{\partial z} = 0, \tag{4.3.24}$$

from which it can be seen that for conservation of mass, $\partial V/\partial y$ and $\partial W/\partial z$ must be of $\mathcal{O}(Re^{-1})$ which in turn implies that V and W are both of $\mathcal{O}(Re^{-1})$ (since y and z are both of $\mathcal{O}(1)$). Following the work of Batchelor [3] we then assume that the vortex flow consists of the undisturbed uniform flow plus a small correction where $\epsilon \ll 1$ so that the total velocity field can be written as

$$(u^*, v^*, w^*) = U_\infty(1 + \epsilon U_p, \epsilon Re^{-1} V_p, \epsilon Re^{-1} W_p), \tag{4.3.25}$$

and

$$p^* = \rho^* U_\infty^2 (P + \delta P_p), \tag{4.3.26}$$

where δ is some small (constant) scaling parameter that will be defined shortly. Assuming that the flow is steady, we can non-dimensionalise by substitution of (4.3.25) and the relevant length scales into (4.3.1) to yield

$$\begin{aligned}\frac{(1+\epsilon U_p)\epsilon}{Re}\frac{\partial U_p}{\partial x} + \frac{\epsilon^2 V_p}{Re^2}\frac{\partial U_p}{\partial y} \quad &+ \quad \frac{\epsilon^2 W_p}{Re^2}\frac{\partial U_p}{\partial z} = -\frac{1}{Re}\frac{\partial}{\partial x}(P + \delta P_p) \\ &+ \quad \frac{\epsilon}{Re}\left(\frac{1}{Re^2}\frac{\partial^2 U_p}{\partial x^2} + \frac{\partial^2 U_p}{\partial y^2} + \frac{\partial^2 U_p}{\partial z^2}\right),\end{aligned}$$

which can be re-arranged to give

$$\begin{aligned}\epsilon\frac{\partial U_p}{\partial x} + \epsilon^2 U_p\frac{\partial U_p}{\partial x} + \frac{\epsilon^2 V_p}{Re}\frac{\partial U_p}{\partial y} \quad &+ \quad \frac{\epsilon^2 W_p}{Re}\frac{\partial U_p}{\partial z} = -\frac{\partial}{\partial x}(P + \delta P_p) \\ &+ \quad \frac{\epsilon}{Re^2}\frac{\partial^2 U_p}{\partial x^2} + \epsilon\frac{\partial^2 U_p}{\partial y^2} + \epsilon\frac{\partial^2 U_p}{\partial z^2}.\end{aligned} \tag{4.3.27}$$

We have already stated that far from the vortices the pressure can be approximated as a constant, that is, it equalises with the surrounding air pressure free of the influences of the wing interaction. Therefore the axial leading order pressure gradient can also be approximated as zero. Equating terms in powers of ϵ and reciprocal powers of Re we can see that, to leading order, (4.3.27) can be approximated by a convection-diffusion equation in terms of the axial perturbation velocity U_p,

$$\frac{\partial U_p}{\partial x} = \frac{\partial^2 U_p}{\partial y^2} + \frac{\partial^2 U_p}{\partial z^2}. \tag{4.3.28}$$

We have shown that $\partial P_p/\partial x \approx 0$ for our basic flow, therefore for the governing equations to remain valid (four equations in four unknowns) the pressure terms must be included in the perturbation portion of the vertical and cross-sectional equations. Equations (4.3.2) and (4.3.3) become respectively

$$\begin{aligned}\frac{(1+\epsilon U_p)\epsilon}{Re^2}\frac{\partial V_p}{\partial x} + \frac{\epsilon^2 V_p}{Re^3}\frac{\partial V_p}{\partial y} &+ \frac{\epsilon^2 W_p}{Re^3}\frac{\partial V_p}{\partial z} = -\delta\frac{\partial P_p}{\partial y} \\ &+ \frac{\epsilon}{Re^2}\left(\frac{1}{Re^2}\frac{\partial^2 V_p}{\partial x^2} + \frac{\partial^2 V_p}{\partial y^2} + \frac{\partial^2 V_p}{\partial z^2}\right),\end{aligned} \tag{4.3.29}$$

$$\begin{aligned}\frac{(1+\epsilon U_p)\epsilon}{Re^2}\frac{\partial W_p}{\partial x} + \frac{\epsilon^2 V_p}{Re^3}\frac{\partial W_p}{\partial y} &+ \frac{\epsilon^2 W_p}{Re^3}\frac{\partial W_p}{\partial z} = -\delta\frac{\partial P_p}{\partial z} \\ &+ \frac{\epsilon}{Re^2}\left(\frac{1}{Re^2}\frac{\partial^2 W_p}{\partial x^2} + \frac{\partial^2 W_p}{\partial y^2} + \frac{\partial^2 W_p}{\partial z^2}\right).\end{aligned} \tag{4.3.30}$$

It can be seen that for equations (4.3.29) and (4.3.30) to be valid at leading order ($\mathcal{O}(Re^{-2})$), $\partial P_p/\partial y$ and $\partial P_p/\partial z$ must be of a compatible size. Therefore, an appropriate approximation for δ is $\delta \approx \epsilon/Re^{-2}$ and as such (to leading order) equations (4.3.29) and (4.3.30) become

$$\frac{\partial V_p}{\partial x} = -\frac{\partial P_p}{\partial y} + \frac{\partial^2 V_p}{\partial y^2} + \frac{\partial^2 V_p}{\partial z^2}, \tag{4.3.31}$$

$$\frac{\partial W_p}{\partial x} = -\frac{\partial P_p}{\partial z} + \frac{\partial^2 W_p}{\partial y^2} + \frac{\partial^2 W_p}{\partial z^2}. \tag{4.3.32}$$

If we consider that our analysis is focussed on a region significantly downstream from the wing edge and that we are seeking short wave-length disturbances (where the disturbance grows over a length scale much smaller than the variation in x) at very high Reynolds numbers, the fact that the axial velocity component is an $\mathcal{O}(Re)$ larger than the radial and azimuthal terms is sufficient to justify the use of only the axial component of the basic flow to ascertain the leading order stability

characteristics of the vortex flow. In order to establish the validity of this analysis, the same non-dimensional variables are applied to the Batchelor equations derived in section 4.3.1.

Now, if we take (the Batchelor) equations (4.3.9) – (4.3.11) and non-dimensionalise using the relationships derived earlier in this section we obtain

$$(1+\epsilon U_p)\epsilon\frac{\partial U_p}{\partial x} = \epsilon\frac{\partial^2 U_p}{\partial r^2} + \frac{\epsilon}{r}\frac{\partial U_p}{\partial r}, \tag{4.3.33}$$

$$\delta\frac{\partial P_p}{\partial r} = \frac{\epsilon^2}{Re^2}\frac{W_p}{r}, \tag{4.3.34}$$

$$(1+\epsilon U_p)\frac{\epsilon}{Re}\frac{\partial W_p}{\partial x} = \frac{\epsilon}{Re}\frac{\partial^2 W_p}{\partial r^2} + \frac{\epsilon}{rRe}\frac{\partial W_p}{\partial r} - \frac{\epsilon}{Re}\frac{W_p}{r^2}, \tag{4.3.35}$$

where as before we set $\delta = (\epsilon/Re)^2$. If we now look at equations (4.3.33) – (4.3.35) to leading order in powers of ϵ and reciprocal powers of Re we can see that equations (4.3.34) and (4.3.35) are at least an $\mathcal{O}(Re)$ smaller than (4.3.33) and as such, in this inviscid (high Re) analysis it is acceptable to only consider the axial component of the perturbed flow. We are left with a diffusion type equation in terms of the axial perturbation velocity,

$$\frac{\partial U_p}{\partial x} = \frac{\partial^2 U_p}{\partial r^2} + \frac{1}{r}\frac{\partial U_p}{\partial r}, \tag{4.3.36}$$

which is the polar equivalent of equation (4.3.28).

4.3.3 Analytical Derivation of Axial Basic Flow

Further to the derivation of the axial component of basic flow described earlier, as (4.3.36) takes the form of a typical convection-diffusion equation it is acceptable to seek solutions of the form commonly associated with this type of equation, namely

$$U_v(x,r) = A(x)e^{-b(x)r^2}, \tag{4.3.37}$$

where $A(x)$ and $b(x)$ are scale parameters that depend on the axial position of the basic flow only. Substituting (4.3.37) into (4.3.36) gives, upon cancelling the common e^{-br^2} term

$$\frac{\partial A}{\partial x} - A\frac{\partial b}{\partial x}r^2 = 4Ab^2r^2 - 4Ab. \tag{4.3.38}$$

From (4.3.38) we can see that as A and b are dependent only on the axial position x, it is acceptable to equate terms with radial dependance so that

$$-\frac{\partial b}{\partial x} = 4b^2,$$

which can be integrated to yield

$$-\frac{1}{b} = 4x + C,$$

where C is some constant of integration which, without loss of generality, can be set equal to zero. Thus,

$$b(x) = -\frac{1}{4x}, \tag{4.3.39}$$

which, when substituted into (4.3.38) gives

$$\frac{\partial A}{\partial x} = -\frac{A}{x},$$

or

$$\ln|A| = -\ln|x| + D,$$

where again, D is a constant that can, without loss of generality, be set equal to zero and so

$$A(x) = \frac{1}{x}. \tag{4.3.40}$$

Therefore, a basic flow that satisfies (4.3.36) is

$$U_v(x, r) = \frac{1}{x} e^{-r^2/4x}, \tag{4.3.41}$$

where, due to the short wave-length nature of the instabilities, the parameters determining the amplitude and e-folding distance can be assumed to be constant in terms of this two-dimensional analysis, and as such we set $\gamma = 1/x$ and $a = 1/4x$ giving

$$U_v(r) = \gamma e^{-ar^2}, \tag{4.3.42}$$

or in Cartesian co-ordinates,

$$U_v(y, z) = \gamma e^{-a(y^2+z^2)}. \tag{4.3.43}$$

If we note here that equation (4.3.36) is linear, it is easy to show that linear combinations of the solution (4.3.41) are also solutions by examination of equation (4.3.42) such that any linear combination is simply defined by a value of γ. We may also infer without any loss of generality that a vortex offset from the co-ordinate origin such as $U_v(y,z) = \gamma e^{-a[(y-y_1)^2+(z-z_1)^2]}$ is also an acceptable solution of (4.3.28).

4.3.4 Dominant Growth Rates

Looking at many of the figures of growth rate versus swirl that have been produced in the literature over the years, it would be quite easy to assume categorically that increased swirl always produces a larger instability growth rate. Whilst this statement is essentially correct, it neglects a fundamental component of Batchelor's [3] similarity solution. We see that whilst C tends rapidly to a constant, C_o (C_∞ in equation (4.3.12)) as $r \to \infty$, it is still explicitly dependent of the axial position, x, and as such is not actually constant in terms of the entire flow field. The swirl decays exponentially with x (the axial distance from the wing-tip) and therefore, for q to be $\mathcal{O}(1)$ in the far field where our analysis is taking place (being the location of most interest in terms of the wake-vortex hazard problem and where Batchelor defines his similarity solution), at the wing-tip or several chord lengths back, q would need to be exponentially large which is unrealistic in a real aircraft trailing flow even in high-lift configurations.

The asymptotic analysis given previously shows that, in the far field ($x \to \infty$) the azimuthal components of the basic flow (and hence the swirl dependent quantities) are of an $\mathcal{O}(Re^{-1})$ smaller than the axial component. We can then assume without loss of generality that in the far field, the swirl q has decayed to a level that renders it less important in terms of a stability analysis than the axial velocity component. For most of the previously published work on swirling inviscid flows to be interpreted correctly with regards to a realistic aircraft wake, a secondary plot illustrating the axial position corresponding to each particular value of the swirl parameter q would be a useful way of clarifying what could perhaps be described as a common misconception.

Figure 4.1 is an example of this concept, noting that the growth rates and their

respective axial placement and swirl rates are purely schematic and do not correspond to any particular flow. The figure shows the dominant growth rates (and associated swirl) for a particular set of axial positions and clearly shows the concept of the 'globally' smaller growth rates being dominant as $x \to \infty$. Effectively this means that whilst it is true that the addition of swirl can produce the largest instability growth rates in a global sense, these instabilities are only relevant for values of swirl that would occur in the near-field. These instabilities are of academic interest due to the fact that the basic flow used in their calculation (Batchelor's [3] similarity solution is derived for the flow in a trailing vortex **far** downstream; asymptotically large x) is not valid at the small to moderate values of x which yield moderate values of swirl.

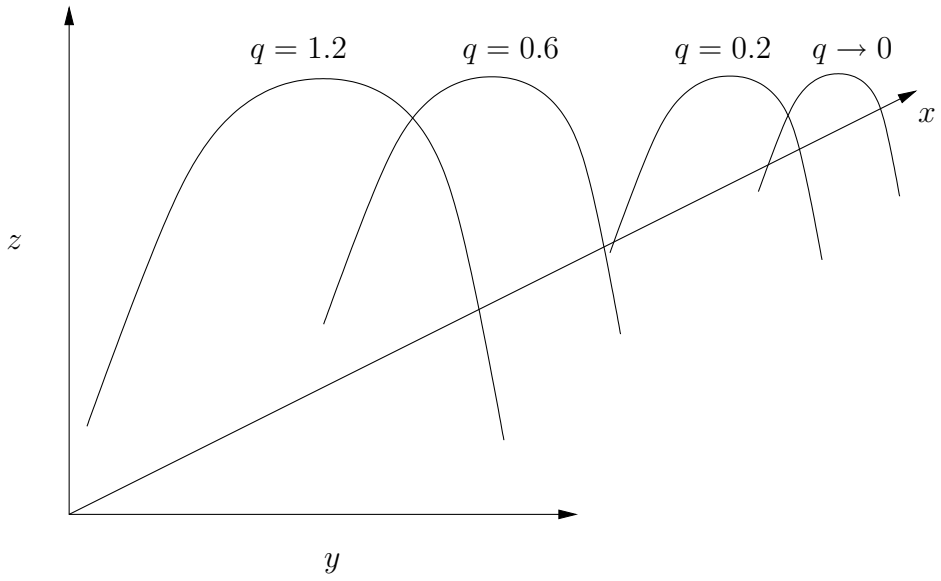

Figure 4.1: Schematic of the axial position of dominant growth rates and their respective swirl rates.

4.4 Computational Domain

We now turn our attention to the numerical methods that will be employed in solving equation (4.2.1). Working in cylindrical polar co-ordinates (r, θ, x), the computational domain is a circular region on the y, z-plane with an outer boundary at r_{max}. The various vortices are placed within this boundary as illustrated in figure 4.2.

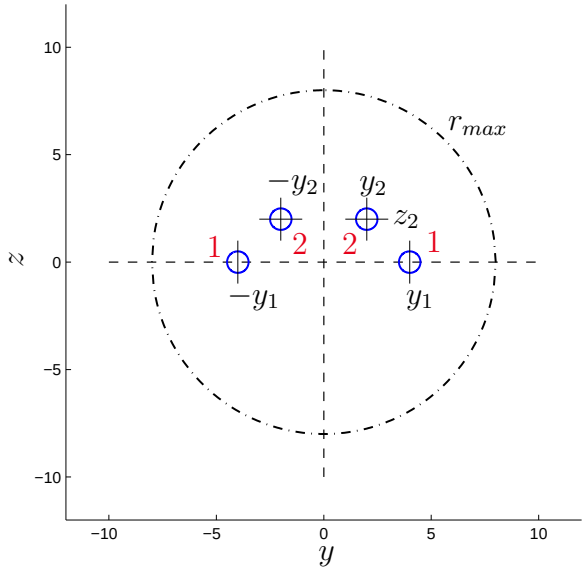

Figure 4.2: Computational domain showing multiple vortex placement.

4.5 Numerical Results

The following results are obtained using the global spectral solver outlined in section 3.2 on the cylindrical polar domain with a boundary set at $r_{max} = 8$. This was found to adequately capture the basic flow decay whilst maintaining a manageable problem size (with respect to the number of collocation points required for eigenvalue convergence) in terms of computational expense. Furthermore, unless otherwise stated the parameters γ_1 (axial strength of the primary vortex) and a_1 (decay rate of the primary vortex) are set equal to unity in all our inviscid, incompressible analyses. It should also be noted that for the single vortex placement, $y_1 = 0.001$ was used to avoid numerical problems that may be associated with $y_1 = 0$. In the results that follow, s is the clustering parameter defined in section 3.2.3.

The differentiation matrices have the homogeneous Dirichlet boundary conditions enforced explicitly, that is, the outer rows and columns of the matrices referring to the grid points on the boundaries are set to zero (and subsequently removed, see section 3.3.2). Therefore, we require the function being multiplied by the differentiation matrix to also decay to zero at the boundaries. If, as in the case of the inviscid basic flow, the flow decays to below machine working precision at the boundaries

the respective differentiation matrices can be used to compute the derivatives of this flow. Care was taken to ensure that the flow has decayed below machine precision thus limiting the effect of numerical inaccuracies which would otherwise occur.

4.5.1 Single Vortex Numerical Convergence

For the single vortex analysis, used primarily as a basis for comparison with previously published work, a convergence history is given for $\alpha = 0.64$ (which was the wave-number of largest instability growth rate found prior to the introduction of grid clustering) for variation in N_r (table 4.1) with $N_\theta = 24$ and for variation in both N_r and N_θ (table 4.2).

N_r	Eigenvalue, $s = 0.9$
40	0.49401772 + 0.07905681i
50	0.49422412 + 0.07893369i
60	0.49424021 + 0.07897890i
70	0.49423090 + 0.07898033i
80	0.49423093 + 0.07897850i
90	0.49423131 + 0.07897844i
100	0.49423121 + 0.07897840i
110	0.49423115 + 0.07897862i
120	0.49423132 + 0.07897863i
130	0.49423127 + 0.07897851i
140	0.49423124 + 0.07897863i
150	0.49423134 + 0.07897857i
160	0.49423126 + 0.07897868i
170	0.49423118 + 0.07897863i
180	0.49423118 + 0.07897852i

Table 4.1: Convergence history of most unstable eigenvalue for a single vortex, varying N_r with $N_\theta = 24$.

(N_r, N_θ)	Eigenvalue, $s = 0$	Eigenvalue, $s = 0.9$
(40,16)	0.47093447 + 0.06171516i	0.49401794 + 0.07905622i
(50,20)	0.50683114 + 0.08077313i	0.49422386 + 0.07893360i
(60,24)	0.49302841 + 0.08543821i	0.49424021 + 0.07897890i
(70,28)	0.48940204 + 0.07663830i	0.49423098 + 0.07898049i
(80,32)	0.49727297 + 0.07783315i	0.49423119 + 0.07897870i
(90,36)	0.49426103 + 0.08073476i	0.49423159 + 0.07897878i
(100,40)	0.49311499 + 0.07852179i	0.49423168 + 0.07897895i
(110,44)	0.49485441 + 0.07855596i	0.49423177 + 0.07897928i

Table 4.2: Convergence history of most unstable eigenvalue for a single vortex varying (N_r, N_θ).

It can be seen that for the single vortex problem, convergence to five or six significant figures occurs at approximately $(N_r, N_\theta) = (80, 32)$ when grid clustering is used, with a higher degree of convergence occurring at higher grid resolutions as expected. It is also apparent that for the single vortex, grid clustering recovers smaller unstable modes for fewer grid points (results not presented here).

4.5.2 Two-Vortex Numerical Convergence

For the two vortex problem, a convergence history for an increase in both spatial parameters for no clustering and for $s = 0.8$ are given. For the clustered values, convergence to five or six significant figures is reached very quickly in both the real and imaginary components of the eigenvalue at this particular vortex spacing. Again, these results illustrate that the chosen number of grid points is sufficiently accurate for graphical illustration purposes.

4.5.3 Four-Vortex Numerical Convergence

Table 4.4 is a convergence history of the most unstable eigenvalue found for the four-vortex configuration. From the convergence histories presented, it can be seen that the number of grid points used to establish the stability characteristics of the

flow, $(N_r, N_\theta) = (80, 32)$, is acceptable from an accuracy standpoint, especially when the computational time required to perform such large region sweeps is considered. Table 4.5 illustrates the convergence of the same eigenvalue at the accuracy presented subject to several degrees of grid clustering parameter s.

(N_r, N_θ)	Eigenvalue, $s = 0$	Eigenvalue, $s = 0.8$
(40,16)	0.50363261 + 0.17202150i	0.50520484 + 0.17304474i
(50,20)	0.50593810 + 0.17316223i	0.50521573 + 0.17302209i
(60,24)	0.50504026 + 0.17308132i	0.50521563 + 0.17302038i
(70,28)	0.50522775 + 0.17300490i	0.50521559 + 0.17302061i
(80,32)	0.50521892 + 0.17301160i	0.50521554 + 0.17302074i
(90,36)	0.50521686 + 0.17302804i	0.50521546 + 0.17302092i
(100,40)	0.50521353 + 0.17301912i	0.50521538 + 0.17302109i
(110,44)	0.50521595 + 0.17302133i	0.50521531 + 0.17302129i

Table 4.3: Convergence history of most unstable eigenvalue for a two-vortex configuration with $\alpha = 0.8$ and varying (N_r, N_θ).

We see that grid clustering for the multiple vortex case, unlike the single vortex case which had a significant effect, for the values in table 4.4 the accuracy is only affected beyond four decimal places for $s = 0.8$ once the number of grid points in the radial direction reaches about 70. If we compare this with the extended clustering convergence history in table 4.5 it becomes apparent that a higher level of clustering only improves the convergence of the eigenvalue to five or six significant figures of its current value at a particular number of grid points and not to those results obtained using the higher number of grid points outlined in table 4.4. This would seem to indicate that beyond $N_r \approx 80$, especially when combined with a degree of clustering, the number of grid points in the radial direction has little effect on the convergence of the eigenvalue.

The influence of the domain size is shown in table 4.6 with $s = 0.8$. It becomes fairly clear that whilst the eigenvalues do not converge completely (a fact discussed later), there is no significant effect on the value for any domain sizes larger than $r_{max} = 8$.

(N_r, N_θ)	Eigenvalue, $s = 0$	Eigenvalue, $s = 0.8$
(40,16)	0.37525551 + 0.13670591i	0.37659569 + 0.13652172i
(50,20)	0.38993202 + 0.13912887i	0.38984032 + 0.13942809i
(60,24)	0.39333029 + 0.13336267i	0.39314144 + 0.13333451i
(70,28)	0.39084047 + 0.13279322i	0.39085973 + 0.13272446i
(80,32)	0.39126799 + 0.13343808i	0.39128817 + 0.13344530i
(90,36)	0.39141647 + 0.13297546i	0.39141389 + 0.13298379i
(100,40)	0.39116107 + 0.13306711i	0.39115779 + 0.13306562i
(110,44)	0.39126572 + 0.13315980i	0.39126647 + 0.13315874i

Table 4.4: Convergence history of most unstable eigenvalue for a four-vortex configuration.

s	Eigenvalue
0.2	0.39127663 + 0.13345982i
0.4	0.39128321 + 0.13344032i
0.6	0.39128817 + 0.13344530i
0.8	0.39128738 + 0.13344594i
0.9	0.39128761 + 0.13344602i
0.95	0.39128730 + 0.13344333i

Table 4.5: Convergence of presented eigenvalues for a four-vortex configuration subject to varying degrees of grid clustering $(N_r, N_\theta) = (80, 32)$.

It is likely that for the four-vortex case, the resolution in θ becomes more important in order to resolve this complex flow. Table 4.7 presents the convergence history for varying N_θ with $N_r = 80$ and $s = 0.8$ and shows an improved convergence to around five significant figures; $(N_r, N_\theta) = (80, 60)$ is the limit of the resolution possible on a single processor (that is available) but as before we can see that the eigenvalue remains unchanged to three or four significant figures from the more manageable problem size $(N_r, N_\theta) = (80, 32)$.

(N_r, N_θ)	Eigenvalue, $r_{max} = 12$	Eigenvalue, $r_{max} = 16$
(40,16)	0.37647743 + 0.13647637i	0.37560232 + 0.13724076i
(50,20)	0.38982144 + 0.13941502i	0.38981165 + 0.13919496i
(60,24)	0.39314094 + 0.13333863i	0.39326877 + 0.13325726i
(70,28)	0.39086005 + 0.13272633i	0.39089617 + 0.13278305i
(80,32)	0.39128707 + 0.13344542i	0.39126516 + 0.13345336i
(90,36)	0.39141349 + 0.13298353i	0.39141052 + 0.13297684i
(100,40)	0.39115727 + 0.13306539i	0.39116000 + 0.13306366i
(110,44)	0.39126595 + 0.13315852i	0.39126644 + 0.13315973i

Table 4.6: Convergence history of most unstable eigenvalue for a four-vortex configuration for variation in r_{max}.

N_θ	Eigenvalue
32	0.39128817 + 0.13344530i
36	0.39141385 + 0.13298378i
40	0.39115780 + 0.13306563i
44	0.39126650 + 0.13315875i
48	0.39127832 + 0.13308314i
52	0.39124037 + 0.13309895i
56	0.39125812 + 0.13311209i
60	0.39125926 + 0.13310030i

Table 4.7: Convergence of eigenvalues for increasing N_θ with $N_r = 80$, $s = 0.8$.

The convergence histories given above show that, to the computational accuracy used in the following four vortex analysis ($(N_r, N_\theta) = (80, 32)$), the eigenvalues are converged to within graphical accuracy. It has also been shown that a degree of grid clustering in the radial direction helps to improve the convergence of these values to a certain extent. However, it is apparent that the numerical scheme cannot converge on the eigenvalue beyond this degree of accuracy without significantly increasing the resolution in the azimuthal direction. Of all the methods used, a variation of the

azimuthal spatial parameter combined with clustering of the radial direction is the best method of improving the degree of convergence.

As the grid clustering algorithm has a negligible effect on the computational time, the inviscid analysis was run employing clustering. It should also be pointed out that the level of grid clustering could be tailored to the specific problem, for example, a problem involving a single vortex will benefit from a greater amount of clustering (as shown previously) than a four-vortex problem whose outer limits are located further away from the co-ordinate origin. In what follows, all eigenvalues are quoted to the number of decimal points they were found to converge to at the resolution used.

4.6 A Single Vortex at the Co-ordinate Origin

It has been shown by Lessen *et al.* [38], and in results re-produced in section 3.7.1 that for a vortex with $q = 0$ (as is essentially the case in this inviscid analysis) as the axial wave-number is increased to approximately $\alpha = 1.2$, the vortex becomes neutrally stable, that is, the growth rate $\alpha c_i \rightarrow 0$. Figure 4.3 is an illustration of the basic flow for a single vortex used in this analysis.

The variation with α of the eigenvalues of the most unstable mode can be found in figure 4.4 which is a higher resolution plot of the imaginary component of figure 3.16 which reproduces the results of Lessen *et al.* [38] with a more appropriate domain boundary size and grid clustering parameter of $s = 0.9$. It is clear that whilst the domain size of Lessen *et al.* [38] is widely considered to be insufficient, comparison with figure 4.4 shows it to be a close representation of the instability when compared to what is found using a more appropriate (ie larger) computational domain. It is also interesting to note that for the $n = 1$ mode in question, the greatest instability as found by Lessen *et al.* [38] is when $q = 0$, the value of swirl which, from our leading order asymptotic analysis (see section 4.3.2), would be expected to produce the greatest inviscid instability.

Figure 4.5 is a plot of the growth rate of the most unstable mode producing a maximum growth rate of $\alpha c_i = 0.05054$ at $\alpha \approx 0.65$. The curve displays a smooth transition throughout the unstable range of α. A number of other unstable modes

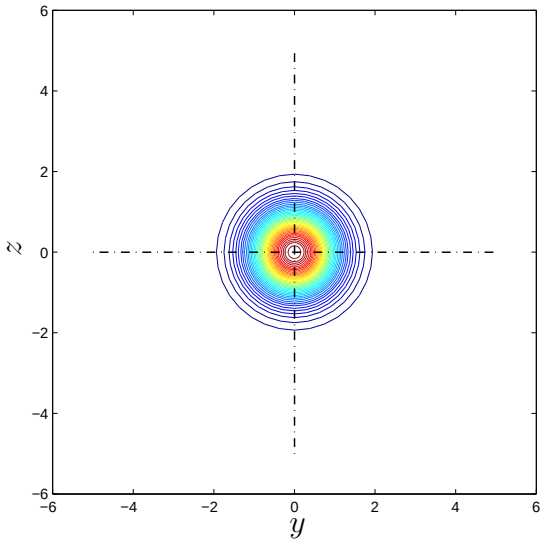

Figure 4.3: Axial component of inviscid basic flow for a single Batchelor vortex located at the co-ordinate origin.

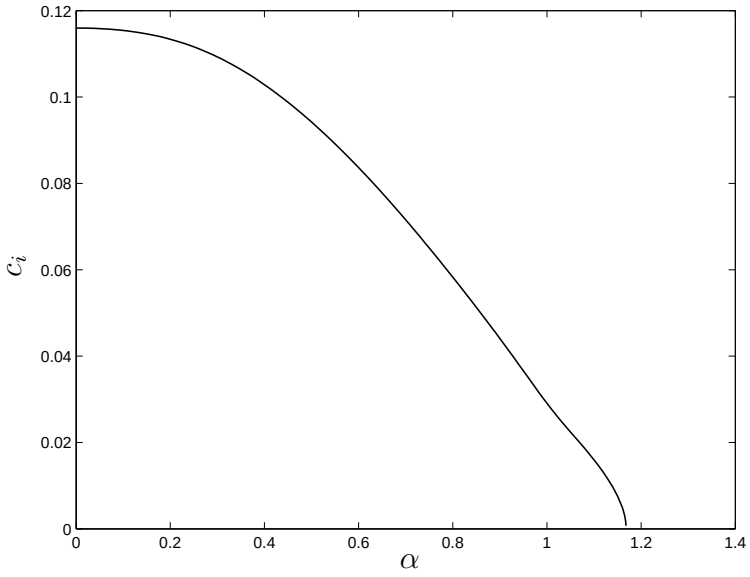

Figure 4.4: The most unstable mode of a single vortex for a range of α.

were recovered with growth rates at least a factor of two smaller than the two most unstable. The second most unstable mode only varies from the first by an order of $\mathcal{O}(10^{-6})$ in both the real and imaginary components as listed in table 4.8, but

despite the closeness of the eigenvalues the plots of the respective eigenfunctions in figure 4.6 show them to be distinct modes.

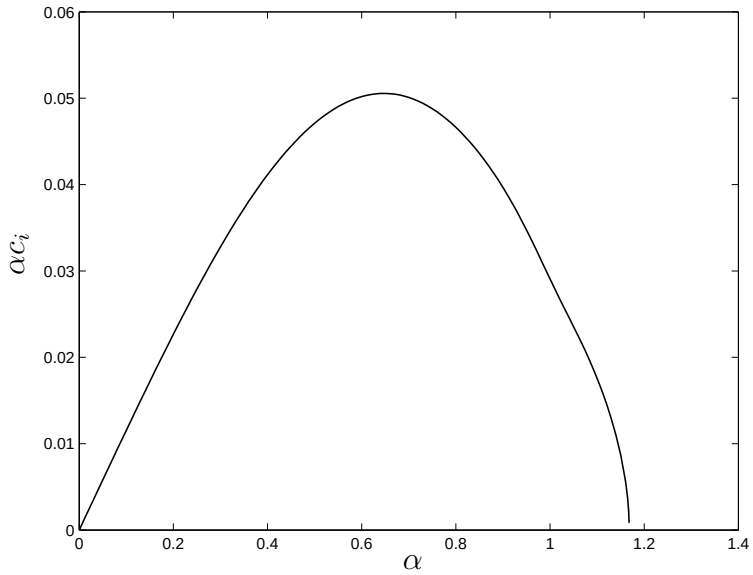

Figure 4.5: Growth rate of single Batchelor vortex at origin.

Mode 1	0.495649 + 0.077775i
Mode 2	0.495648 + 0.077774i

Table 4.8: Single vortex, unstable eigenvalues.

In figure 4.6, we present plots of the amplitudes of the perturbation pressure $P_p(y, z)$ from a single vortex with $\alpha = 0.65$ corresponding to the two most unstable eigenvalues at the point of maximum instability growth rate. Stable complex conjugate eigenvalues of the two unstable modes found are also present, each exhibiting a similar modal structure to their unstable counterparts.

4.7 Two-Vortex Configuration

The two-vortex model consists of only the primary vortices (y_1 in figure 4.2), positioned on the $z = 0$ axis. The variable parameters γ and a are set equal to 1. Figure 4.7 represents the superposed basic flow of a typical two-vortex configuration. For

the purpose of analysis the wave-number α and the horizontal placement y_2 are varied. Our aim is to determine the configuration of vortices which promote the largest instabilities and the corresponding growth rates.

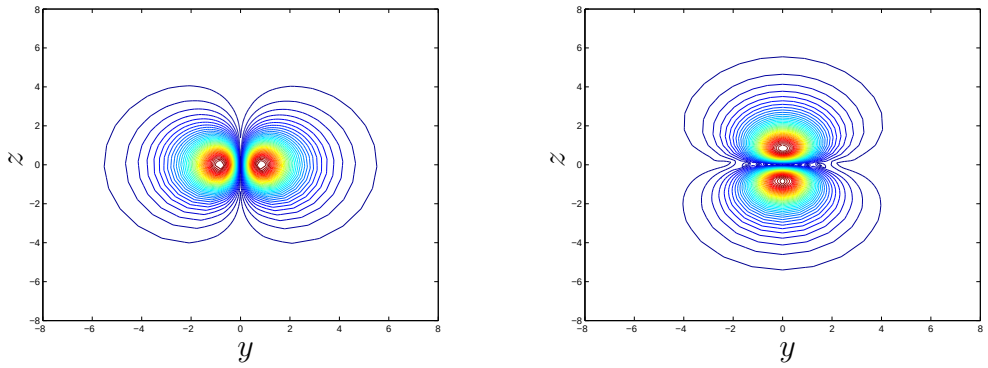

Figure 4.6: Two most unstable eigenmodes representing the perturbation pressure for single Batchelor vortex at origin. (a) Mode 1, (b) Mode 2.

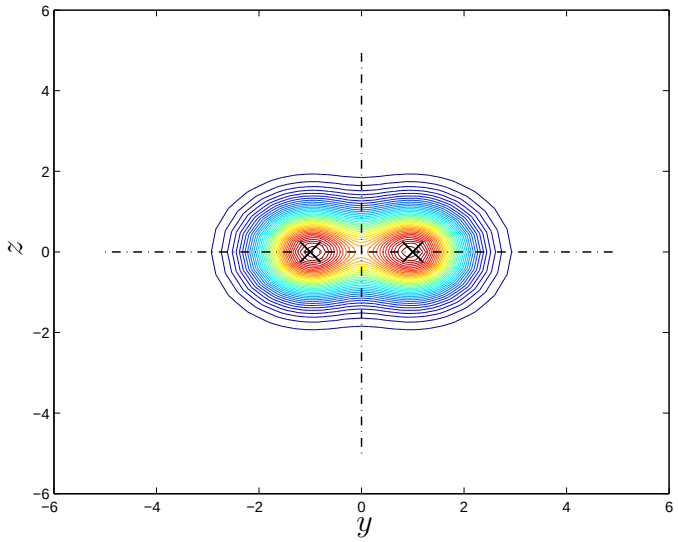

Figure 4.7: Axial component of inviscid basic flow for a typical two-vortex configuration. '×' marks the vortex positions of the basic flow.

In figure 4.8 we present a contour plot of the 'global' (maximum) growth rate. From this figure we can clearly identify the parameter region in which the growth rate of the instability is at its greatest. The region is well defined in terms of vortex placement and axial wave-number. Whilst a change to a second dominant mode is

evident in the plot as the vortex spacing increases (around $y = 1.2$), the size of this new dominant mode is almost an order of magnitude smaller than the first mode. The plot then clearly demonstrates that, for this particular set of parameters, the most unstable mode occurs for $(y, \alpha) \approx (0.8, 0.86)$.

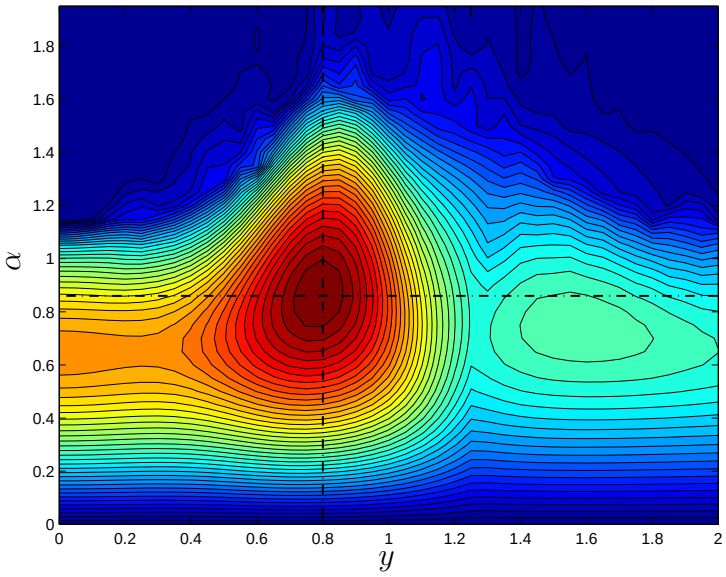

Figure 4.8: Contours of 'global' growth rate for varying vortex positions at $z = 0$ for a two-vortex configuration.

Figure 4.9 is a local growth rate plot taken through $y = 0.8$ as described by the dashed line on figure 4.8. It is worth noting that as α increases, the curve appears to asymptote towards a non-zero growth rate rather than the expected behaviour of $\alpha c_i = 0$ at $\alpha \approx 1.8$. This behaviour is typical of resolution issues that are encountered at higher wave numbers when attempting to resolve a near-neutral mode of instability as a result of the critical layer which arises at positions (y, z) where $U = c_r$. We also note that at $\alpha \approx 1.55$ the mode presented in this figure ceases to be the most dominant with the secondary mode becoming more unstable.

In figure 4.10 we present a plot of the maximum instability versus the location of the two vortices. Here we see that the two-vortex system produces a maximum instability at approximately $y = 0.8$ for the most unstable mode with this set of parameters. The first point to note is that as the vortices approach each-other,

the instability changes form and approaches the value for a single vortex of double strength located at the origin, as is to be expected. This was verified by running the code with a single vortex of double axial strength. The second interesting point is that the plot exhibits a distinct turning point after $y \approx 1.3$ and it becomes obvious when comparing figures 4.10 and 4.8 for the appropriate value of α that at the spacing $y \approx 1.3$ the 'first' tracked mode is no longer dominant and a modal shift has occurred which is discussed in more detail later. The greatest instability is found at $y = 0.78$ and corresponds to a growth rate of 0.139507 from which we find that $(\alpha, y) = (0.86, 0.78)$ results in an eigenvalue of $c_1 = 0.529072 + 0.162217\text{i}$ for this configuration.

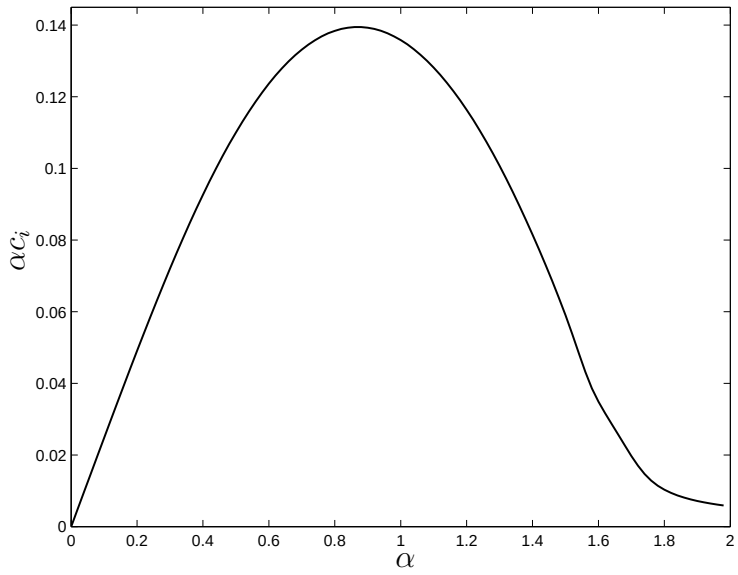

Figure 4.9: 'Local' growth rate for most unstable vortex position in a two-vortex configuration. $y \approx \pm 0.8$ corresponding to a maximum growth rate of 0.139461 with $\alpha = 0.86$.

Figure 4.11 below plots the first eight unstable modes arranged in order of the imaginary component of the eigenvalue. The curve in figure 4.10 can clearly be seen but it also shows the extension of this mode beyond the value of y where the previously less dominant second mode becomes the most unstable.

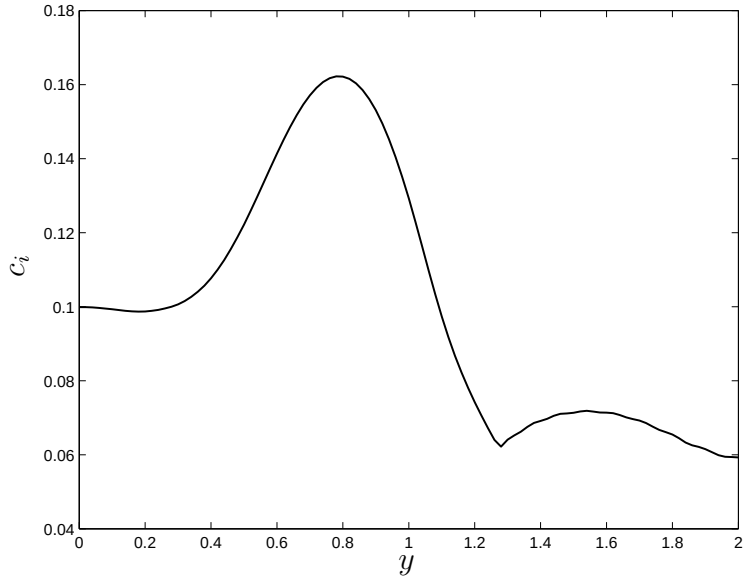

Figure 4.10: Inviscid instability of the most dominant mode for varying vortex placement in a two-vortex configuration.

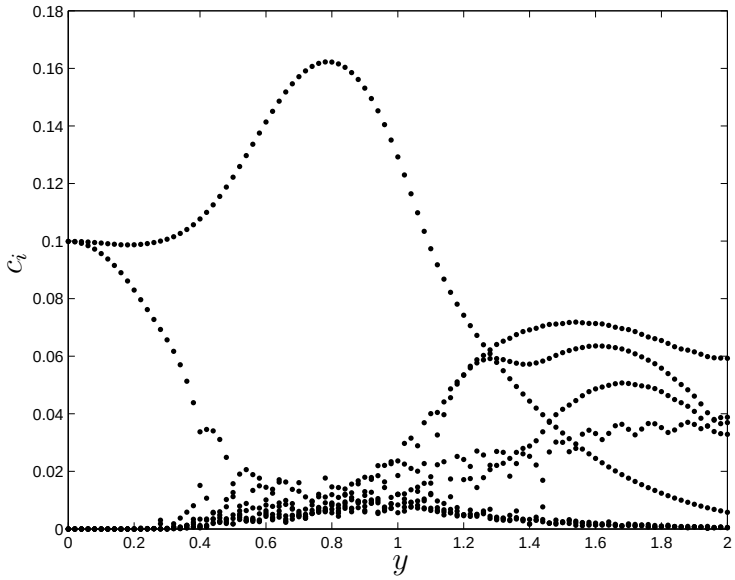

Figure 4.11: Inviscid instability of the first eight modes recovered in order of highest imaginary component for varying vortex placement in a two-vortex configuration.

As was mentioned earlier, a change in the most unstable (or dominant) mode can be seen in the results. By plotting the amplitude of the perturbation pressure

(the eigenfunction) for values at a few intervals of vortex placement along the y-axis with $\alpha = 0.86$, a modal transition can be seen to take place as is illustrated in the shape of the functions plotted in figure 4.12. As noted earlier, this occurs at $y \approx 1.3$.

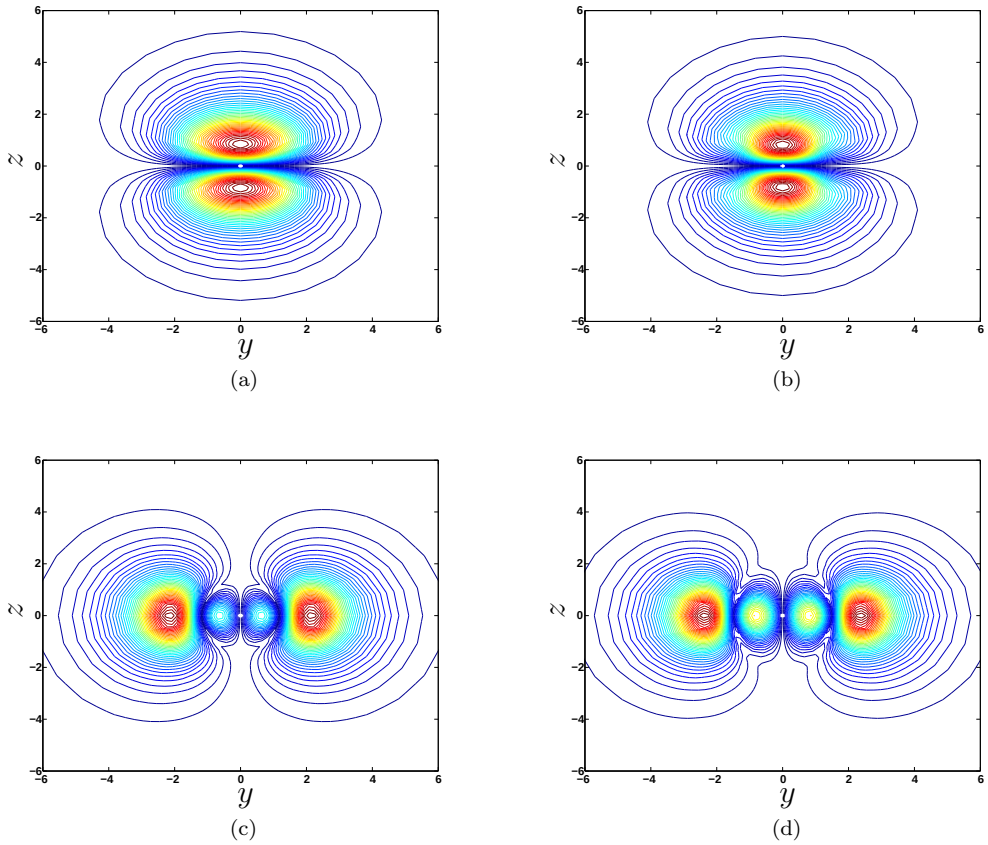

Figure 4.12: Plots of the magnitude of the most rapidly growing perturbation pressure eigenfunction for $\alpha = 0.86$ and various values of y for two-vortex system. Shown are (a) $y = 1.0$, (b) $y = 1.2$, (c) $y = 1.4$, and (d) $y = 1.6$ with a change in dominant mode at $y \approx \pm 1.3$.

4.8 Four-Vortex Configuration

Turning our attention to a four-vortex configuration (representing the wing-tip and a single inboard vortex, for example) as set out in figure 4.2, the position of the primary (wing-tip) vortices are fixed at $(y_1, z_1) = (\pm 2, 0)$ with the set of parameters γ_2 and a_2 set at 0.5 and 1 respectively, γ_1 and a_1 are set to unity (as in section

4.7). The secondary vortex positions and α are the problem variables with positions moved about the computational domain and the eigenvalues corresponding to the most unstable mode (largest positive imaginary component of c) found for each position and value of α. The problem's geometry ensures symmetry about the z-axis whist the results show that symmetry exists about the y-axis and therefore only a single quadrant of the domain need be analysed.

Figure 4.13 illustrates the axial velocity (the only velocity component relevant to our inviscid analysis, see section 4.3.2) for a typical four-vortex layout similar to that described in figure 4.2. Vortex placements are $(y_1, z_1) = (\pm 2, 0), (y_2, z_2) = (\pm 1, 1)$, and shows the extent of merging of the axial velocity at these vortex locations.

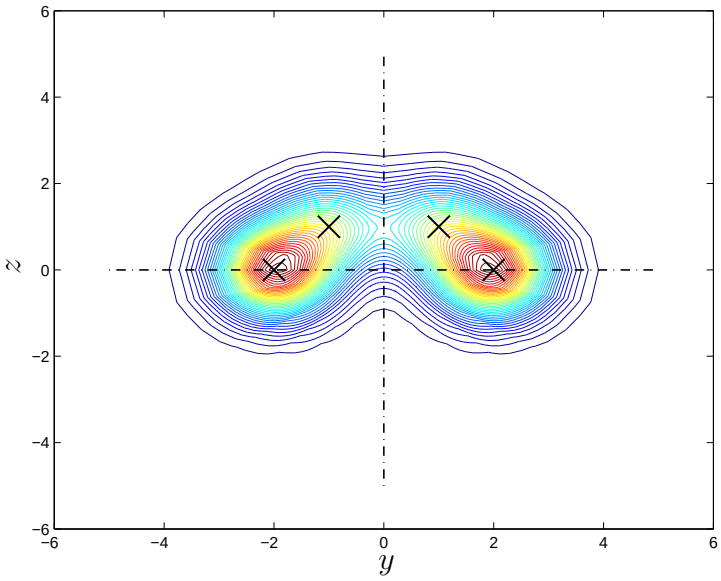

Figure 4.13: Axial component of basic flow for a typical four-vortex configuration. '×' marks the vortex positions of the basic flow.

Figures 4.14 and 4.15 show contours of varying instability for the secondary vortices, progressively moved about the interior of the domain with the parameters $\gamma_2 = 0.5$ and $a_2 = 1$, for the first (figure 4.14) and second (figure 4.15) most unstable modes. It can be readily seen from the figures that the configuration of greatest instability for the most dominant mode (mode 1) is located at $(y_2, z_2) \approx (0.35, 0)$ which corresponds to an eigenvalue of $c_1 = 0.39127 + 0.13344\mathrm{i}$ with $\alpha = 1$. For the second mode (mode 2), a similar position of instability can be seen although this is

more evenly spread from $y_2 = 0$ to the vortex position of maximum instability than the localised area of instability for mode 1.

It can be seen from figures 4.14 and 4.15 that the greatest inviscid instability lies when the inboard vortices approach one-another and consequently move away from the fixed primary vortices. This would seem to indicate that it is preferable to force the secondary vortices to interact with each-other rather than their respective outboard counterparts in order to produce the greatest trailing vortex system instability.

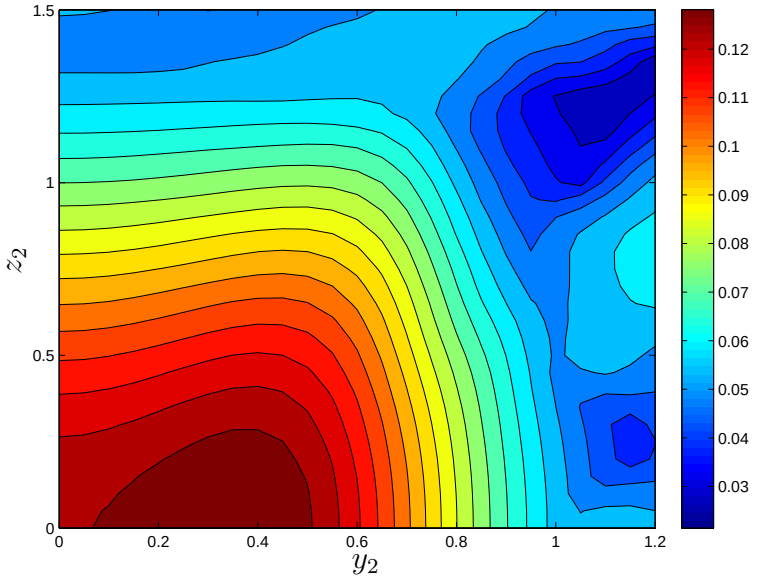

Figure 4.14: Contour plot of instability of the most dominant mode for varying secondary vortex placement in a four-vortex configuration. Maximum instability when $c_1 = 0.39127 + 0.13344i$ at $\alpha = 1$.

The first four perturbation pressure eigenfunctions $P_p(y, z)$ corresponding to the choice $(y_2, z_2) = (\pm 0.35, 0)$ are illustrated in figure 4.16. With this vortex spacing, the two inboard vortices have merged into a single elliptically shaped vortex, whereas the outboard vortices maintain their separate identities.

Figure 4.17 is a global growth rate plot for the set of parameters being analysed, global in this sense being the $+y_2$ half of the computational domain. It would be expected that the growth rates would be mirrored about the $z-$axis if we were to show the $-y_2$ components.

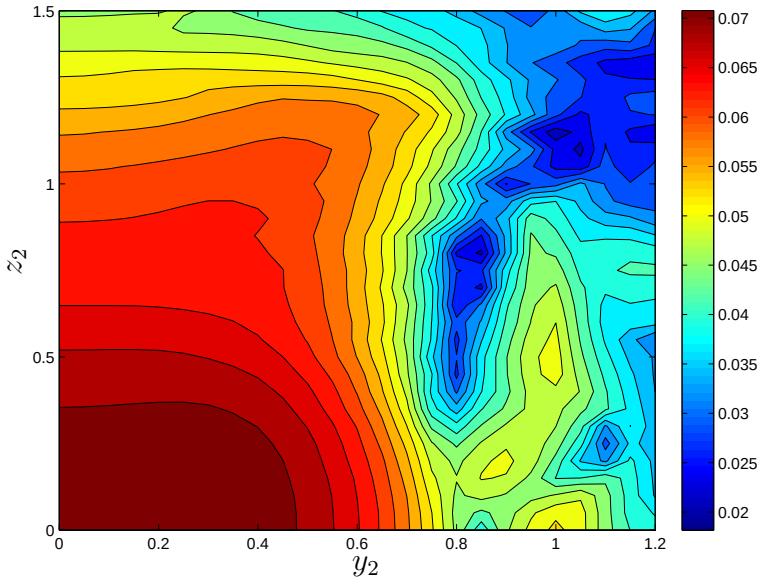

Figure 4.15: Contour plot of instability of the second most dominant mode for varying secondary vortex placement in a four-vortex configuration.

It can be seen that the region of largest instability growth occurs when $(y_2, \alpha) \approx (0.35, 0.9)$ and is strongly correlated to the interaction of the two secondary vortices when they are situated in close proximity to one another. Figures 4.14 and 4.15 demonstrate that the most unstable configuration of our four-vortex system is found when all four vortices are co-linear (ie; when $z_2 = 0$). As the secondary vortices are moved away from the origin, the diminishing interaction between them causes the growth rate to drop. At $y_2 \approx 0.9$ it would appear that the effect on the growth rate from secondary vortex interaction is minimal with interaction between the respective primary and secondary vortices being the dominant factor in the magnitude of the growth rate from this point on.

Figure 4.18 is the local (ie, for a particular vortex placement) temporal growth rate plot taken through the y_2 position of maximum instability ($y_2 \approx 0.35$) as indicated by the dashed line on figure 4.17. It shows a typical growth rate plot with a maximum of $\alpha c_i = 0.13557$ at $\alpha = 0.9$. As α increases the curve asymptotes towards a non-zero growth rate which, as noted earlier, is an artefact of the numerical scheme due to the singular nature of the eigenvalue problem at the near-neutral modes.

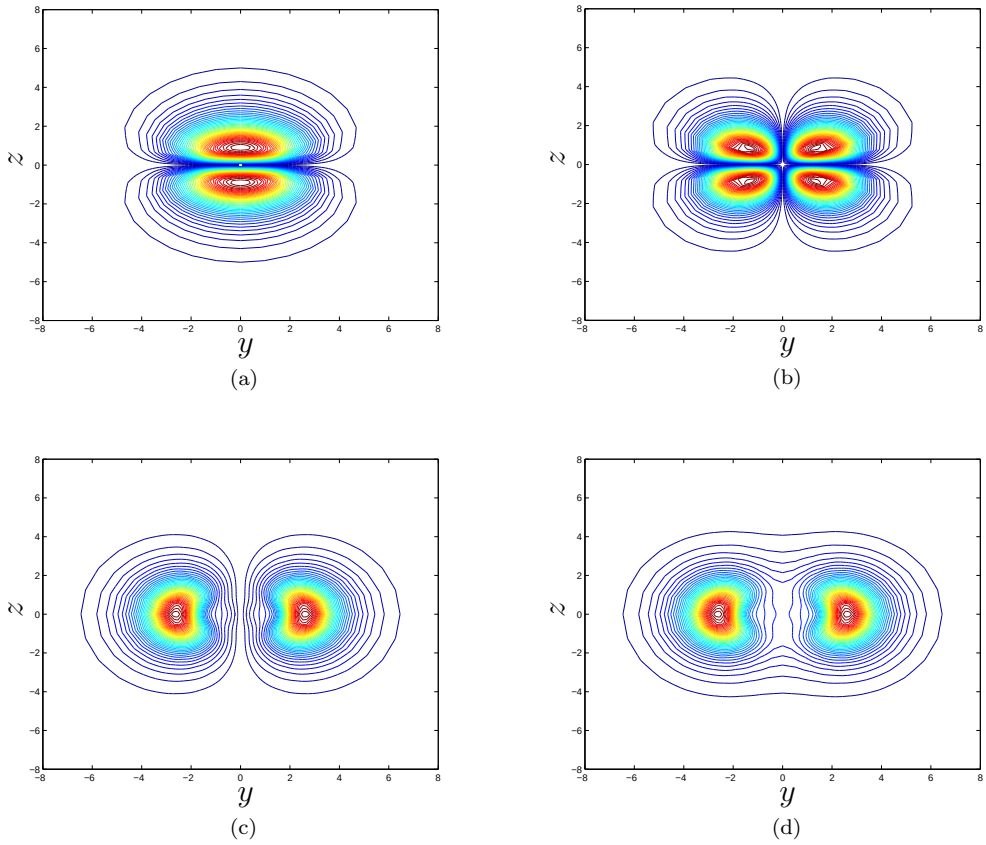

Figure 4.16: (a)–(d): eigenfunctions representing the perturbation pressure $|p(y,z)|$ for the first four modes, with $(y_2, z_2) = (\pm 0.35, 0)$, which is the most unstable choice of secondary vortex locations in a four-vortex configuration.

It can be seen from figure 4.19, which is a plot of the instability for varying the position of the secondary vortices at $\alpha = 0.9$, that there is a change in the dominant mode, firstly after $y_2 \approx 0.9$ and then again at $y_2 \approx 1.5$. The figure further refines the parameters for (maximum) instability at $(\alpha, y_2) = (0.9, 0.36)$ with a resulting eigenvalue of $c_1 = 0.37596 + 0.15063\mathrm{i}$.

The first eight unstable modes in order of the magnitude of the imaginary component of the eigenvalue for a variation in the y-position of the secondary vortices can be found in figure 4.20. As with the two-vortex case, the curve in figure 4.20 clearly shows the extension of this mode beyond the value of y where the previously less dominant second mode becomes the most unstable. These modes and others can clearly be traced in this plot.

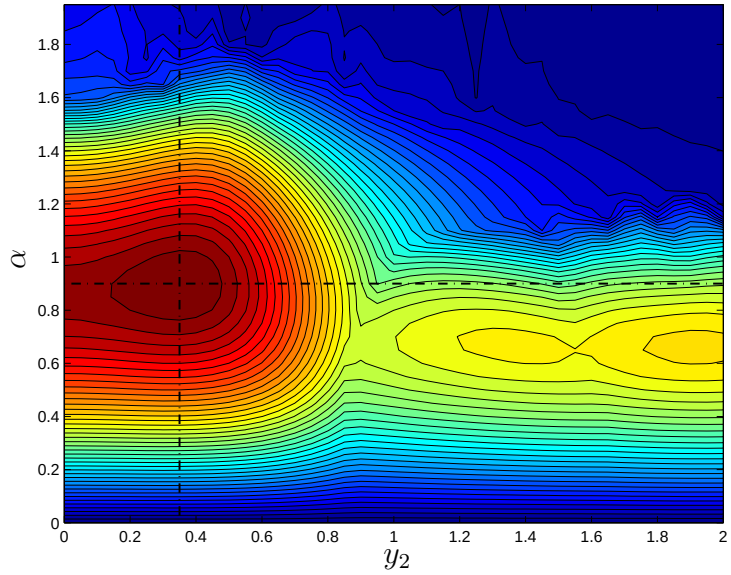

Figure 4.17: Contours of 'global' growth rate for varying secondary vortex positions at $z_2 = 0$ in a four-vortex configuration.

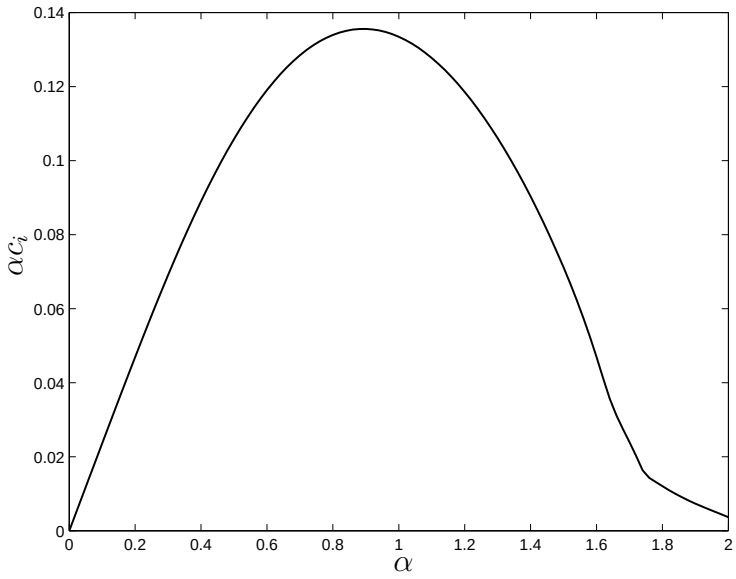

Figure 4.18: 'Local' growth rate for most unstable secondary vortex position in four-vortex configuration. $(y_2, z_2) \approx (\pm 0.35, 0)$ corresponding to a maximum growth rate of 0.13557 at $\alpha = 0.9$.

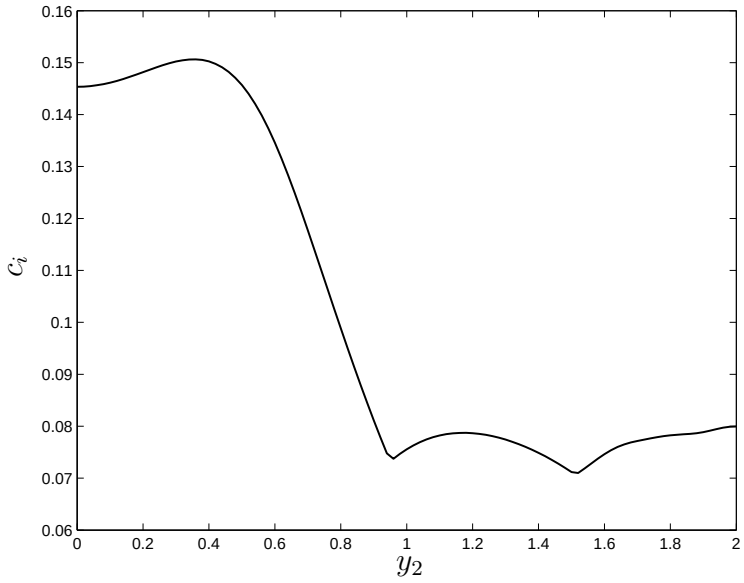

Figure 4.19: Inviscid instability of the most dominant mode for varying secondary vortex placement in a four-vortex configuration.

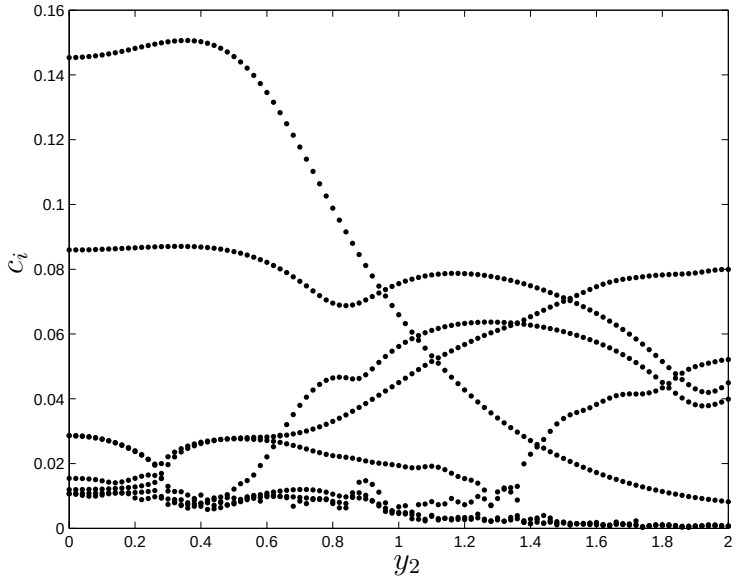

Figure 4.20: Inviscid instability of the first eight modes recovered in order of highest imaginary component for varying secondary vortex placement in four-vortex configuration.

In figure 4.21 we plot the eigenfunctions of the most unstable eigenvalue for sequential positions of y_2. It can clearly be seen that between $y_2 = 0.75$ and $y_2 = 1.0$ the shape of the function undergoes a change from symmetric about the $y = 0$ axis to symmetric about both y and z. This corresponds to the variation in the growth rate shown in figure 4.17.

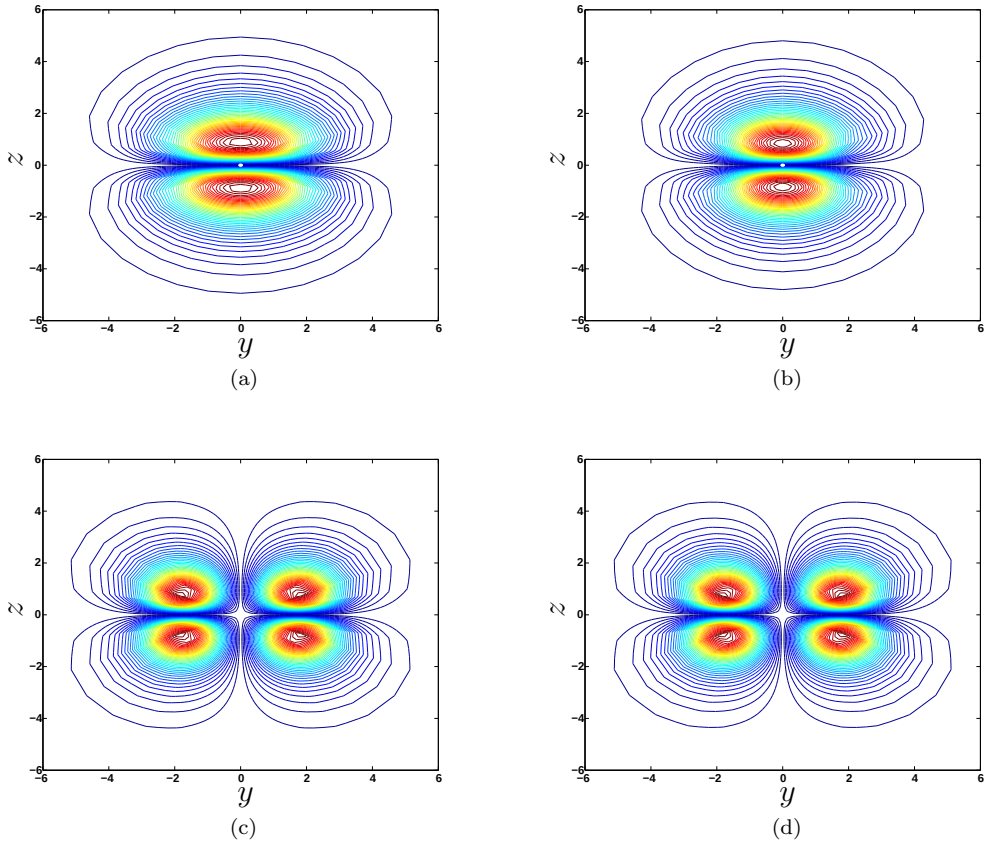

Figure 4.21: Plots of the magnitude of the most rapidly growing perturbation pressure eigenfunction for $\alpha = 0.9$ and various values of y_2 for four-vortex system. Shown are (a) $y_2 = 0.5$, (b) $y_2 = 0.75$, (c) $y_2 = 1.0$, and (d) $y_2 = 1.25$ with a change in dominant mode at $y_2 \approx \pm 0.9$.

4.9 Discussion

It has been demonstrated that the most unstable configuration of a four-vortex system occurs when the axes of the vortices are colinear. The relative spacing of the vortex pairs which leads to the largest growth rate, for an inviscid disturbance to the flow, is also found. The presence of a second pair of vortices, inboard to the primary pair, is shown to affect the growth rate of the inviscid instability of the primary vortex system. If there was no effect from the secondary vortices we would expect the two plots to be identical with the primary system being dominant. This is not the case as can be seen when comparing figure 4.9 for the two-vortex case with the corresponding figure 4.18 for the four-vortex case, although, for this set of parameters, we have found that the magnitude of the growth rate remains similar for both the two-vortex system and the four-vortex system. Furthermore, as the relative vortex spacing is changed, the dominant form of instability (that is, the fastest growing mode) changes from that which would arise in the case of a simple two-vortex model of an aircraft wing, as is shown by comparing the shape of the modes in figures 4.12 and 4.21.

If we extend the placement of the secondary vortex in the four-vortex case past the point at which it coincides with the primary vortex placement, as found in figure 4.22, several interesting points arise. Firstly, the dominant mode at $y_2 \approx 2$ appears to be almost symmetric about $y_2 = 2$ which would suggest that for this particular mode, the vortex pairs on the opposing sides of the z-axis are having limited influence on the stability characteristics of each-other. However, if we compare the instability at $y_1 = y_2 = 2$ for the four-vortex case with a single vortex using $\gamma = 1.5$ to simulate one pair of vortices only, we produce a maximum instability of $c = 0.79920 + 0.06493\text{i}$ as opposed to $c = 0.81002 + 0.07994\text{i}$, the difference would suggest that there is some degree of interaction between the vortex pairs. Finally, if we compare these results to a two-vortex configuration with $y = 2$ and $\gamma = 1.5$ this results in $c = 0.81002 + 0.07994\text{i}$ which is, as expected, the same. This shows that there is some interaction between the vortex pairs in the four-vortex case that contributes to a larger instability than would otherwise be present if there was no interaction.

4.10 Parameter Variations

In the previous section, γ_2 and a_2 were chosen to produce secondary vortices of comparable dimension but with half the axial strength of the primary vortices. Here the vortex axial strength parameter γ_2 and the decay rate a_2 of the secondary vortices are varied from the values chosen above for the detailed analysis, to examine the change in respective position of the first and second most unstable modes with these parameters. As with the previous analysis, the primary vortex position and the axial wave-number remain unchanged at $(y_1, \alpha) = (2, 1)$, whilst the position (y_2, z_2) is varied.

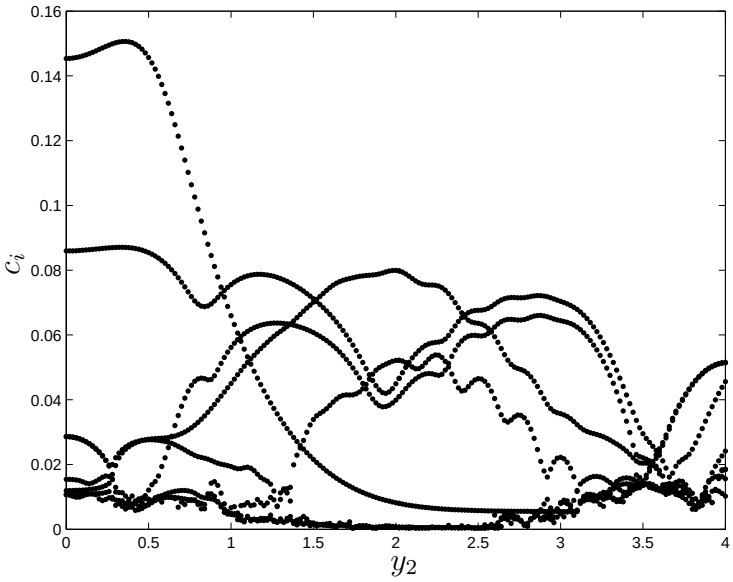

Figure 4.22: Inviscid instability of the first eight modes recovered in order of highest imaginary component for varying secondary vortex placement up to and past $y_2 = 2$ in four-vortex configuration.

4.10.1 The case $\gamma_2 = 0.5$, $a_2 = 0.5$

With this choice of parameters the axial strength of the secondary vortices remains unchanged whilst the decay rate is reduced to half of that used previously. From figure 4.23 it is apparent that the reduction in the relative size of the secondary vortices results in them having a diminished effect on the overall system instability for the most unstable mode. The region of greatest instability has moved to include a

region consisting of approximately $0 < y_2 < 0.35$ although the maximum instability is now found at $(y_2, z_2) = (0, 0)$ corresponding to an eigenvalue of $c = 0.53317 + 0.12288\text{i}$. This is equivalent to an equi-spaced three-vortex problem in which each vortex is of equal strength, the centre vortex being smaller in dimension. The second most unstable mode shown in figure 4.24 however, has a much less defined region of instability with almost any z-position at $y_2 \approx 0$ producing the greatest instability. There is also a small region of instability seen at $(y_2, z_2) \approx (1.25, 0)$ which, using the previous analysis as a benchmark, represents a change in the dominant mode at this location.

4.10.2 The case $\gamma_2 = 1.0$, $a_2 = 0.5$

The strength of the secondary vortices γ_2 is increased to match that of the primary ones whilst the decay rate is again reduced to half on the previous value. Figures 4.25 and 4.26 present contour plots of the instabilities for the first and second most unstable modes respectively. What is interesting about the region of instability in figure 4.25 is that the location and magnitude of the greatest instability resembles that of the two-vortex system with the vortices positioned such that at $(y_2, z_2) = (0.75, 0)$ with $c = 0.83270 + 0.16276\text{i}$. It is also interesting to note here the significant change in the real component of the eigenvalue. This would indicate that the inboard vortices significantly contribute to the overall instability of the system and that by increasing the strength of these vortices the instability of the system depends more on the secondary vortices than the primary ones alone. Figure 4.26 also suggests that the greatest instability of the second mode arises when the inboard vortices are moved closer together and away from the primaries.

4.10.3 The case $\gamma_2 = 1.0$, $a_2 = 1.0$

Continuing on from section 4.10.2 where we explored the influence of the secondary vortices by increasing γ_2 and decreasing a_2, we now observe the effects of increasing both parameters to the same level as the primary vortices. From the previous results we would expect this to increase the systems dependence on the secondary vortices further. From figure 4.27 we see this is indeed the case for the most unstable mode. Whilst the configuration of the vortices which produces the most unstable mode

is similar, $(y_2, z_2) = (0.65, 0)$, the magnitude of the instability is noticeably larger, $c = 0.61239 + 0.20593\text{i}$ with the region of greatest instability being more focussed about the secondary vortex position that produces the greatest instability. The second most unstable mode (figure 4.28) appears to display several regions where the instability is quite large and this would seem to suggest that whilst the primary mode is quite specific in its region of instability, the secondary exhibits a less well defined region of maximum instability for a range of (y_2, z_2).

It can be seen from the three variations in the parameters governing the secondary vortex that they have a significant effect on not just the magnitude but also the location of the greatest system instability and it goes some way to describing the importance of the secondary vortices in determining the overall stability of the four-vortex system.

4.11 Concluding Remarks

It is interesting to note the results of the four-vortex stability analysis when considered in the realm of a real-life application. Our results demonstrate that the most unstable configuration occurs when all four vortices are co-linear. If we are to look at modern commercial aircraft design, 'winglets' or curved up wing edges that are designed to restrict the amount of high-pressure air rolling up around the wing edge in order to maximise lift efficiency are becoming more prevalent. Either through experimental design or chance, they also have the effect of raising the level of the wing-tip vortex (when combined with the wing's natural flex due to lift) to approximately in line with those produced by the aircraft's lateral tail-plane thus producing the co-linear configuration that has been found here to be the most unstable. Obviously lateral spacing is important, but it would seem that for a typical Boeing 747 shown in figure 4.29, with respect to the dimensions used in this study puts the secondary vortices at $y_2 \approx 0.7$ which in terms of figure 4.19 for the most unstable mode still represents a region of relatively high instability at $c = 0.32766 + 0.11771\text{i}$ for $\alpha = 0.9$. One possible way of improving the correlation between aircraft dimensions and the theory presented here would be the addition of 'winglets' that not only extend up but also outwards, effectively increasing the primary vortices spacing.

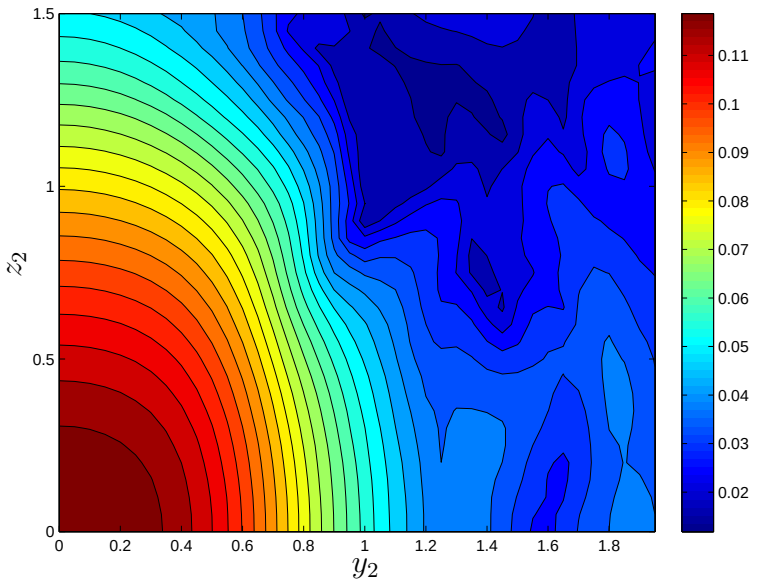

Figure 4.23: Contours of inviscid instability of the most dominant mode for varying secondary vortex placement with $\gamma_2 = 0.5$, $a_2 = 0.5$.

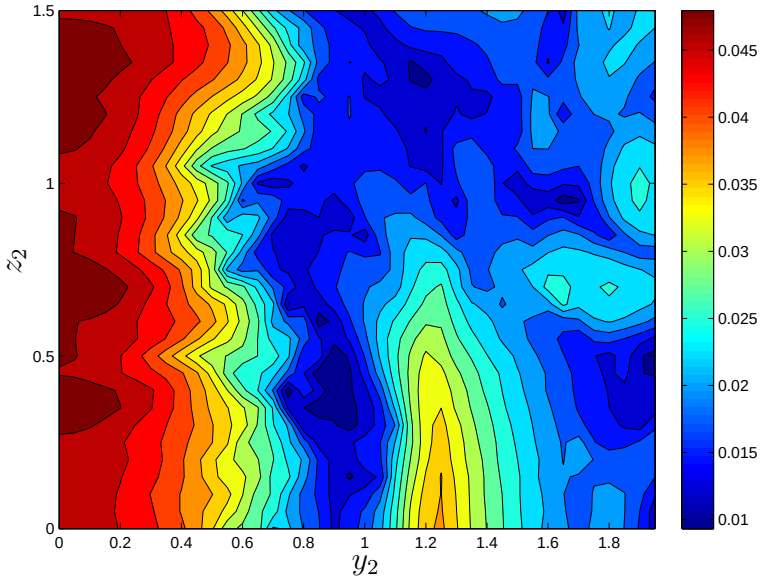

Figure 4.24: Contours of inviscid instability of the second most dominant mode for varying secondary vortex placement with $\gamma_2 = 0.5$, $a_2 = 0.5$.

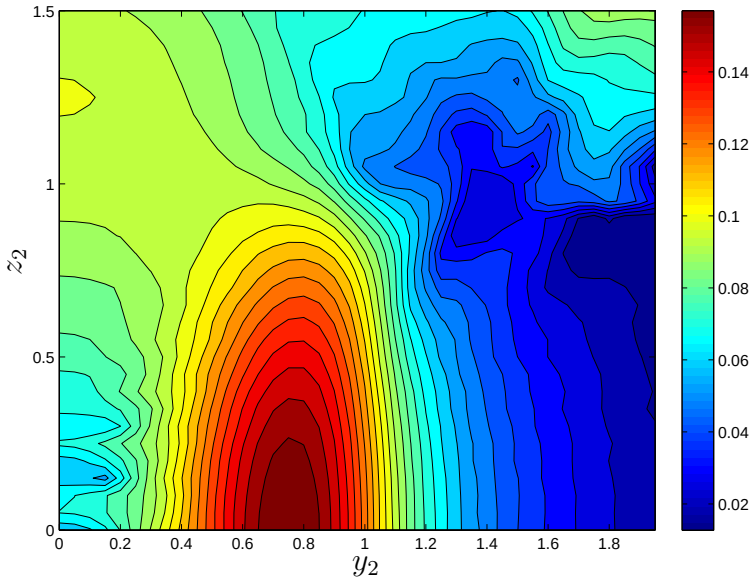

Figure 4.25: Contours of inviscid instability of the most dominant mode for varying secondary vortex placement with $\gamma_2 = 1.0$, $a_2 = 0.5$.

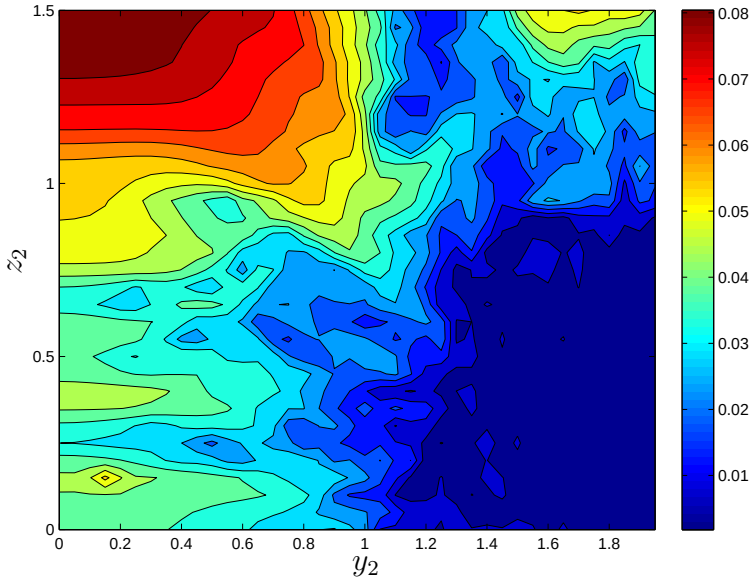

Figure 4.26: Contours of inviscid instability of the second most dominant mode for varying secondary vortex placement with $\gamma_2 = 1.0$, $a_2 = 0.5$.

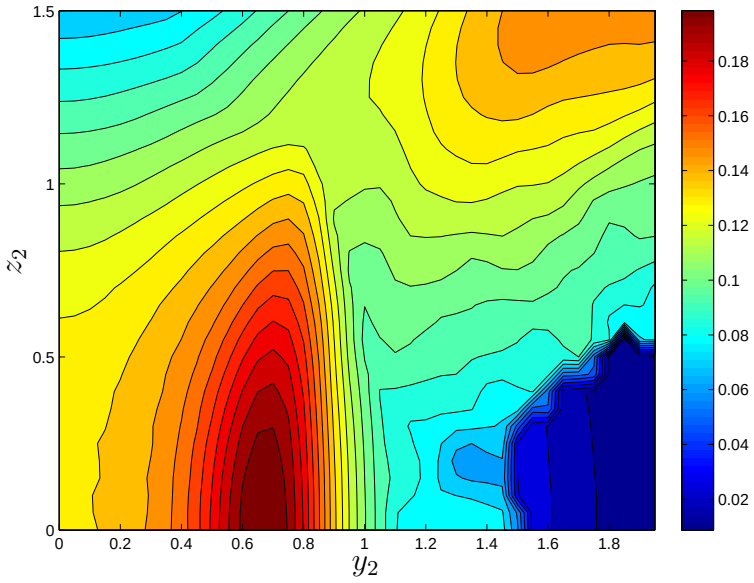

Figure 4.27: Contours of inviscid instability of the most dominant mode for varying secondary vortex placement with $\gamma_2 = 1.0$, $a_2 = 1.0$.

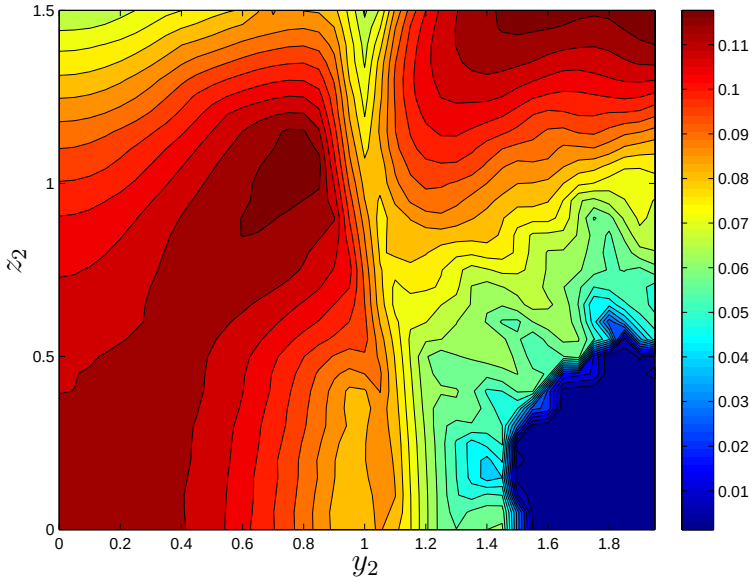

Figure 4.28: Contours of inviscid instability of the second most dominant mode for varying secondary vortex placement with $\gamma_2 = 1.0$, $a_2 = 1.0$.

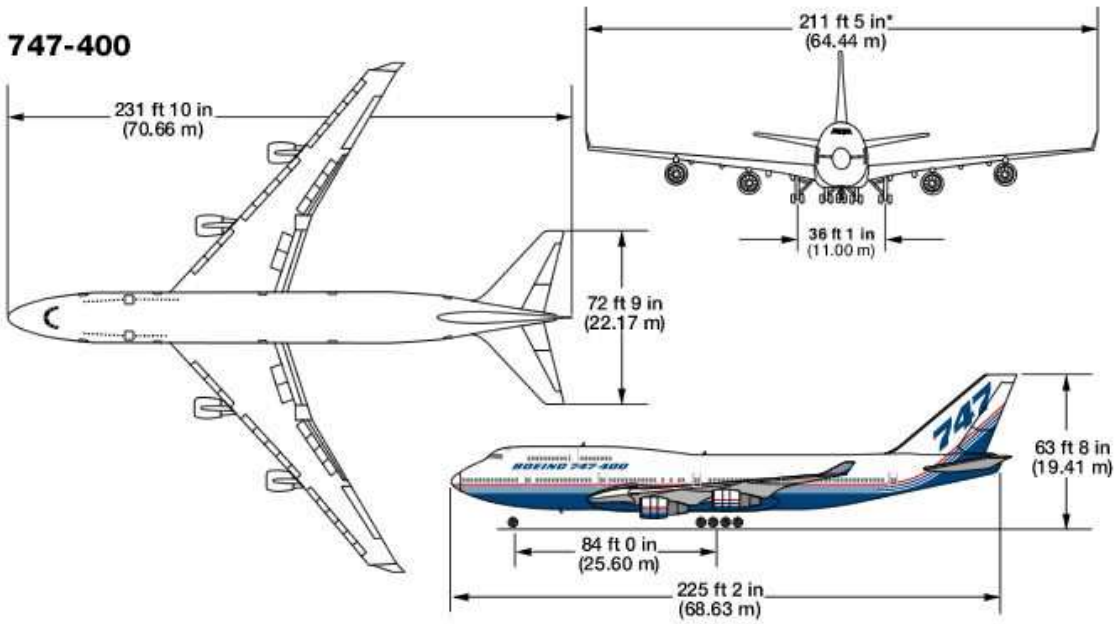

Figure 4.29: Relevant dimensions of a typical Boeing 747-400 (source: Boeing).

Chapter 5

Compressible Inviscid Flow

5.1 Introduction

We now aim to expand the inviscid analysis of the multiple vortex flows into the compressible regime. Our inviscid analysis makes the assumption that air is incompressible at any Reynolds number. Whilst this may hold true for low, subsonic speeds such as those encountered in landing and taking off situations, it is not necessarily the case in cruising when aircraft approach supersonic speeds. The aim of this chapter is to examine the effect of compressibility on the trailing vortex configurations whose stability characteristics have been found and documented for the inviscid case (see sections 4.6 – 4.8). In each case the Mach number is increased up to and beyond the supersonic and towards the hypersonic regime ($M > 5$) to establish at which point the inviscid modes cease to be unstable. Our analysis also aims to explore whether any stability characteristics arise which are purely dependent on the fluid compressibility.

5.2 Governing Equations

The governing equations for a compressible flow consist of those used for the analysis of an incompressible swirling flow plus the addition of two further equations, namely the energy equation and an equation of state, to describe the compressibility of the flow. In terms of (dimensional) cylindrical polar co-ordinates (r^*, θ, x^*), following

the notation of Stott and Duck [59], the governing equations are

$$\frac{\partial \rho^*}{\partial t^*} + \frac{\rho^* v^*}{r^*} + \frac{\partial(\rho^* v^*)}{\partial r^*} + \frac{1}{r^*}\frac{\partial(\rho^* w^*)}{\partial \theta} + \frac{\partial(\rho^* u^*)}{\partial x^*} = 0, \tag{5.2.1}$$

$$\begin{aligned}\rho^* \frac{Du^*}{Dt^*} = -\frac{\partial p^*}{\partial x^*} &+ \frac{\partial}{\partial r^*}\left(\mu^*\left[\frac{\partial v^*}{\partial x^*} + \frac{\partial w^*}{\partial r^*}\right]\right) + \frac{1}{r}\frac{\partial}{\partial \theta}\left(\mu^*\left[\frac{\partial u^*}{\partial x^*} + \frac{1}{r}\frac{\partial w^*}{\partial \theta}\right]\right) \\ &+ \frac{\partial}{\partial x^*}\left(2\mu^*\frac{\partial u^*}{\partial x^*} + \lambda^* \nabla.\mathbf{u}^*\right) + \frac{1}{r^*}\left(\mu^*\left[\frac{\partial v^*}{\partial x^*} + \frac{\partial w^*}{\partial r^*}\right]\right),\end{aligned} \tag{5.2.2}$$

$$\begin{aligned}\rho^*\left[\frac{Dv^*}{Dt^*} - \frac{w^{*2}}{r^*}\right] &= -\frac{\partial p^*}{\partial r^*} + \frac{\partial}{\partial r^*}\left(2\mu^*\frac{\partial v^*}{\partial r^*} + \lambda^*\nabla.\mathbf{u}^*\right) + \frac{1}{r^*}\frac{\partial}{\partial \theta}\left(\mu^*\left[\frac{1}{r^*}\frac{\partial v^*}{\partial \theta}\right.\right. \\ &+ \left.\left. r^*\frac{\partial}{\partial r^*}\left(\frac{u^*}{r^*}\right)\right]\right) + \frac{\partial}{\partial x^*}\left(\mu^*\left[\frac{\partial v^*}{\partial x^*} + \frac{\partial w^*}{\partial r^*}\right]\right) + \frac{1}{r^*}\left[\left(2\mu^*\frac{\partial v^*}{\partial r^*}\right.\right. \\ &+ \left.\left.\lambda^*\nabla.\mathbf{u}^*\right) - \left(2\mu^*\left[\frac{1}{r^*}\frac{\partial w^*}{\partial \theta} + \frac{v^*}{r^*}\right] + \lambda^*\nabla.\mathbf{u}^*\right)\right],\end{aligned} \tag{5.2.3}$$

$$\begin{aligned}\rho^*\left[\frac{Dw^*}{Dt^*} - \frac{v^* w^*}{r^*}\right] &= -\frac{1}{r^*}\frac{\partial p^*}{\partial \theta} + \frac{\partial}{\partial r^*}\left(\mu^*\left[\frac{1}{r^*}\frac{\partial v^*}{\partial \theta} + r^*\frac{\partial}{\partial r^*}\left(\frac{u^*}{r^*}\right)\right]\right) \\ &+ \frac{\partial}{\partial \theta}\left[2\mu^*\left(\frac{1}{r^*}\frac{\partial w^*}{\partial \theta} + \frac{v^*}{r^*}\right) + \lambda^*\nabla.\mathbf{u}^*\right] + \frac{\partial}{\partial x^*}\left(\mu^*\left[\frac{\partial u^*}{\partial x^*}\right.\right. \\ &+ \left.\left.\frac{1}{r^*}\frac{\partial w^*}{\partial \theta}\right]\right) + \frac{2}{r^*}\left(\mu^*\left[\frac{1}{r^*}\frac{\partial v^*}{\partial \theta} + r^*\frac{\partial}{\partial r^*}\left(\frac{u^*}{r^*}\right)\right]\right),\end{aligned} \tag{5.2.4}$$

$$\begin{aligned}\rho^*\frac{Dh^*}{Dt^*} - \frac{Dp^*}{Dt^*} = \Phi^* &+ \frac{\partial}{\partial x^*}\left(\kappa^*\frac{\partial T^*}{\partial x^*}\right) + \frac{1}{r^*}\frac{\partial}{\partial r^*}\left(\kappa^* r^*\frac{\partial T^*}{\partial r^*}\right) \\ &+ \frac{1}{r^{*2}}\frac{\partial}{\partial \theta}\left(\kappa^*\frac{\partial T^*}{\partial \theta}\right),\end{aligned} \tag{5.2.5}$$

$$p^*\gamma M^{*2} = \rho^* T^*, \tag{5.2.6}$$

where the Eulerian operator is defined by

$$\frac{D}{Dt^*} = \frac{\partial}{\partial t^*} + u^*\frac{\partial}{\partial x^*} + v^*\frac{\partial}{\partial r^*} + \frac{w^*}{r^*}\frac{\partial}{\partial \theta}, \tag{5.2.7}$$

and the viscous dissipation parameter is given by

$$\begin{aligned}\Phi^* &= 2\mu^*\left[\left(\frac{\partial u^*}{\partial x^*}\right)^2 + \left(\frac{\partial v^*}{\partial r^*}\right)^2 + \left(\frac{1}{r^*}\frac{\partial w^*}{\partial \theta} + \frac{v^*}{r^*}\right)^2 + \frac{1}{4}\left(\frac{\partial u^*}{\partial r^*} + \frac{\partial v^*}{\partial x^*}\right)^2\right. \\ &+ \left.\frac{1}{4}\left(\frac{\partial w^*}{\partial x^*} + \frac{1}{r^*}\frac{\partial u^*}{\partial \theta}\right)^2 + \frac{1}{4}\left(\frac{1}{r^*}\frac{\partial v^*}{\partial \theta} + r^*\frac{\partial}{\partial x^*}\left(\frac{w^*}{r^*}\right)\right)^2\right] \\ &+ (\lambda^* - \frac{2}{3}\mu^*)(\nabla.\mathbf{u}^*)^2.\end{aligned} \tag{5.2.8}$$

The coefficients λ^* and μ^* are the first coefficients of viscosity and dynamic viscosity respectively where λ^* can be defined by $\lambda^* = \mu_2^* + \frac{2}{3}\mu^*$ where μ_2^* is the second coefficient of viscosity. It is also useful to define the following quantities;

$$\text{Reynolds Number, } Re = \frac{\rho_\infty^* U_s^* l}{\mu_\infty^*}. \tag{5.2.9}$$

$$\text{Mach Number, } M = \frac{U_s^*}{(\gamma R^* T_\infty^*)^{1/2}}. \tag{5.2.10}$$

$$\text{Prandtl Number, } \sigma = \frac{\mu^* c_p}{\kappa^*}. \tag{5.2.11}$$

It can also be stated that, for an ideal gas, the enthalpy h is a function of temperature only and as such the specific heat (at constant pressure), c_p can be written as

$$c_p = \frac{\mathrm{d}h}{\mathrm{d}T},$$

$$\Delta h = c_p \Delta T.$$

If we assume that the temperature is constant, then the enthalpy is also constant resulting in

$$h = c_p T. \tag{5.2.12}$$

In equations (5.2.1) – (5.2.11), $\mathbf{u}^* = (u^*, v^*, w^*)$ are the (dimensional) velocity components in the axial, radial and azimuthal directions x^*, r^*, θ respectively. ρ^*, T^* and p^* are the dimensional density, temperature and pressure fields of the flow, γ is the ratio of the specific heats, R is the gas constant for an ideal gas, κ^* is the coefficient of heat conduction and as usual, μ^* is the dynamic viscosity of the fluid. A subscript ∞ represents the value of the parameter in the free stream, that is, a long distance down-stream or away from the vortex centre. It will also be of value in what follows to define the following relationships;

$$R = \frac{1}{\gamma M^2}, \tag{5.2.13}$$

$$c_p = \frac{1}{(\gamma - 1)M^2}. \tag{5.2.14}$$

5.3 Basic Flow

The basic flow for a trailing-line vortex used in this analysis is that which was first described by Batchelor [3] and his similarity solution for an incompressible flow derived in detail in section 4.3.1. Here we aim to show that the same similarity solution is still valid in a compressible regime. Our derivation follows that of Stott and Duck [59]. For the far-field solution, we seek steady, axisymmetric flows such that

$$\frac{\partial}{\partial t^*} \equiv 0, \qquad \frac{\partial}{\partial \theta} \equiv 0. \tag{5.3.1}$$

This analysis also requires the flow field to have axial gradients which are much smaller in magnitude than those in the radial direction thus allowing us to utilise a boundary-layer type approximation

$$\frac{\partial}{\partial x^*} \ll \frac{\partial}{\partial r^*}, \qquad v^* \ll u^*. \tag{5.3.2}$$

Therefore, when (5.3.1) and (5.3.2) are substituted into equations (5.2.1) – (5.2.6) along with the relationships (5.2.12) and (5.2.13) we are left with

$$\frac{\partial}{\partial x^*}(\rho^* u^*) + \frac{\partial}{\partial r^*}(\rho^* v^*) + \frac{\rho^* v^*}{r^*} = 0, \tag{5.3.3}$$

$$\rho^* u^* \frac{\partial u^*}{\partial x^*} + \rho^* v^* \frac{\partial u^*}{\partial r^*} = \frac{1}{r^*}\frac{\partial}{\partial r^*}\left(r^* \mu^* \frac{\partial u^*}{\partial r^*}\right) - \frac{\partial p^*}{\partial x^*}, \tag{5.3.4}$$

$$\frac{\rho^* w^{*2}}{r^*} = \frac{\partial p^*}{\partial r^*}, \tag{5.3.5}$$

$$\begin{aligned} \rho^* u^* \frac{\partial w^*}{\partial x^*} + \rho^* v^* \frac{\partial w^*}{\partial r^*} + \rho^* \frac{v^* w^*}{r^*} &= \frac{\partial}{\partial r^*}\left(\mu^* r^* \frac{\partial}{\partial r^*}\left(\frac{w^*}{r^*}\right)\right) \\ &+ 2\mu^* \frac{\partial}{\partial r^*}\left(\frac{w^*}{r^*}\right), \end{aligned} \tag{5.3.6}$$

$$\begin{aligned} \rho^* c_p \left(u^* \frac{\partial T^*}{\partial x^*} + v^* \frac{\partial T^*}{\partial r^*}\right) &= \mu^* \left(\frac{w^{*2}}{r^{*2}} - \frac{2w^*}{r^*} u^* \frac{\partial w^*}{\partial r^*} + \left(u^* \frac{\partial w^*}{\partial r^*}\right)^2 \right. \\ &\left. + \left(u^* \frac{\partial u^*}{\partial r^*}\right)^2\right) + \frac{1}{r}\frac{\partial}{\partial r^*}\left(\kappa^* r^* \frac{\partial T^*}{\partial r^*}\right) + u^* \frac{\partial p^*}{\partial x^*} + v^* \frac{\partial p^*}{\partial r^*}, \end{aligned} \tag{5.3.7}$$

$$p^* = \rho^* R T^*. \tag{5.3.8}$$

For the far-field analysis we observe that far downstream of the tailing edge the values of the axial velocity and temperature are approximately the same as those of the free stream, U_∞ and T_∞ respectively and so, following Batchelor [3] and Stott and Duck [59] we note the approximations

$$|u^* - U_\infty| \ll U_\infty, \qquad |T^* - T_\infty| \ll T_\infty. \tag{5.3.9}$$

Now, again following Stott and Duck [59], T^*, ρ^* and p^* are developed asymptotically as

$$T^* = T_\infty(1 + T_1 + \cdots), \tag{5.3.10}$$

$$\rho^* = \rho_\infty(1 + \rho_1 + \cdots), \tag{5.3.11}$$

$$p^* = p_\infty(1 + p_1 + \cdots), \tag{5.3.12}$$

where $|T_1|, |\rho_1|, |p_1| \ll 1$ and it can be assumed that viscosity is a function of temperature only, which implies that, to leading order, μ^*, ρ^* and T^* are constants. Therefore, by applying the afore-mentioned approximations to equations (5.3.1) – (5.3.6) we are left with, at leading order,

$$U_\infty \frac{\partial u^*}{\partial x^*} = -\frac{1}{\rho_\infty}\frac{\partial p^*}{\partial x^*} + \nu_\infty \left(\frac{\partial^2 u^*}{\partial r^{*2}} + \frac{1}{r^*}\frac{\partial u^*}{\partial r^*} \right), \tag{5.3.13}$$

$$\frac{p_\infty - p^*}{p_\infty} = \int_{r^*}^{\infty} \frac{C^{*2}}{r^{*3}} dr^*, \tag{5.3.14}$$

$$U_\infty \frac{\partial w^*}{\partial x^*} = \nu_\infty \left(\frac{\partial^2 w^*}{\partial r^{*2}} + \frac{1}{r^*}\frac{\partial w^*}{\partial r^*} - \frac{w^*}{r^{*2}} \right), \tag{5.3.15}$$

$$\begin{aligned} \rho_\infty c_p U_\infty T_\infty \frac{\partial T_1}{\partial x^*} &= \mu_\infty \left(\frac{w^{*2}}{r^*} - \frac{2w^{*2}}{r^*}\frac{\partial w^*}{\partial r^*} + \frac{\partial w^*}{\partial r^*} \right) \\ &+ \frac{T_\infty}{r^*}\frac{\partial}{\partial r^*}\left(\kappa^* r^* \frac{\partial T_1}{\partial r^*} \right) + \rho_\infty U_\infty^3 \frac{\partial p_1}{\partial x^*}. \end{aligned} \tag{5.3.16}$$

Equations (5.3.13) – (5.3.15) are identical to equations (4.3.9) – (4.3.11), with equation (5.3.16) representing the contribution of the compressibility of the flow. We therefore note, as Stott and Duck [59] have done before us, that to leading order the velocity profile of Batchelor [3] does not change with compressibility. Also, it can

be shown that, as in Stott and Duck [59], the equations for p_1 and T_1 can be solved to give

$$p_1 = \frac{C_\infty^2}{8x^*\rho_\infty U_\infty \nu_\infty}\left[\frac{(1-\mathrm{e}^{-\eta})^2}{\eta} + 2\mathrm{ei}(\eta) - 2\mathrm{ei}(2\eta)\right], \tag{5.3.17}$$

$$\begin{aligned} T_1 &= \frac{\mathrm{e}^{-\frac{-\sigma\xi^2}{4}}}{x^*}\left(\frac{A}{2}\mathrm{ei}(\frac{1}{4}\sigma\xi^2) + B + \frac{(\gamma-1)M_\infty^2 C_\infty^2}{8U_\infty\nu_\infty}\left[\mathrm{ei}\left((\frac{1}{4}\sigma - \frac{1}{4})\xi^2\right)\right.\right. \\ &+ \int\left(-8\sigma\frac{\mathrm{e}^{\frac{\sigma\xi^2}{4}}}{\xi^2} + 16\sigma\frac{\mathrm{e}^{\frac{1}{4}(\sigma-1)\xi^2}}{\xi^2} + \frac{8\sigma\pi^{\frac{1}{2}}}{\xi}\mathrm{e}^{\frac{\sigma\xi^2}{4}}\mathrm{erf}(\frac{\xi}{2}) - 8\frac{\mathrm{e}^{(\frac{\sigma}{4}-\frac{1}{2})\xi^2}}{\xi^2}\right. \\ &- \left.\left.4\frac{\sigma 2\pi^{\frac{1}{2}}}{x^*}\mathrm{e}^{\frac{\sigma\xi^2}{4}}\mathrm{erf}(\frac{\xi}{2^{\frac{1}{2}}})\right)d\xi + \int \mathrm{e}^{\frac{\sigma\xi^2}{4}}\int\frac{1}{\xi_1}\left(-2\sigma\left(-2\mathrm{e}^{\frac{\xi_1^2}{4}} + 2\right.\right.\right. \\ &- \left.\left.\left.\xi_1^2\mathrm{e}\frac{\sigma\xi_1^2}{4}\mathrm{ei}(\frac{\xi_1^2}{4}) + \xi_1^2\mathrm{e}\frac{\sigma\xi_1^2}{4}\mathrm{ei}(\frac{\xi_1^2}{2})\right) + \frac{\mathrm{e}-\frac{\sigma\xi_1^2}{4}}{\xi_1}\right)d\xi_1 d\xi\left.\right]\right), \end{aligned} \tag{5.3.18}$$

where A and B are constants, $\mathrm{erf}(z)$ is the error function and $\mathrm{ei}(z)$ is the exponential integral. Following the notation of Stott and Duck [59] $\xi = 2\eta^{\frac{1}{2}}$ and the subscript ξ_1 allows us to differentiate between two integrals involving ξ.

For the purposes of this stability analysis we can neglect the quantities p_1, T_1, ρ_1 as they are found to be approximately $\mathcal{O}(1/(logx^*)^2)$ smaller than the non-dimensionalised leading order terms and so the appropriate basic flow for this compressible inviscid analysis is identical to that of the incompressible case,

$$(U, V, W) = \left(\frac{U_\infty}{U_s} - \mathrm{e}^{-r^2}, 0, \frac{q}{r}(1-\mathrm{e}^{-r^2})\right). \tag{5.3.19}$$

5.4 Stability Equations

The set of governing equations are as follows, taking the inviscid form of equations (5.2.1) – (5.2.6)

$$\frac{\partial\rho^*}{\partial t^*} + \frac{\rho^* v^*}{r^*} + \frac{\partial(\rho^* v^*)}{\partial r^*} + \frac{1}{r^*}\frac{\partial(\rho^* w^*)}{\partial\theta} + \frac{\partial(\rho^* u^*)}{\partial x^*} = 0, \tag{5.4.1}$$

$$\frac{\partial u^*}{\partial t^*} + u^*\frac{\partial u}{\partial x^*} + v^*\frac{\partial u^*}{\partial r^*} + \frac{w^*}{r^*}\frac{\partial u^*}{\partial\theta} = -\frac{1}{\rho^*}\frac{\partial p^*}{\partial x^*}, \tag{5.4.2}$$

$$\frac{\partial v^*}{\partial t^*} + u^*\frac{\partial v^*}{\partial x^*} + v^*\frac{\partial v^*}{\partial r^*} + \frac{w^*}{r^*}\frac{\partial v^*}{\partial\theta} - \frac{w_\theta^{*2}}{r^*} = -\frac{1}{\rho^*}\frac{\partial p^*}{\partial r^*}, \tag{5.4.3}$$

$$\frac{\partial w^*}{\partial t^*} + u^*\frac{\partial w^*}{\partial x^*} + v^*\frac{\partial w^*}{\partial r^*} + \frac{w^*}{r^*}\frac{\partial w^*}{\partial \theta} - \frac{v^* w^*}{r^*} = -\frac{1}{\rho^* r^*}\frac{\partial p^*}{\partial \theta}, \tag{5.4.4}$$

$$\rho^*\left[\frac{\partial h^*}{\partial t^*} + u^*\frac{\partial h^*}{\partial x^*} + v^*\frac{\partial h^*}{\partial r^*} + \frac{w^*}{r^*}\frac{\partial h^*}{\partial \theta}\right] = \frac{\partial p^*}{\partial t^*} + u^*\frac{\partial p^*}{\partial x^*} + v^*\frac{\partial p^*}{\partial r^*} + \frac{w^*}{r^*}\frac{\partial p^*}{\partial \theta}, \tag{5.4.5}$$

$$p^*\gamma M^{*2} = \rho^* T^*. \tag{5.4.6}$$

Equations (5.2.1) – (5.2.6) can be non-dimensionalised in the same way as in section (2.3) and in a similar fashion we subject the basic state to small perturbations of the form,

$$\begin{aligned}(u, v, w, p, T, \rho) &= \{U(r,\theta), V(r,\theta), W(r,\theta), p_o(r,\theta), T_o(r,\theta), \rho_o(r,\theta)\} \\ &+ \epsilon\{U_p(r,\theta), V_p(r,\theta), W_p(r,\theta), P_p(r,\theta), \tau(r,\theta), \Gamma(r,\theta)\}\mathrm{e}^{\mathrm{i}\alpha(x-ct)},\end{aligned} \tag{5.4.7}$$

where the general basic state (which was described in detail in section 5.3) is given by

$$(U, V, W) = (U(r,\theta), 0, W(r,\theta)). \tag{5.4.8}$$

Substituting (5.4.7) into (5.4.1) – (5.4.6) and retaining terms linear in ϵ yields the disturbance equations

$$\begin{aligned}-\mathrm{i}\alpha c\Gamma &+ \frac{\rho_o V_p}{r} + V_p\rho_o' + \rho_o V_p' + \frac{1}{r}[W\Gamma_\theta + \Gamma W_\theta \\ &+ W_p\rho_{o,\theta} + \rho_o W_{p,\theta}] + U\mathrm{i}\alpha\Gamma + \rho_o\mathrm{i}\alpha U_p = 0,\end{aligned} \tag{5.4.9}$$

$$\begin{aligned}\rho_o[-\mathrm{i}\alpha c U_p &+ U\mathrm{i}\alpha U_p + V_p U' + \frac{W}{r}U_{p,\theta} + \frac{W_p}{r}U_\theta] \\ &+ \frac{\Gamma W}{r}U_\theta = -\mathrm{i}\alpha P_p,\end{aligned} \tag{5.4.10}$$

$$\rho_o[-\mathrm{i}\alpha c V_p + U\mathrm{i}\alpha V_p + \frac{W}{r}V_{p,\theta} - \frac{2WW_p}{r}] - \frac{\Gamma W^2}{r} = -P_p', \tag{5.4.11}$$

$$\begin{aligned}\rho_o[-\mathrm{i}\alpha c W_p &+ U\mathrm{i}\alpha W_p + V_p W' + \frac{W}{r}W_{p,\theta} + \frac{W_p}{r}W_\theta + \frac{V_p W}{r}] \\ &+ \frac{\Gamma W}{r} = -\frac{1}{r}P_{p,\theta},\end{aligned} \tag{5.4.12}$$

$$\begin{aligned}\rho_o c_p[-\mathrm{i}\alpha c\tau &+ U\mathrm{i}\alpha\tau + V_p T_o' + \frac{W}{r}\tau_\theta + \frac{W_p}{r}T_o'] + \frac{\Gamma c_p W}{r}T_{o,\theta} \\ &= -\mathrm{i}\alpha c P_p + U\mathrm{i}\alpha P_p + V_p p_o' + \frac{W}{r}P_{p,\theta} + \frac{W_p}{r}p_{o,\theta},\end{aligned} \tag{5.4.13}$$

$$P_p\gamma M^2 = \rho_o\tau + \Gamma T_o, \tag{5.4.14}$$

where a superscript of a prime indicates a derivative by r and a subscript of θ indicates a derivative by θ.

Following the work of Stott and Duck [59], we have been able to show that a basic flow consisting of a typical Batchelor vortex is, unchanged to leading order, by the effects of compressibility. This allows us to state that Batchelor's [3] similarity solution for an incompressible inviscid flow is also valid for our compressible inviscid flow. Following this, we can also state that, without loss of generality, the leading order asymptotic analysis of this similarity solution obtained in section 4.3 with regards to Batchelor's [3] equations is valid for this compressible extension of the inviscid work. From section 5.3 we can take our basic state to be

$$U = \mathrm{e}^{-r^2}, \qquad V = 0, \qquad W = 0,$$

$$\rho_o = 1, \qquad p_o = \frac{1}{\gamma M^2}, \qquad T_o = 1.$$

Therefore, equations (5.4.9) – (5.4.14) become

$$\mathrm{i}\alpha(U-c)\Gamma + \mathrm{i}\alpha U_p + \frac{V_p}{r} + \frac{\partial V_p}{\partial r} + \frac{1}{r}\frac{\partial W_p}{\partial \theta} = 0, \tag{5.4.15}$$

$$\mathrm{i}\alpha(U-c)U_p + V_p\frac{\partial U}{\partial r} + \frac{W_p}{r}\frac{\partial U}{\partial \theta} = -\mathrm{i}\alpha P_p, \tag{5.4.16}$$

$$\mathrm{i}\alpha(U-c)V_p = -\frac{\partial P_p}{\partial r}, \tag{5.4.17}$$

$$\mathrm{i}\alpha(U-c)W_p = -\frac{1}{r}\frac{\partial P_p}{\partial \theta}, \tag{5.4.18}$$

$$\tau - (\gamma-1)M^2P_p = 0, \tag{5.4.19}$$

$$P_p\gamma M^2 = \tau + \Gamma. \tag{5.4.20}$$

Equations (5.4.15) – (5.4.20) can be combined to form a single equation in terms of the perturbation pressure, P_p,

$$(U-c)\left[\frac{\partial^2}{\partial r^2} + \frac{1}{r}\frac{\partial}{\partial r} + \frac{1}{r^2}\frac{\partial^2}{\partial \theta^2} - \alpha^2\right]P_p \;-\; 2\left[\frac{\partial U}{\partial r}\frac{\partial}{\partial r} + \frac{1}{r^2}\frac{\partial U}{\partial \theta}\frac{\partial}{\partial \theta}\right]P_p$$

$$+\; \alpha^2(U-c)^3M^2P_p = 0. \tag{5.4.21}$$

It can be seen that equation (5.4.21) is our standard two-dimensional inviscid Rayleigh equation (4.2.1) with an additional component that takes into account the compressible nature of the flow.

5.5 Numerical Methods

It is possible to solve the non-linear eigenvalue problem (5.4.21) in a global sense, in a similar fashion to that of the original incompressible inviscid problem with a Chebyshev pseudo-spectral collocation scheme, by employing a transformation (due to the $(U-c)^3$ component) to a linear problem by way of a quadratic conversion parameter or companion matrix [5, 32]. Stott and Duck [59] reported a large amount of spurious eigenvalues using this method. For this reason, and also to preserve resolution with the available computational facilities, equation (5.4.21) is best solved using the iterative finite-difference method outlined in section 3.3. For reference, the Cartesian computational domain is included here again in figure 5.1 with a typical four-vortex configuration indicated by the positions y_1, y_2, z_1, z_2.

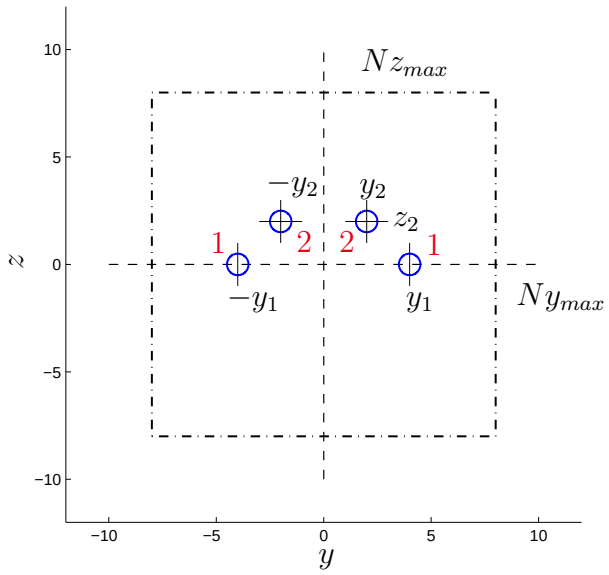

Figure 5.1: The four-vortex configuration whose stability we investigate. Here y and z are Cartesian coordinates in the cross-section; the axial co-ordinate, x, is directed out of the plane of the page.

As the inviscid results of sections 4.6 – 4.8 are obtained using the global pseudo-spectral code, whereas the compressible results extended from these are to be found via the local finite-difference code, the following figures aim to illustrate the compatibility of the two numerical methods. The (global) pseudo-spectral code in cylindrical polar co-ordinates uses $(N_r, N_\theta) = (80, 32)$ with a clustering parameter of $s = 0.9$ for the single vortex and $s = 0.8$ for both the two and four-vortex cases. The (local) finite-difference code uses up to $(N_y, N_z) = (81, 81)$ with a clustering parameter of $(s_y, s_z) = (8, 8)$ for the single vortex and $(s_y, s_z) = (6, 8)$ for the two and four-vortex cases noting that the clustering algorithm used in each case is different.

Figures 5.2, 5.3 and 5.4 are the curves of greatest instability found in sections 4.6, 4.7 and 4.8 respectively with the results obtained using the finite-difference code superimposed as a dashed curve (and also marked accordingly). It can be seen that for the single vortex case agreement is good with only a small deviation of the FD curve after $\alpha > 0.9$ and around $\alpha = 0$, for the two-vortex case ($y = \pm 0.8$), the comparison is excellent except for the deviation after $\alpha \approx 1.45$ and $\alpha < 0.2$. The four-vortex configuration ($(y_1, z_1) = (\pm 2.0, 0), (y_2, z_2) = (\pm 0.35, 0)$) is much the same with a slight discrepancy for $\alpha < 0.2$ and $\alpha > 1.5$. We therefore restrict our analysis to the regions of $0.08 \leq \alpha \leq 0.88$ for the single vortex, $0.3 \leq \alpha \leq 1.4$ for the two-vortex configuration and $0.3 \leq \alpha \leq 1.4$ for four vortices thus ensuring that for the extent of the analysis we can state with confidence that both numerical schemes are consistent (to at least four significant figures). The deviation of the curves at large α can be attributed to the issues that arise due to the critical layer as explained in more detail in section 4.7 where the two numerical methods behave differently.

These results give us confidence that the solution (i.e. eigenvalues) for the compressible problem are accurately captured using the finite-difference approach.

5.6 Inviscid Stability for $M > 0$

The fact that equation (5.4.21) mimics our governing inviscid equation with only the addition of a single term representing the effect of compressibility means that the process of tracking the effects of an unstable mode through the compressible

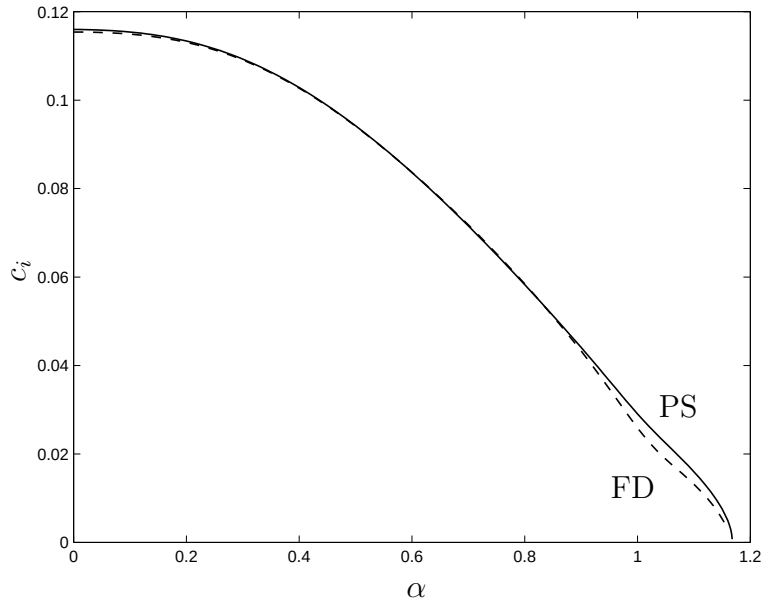

Figure 5.2: Comparison of pseudo-spectral (solid) and finite-difference (dashed) inviscid instability results for a single vortex with $M = 0$.

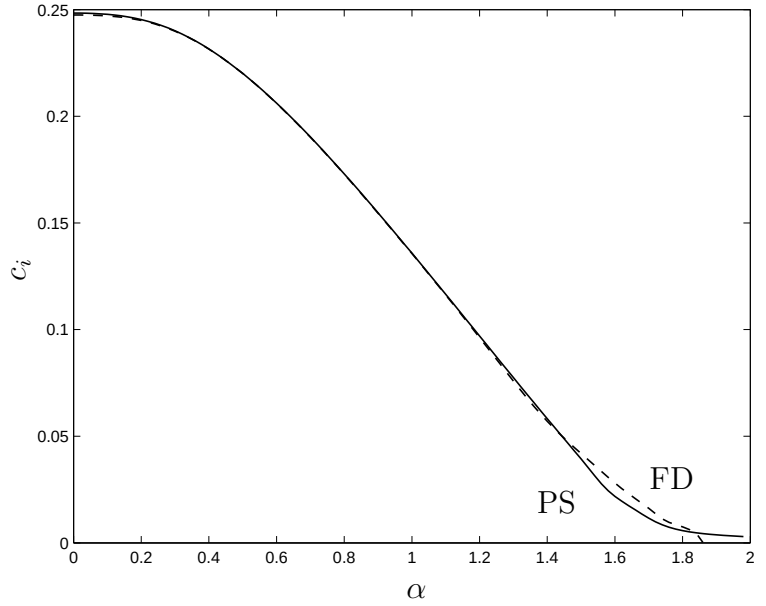

Figure 5.3: Comparison of pseudo-spectral (solid) and finite-difference (dashed) inviscid instability results for a two-vortex configuration with $M = 0$.

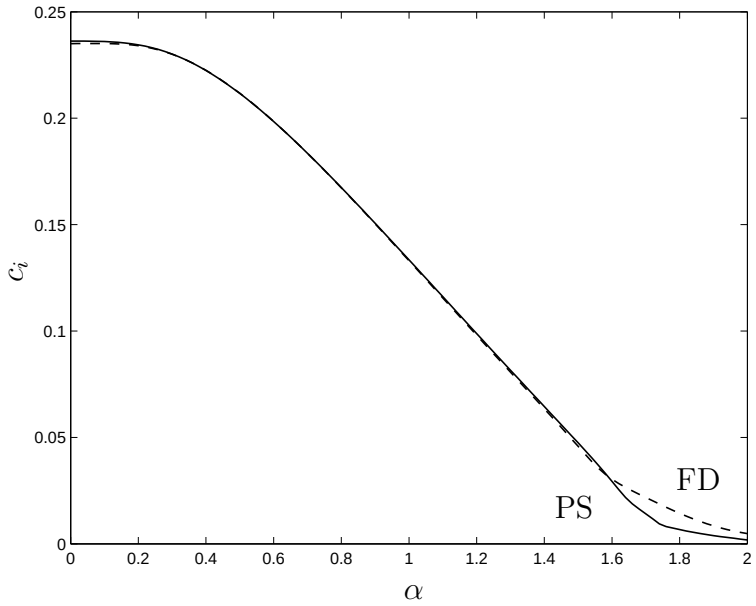

Figure 5.4: Comparison of pseudo-spectral (solid) and finite-difference (dashed) inviscid instability results for a four-vortex configuration with $M = 0$.

region is a relatively straight forward process. Minor modifications to the finite difference code, using the Mach number as the continuation parameter, allow us to track the mode as the Mach number is increased. Starting values are those listed for the vortex configurations outlined in sections 4.7 and 4.8, found using a global numerical scheme with a second starting value for the iteration scheme being a small deviation from this in both the real and imaginary components. Initially the number of grid points is used as a continuation parameter to increase the accuracy of the starting values and then the Mach number is varied.

5.6.1 A Single Vortex Flow

The effects of compressibility on a single Batchelor vortex have been studied in detail by Stott and Duck [59] for a variety of azimuthal wave-numbers and (non-zero) swirl rates. As this particular inviscid analysis is concerned with vortices that effectively have $q = 0$ for the entire spectra of n-values it is interesting to follow the unstable single vortex modes found in section 4.6 through the compressible regime. From section 4.6 we can see that for the wave-number corresponding to the maximum

growth rate of the most unstable mode, $\alpha = 0.65$, the 'starting' growth rate is 0.050554 which corresponds to an eigenvalue of $c = 0.495649 + 0.077775\text{i}$ which is found as $c = 0.49531 + 0.07791\text{i}$ by the finite difference iterative code and stepped through the compressible regime in figure 5.5.

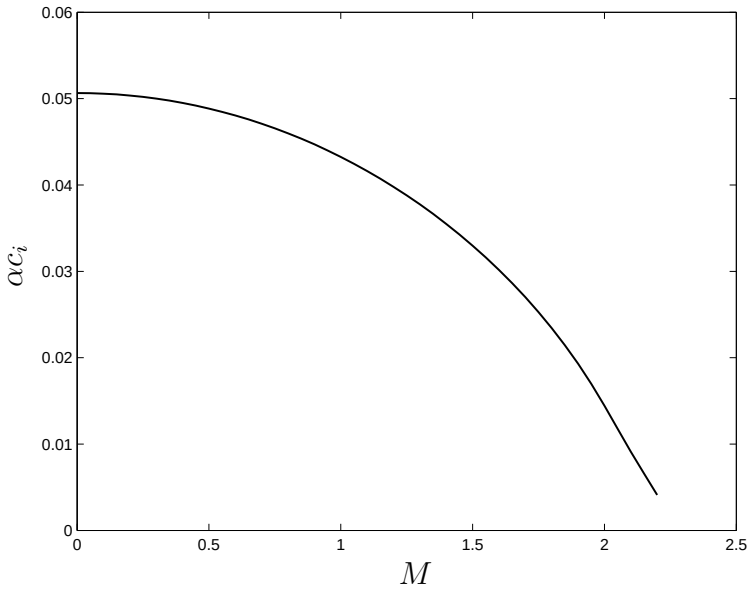

Figure 5.5: Growth rate (αc_i) versus Mach number (M) for a single vortex at $\alpha = 0.65$.

It is apparent from figure 5.5 that increasing the Mach number has a stabilising effect on the unstable mode presented here. Although the numerical scheme encountered difficulties resolving the equation close to $c_i = 0$ it is apparent that the transition to a neutrally stable state occurs at $M \approx 2.3$. The effect on the real component of the eigenvalues is shown in figure 5.6. In order to ensure that we are observing the transition of the same (ie first or most unstable) incompressible mode, figure 5.7 plots the normalised modal amplitudes at $M = 0$ and $M = 2.0$ from which it can be seen, despite some small 'stretching' of the mode (perhaps as a result of boundary interactions at higher Mach numbers; the choice of N_{max} is governed by the trade-off between resolution and the requirement of a larger boundary for high Mach numbers), they are in fact the same mode.

Figure 5.8 extends the compressibility analysis for a single vortex to all unstable values of α (in the range mentioned earlier) from which it can be seen that increasing

M has a stabilising effect. For low wave-numbers, the most unstable mode at $M = 0$, whilst reducing in instability, remains unstable up to very high values of M. The figure also shows a smooth transition from unstable towards stable throughout the entire $\alpha - M$ region with the approximate neutral curve superimposed as a dashed line.

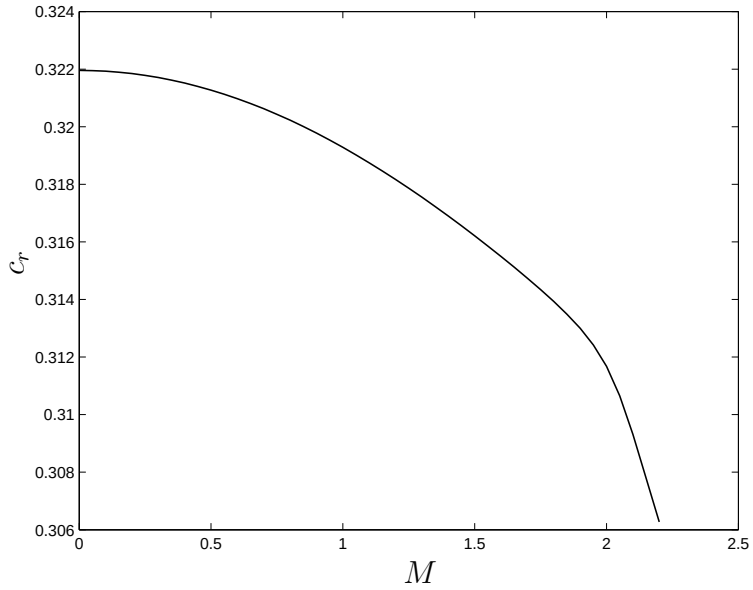

Figure 5.6: The real component of the eigenvalue (c_r) versus Mach number (M) for a single vortex at $\alpha = 0.65$.

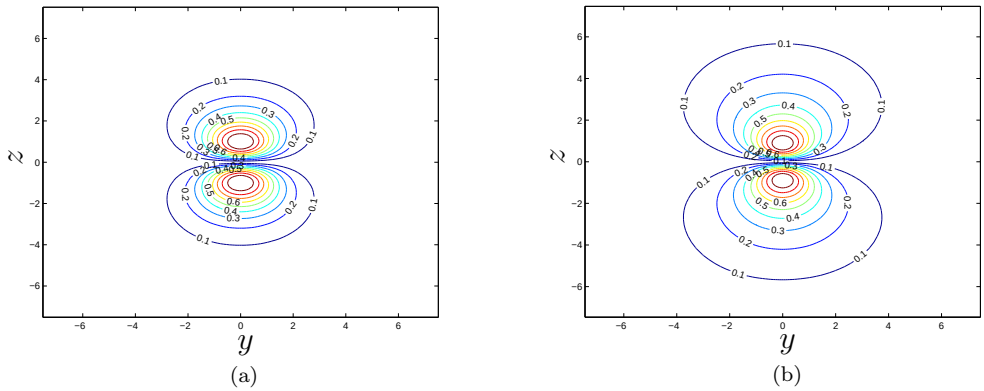

Figure 5.7: Normalised amplitude of eigenmodes for the single vortex growth rates given in figure 5.5 at (a) $M = 0$, (b) $M = 2.0$.

It is difficult to accurately compare (or reproduce) the results of Stott and Duck

[59] due to their use of a one-dimensional code with the azimuthal wave-number as a parameter and a non-zero q. However, a visual comparison of the shape of the curve and magnitude of the growth rates and Mach numbers shows that the curves for a single Batchelor vortex produced herein agree qualitatively with Stott and Duck [59].

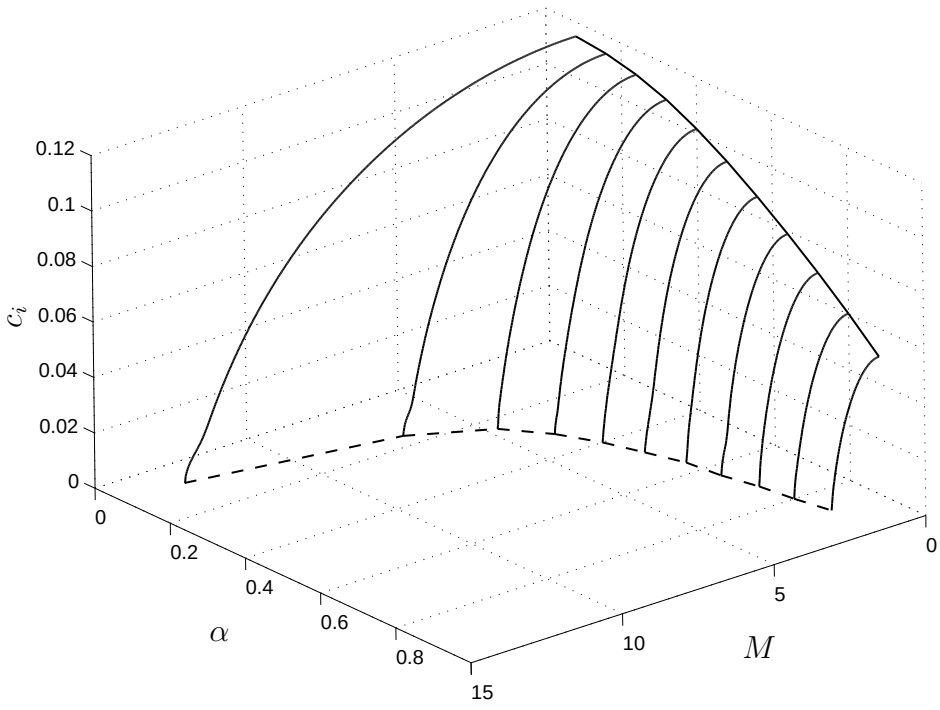

Figure 5.8: Instability (c_i) for single vortex versus Mach number (M) and wave-number (α).

5.6.2 Two-Vortex Flow

The maximum growth rate of the primary two-vortex mode found previously at $(\alpha, y) = (0.86, 0.78)$ is 0.139507 corresponding to $c_1 = 0.529072 + 0.162217\text{i}$ which is found as $c = 0.51550 + 0.16202\text{i}$ using $r_{max} = 8$ in the finite difference code. For the second and third modes (at their maximum growth rates) we find the eigenvalues $c = 0.70835 + 0.07767\text{i}$ for $c_2 = 0.705575 + 0.080529\text{i}$ at $\alpha = 0.46$ and $c = 0.92491 + 0.05052\text{i}$ for $c_3 = 0.930655 + 0.052500\text{i}$ at $\alpha = 0.50$. The curves of the growth rates for the first three modes are given in figure 5.9 along with their extension, at maximum αc_i, into the compressible regime in figure 5.10. The effect of compressibility on the

real component of the eigenvalues is shown in figure 5.11.

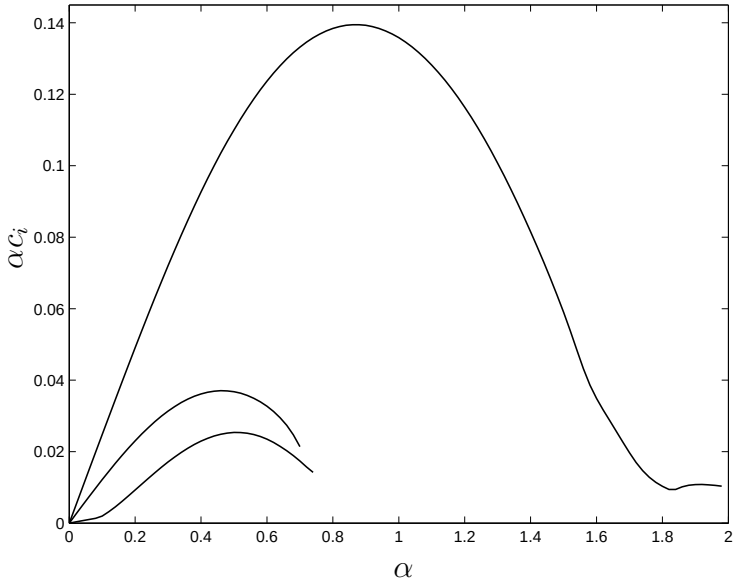

Figure 5.9: Growth rate (αc_i) versus wave-number (α) of the first three unstable modes for a two-vortex configuration with $M = 0$.

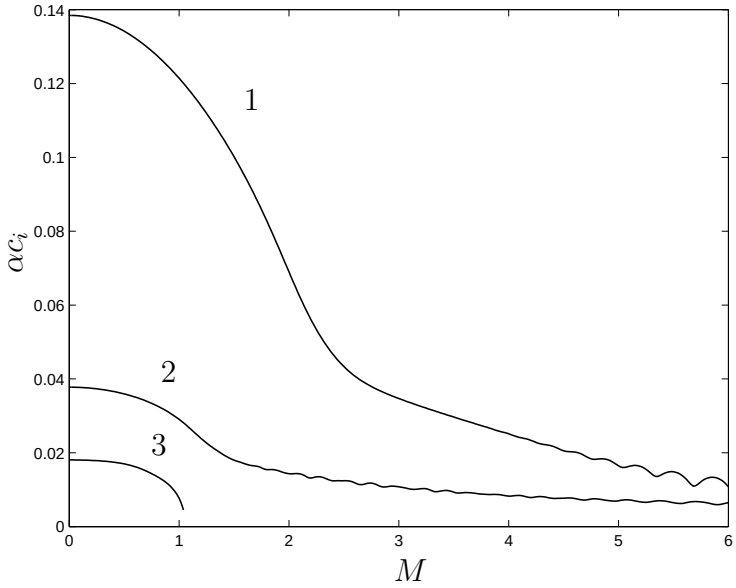

Figure 5.10: Growth rate (αc_i) versus Mach number (M) of the three most unstable modes for a two-vortex configuration at $\alpha = 0.86, 0.46, 0.50$ respectively.

Here the initial starting error at small M is obvious, however as is shown in section 5.5 both numerical schemes converge quickly thereafter. A further small initial deviation is seen when the boundary is extended to $r_{max} = 20$ as the grid points are now stretched over a larger area.

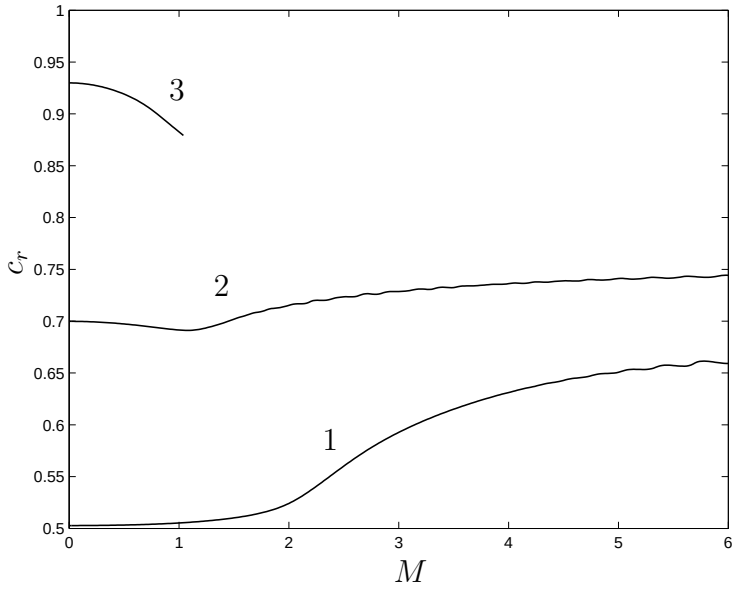

Figure 5.11: The real component of the first three unstable eigenvalues (c_r) versus Mach number (M) for a two-vortex configuration at $\alpha = 0.86, 0.46, 0.50$ respectively.

In a similar manner to the single vortex case, compressibility has a stabilising effect on the most unstable modes. Unlike the plot of instability decay for a single vortex however, the two-vortex configuration exhibits a change in the rate of decay which enables the instability to exist to higher Mach numbers than might be expected if we use the behaviour of the single vortex case as a guide. We find that as the growth rate decreases, the ability of the code to accurately track the mode is lost. This is common through all (studied) values of α as can be seen in figure 5.13. Figure 5.12 illustrates the normalised modal amplitudes of the most unstable mode at $M = 0, 2.0, 2.5, 3.5$ along the curve of figure 5.10. We can see that whilst the structure of the mode is essentially the same, ie; symmetric about $z = 0$, as $M > 1.8$, some distortion of the mode takes place as M increases. It appears that the increase in Mach number has the effect of increasing the spatial range of the

decay of the pressure perturbation which is why, as was pointed out earlier, a larger N_{max} than is used for the incompressible case is required.

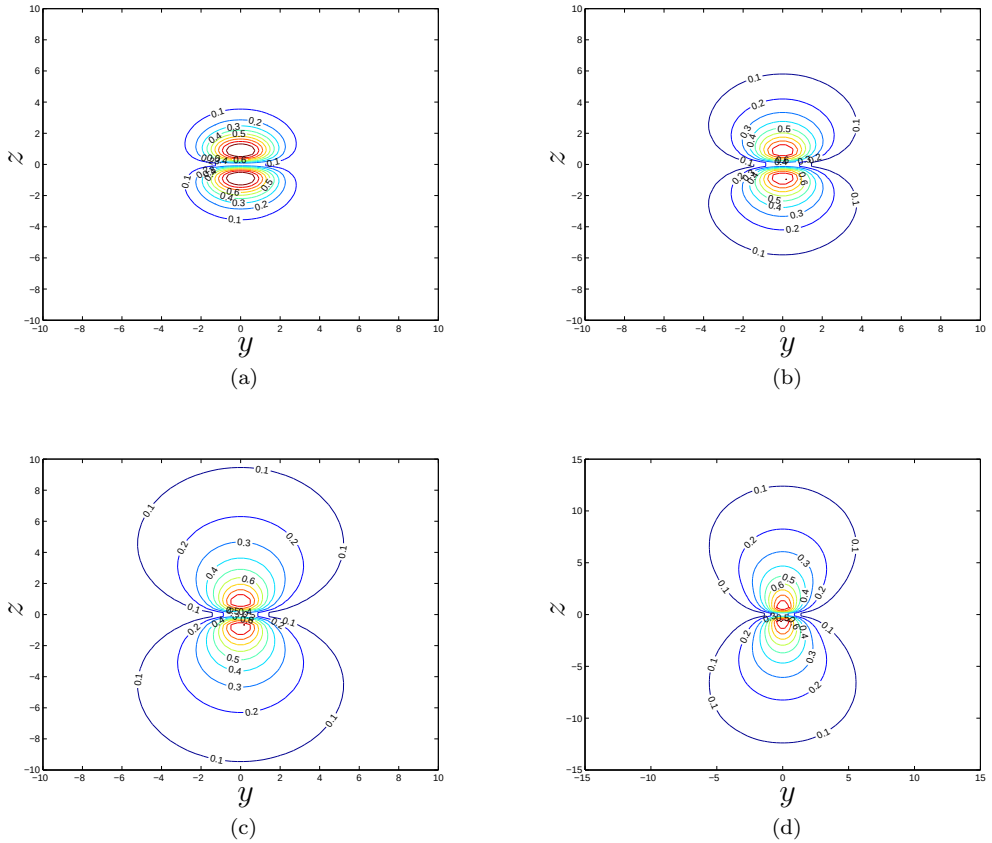

Figure 5.12: Normalised amplitude of eigenmodes for the two-vortex growth rates given in figure 5.10 for the most unstable mode at (a) $M = 0$, (b) $M = 2.0$, (c) $M = 2.5$ and (d) $M = 3.5$.

Figure 5.13 provides the picture of the effects of compressibility on the primary mode as found in the two-vortex configuration over the studied $\alpha - M$ domain. It is apparent that the general form of the stabilising effect of compressibility is found throughout all values of α with the Mach number required to stabilise the flow growing exponentially as $\alpha \to 0$. The dashed line represents a level of $c_i = 0.03$, the point at approximately which the numerical scheme ceased to resolve a smooth curve.

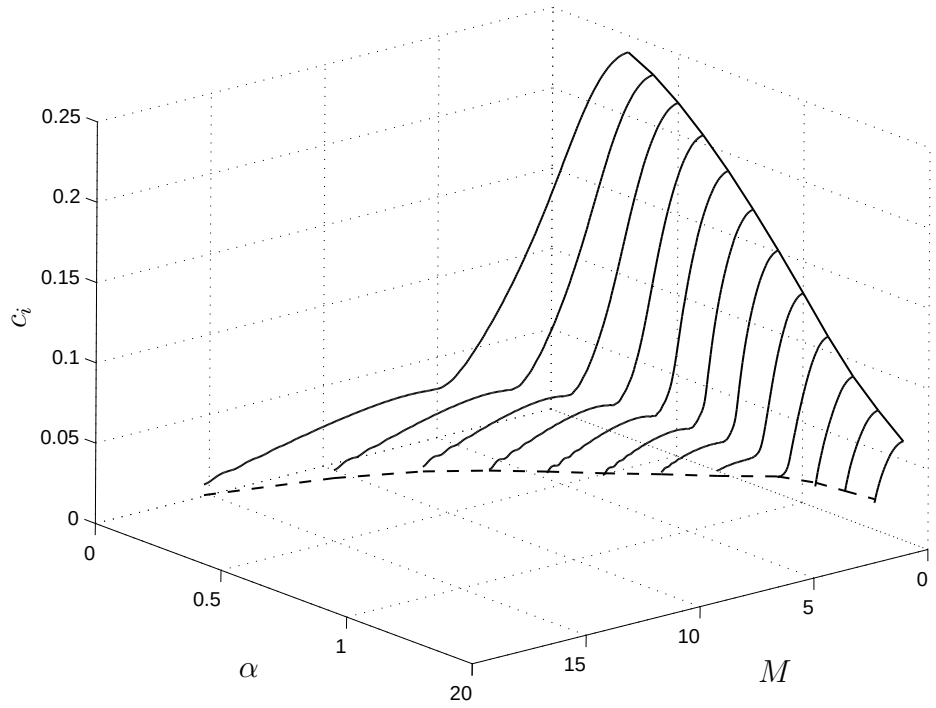

Figure 5.13: Instability (c_i) versus Mach number (M) and wave-number (α) for the most unstable two-vortex mode.

5.6.3 Four-Vortex Flow

In the most unstable four-vortex configuration, for which $(y_2, z_2) \approx (0.36, 0)$, the growth rate of the primary mode is 0.13557 which corresponds to $c_1 = 0.37596 + 0.15063\text{i}$ at $\alpha = 0.9, M = 0$, with the iterative starting result being $c = 0.37588 + 0.15039\text{i}$ again, with $r_{max} = 8$. For the subsequent modes we find eigenvalues of $c = 0.43303 + 0.10117\text{i}$ for $c_2 = 0.43329 + 0.10368\text{i}$ at $\alpha = 0.78$ and $c = 0.68850 + 0.07262\text{i}$ for $c_3 = 0.69009 + 0.07485\text{i}$ at $\alpha = 0.56$. The growth rates corresponding to these modes are given in figure 5.14. The slight discrepancy in these values is explained earlier but is negligible in terms of the graphical representation presented here.

As in the two-vortex case, we see a similar result in terms of the effect of compressibility on the growth rates given in figure 5.15, with the real component of the eigenvalue shown in figure 5.16. It is also worth noting that, whilst the growth rate

of the primary mode of the four-vortex system is marginally less than that of the two-vortex system, the appearance of the extra vortices does seem to extend the instability through to a higher range of M. As before the numerical scheme is not well defined near $c_i = 0$ and the nature of the curve makes it impossible to accurately determine the point of neutral stability. Figure 5.17 plots the normalised modal amplitudes of the most unstable mode at $M = 0, 2.7, 3.7, 4.8$ from which we can see a similar 'stretching' of the decay of pressure perturbation as the Mach number is increased, to that of the previous vortex configurations.

Again, it is apparent from figure 5.18 that the general form of the primary mode curve in figure 5.15 continues throughout the entire range of α, and, as was the case for the two-vortex system, approaches a stable state for all M in the range of α studied.

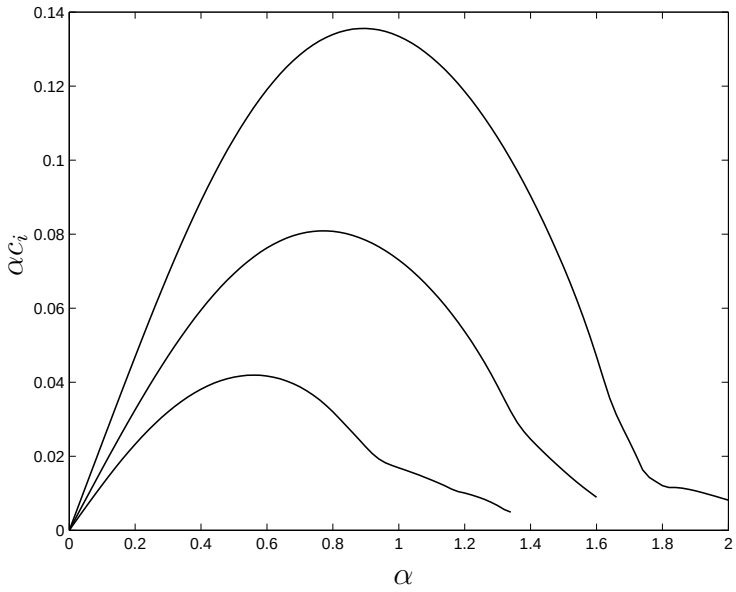

Figure 5.14: Growth rate (αc_i) versus wave-number (α) of the first three unstable modes for a four-vortex configuration with $M = 0$.

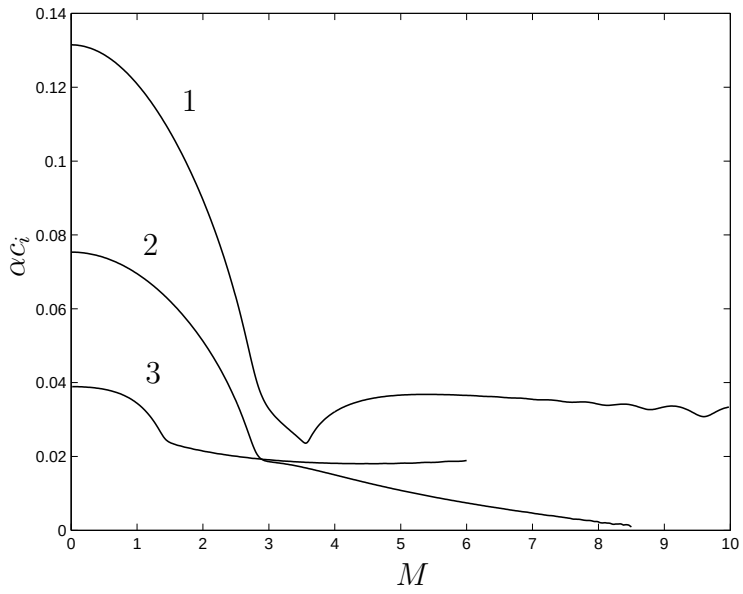

Figure 5.15: Growth rate (αc_i) versus Mach number (M) of the three most unstable modes for a four-vortex configuration at $\alpha = 0.9, 0.78, 0.56$ respectively.

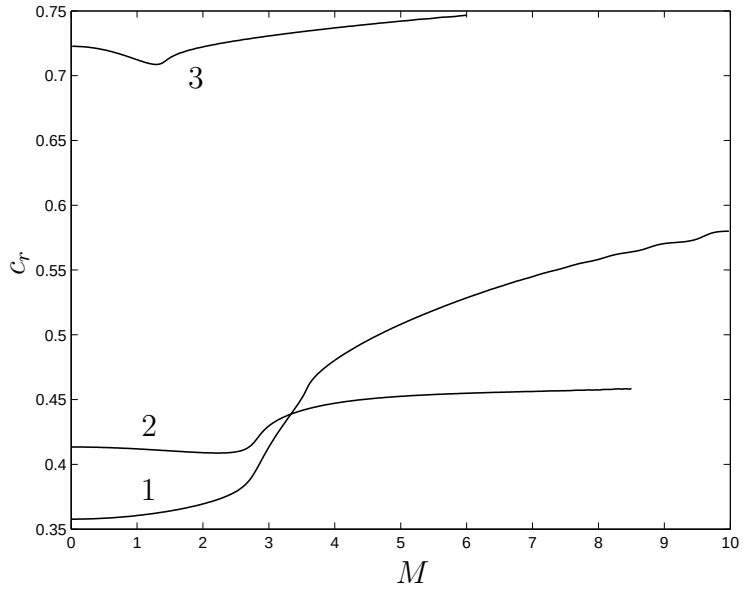

Figure 5.16: The real component of the first three unstable eigenvalues (c_r) versus Mach number (M) for a four-vortex configuration at $\alpha = 0.9, 0.78, 0.56$ respectively.

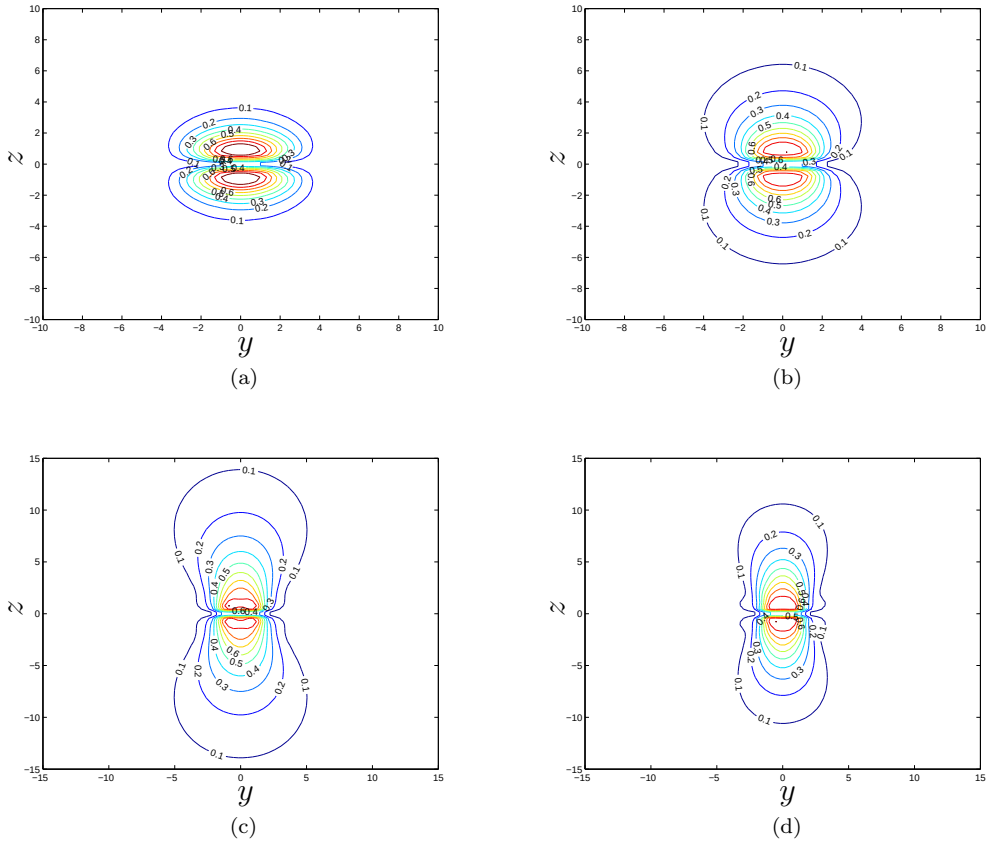

Figure 5.17: Normalised amplitude of eigenmodes of the most unstable mode for the four-vortex growth rates given in figure 5.15 at (a) $M = 0$, (b) $M = 2.7$, (c) $M = 3.7$ and (d) $M = 4.8$.

5.7 Discussion

It should be remembered that we have tracked the effect of compressibility on the most unstable inviscid incompressible mode found in chapter 4. From Stott and Duck [59] we know that the most unstable single vortex mode persists to higher M for large azimuthal wave-numbers of which, due to our two-dimensional global analysis, we are unable to specify.

We have shown that for the single vortex case, the curves illustrating the reduction in instability as the Mach number increases are stabilised and that the most unstable (incompressible) mode heads towards a definite point of neutral stability which, although not being resolved exactly, can be extrapolated to a close approximation. Each of these individual curves displays the characteristics of similar curves (for non-zero swirl numbers) that appear in the literature. For both multiple vortex

configurations studied here, a different shape of stability curve is observed. We see that whilst the multiple vortex curves behave similarly to those of the single vortex at low Mach numbers, as we increase M further, a change in the rate of instability decay is seen, thus prolonging the instability of the mode longer than would be expected if we were to use the behaviour of the single vortex mode as a guide. We have also presented evidence that compressibility will cause the eigenmode to expand in the computational domain, demonstrating that, spatially, the mode perturbations persist further from the co-ordinate origin.

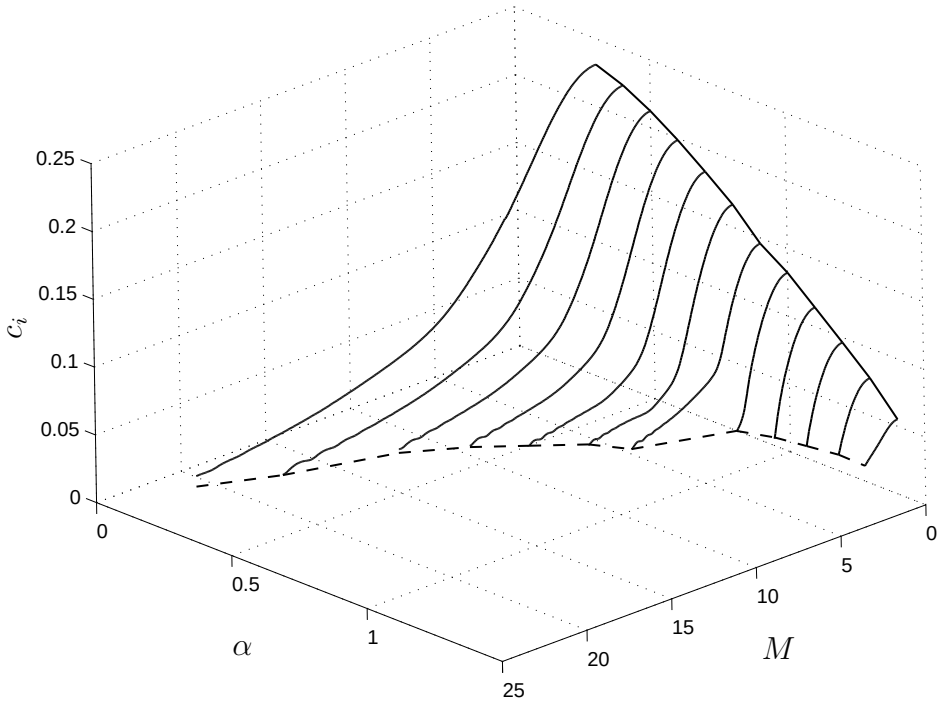

Figure 5.18: Instability (c_i) versus Mach number (M) and wave-number (α) for the most unstable four-vortex mode.

In general, it has been shown that the most unstable inviscid modes are stabilised by the inclusion of compressibility from which we can infer with some confidence that compressibility has a stabilising effect on all unstable inviscid modes. We also note that, for increasing M, an increasingly large domain than would ordinarily be expected for an inviscid stability analysis is required in order to ensure that the boundary conditions are explicitly satisfied. This makes the approximation of a

distinct transition to stability difficult (primarily for the multiple vortex cases) and as such only an indication of where the numerical scheme starts to become unresolved has been presented. However, we can state with confidence that increased computing resources, allowing for sufficient numerical accuracy, would only aid in the detection of the point of transition to stability and not qualitatively change the general results presented here.

Chapter 6

Viscous Flow

6.1 Introduction

In order to better capture the important physics of instabilities in wake vortices, we now consider the extension of the inviscid (incompressible) model studied earlier to include the effects of viscosity. The basic flow is three dimensional as the cross-flow components previously neglected in the inviscid analysis of section 4.3 become important to the stability characteristics of the flow at finite Reynolds numbers. This will enable examination of lower Reynolds number problems near the critical point of neutral stability for a variety of modes.

6.2 Disturbance Equations

From section 2.4.2 we find that the viscous disturbance equations, when written in the form of an eigenvalue problem are, in Cartesian co-ordinates,

$$\begin{bmatrix} \mathcal{Q} & \frac{\partial U}{\partial y} & \frac{\partial U}{\partial z} & \mathrm{i}\alpha \\ 0 & \mathcal{Q}+\frac{\partial V}{\partial y} & \frac{\partial V}{\partial z} & \frac{\partial}{\partial y} \\ 0 & \frac{\partial W}{\partial y} & \mathcal{Q}+\frac{\partial W}{\partial z} & \frac{\partial}{\partial z} \\ \mathrm{i}\alpha & \frac{\partial}{\partial y} & \frac{\partial}{\partial z} & 0 \end{bmatrix} \begin{bmatrix} U_p \\ V_p \\ W_p \\ P_p \end{bmatrix} = \omega \begin{bmatrix} \mathrm{i} & 0 & 0 & 0 \\ 0 & \mathrm{i} & 0 & 0 \\ 0 & 0 & \mathrm{i} & 0 \\ 0 & 0 & 0 & 0 \end{bmatrix} \begin{bmatrix} U_p \\ V_p \\ W_p \\ P_p \end{bmatrix},$$

where

$$\mathcal{Q} = \mathrm{i}\alpha U + V\frac{\partial}{\partial y} + W\frac{\partial}{\partial z} - \frac{1}{Re}\left(-\alpha^2 + \frac{\partial^2}{\partial y^2} + \frac{\partial^2}{\partial z^2}\right). \tag{6.2.1}$$

Equivalently in cylindrical polar co-ordinates,

$$\begin{bmatrix} \mathcal{Q} & \frac{\partial U_B}{\partial r} & \frac{1}{r}\frac{\partial U_B}{\partial \theta} & \mathrm{i}\alpha \\ 0 & \mathcal{Q}+\frac{1}{r^2 Re} & \frac{2}{r^2 Re}\frac{\partial}{\partial \theta} & \frac{\partial}{\partial r} \\ 0 & \mathcal{M} & \mathcal{Q}+\mathcal{N} & \frac{1}{r}\frac{\partial}{\partial \theta} \\ \mathrm{i}\alpha & \frac{1}{r}+\frac{\partial}{\partial r} & \frac{1}{r}\frac{\partial}{\partial \theta} & 0 \end{bmatrix} \begin{bmatrix} U_p \\ V_p \\ W_p \\ P_p \end{bmatrix} = \omega \begin{bmatrix} \mathrm{i} & 0 & 0 & 0 \\ 0 & \mathrm{i} & 0 & 0 \\ 0 & 0 & \mathrm{i} & 0 \\ 0 & 0 & 0 & 0 \end{bmatrix} \begin{bmatrix} U_p \\ V_p \\ W_p \\ P_p \end{bmatrix},$$

where

$$\mathcal{Q} = \mathrm{i}\alpha U + \frac{W}{r}\frac{\partial}{\partial \theta} - \frac{1}{Re}\left(\frac{1}{r}\frac{\partial}{\partial r} + \frac{\partial^2}{\partial r^2} + \frac{1}{r^2}\frac{\partial^2}{\partial \theta^2} - \alpha^2\right), \tag{6.2.2}$$

and

$$\mathcal{M} = \frac{\partial W_B}{\partial r} + \frac{W_B}{r} - \frac{2}{r^2 Re}\frac{\partial}{\partial \theta}, \quad \mathcal{N} = \frac{1}{r}\frac{\partial W_B}{\partial \theta} + \frac{1}{r^2 Re}. \tag{6.2.3}$$

6.3 Basic Flow

6.3.1 Linear Superposition of Batchelor Vortices

A linear superposition of Batchelor vortices is used in various configurations with one or two vortex pairs. The basic flow is the similarity solution derived by Batchelor [3] and presented in section 4.3.1 and subsequently, when written in terms of cylindrical polar co-ordinates the flow is given by

$$U = \gamma e^{-ar^2}, \tag{6.3.1}$$

$$V = 0, \tag{6.3.2}$$

$$W = -\frac{q}{r}(1 - \gamma e^{-ar^2}). \tag{6.3.3}$$

For vortices situated away from the co-ordinate origin we replace r with $(r - r_n)$ where we note that r_n is the vortex placement and also note the relationships,

$$r_n^2 = y_n^2 + z_n^2, \qquad y_n = r_n \sin\theta, \qquad z_n = r_n \cos\theta, \tag{6.3.4}$$

with,

$$(r - r_n)^2 = r^2 - 2rr_n + r_n^2,$$

and using the relationship $\sin^2\theta + \cos^2\theta = 1$ we find that,

$$r_n = y_n \sin\theta + z_n \cos\theta, \tag{6.3.5}$$

we can derive the relationships

$$(r - r_n)^2 = r^2 - 2r(y_n \sin\theta + z_n \cos\theta) + y_n^2 + z_n^2, \tag{6.3.6}$$

$$(r - r_n) = r - y_n \sin\theta - z_n \cos\theta. \tag{6.3.7}$$

Our basic flow, consisting of multiple vortices situated away from the co-ordinate origin can be written as

$$U = \sum_{n=1}^{N} \gamma_n e^{-a_n(r^2 - 2ry_n \sin\theta - 2rz_n \cos\theta + y_n^2 + z_n^2)}, \qquad n = 1, ..., \infty, \tag{6.3.8}$$

$$V = 0, \tag{6.3.9}$$

$$W = -\sum_{n=1}^{N} \frac{q_n[1 - \gamma_n e^{-a_n(r^2 - 2ry_n \sin\theta - 2rz_n \cos\theta + y_n^2 + z_n^2)}]}{r - y_n \sin\theta - z_n \cos\theta}, \quad n = 1, ..., \infty, \tag{6.3.10}$$

where γ is the axial strength parameter, a is the decay rate and N is the number of vortices. The mean velocity profiles are illustrated in figure 6.1 with both γ and a set equal to unity and $n = 1$ for a single vortex located at the co-ordinate origin. The basic flow for use in the Cartesian implementation of the viscous stability equation solver where the variables are the same as above is

$$U = \sum_{n=1}^{N} \gamma_n e^{-a_n[(y-y_n)^2 + (z-z_n)^2]}, \qquad n = 1, ..., \infty, \tag{6.3.11}$$

$$V = \sum_{n=1}^{N} \frac{q_n(z - z_n)[1 - \gamma_n e^{-a_n[(y-y_n)^2 + (z-z_n)^2]}]}{(y - y_n)^2 + (z - z_n)^2}, \qquad n = 1, ..., \infty, \tag{6.3.12}$$

$$W = -\sum_{n=1}^{N} \frac{q_n(y - y_n)[1 - \gamma_n e^{-a_n[(y-y_n)^2 + (z-z_n)^2]}]}{(y - y_n)^2 + (z - z_n)^2}, \quad n = 1, ..., \infty. \tag{6.3.13}$$

6.4 Computational Domain

For each co-ordinate system, vortex placement is essentially the same as that shown in figure 4.2 for the inviscid instability analysis, the difference being the shape of the

domain, either $-N_{r,max} \leq r \leq N_{r,max}$ for polar or between $-N_{y,max} \leq y \leq N_{y,max}$ and $-N_{z,max} \leq z \leq N_{z,max}$ in the case of the Cartesian system (see figure 3.7).

Unlike the inviscid case, where the cross-flow perturbation components are of an order of magnitude smaller than the axial flow and so it was that the decay of the axial component was the determining factor in choosing the size of the computational domain, the finite Reynolds numbers in the viscous case bring all perturbation quantities to a similar order requiring a significantly larger domain size. Mayer and Powell [41] state that they find a domain size of $\mathcal{O}(10)$ to be sufficient for six-figure accuracy and use $20 \leq r \leq 50$ except for very low Reynolds numbers or long-wave disturbances. In Hein and Theofilis [25], their Cartesian domain is set to approximately $N_{max} = 40$ (equivalent to $r_{max} = 40$ in our polar domain) for the single vortex case and slightly higher for the multiple vortex cases. Our analysis uses similar sized domains.

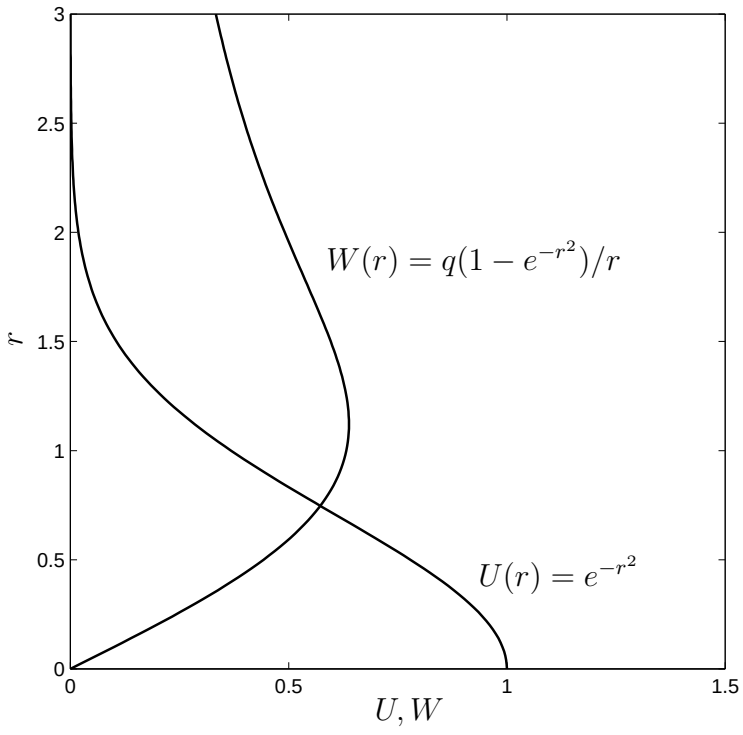

Figure 6.1: Mean velocity profiles for axial (U) and azimuthal (W) basic flow in cylindrical polar co-ordinates.

6.5 Numerical Methods

For the viscous problem it proved convenient to produce codes firstly in Cartesian and then cylindrical polar co-ordinates. This was done initially due to a number of problems encountered (and later overcome) with implementing the polar co-ordinate version of the code. It also allowed for various cross-checking to be performed between the two quite distinct implementations of the numerical scheme. The Cartesian code was also adaptable to use either pseudo-spectral techniques or finite-differences, whilst the polar form used spectral methods exclusively. As was outlined in section 3.7.3, values recovered from both versions were able to be verified against published results for plane Poiseuille flow in a duct, Hagen-Poiseuille flow in a pipe, and for the general structure found in the single Batchelor vortex stability analysis. The convergence histories following are for the polar code with the Cartesian case as detailed in Appendix C. It is important to note here that the differentiation matrices used to discretise the system of equations are identical to those used in the inviscid analysis in chapter 4 and described in detail in section 3.2; the accuracy of these has been demonstrated in section 3.

6.5.1 Single Vortex Numerical Convergence

Whilst the integrity of the numerical scheme is assured as a result of our earlier benchmarking, it is useful to provide a convergence history of the eigenvalues for changes in spectral accuracy and degree of grid clustering. In doing this we provide information on the lowest resolution required for acceptable accuracy (to aid in efficient use of computational resources) and also give a clearer picture of the range of convergence.

Figure 6.2 is a plot of the smallest stable eigenvalues found by setting the ARPACK shift parameter $\sigma = 0 - 0\mathrm{i}$ (to find eigenvalues about the neutral axis) for $(N_r, N_\theta) = (51, 28); (61, 32); (71, 42); (81, 52)$ with $s_r = 0.97$, from which it can be seen that good convergence is reached right from $(N_r, N_\theta) = (51, 28)$ for the first 30 or so modes. The values $\alpha = 0.418, q = 0.475$ and $Re = 100$ correspond to those used by Hein and Theofilis [25] and provide a useful visual comparison with the results presented herein. Increasing the spectral accuracy does improve the conver-

gence further, but this involves large increases in run times and stretches available computer resources to their limits.

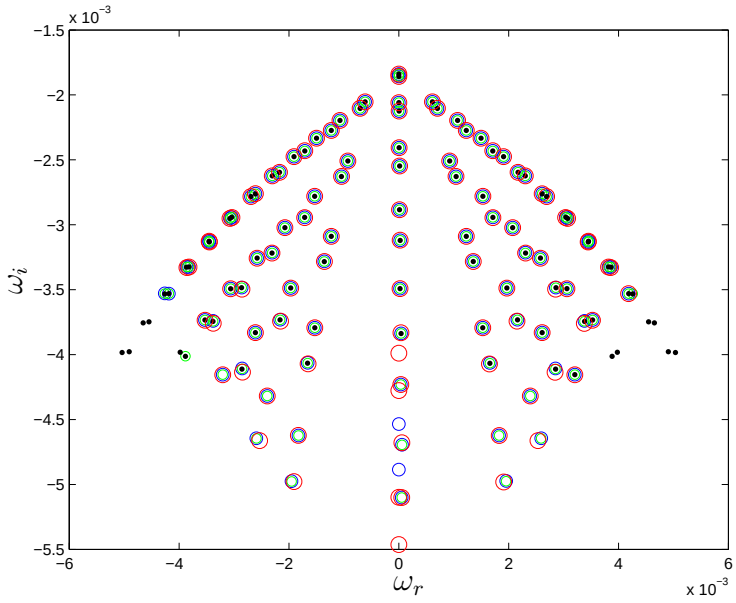

Figure 6.2: Convergence of eigenvalues for the viscous stability of a single vortex. $(N_r, N_\theta) = (51, 28), (61, 32), (71, 42), (81, 52)$ in descending size of marker, the $\bullet$ corresponding to the case $(81, 52)$.

The fact that good numerical convergence occurs near the neutral stability axis is particularly useful for the analysis that follows as we are interested in locating regions of neutral stability for various vortex configurations and following their respective neutral curves. Looking at the eigenvalues for a range of (N_r, N_θ), table 6.1 shows that, for the two 'least-stable' modes, approximately eight decimal place convergence is achievable from $(N_r, N_\theta) = (41, 24)$ in both the real and imaginary components using a clustering parameter of $s_r = 0.97$.

Table 6.2 gives the convergence history of the same least-stable modes for a variation in the grid clustering rate from zero through to very heavy clustering about the co-ordinate origin with $(N_r, N_\theta) = (61, 32)$. The results indicate that in both cases, a high degree of convergence is seen at $s_r = 0.95$ but the eigenvalue appears to be relatively well resolved for lower degrees of clustering. To further illustrate the numerical convergence of the scheme for those values found closest to

the neutral axis, convergence histories of the subsequent four modes are given in tables 6.3 and 6.4 showing the effect of an increase in spectral accuracy.

(N_r, N_θ)	'Mode 1'	'Mode 2'
(41,24)	-0.00000979032 - 0.00180730689i	0.00000583294 - 0.00181594761i
(51,28)	-0.00000977657 - 0.00180733018i	0.00000581530 - 0.00181599549i
(61,32)	-0.00000977253 - 0.00180733399i	0.00000581037 - 0.00181600582i
(71,42)	-0.00000976959 - 0.00180733964i	0.00000580649 - 0.00181601753i
(81,52)	-0.00000976735 - 0.00180734513i	0.00000580342 - 0.00181602813i

Table 6.1: Convergence history of the two least-stable eigenvalues for a single vortex, varying (N_r, N_θ).

s	'Mode 1'	'Mode 2'
0	-0.00000958838 - 0.00181135941i	0.00000703256 - 0.00181472788i
0.5	-0.00001299084 - 0.00181056539i	0.00000731066 - 0.00181436248i
0.6	-0.00001255333 - 0.00180856800i	0.00000824824 - 0.00181564272i
0.7	-0.00001230743 - 0.00180684156i	0.00000712883 - 0.00181719066i
0.8	-0.00000897364 - 0.00180595265i	0.00000502059 - 0.00181663903i
0.9	-0.00000979456 - 0.00180738334i	0.00000582731 - 0.00181602352i
0.95	-0.00000977114 - 0.00180734609i	0.00000580923 - 0.00181601767i
0.97	-0.00000977253 - 0.00180733399i	0.00000581037 - 0.00181600582i

Table 6.2: Convergence history of the two least-stable eigenvalues for a single vortex, varying the clustering parameter, s.

It is also useful to observe the effects of increasing the number of grid points in the azimuthal direction on the convergence of the eigenvalues. As the modes become more complex in structure (associated with higher azimuthal wave-numbers) more grid points will be required, however for those values that are found around the neutral axis, the maximum number of azimuthal grid points with $N_r = 81$ is shown to be sufficient at resolving both real and imaginary components of the eigenvalue to a significant degree of accuracy as demonstrated by the results presented in table

6.5. If we compare table 6.5 to table 6.1 we see that the imaginary component of the second mode converges faster using a larger N_r, even with the smaller value of N_θ. This would suggest that for the following analysis, a high number of grid points in r is required combined with a manageable number of points in θ.

(N_r, N_θ)	'Mode 3'	'Mode 4'
(41,24)	0.00035589648 - 0.00186044698i	-0.00036661513 - 0.00186561797i
(51,28)	0.00032196067 - 0.00176234959i	-0.00036940265 - 0.00186565761i
(61,32)	0.00037953703 - 0.00187419939i	-0.00037111090 - 0.00186042891i
(71,42)	0.00037126874 - 0.00187025928i	-0.00036571556 - 0.00185974913i
(81,52)	0.00036912128 - 0.00186890603i	-0.00036469955 - 0.00186170426i

Table 6.3: Convergence history of the third and fourth least-stable eigenvalues for a single vortex, varying (N_r, N_θ).

(N_r, N_θ)	'Mode 5'	'Mode 6'
(41,24)	0.00065614028 - 0.00194155601i	-0.00065613646 - 0.00194155976i
(51,28)	0.00065654564 - 0.00194191463i	-0.00065654324 - 0.00194191723i
(61,32)	0.00065657933 - 0.00194193481i	-0.00065657807 - 0.00194193639i
(71,42)	0.00065665044 - 0.00194196802i	-0.00065664969 - 0.00194196906i
(81,52)	0.00065671719 - 0.00194199928i	-0.00065671670 - 0.00194200001i

Table 6.4: Convergence history of the fifth and sixth least-stable eigenvalues for a single vortex, varying (N_r, N_θ).

Figure 6.3 shows the eigenvalue spectra of Hein and Theofilis [25] (using the parameters of Mayer and Powell [41]) with particular emphasis on the unstable modes. In section 3.7.3 we established that the two-dimensional global code recovers correct stable values at relatively low grid resolutions, here we examine the convergence of unstable values. Firstly, we can see that numerical convergence is far from that for the stable values. The plot in figure 6.3 and corresponding values in table 6.6 show that whilst the values are not exact, they are generally within 0.01 (with the real components approaching an accuracy of ± 0.005) of the values of Mayer and Powell

[41] and subsequently recovered using our one-dimensional, n-dependent code. This enables us to state with some confidence that whilst the neutral curves produced hereafter are not exact, they are a close representation of where we would expect the converged values to be found.

(N_r, N_θ)	'Mode 1'	'Mode 2'
(81,24)	-0.00000976735 - 0.00180734513i	0.00000580342 + -0.00181602813i
(81,32)	-0.00000976735 - 0.00180734513i	0.00000580342 + -0.00181602813i
(81,40)	-0.00000976735 - 0.00180734513i	0.00000580342 + -0.00181602813i
(81,48)	-0.00000976735 - 0.00180734513i	0.00000580342 + -0.00181602813i
(81,52)	-0.00000976735 - 0.00180734513i	0.00000580342 + -0.00181602813i

Table 6.5: Convergence history of the first and second least-stable eigenvalues for a single vortex, varying N_θ.

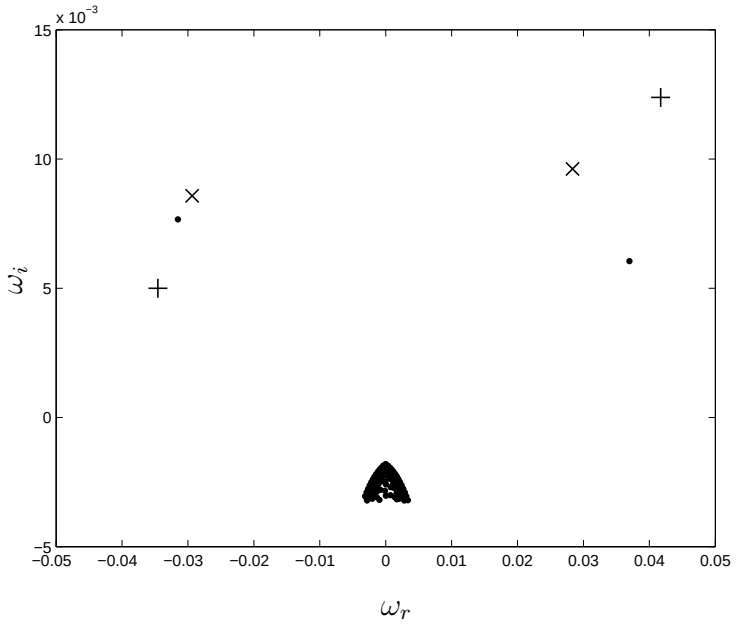

Figure 6.3: Eigenvalue spectra for the parameters of Mayer and Powell [41] (dots): $N_r = 120$, obtained with a one-dimensional code compared with those obtained using a two-dimensional code; $+ : (N_r, N_\theta) = (50, 24)$, $\times : (N_r, N_\theta) = (80, 52)$.

$N_r = 120$	$(N_r, N_\theta) = (50, 24)$	$(N_r, N_\theta) = (81, 52)$
-0.029367 + 0.008576i	-0.034563 + 0.004998i	-0.031528 + 0.007662i
0.028351 + 0.009616i	0.041709 + 0.012382i	0.036989 + 0.006046i

Table 6.6: The two unstable eigenvalues of the Mayer and Powell [41] parameters as found using the one-dimensional code compared to those results obtained using the two-dimensional code.

6.5.2 Two-Vortex Numerical Convergence

As with the single vortex case, the values of Hein and Theofilis [25] are used as our benchmark to check convergence. Again, convergence with respect to a variation in the number of grid points and gradual increase in the clustering parameter is examined. Figure 6.4 represents the spectra of least-stable values as found by setting the vortices at $(y, z) = (2.0, 0)$.

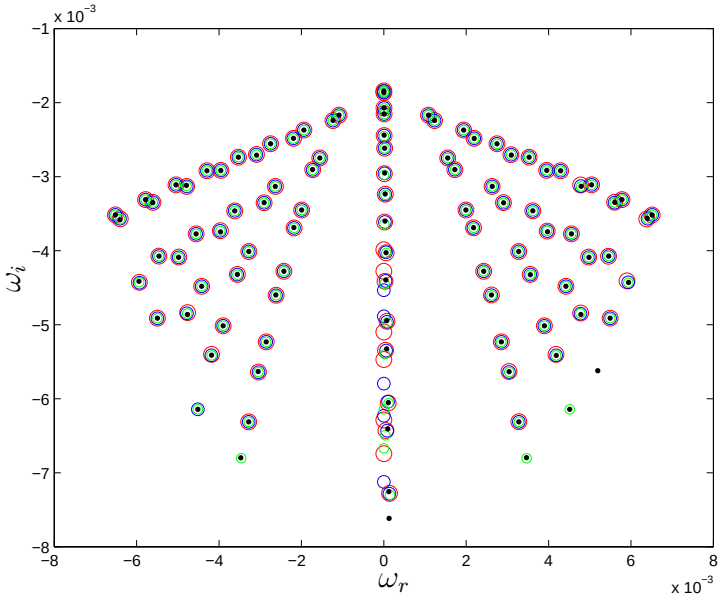

Figure 6.4: Convergence of eigenvalues for the viscous stability of a two-vortex configuration. $(N_r, N_\theta) = (51, 28), (61, 32), (71, 42), (81, 52)$ in descending size of marker, the • corresponding to the case $(81, 52)$.

Again, as expected from the results of the single vortex study, good convergence

is limited to those values that are least stable at grid resolutions achievable using the computational resource available. Table 6.7 gives the two least-stable eigenvalues for the same variation in (N_r, N_θ) as was used earlier. The clustering for the two-vortex configuration is set at $s_r = 0.95$; the value $s_r = 0.95$ was chosen so as to slightly relax the clustering in the plane of the two vortices as they sit away from the origin. It can be seen that again, five significant figures convergence is achieved at relatively low grid resolutions with at least six significant figures convergence for a higher number of grid points.

(N_r, N_θ)	'Mode 1'	'Mode 2'
(41,24)	-0.00015216290 - 0.00189727128i	0.00015204415 - 0.00189738281i
(51,28)	-0.00015216504 - 0.00189739030i	0.00015198122 - 0.00189742099i
(61,32)	-0.00015225425 - 0.00189768836i	0.00015214529 - 0.00189745625i
(71,42)	-0.00015295714 - 0.00189767394i	0.00015472039 - 0.00189618982i
(81,52)	-0.00015215702 - 0.00189786790i	0.00015156123 - 0.00189765844i

Table 6.7: Convergence history of the two least-stable eigenvalues for a two-vortex configuration, varying (N_r, N_θ).

(N_r, N_θ)	'Mode 3'	'Mode 4'
(41,24)	0.00063861283 - 0.00191824514i	-0.00063865035 - 0.00191834047i
(51,28)	0.00063884106 - 0.00191818958i	-0.00063876346 - 0.00191872101i
(61,32)	0.00063875515 - 0.00191823128i	-0.00063904498 - 0.00191772035i
(71,42)	0.00064118119 - 0.00191342791i	-0.00063943174 - 0.00191535376i
(81,52)	0.00063902597 - 0.00191696204i	-0.00063758393 - 0.00191766873i

Table 6.8: Convergence history of the third and fourth least-stable eigenvalues for a two-vortex configuration, varying (N_r, N_θ).

The convergence histories of four further modes are given below for comparison. It should be noted that for all the convergence histories proceeding and following, the mode numbers stated are purely arbitrary and assigned only by descending order of magnitude of the imaginary component of the eigenvalue as obtained from

the initial resolution study. Hence, a mode listed as five for example, may have an imaginary component less than that of the subsequent mode six by the time adequate convergence is realised.

(N_r, N_θ)	'Mode 5'	'Mode 6'
(41,24)	0.00119348664 - 0.00203020983i	-0.00119369010 - 0.00203046518i
(51,28)	0.00119323659 - 0.00203056447i	-0.00119422428 - 0.00203024708i
(61,32)	0.00119321576 - 0.00203100265i	-0.00119287833 - 0.00203082166i
(71,42)	0.00119596281 - 0.00203761761i	-0.00119788587 - 0.00203353546i
(81,52)	0.00119247744 - 0.00203010867i	-0.00119264956 - 0.00203144941i

Table 6.9: Convergence history of the fifth and sixth least-stable eigenvalue for a two-vortex configuration, varying (N_r, N_θ).

As in the single vortex case we finish the convergence study by examining the effect the number of grid points in the azimuthal direction has on the convergence at the highest value of N_r used previously. As before, we see that for the values shown, N_r is the governing spatial parameter for the convergence of the least-stable values and N_θ does little to improve the results further.

(N_r, N_θ)	'Mode 1'	'Mode 2'
(81,24)	-0.00015272674 - 0.00189781524i	0.00015223718 - 0.00189727238i
(81,32)	-0.00015197893 - 0.00189749315i	0.00015199639 - 0.00189761554i
(81,40)	-0.00015214774 - 0.00189749626i	0.00015198105 - 0.00189764559i
(81,48)	-0.00015196625 - 0.00189739461i	0.00015203856 - 0.00189771140i
(81,52)	-0.00015215702 - 0.00189786790i	0.00015156123 - 0.00189765844i

Table 6.10: Convergence history of the first and second least-stable eigenvalues for a two-vortex configuration, varying N_θ.

6.5.3 Four-Vortex Numerical Convergence

For the four-vortex case, convergence of a configuration where all four vortices are co-linear is examined. Whilst the system is not restricted to this configuration,

it provides a means for comparison with published results. The vortices are at $(y_1, y_2) = (5, 0.7)$, $a_2 = 0.5$ and $q_2 = -0.19$ corresponding to the ratios of Hein and Theofilis [25], $\alpha = 0.3$ and $Re = 100$. The clustering was reduced to $s_r = 0.93$ to allow for the extra 'spread' of the primary vortices. Figure 6.5 illustrates the region of convergence of the eigenvalues showing the now familiar convergence of least-stable values at manageable problem dimensions. In figure 6.5 we can see that the numerical convergence of the eigenvalue is poor about $\omega_r = 0$ but as we move away from this axis, much faster convergence is realised. We would expect that as the resolution is increased further (beyond what is capable in this study), the eigenvalues approaching $\omega_r = 0$ would become more resolved. The fact that the primary vortices are spaced relatively far apart with the clustering parameter relaxed to compensate for this, contributes further to the resolution problem. However, we can see from the figure that as we move away from the real axis, good eigenvalue convergence is obtained at relatively low grid resolutions.

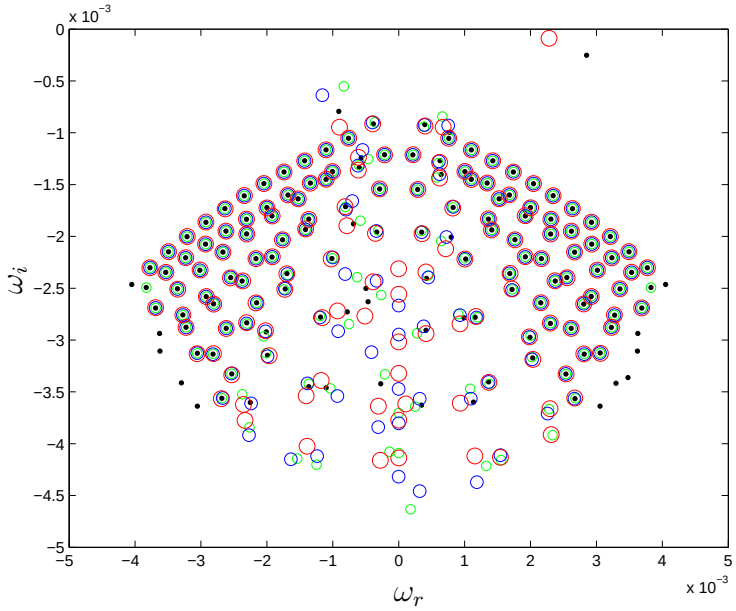

Figure 6.5: Convergence of eigenvalues for the viscous stability of a four-vortex configuration. $(N_r, N_\theta) = (51, 28), (61, 32), (71, 42), (81, 52)$ in descending size of marker, the • corresponding to the case $(81, 52)$.

In table 6.11 we follow those least stable modes that remain as the resolution is increased, where we see a similar pattern of numerical convergence to that observed previously; approximately four significant figures at the starting resolution and approaching five or six significant figures as the resolution increases with some fluctuation in predominantly the real component. Whilst this degree of accuracy is acceptable for illustration purposes, variations in the amount of clustering may provide slightly better results.

(N_r, N_θ)	'Mode 3'	'Mode 4'
(41,24)	-0.00037150331 - 0.00089234691i	0.00070827163 - 0.00090571903i
(51,28)	-0.00039469804 - 0.00091499517i	0.00067373574 - 0.00094588024i
(61,32)	-0.00039686323 - 0.00090044395i	0.00074950321 - 0.00092949619i
(71,42)	-0.00036361627 - 0.00089823189i	0.00066299307 - 0.00084369963i
(81,52)	-0.00038521019 - 0.00091411661i	0.00077204848 - 0.00099602207i

Table 6.11: Convergence history of the third and fourth least-stable eigenvalues for a four-vortex configuration, varying (N_r, N_θ).

As before, we present convergence histories of some further eigenvalues to illustrate, in this case, that the convergence of the numerical scheme improves as ω moves away from the purely imaginary. We see that for the modes still close to the neutral axis but having a real component of $\mathcal{O}(10^{-4})$ or greater, the convergence is greatly improved.

(N_r, N_θ)	'Mode 5'	'Mode 6'
(41,24)	0.00039512849 - 0.00092729386i	-0.00076088958 - 0.00105306498i
(51,28)	0.00039869219 - 0.00093449241i	-0.00075842193 - 0.00105231836i
(61,32)	0.00039239419 - 0.00092442545i	-0.00076043632 - 0.00105225592i
(71,42)	0.00038316494 - 0.00094139865i	-0.00076097031 - 0.00105223551i
(81,52)	0.00039632745 - 0.00092033773i	-0.00075970119 - 0.00105250559i

Table 6.12: Convergence history of the fifth and sixth least-stable eigenvalues for a four-vortex configuration, varying (N_r, N_θ).

(N_r, N_θ)	'Mode 7'	'Mode 8'
(41,24)	0.00076011216 - 0.00105376238i	-0.00110120696 - 0.00116453259i
(51,28)	0.00075839949 - 0.00105300488i	-0.00110201957 - 0.00116481865i
(61,32)	0.00076050172 - 0.00105144663i	-0.00110092052 - 0.00116496984i
(71,42)	0.00076049988 - 0.00105203374i	-0.00110187457 - 0.00116418143i
(81,52)	0.00075956851 - 0.00105425746i	-0.00110240423 - 0.00116518162i

Table 6.13: Convergence history of the seventh and eighth least-stable eigenvalue for a four-vortex configuration, varying (N_r, N_θ).

Table 6.14 documents the convergence of the third and sixth least stable eigenvalues found at $(N_r, N_\theta) = (81, 24)$ as N_θ is increased with N_r fixed. We can see that these values exhibit the same convergence to only four or five significant figures as in table 6.11. However, as is also the case with the subsequent modes, increased convergence is seen as the eigenvalues move away from the $\omega_r = 0$ axis.

(N_r, N_θ)	'Mode 3'	'Mode 6'
(81,24)	0.00039977700 - 0.00091215334i	0.00076092045 - 0.00105153408i
(81,32)	0.00040328533 - 0.00095814607i	0.00076059605 - 0.00104910178i
(81,40)	0.00039284729 - 0.00091980759i	0.00076348406 - 0.00105486634i
(81,48)	0.00039365252 - 0.00092332449i	0.00076514855 - 0.00098139497i
(81,52)	0.00039632745 - 0.00092033773i	0.00075956851 - 0.00105425746i

Table 6.14: Convergence history of the third and sixth least-stable eigenvalues for a four-vortex configuration, varying N_θ.

For the remainder of this section we use $(N_r, N_\theta) = (51, 24)$ for the production of our neutral curves. The reasons for this are two-fold. First, we have shown that for stable modes, the convergence of the eigenvalue is not greatly improved upon within the range of grid resolutions available, and secondly, this grid size is the maximum which can be performed on an available single processor machine, allowing for multiple Re-steps to be run concurrently thus reducing the overall time required to produce a single neutral curve.

6.6 A Comparison of Local and Global Codes

Figure 6.6 shows the neutral curve obtained by locally tracking a particular mode using the finite-difference iterative methods outlined in section 3.3, superimposed over a plot of the $\omega_i = 0$ contour generated using the global pseudo-spectral solver for a single Batchelor vortex. The pseudo-spectral solver was used to provide a starting value for the local code.

In order to concentrate the available resolution closer to the vortex centres, $r_{max} = 8$ was used whereby the axial component of velocity has decayed to zero and the azimuthal component is essentially a potential vortex as $W_p \to q/r$ (but has not decayed to zero as is explicitly required by the boundary conditions). The domain size and azimuthal resolution (as the global results are from a two-dimensional code and not n-dependent) impact on the accuracy of the results at low axial wave-numbers where the additional demands on the domain size is introduced due to the slow decay rate of the disturbance in the large r limit.

It can be seen in figure 6.6 that the solid line representing a neutral curve produced using the finite-difference iterative code closely follows a similar contour produced by the pseudo-spectral global code with greater agreement as the wave-number increases. The dashed curves of the global solver are shown to be unresolved at this resolution for wave-numbers less than $\alpha \approx 0.8$. It is also obvious from the results of the global code that the solid curve would likely level out as the Reynolds number is increased and that a second neutral curve exists at higher wave-numbers and Reynolds numbers but has not been reproduced by the local code here.

Figure 6.6 was produced as an example of what could be achieved when certain concessions are made at the limit of the resolution that our computational resources allow which is why only a single curve is discussed. For this reason, the results following consist of global results only which have been shown to be adequately accurate about the region of neutral stability. The disadvantage of this is the computational time needed to obtain these results and the lack of exact convergence onto the neutral curve. Despite this however, the results are indicative of the curves of neutral stability for the vortex configurations and parameters tested.

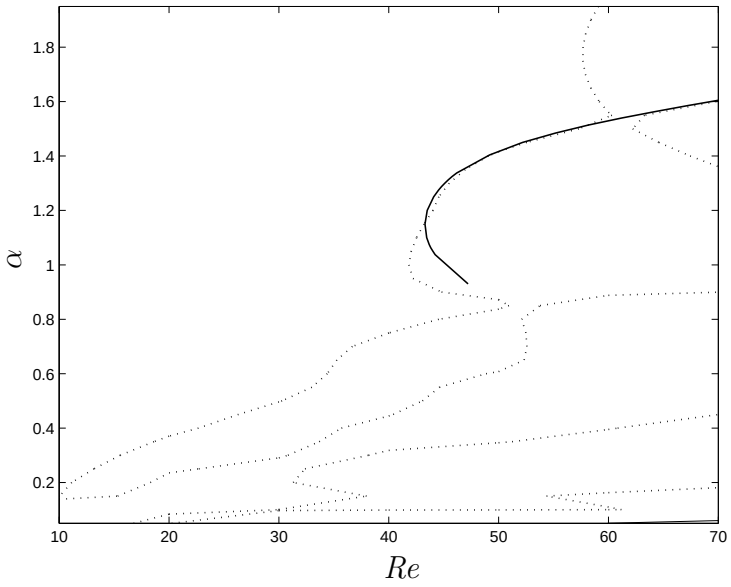

Figure 6.6: Neutral curve generated using local code (solid line) superimposed on the neutral level contours generated using the global pseudo-spectral code.

6.7 A Single Vortex at the Co-ordinate Origin

Unlike the inviscid case where we searched the parameter space for regions of maximum instability, the number of extra parameters in the finite Reynolds number problem make such a study significantly more challenging. The ARPACK routine that is used to compute the eigenvalues makes use of a shift-and-invert Arnoldi process that returns a few eigenvalues in the region of a 'shift' value that satisfies a user specified criterion such as largest magnitude or smallest real component, etc. The search for a maximum unstable eigenvalue is therefore made difficult as these values are always clustered about our 'shift' parameter, and not simply the most unstable values of the system. In light of the large amount of previous research into the linear stability of a single Batchelor vortex we will not present results beyond that which can be found in sections 3.7.3 and 6.5.1, and concentrate on the multiple vortex configurations only. It is also useful, in order to best describe particular features of the neutral stability curves presented, that we define that part of the curve whose wave-number, α falls above the nose of the curve (critical Reynolds number, Re_{cr}) as the upper branch, and that which falls below, the lower branch.

6.8 Two-Vortex Configuration

In order to reduce the number of degrees of freedom in our parameter space, we restrict ourselves to the parameter set used in the inviscid analysis and use the axial wave-number, α, the swirl rate, q and Reynolds number as our variables. The vortices are placed at $(y, z) = (\pm 2, 0)$ unless otherwise stated. This will be the same as the primary vortex spacing to be presented subsequently for the four-vortex case, allowing us to examine the general effect a secondary set of vortices has on the region of neutral stability. The axial strength and decay parameters are, as before, set to unity.

We have endeavoured to find those neutral stability curves which exhibit the lowest critical Reynolds numbers for each set of parameters explored. Due to limitations in the iterative process, some modes that clearly cross the neutral axis at certain wave-numbers are not able to be tracked at others. Further to this, we believe that the sets of individual eigenvalues predominantly situated at low Reynolds numbers and higher growth rates are artefacts of the numerical scheme and are spurious. We also see examples where well structured modes suddenly stop or start. These are unlikely to be spurious as they persist through several steps of the wave-number, but rather require a much smaller Reynolds number resolution to obtain the detail between the current Reynolds number step size. Therefore, the curves shown are for modes where we could obtain a smooth and continuous curve.

6.8.1 The Swirl $q = 1.0$

Figure 6.7 shows the growth rates of eight modes situated near the neutral axis for $\alpha = 0.5, 0.6, 0.7, 0.8, 0.9, 1.0$ and $5 \leq Re < 500$ as labelled. Clearly, there are several distinct modal patterns that, in the sense of this global two-dimensional analysis, are categorised by the magnitude of their imaginary components. It can be seen that in several regions of Re, a transition from stable to unstable is observed. By dividing the $\alpha - Re$ domain into discrete 'slices' of α and varying Re we can build up a complete stability map of the vortex problem for a given set of parameters. Only a single slice is shown in each plot though, as clarity is lost when several modes at every α step are shown on the same diagram.

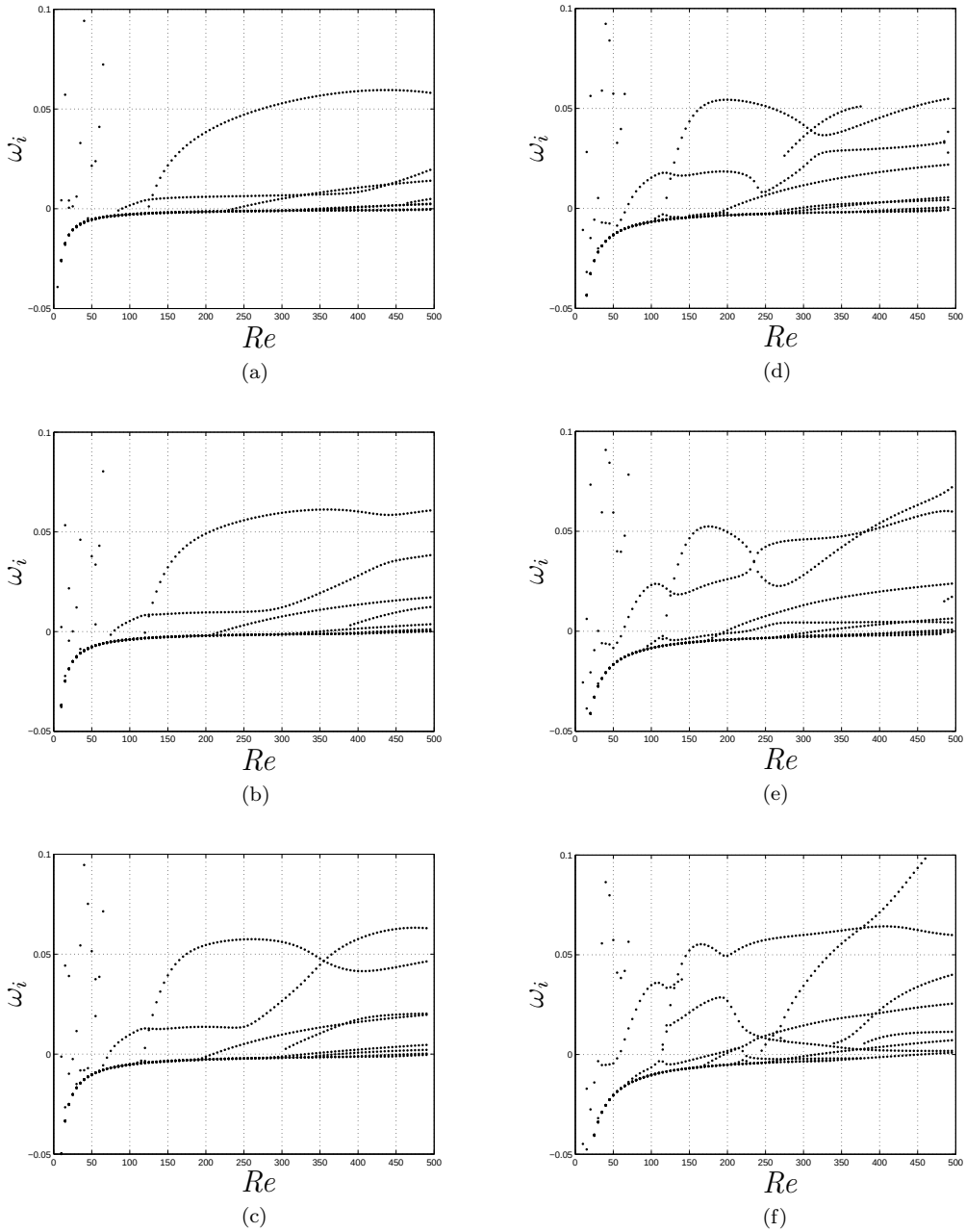

Figure 6.7: The growth rates of eight modes near the neutral axis for a two-vortex configuration with $q = 1.0$ recovered using a two-dimensional global analysis. (a) $\alpha = 0.5$, (b) $\alpha = 0.6$, (c) $\alpha = 0.7$, (d) $\alpha = 0.8$, (e) $\alpha = 0.9$, (f) $\alpha = 1.0$.

If we focus our attention near $Re \approx 200$ and $Re \approx 320$ as shown in closer detail in figure 6.8 for $\alpha = 1.0$, we can see that two of the 'smoother' modal structures become unstable as Re is increased. The notation A and B is consistently used throughout the following plots. We can 'manually' track these particular modes over the range of α, distinguishing the mode being tracked from others when two become very close

by considering the value of the real part of the eigenvalue. By refining the Reynolds number we can determine the critical Reynolds number for which $\omega_i \leq 10^{-6}$ (thus ensuring that the maximum error in the $Re - \alpha$ position of the neutral curve is that of the numerical scheme itself as described earlier) and deem this to be a point on the neutral curve. Note that this is the limit of the accuracy of our scheme as detailed in section 6.5. Examining ω_r at each α-step allows us to be confident we are tracking the same mode. Admittedly, this process is labour intensive but as we are working in regions that have been shown to converge at lower grid resolutions, the time taken is more acceptable than would otherwise be the case if we had to perform the iterations at maximum available resolution.

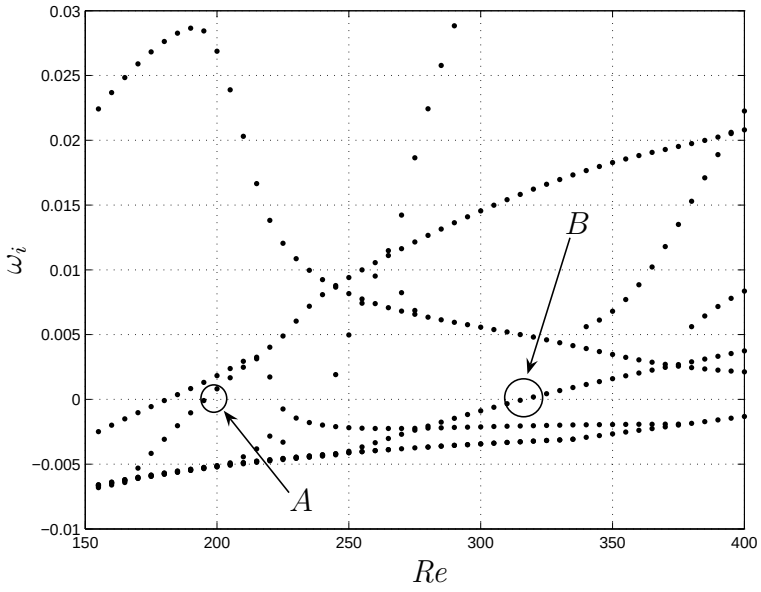

Figure 6.8: The growth rates of eight modes near the neutral axis for a two-vortex configuration at $\alpha = 1.0$ recovered using a two-dimensional global analysis.

Two curves generated in this way, representing the neutral stability of the two-vortex system, can be seen in figure 6.9 corresponding to the two modes in figure 6.8; the corresponding wave-speeds are given in 6.10. Whilst there are many more modes relating to the eigenvalues at each $\alpha - Re$ step, the ones given were the clearest found using the process described. We can see that they are distinct modes that, at these parameters, exhibit a critical Reynolds number that is significantly

higher than has been found for a single Batchelor vortex at similar parameters (see refs [37, 56] among others) whilst remaining in a similar region of α.

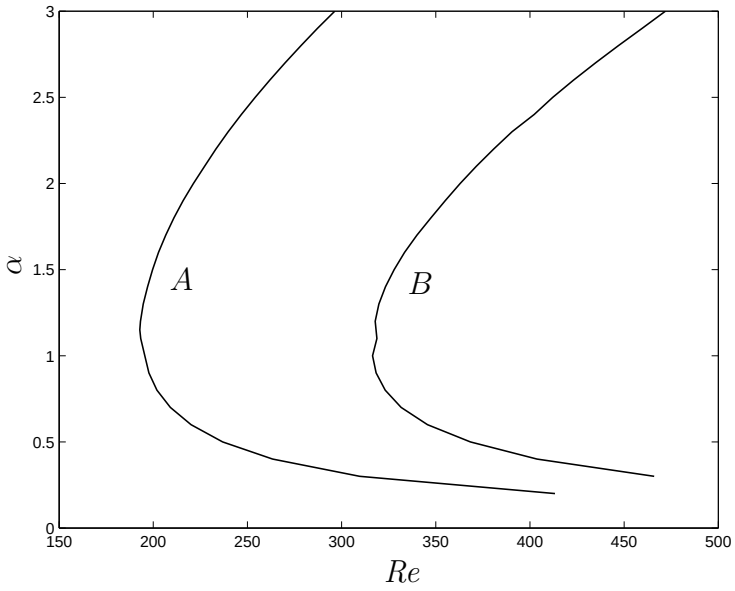

Figure 6.9: Curves of neutral stability for a viscous two-vortex system, $q = 1$, found using the same parameters as used in the two-vortex inviscid analysis.

We were unable to track the curves below $\alpha \approx 0.2$ but from figure 6.9, the curves appear to asymptote towards $\alpha \approx 0.15$. It is interesting to examine the behaviour of the curves as α is increased beyond the critical Reynolds number (upper branch). Compared to published neutral stability curves for a single Batchelor vortex, the two-vortex curves span a much larger range of α. We can speculate that this is due to the increased instability of a two-vortex system over the single vortex case, however, it should also be noted that ω_r is increasing beyond the range where we can be confident that our numerical scheme has converged for the resolution used as detailed in section 3.7.3.

We choose to examine several further values of swirl, chosen due to their significance in the stability of an isolated Batchelor vortex. The values chosen are to be the upper neutral limits of $q = \sqrt{2}$ as found by Stewartson and Brown [57] and later by Denier and Stott [13], and $q = 2.31$ as found recently by Heaton [24]. These values were obtained from an inviscid analysis.

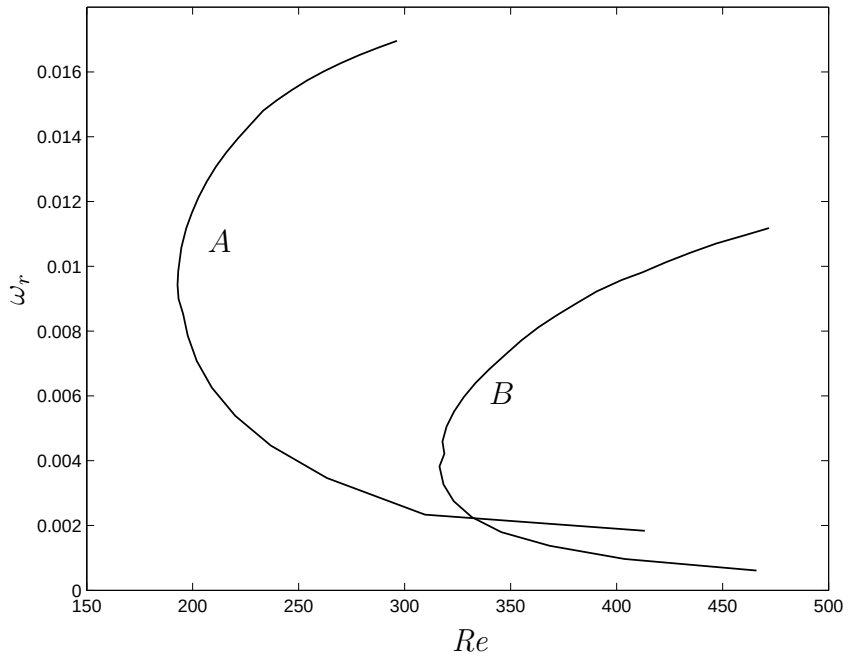

Figure 6.10: Curves of ω_r vs Re for a viscous two-vortex system with $q = 1$, found using the same parameters as used in the two-vortex inviscid analysis.

6.8.2 The Swirl $q = \sqrt{2}$

In what follows we set the swirl parameter to $q = \sqrt{2}$. Figure 6.11 displays the eight least stable modes from which we can see a more consistent pattern of modes than is found in figure 6.7, all following a similar shape and relatively closely spaced. For our analysis, we chose to follow the mode that appears as the second least stable over most of the domain shown and crosses the neutral axis at $Re \approx 130$ as illustrated more clearly in figure 6.12, marked as A.

We can see from figure 6.13 that the curve formed is smooth and continuous throughout the wave-numbers displayed. We find the critical Reynolds number to be at $\alpha \approx 1.2$ on the nose of the curve. Similarly to the previous case, we encounter problems tracking the curve as it approaches a constant wave-number in the lower branch. This is emphasised in figure 6.14, the plot of ω_r, from which we can see at a Reynolds number of approximately 130 the curve appears to diverge. We could speculate that this is due to mode crossing, however, we do not recover a second eigenvalue with a similar wave-speed at this point.

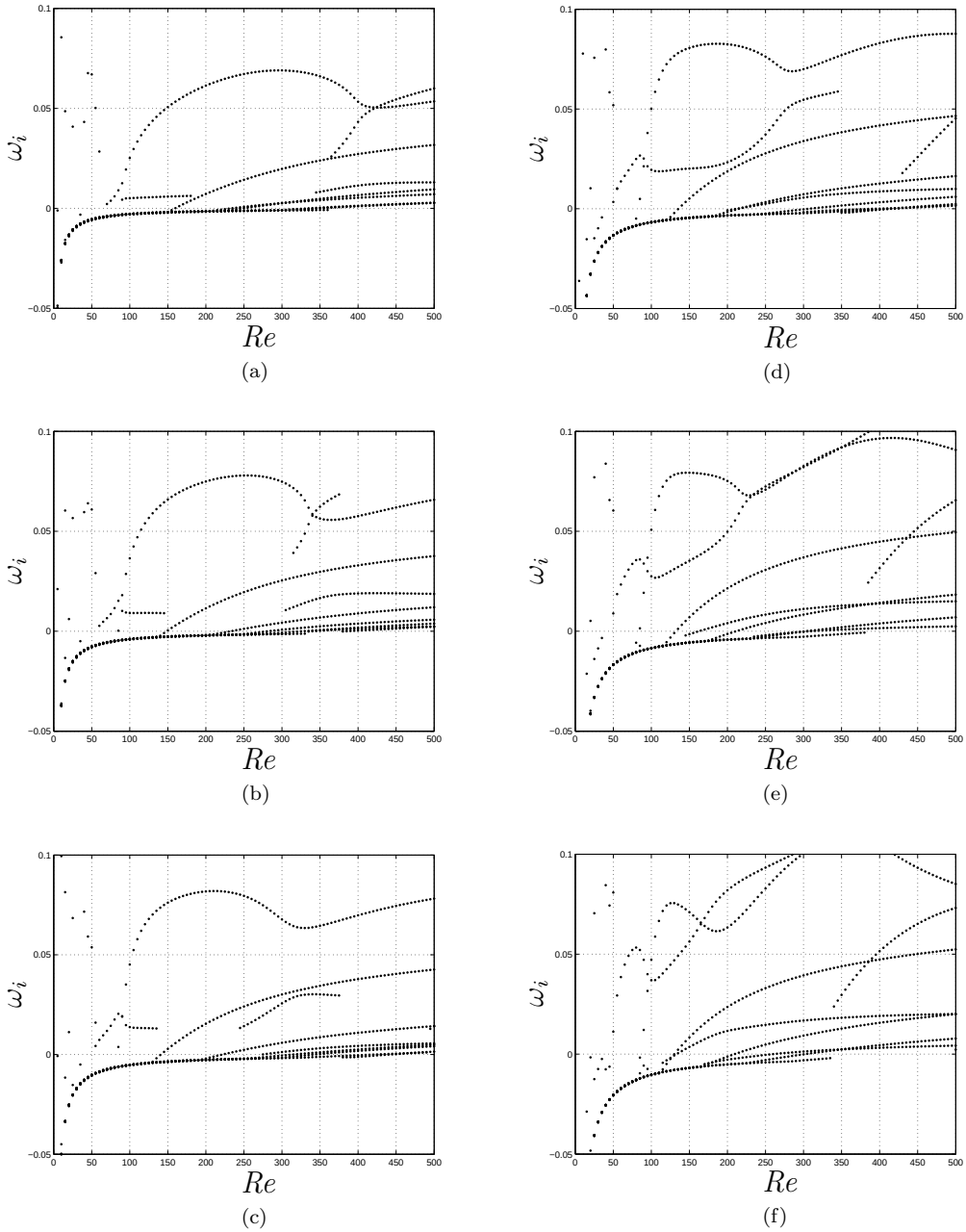

Figure 6.11: The growth rates of eight modes near the neutral axis for a two-vortex configuration with $q = \sqrt{2}$ recovered using a two-dimensional global analysis. (a) $\alpha = 0.5$, (b) $\alpha = 0.6$, (c) $\alpha = 0.7$, (d) $\alpha = 0.8$, (e) $\alpha = 0.9$, (f) $\alpha = 1.0$.

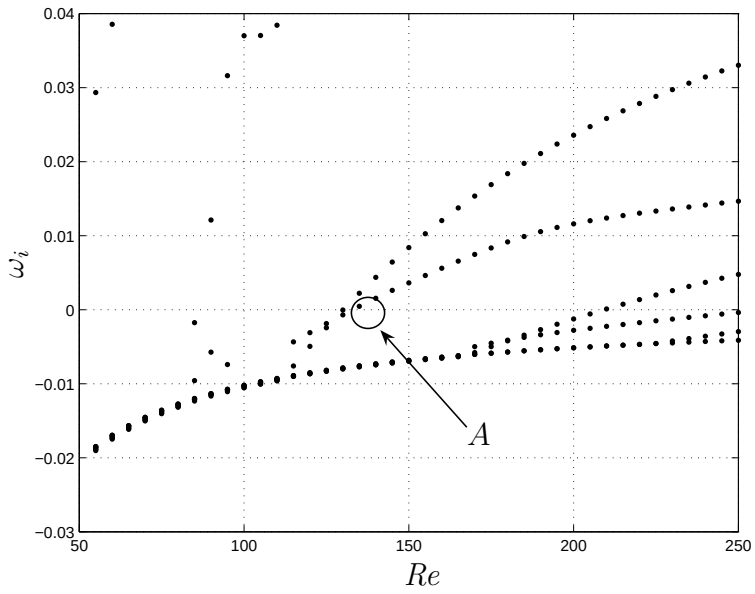

Figure 6.12: The growth rates of eight modes near the neutral axis for a two-vortex configuration with $q = \sqrt{2}$ at $\alpha = 1.0$ recovered using a two-dimensional global analysis.

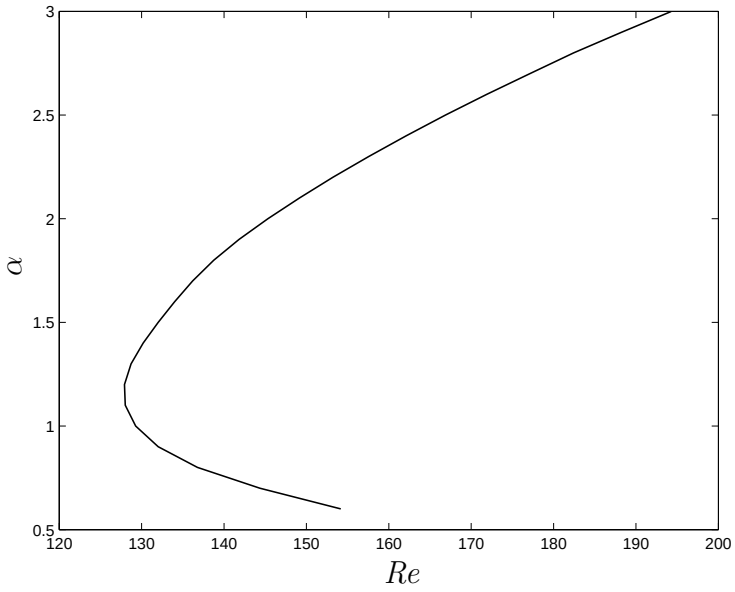

Figure 6.13: A curve of neutral stability for a viscous two-vortex system with $q = \sqrt{2}$, found using the same parameters as used in the two-vortex inviscid analysis.

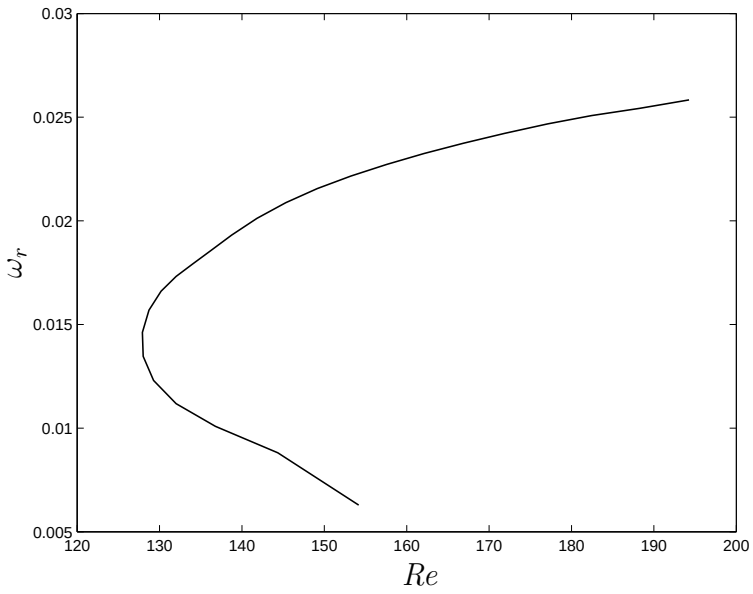

Figure 6.14: A curve of ω_r vs Re for a viscous two-vortex system, $q = \sqrt{2}$, found using the same parameters as used in the two-vortex inviscid analysis.

6.8.3 The Swirl $q = 2.31$

As the swirl number is increased from $\sqrt{2}$ to 2.31, we can see that the growth rates of the least stable modes (figure 6.15) are very similar, consisting of a distinct dominant mode that appears to have a rapid transition through neutral stability, followed by one or two well defined modes with the rest being very similar and located near the neutral axis.

As before we choose to follow the unstable mode that crosses the neutral axis at $Re \approx 120$ when $\alpha = 1.0$, marked A in figure 6.16, due to it being well defined about the neutral axis. However, figure 6.17 shows a region just above the nose of the curve where the curve fails to maintain a smooth form, a feature also exhibited in the real component, figure 6.18. This behaviour is quite unexpected as we find only one distinct near-neutral mode at each $\alpha - Re$ combination. We believe this is more likely due to the numerical limitations alluded to earlier although the general shape of the curve is not adversely affected. Unlike the case where $q = \sqrt{2}$, however, at lower wave-numbers we see a continuous smooth transition towards a constant value in both the real and imaginary components of ω.

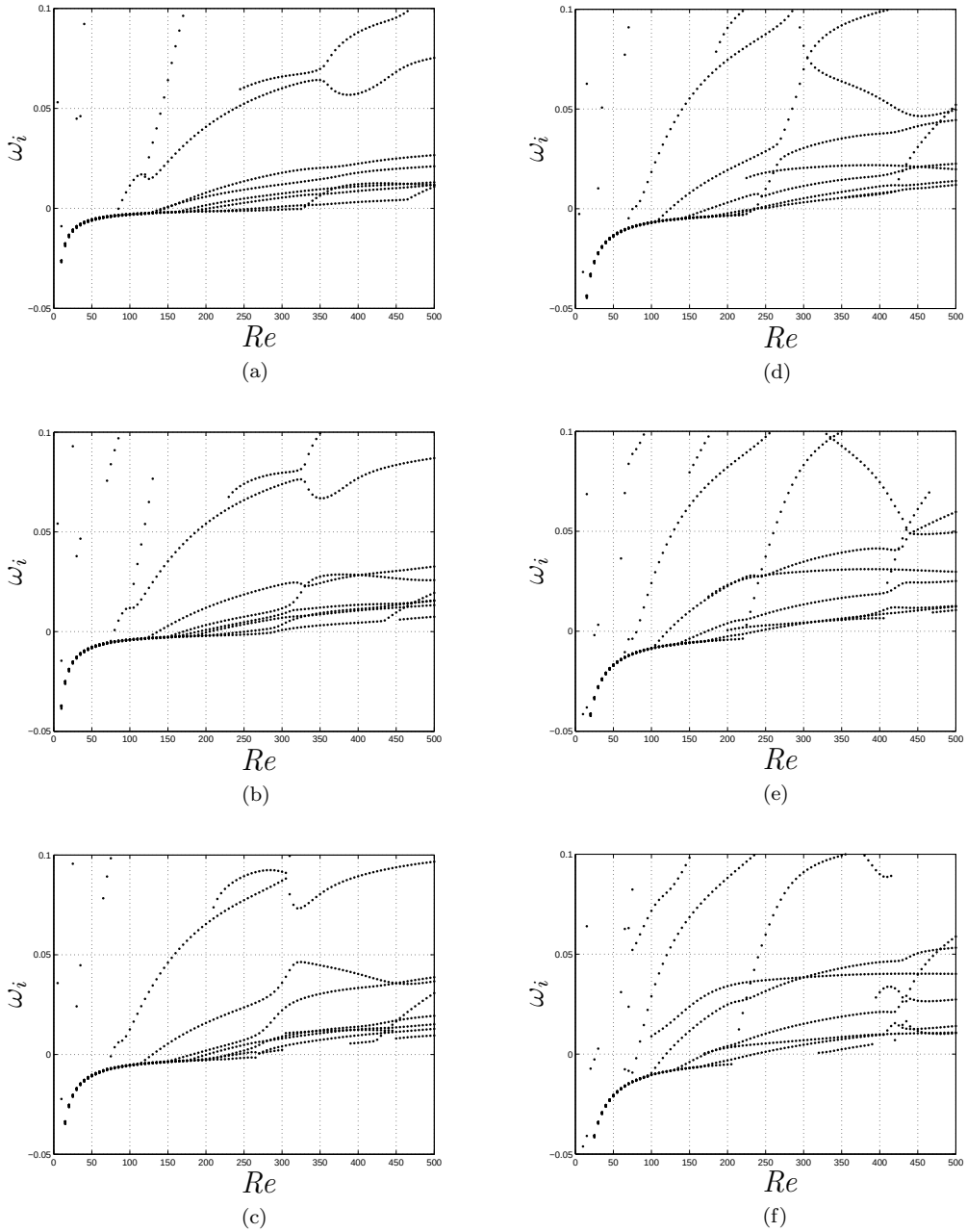

Figure 6.15: The growth rates of eight modes near the neutral axis for a two-vortex configuration with $q = 2.31$ recovered using a two-dimensional global analysis. (a) $\alpha = 0.5$, (b) $\alpha = 0.6$, (c) $\alpha = 0.7$, (d) $\alpha = 0.8$, (e) $\alpha = 0.9$, (f) $\alpha = 1.0$.

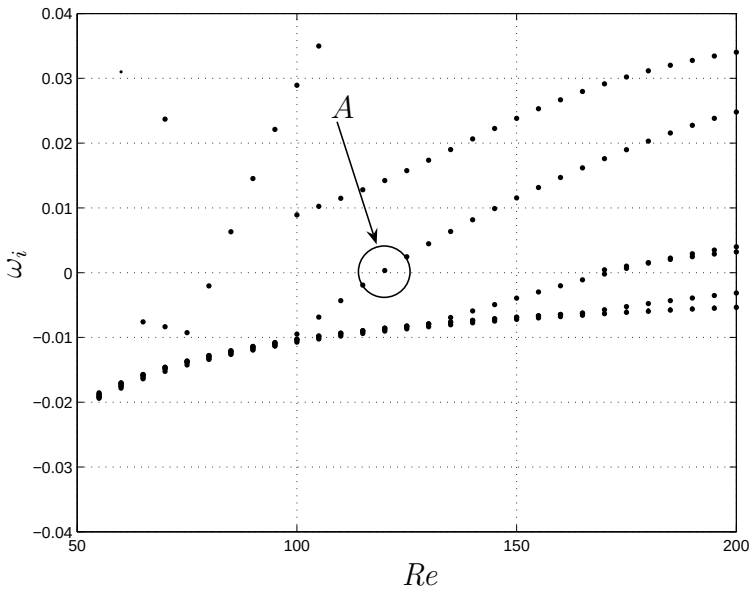

Figure 6.16: The growth rates of eight modes near the neutral axis for a two-vortex configuration with $q = 2.31$ at $\alpha = 1.0$ recovered using a two-dimensional global analysis.

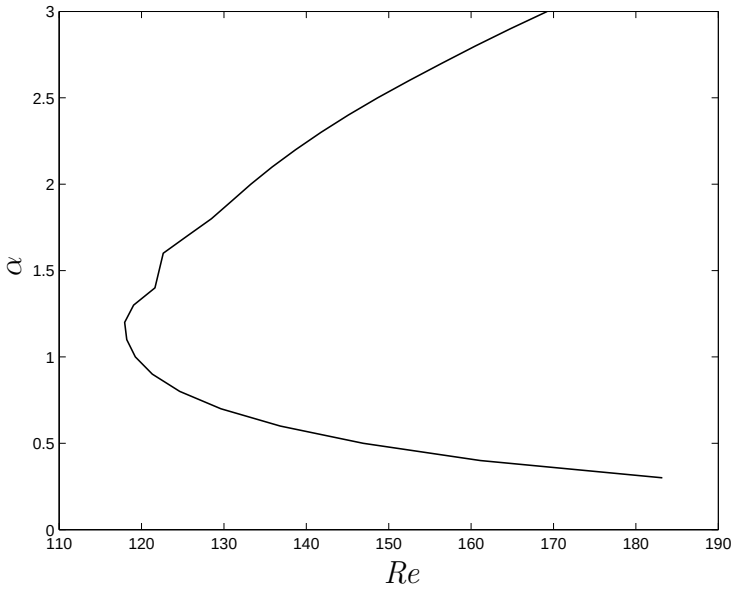

Figure 6.17: A curve of neutral stability for a viscous two-vortex system with $q = 2.31$, found using the same parameters as used in the two-vortex inviscid analysis.

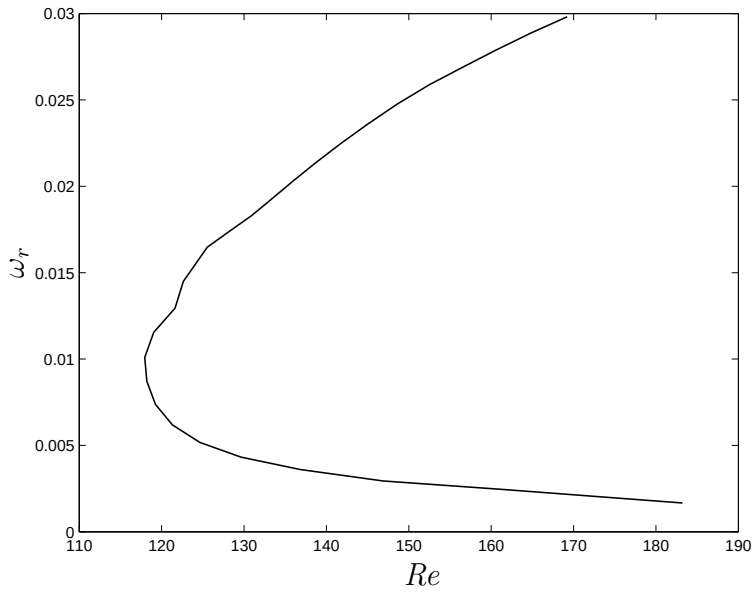

Figure 6.18: A curve of ω_r vs Re for a viscous two-vortex system, $q = 2.31$, found using the same parameters as used in the two-vortex inviscid analysis.

6.8.4 The Swirl $q = 2.31$, with $y = 0.8$

In our inviscid analysis, we established that a two-vortex configuration was at its most unstable when the vortex spacing was $y = 0.8$ from the origin. Here we present a neutral curve found using this spacing and a swirl value of $q = 2.31$. In figure 6.19 we can see that the pattern of modes are significantly more localised about the neutral axis than for $y = 2$. Figure 6.20 shows, for $\alpha = 1.0$, a single dominant mode, marked as A, becoming unstable at $Re \approx 160$. Further modes which become unstable at higher Reynolds numbers are generally too close numerically to each-other for this type of 'manual' iteration to be effective.

In figures 6.21 and 6.22 we present plots of the neutral curve and real component of the eigenvalue respectively, for the mode in figure 6.19 that becomes neutrally stable at $Re \approx 160$. If we compare these plots with those for the same value of swirl at $y = 2$ we can see that in figure 6.19 the narrower spacing has the effect of producing a more distinct set of curves which, as the Reynolds number is increased, approach a constant, stable value. At low Reynolds numbers, this stable form can be

seen for both vortex separation distances. We might expect that as the separation distance progressively narrows towards the point where a single, double strength vortex is approximated, the unstable curves seen in figure 6.19 will all become stable at the Reynolds numbers examined here.

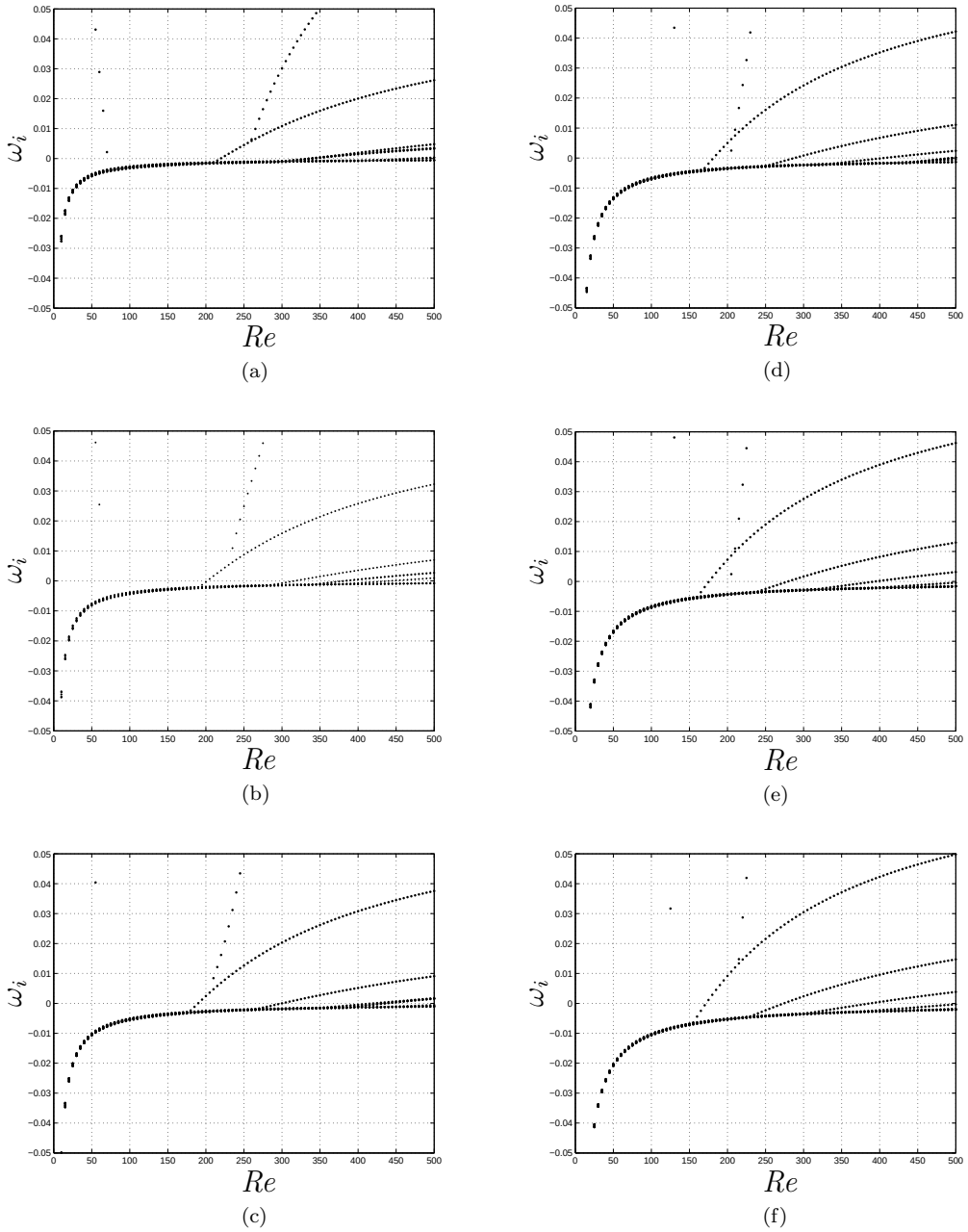

Figure 6.19: The growth rates of eight modes near the neutral axis for a two-vortex configuration with $q = 2.31$ and $y = 0.8$ recovered using a two-dimensional global analysis. (a) $\alpha = 0.5$, (b) $\alpha = 0.6$, (c) $\alpha = 0.7$, (d) $\alpha = 0.8$, (e) $\alpha = 0.9$, (f) $\alpha = 1.0$.

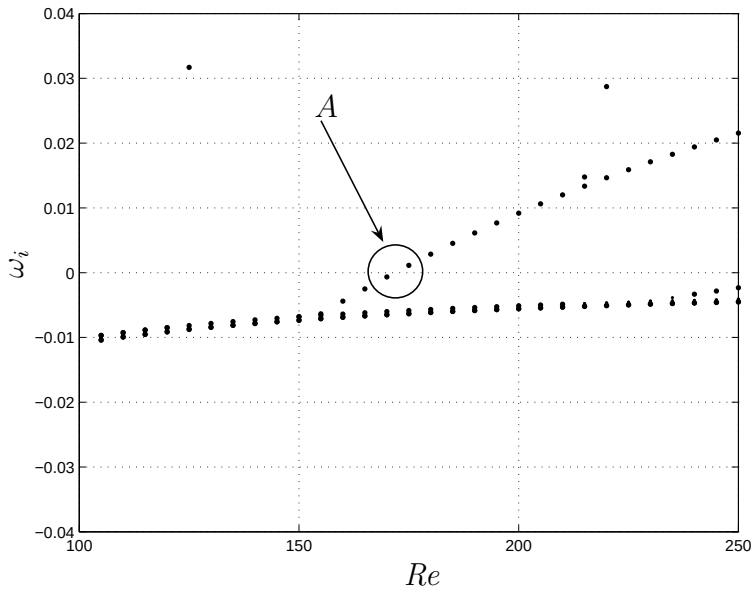

Figure 6.20: The growth rates of eight modes near the neutral axis for a two-vortex configuration with $q = 2.31$ and $y = 0.8$ at $\alpha = 1.0$ recovered using a two-dimensional global analysis.

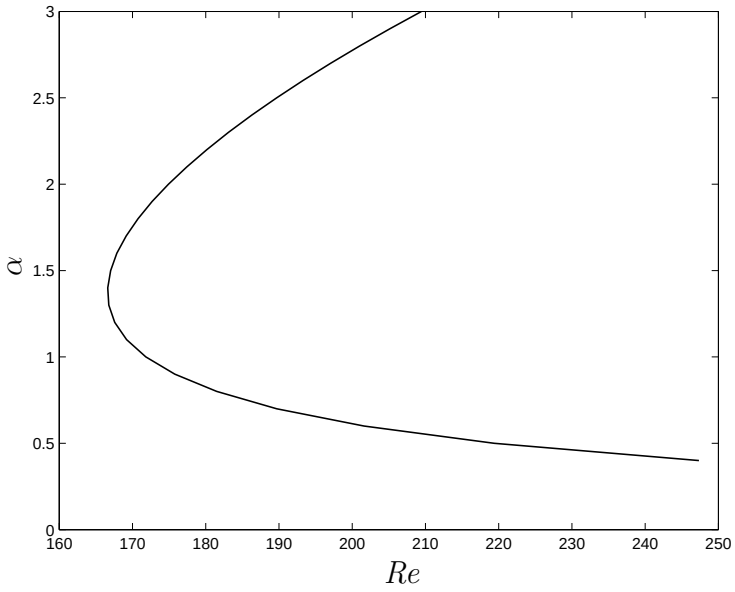

Figure 6.21: A curve of neutral stability for a viscous two-vortex system with $q = 2.31$ anad $y = 0.8$, using the same parameters as the two-vortex inviscid analysis.

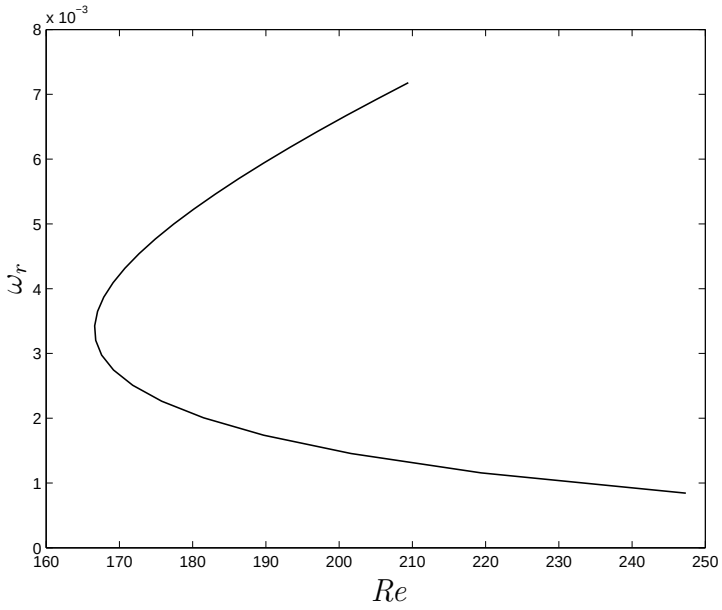

Figure 6.22: A curve of ω_r vs Re for a viscous two-vortex system, $q = 2.31$ and $y = 0.8$, found using the same parameters as used in the two-vortex inviscid analysis.

6.9 Four-Vortex Configuration

We now present curves of neutral stability for a four-vortex configuration with the primary (outboard) vortices being represented by the two-vortex configuration studied previously ($y = 2$). Secondary vortices are placed at $(y_2, z_2) = (0.35, 0)$ as used in the inviscid analysis.

6.9.1 The Swirl $q = 1.0$

Figure 6.23 gives the eight least stable modes recovered close to neutral stability for α as stated. As with the two-vortex case there exist several clearly defined modes that undergo a transition from a state of stability to instability. We then follow the curves belonging to the growth rate curves found at $Re \approx 150$ and 250 highlighted in figure 6.24 as A and B respectively which are given in figures 6.25 and 6.26 for ω_i and ω_r respectively. We can see that from figure 6.25, both curves exhibit critical Reynolds numbers between $1.0 \leq \alpha \leq 1.3$. We see evidence of the

disjointedness experienced in section 6.8.2 for the curve A as we approach lower wave-numbers which can be attributed to numerical difficulties in tracking these modes along the lower branch of the neutral curve. Importantly though, the critical Reynolds numbers for both curves can be ascertained as $Re_{cr} \approx 152.3$ and 250.6 at $\alpha = 1.1$ in both cases.

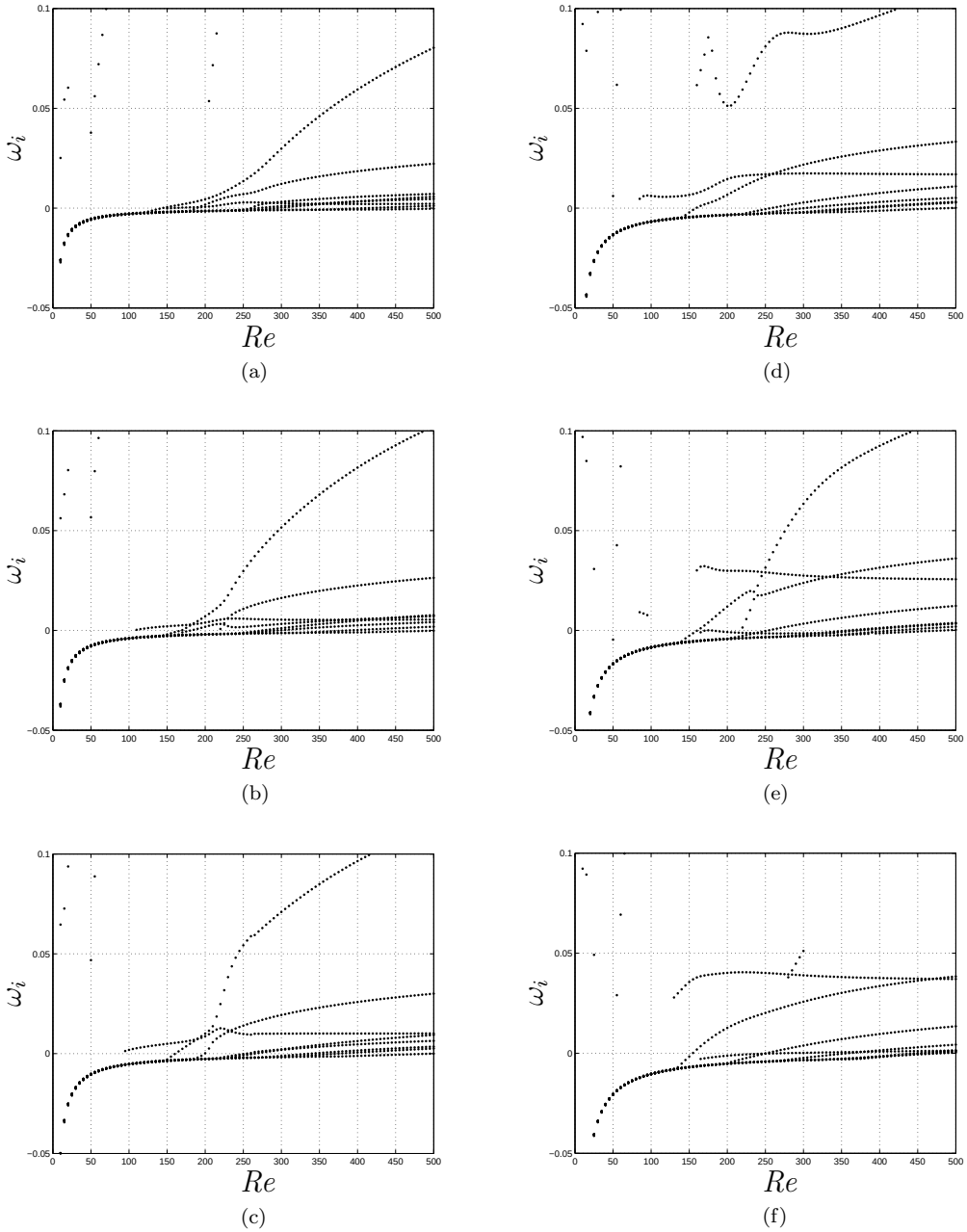

Figure 6.23: The growth rates of eight modes near the neutral axis for a four-vortex configuration with $q = 1.0$ recovered using a two-dimensional global analysis. (a) $\alpha = 0.5$, (b) $\alpha = 0.6$, (c) $\alpha = 0.7$, (d) $\alpha = 0.8$, (e) $\alpha = 0.9$, (f) $\alpha = 1.0$.

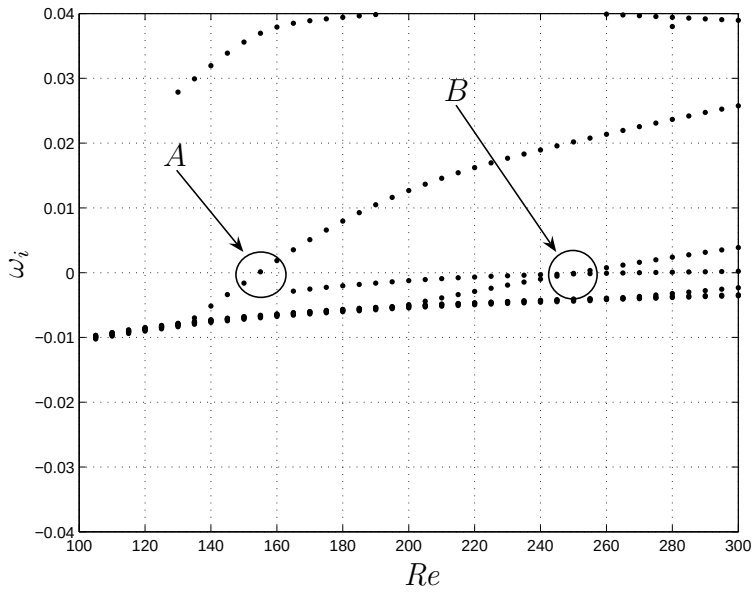

Figure 6.24: The growth rates of eight modes near the neutral axis for a four-vortex configuration with $q = 1.0$ at $\alpha = 1.0$ recovered using a two-dimensional global analysis.

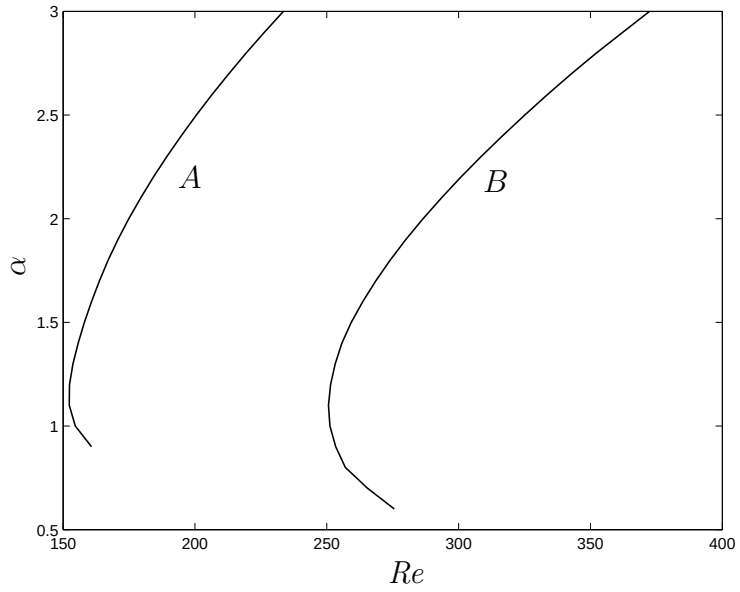

Figure 6.25: Curves of neutral stability for a viscous four-vortex system with $q = 1.0$, found using the same parameters as used in the four-vortex inviscid analysis.

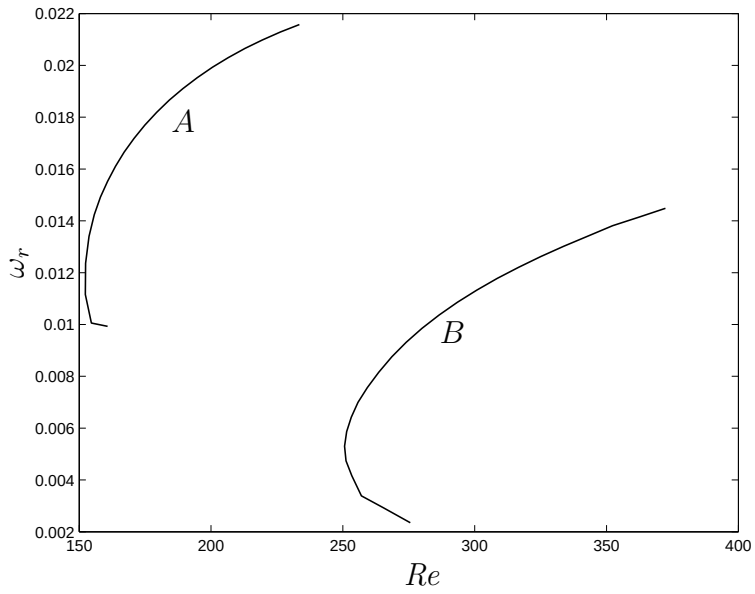

Figure 6.26: Curves of ω_r vs Re for a viscous four-vortex system with $q = 1.0$, found using the same parameters as used in the four-vortex inviscid analysis.

6.9.2 The Swirl $q = \sqrt{2}$

As with the previous analyses, we present the growth rates of the eight least stable modes through $5 \leq Re < 500$ for a number of values of α in figure 6.27 and for $\alpha = 1.0$ in figure 6.28, followed by the neutral curve and curve of ω_r for the first continuous mode that crosses the neutral axis. In figure 6.28 this can be seen to cross $\omega_i = 0$ at $Re \approx 105$.

From figure 6.29 we can obtain a critical Reynolds number at $\alpha \approx 1.25$ with the lower portion of the curve approaching a constant value. It is probable that, from the disjointed nature of the curve at $Re \approx 130$ on the lower branch (noting the similarity between this and the two-vortex case for $q = \sqrt{2}$ in section 6.8.2), a smaller α step size would be better suited to resolve the lower branch of the neutral curve.

If we then compare the neutral curve plots for the two-vortex case (figure 6.13) with that of the four-vortex configuration for $q = \sqrt{2}$ (figure 6.29) we can see that the shape of the curves are very similar and that the secondary vortices in the four-vortex configuration has the effect of lowering the critical Reynolds number slightly.

The real components of the eigenvalues are of a similar magnitude in both the two and four-vortex configurations which leads us to believe that we are seeing the effects of including a secondary set of vortices on the four-vortex neutral curve and not just an altogether different mode.

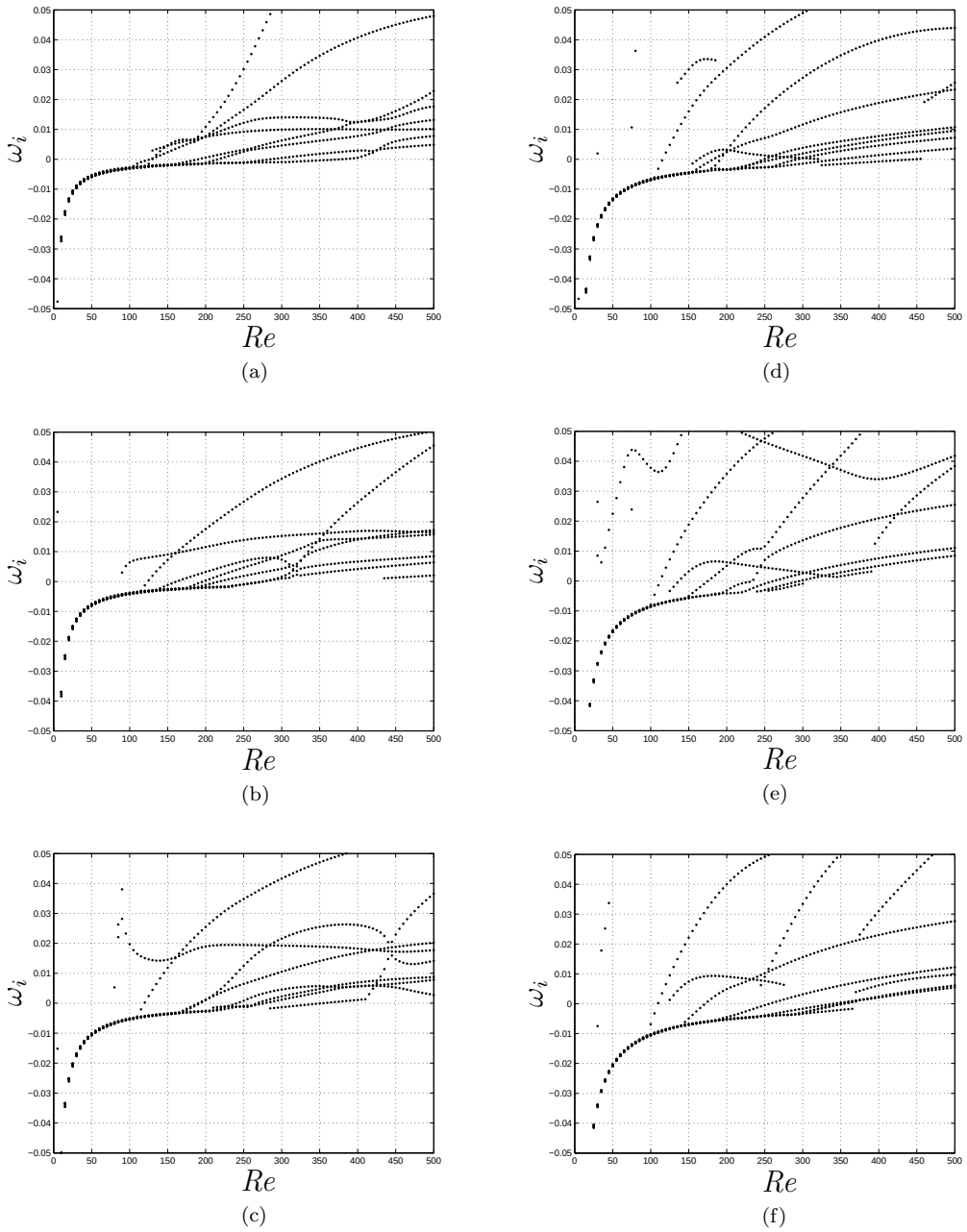

Figure 6.27: The growth rates of eight modes near the neutral axis for a four-vortex configuration with $q = \sqrt{2}$ recovered using a two-dimensional global analysis. (a) $\alpha = 0.5$, (b) $\alpha = 0.6$, (c) $\alpha = 0.7$, (d) $\alpha = 0.8$, (e) $\alpha = 0.9$, (f) $\alpha = 1.0$.

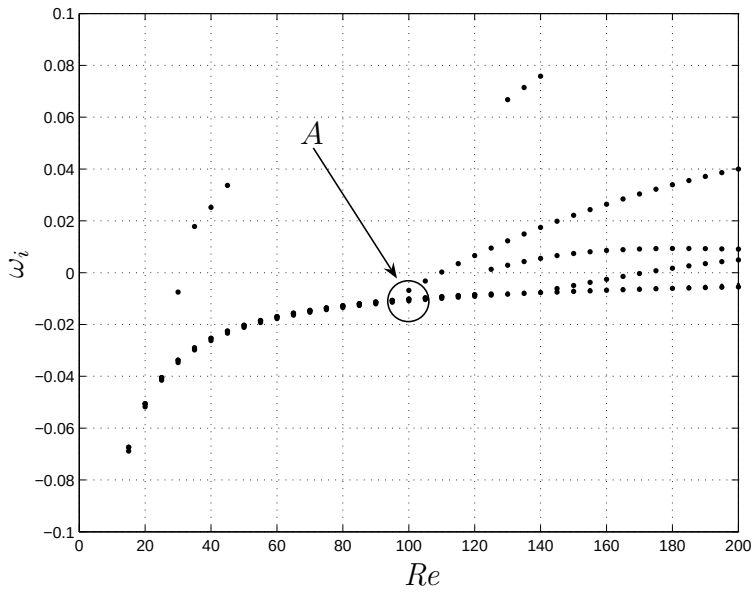

Figure 6.28: The growth rates of eight modes near the neutral axis for a four-vortex configuration with $q = \sqrt{2}$ at $\alpha = 1.0$ recovered using a two-dimensional global analysis.

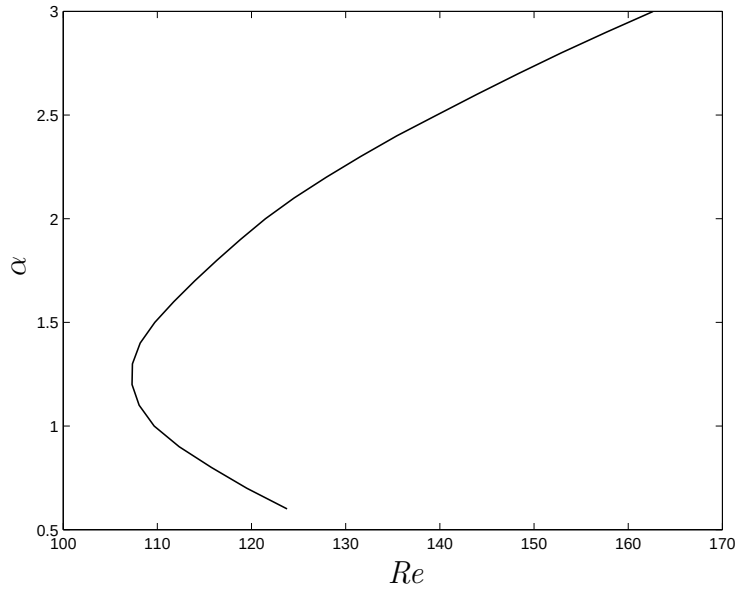

Figure 6.29: Curves of neutral stability for a viscous four-vortex system with $q = \sqrt{2}$, found using the same parameters as used in the four-vortex inviscid analysis.

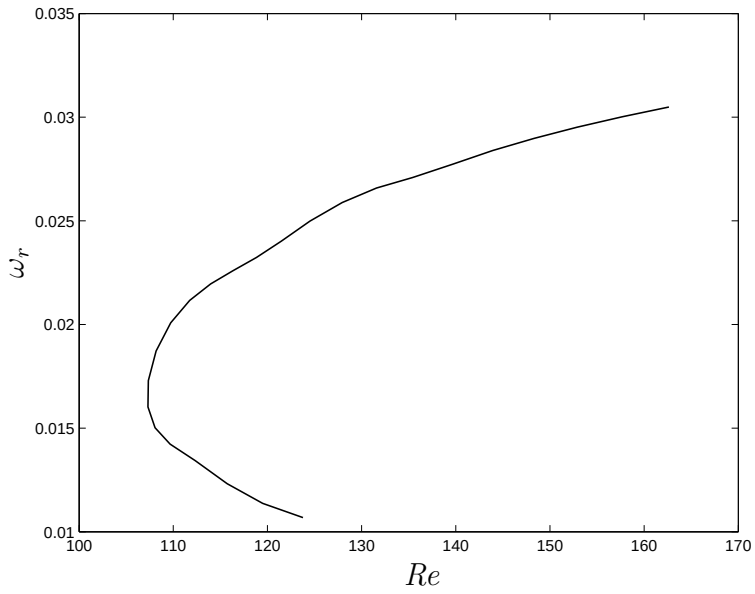

Figure 6.30: Curves of ω_r vs Re for a viscous four-vortex system with $q = \sqrt{2}$, found using the same parameters as used in the four-vortex inviscid analysis.

6.10 Conclusions

We have utilised a two-dimensional, global numerical scheme that has been shown to be accurate near the neutral stability limit, however, computational limitations mean that large global studies such as those presented here have to be performed at a lower resolution for them to be feasible in terms of computational time. The results presented allow us to identify some general trends in the stability of multiple vortex configurations. These facts notwithstanding, the curves of neutral stability produced herein are expected to be a good representation of the true form and provide a useful insight into the viscous stability of multiple tip vortices.

The introduction of a second pair of vortices modifies the stability characteristics of the flow by appearing to lower the critical Reynolds number of the first trackable mode. We also see that for $q = 1$, the four-vortex case produces curves whose nose is spread over a greater range of α but are less defined for lower wave-numbers as opposed to the well defined two-vortex curves at low α. For $q = \sqrt{2}$, the curves of the two and four-vortex configurations are quite similar in form yet the four-

vortex curve still displays a lower Re_{cr}. Our results indicate that a second pair of vortices has a destabilising effect whose influence will depend on the spacing of the secondary vortex pair and the value of swirl (the lower the swirl, the more the flow is destabilised as seen by the larger range of α).

Chapter 7

Concluding Remarks

This study has aimed to provide a comprehensive description of the linear stability analysis of multiple component axial and swirling flows, primarily the wing-tip vortex problem as modelled using the classical Batchelor (or q) vortex. The results presented are for this category of basic flow, however, the methods used are not restricted to this case and can readily be applied to many different forms of steady flow (such as the pipe Hagen-Poiseuille flow used to verify the codes) over a closed domain where the shape and focus of the discretisation grid can be controlled by applying an appropriate grid transformation algorithm.

Results have been presented that outline particular vortex configurations and parameters that are effective at increasing the system instability as in the inviscid case, that explain what happens to these instabilities as the aircraft speed increases and also where the transition from stable to unstable occurs for particular viscous modes. But where do these results fit into the overall wake vortex hazard problem?

It was stated in the introduction that no single piece of research will be the defining solution to this particular problem, the preceding study is no exception to this, however, in terms of an inviscid analysis we have identified a set of parameters that will lead to faster vortex dissipation. Until now, two-dimensional global studies of viscous instabilities in a vortex flow have been limited to either a single Batchelor vortex or simply the recovery of the eigenspectra of multiple vortex configurations. Our work is the first to produce a series of curves of neutral stability for the multiple vortex case using a two-dimensional global approach and as such provide predictions

for the critical Reynolds number of such flows.

In light of the previous comments, several recommendations to the progression of this work can be made. It would be of great interest to attempt to reproduce some of the results experimentally, the nature of the inviscid basic flow lends itself to replication by experimentalists. Whilst it would be difficult to obtain specific stability values, observing the transition to turbulence of various configurations of vortices would be more straight forward. In terms of the viscous stability analysis presented here, it would be useful to produce a full range of neutral stability curves for the multiple vortex configurations and, as has been done extensively for a single Batchelor vortex, explore the values of swirl for which the flow remains unstable. The results of this study indicate that it is much higher than for a single vortex. Perhaps though, the most important future development in terms of the numerical treatment of the wake vortex problem will be the improvement in computational techniques and resources to allow for much larger, more accurate viscous stability studies to be undertaken in more realistic time-frames.

Appendix A

A.1 Constructing Two-dimensional Differentiation Matrices

Using the one-dimensional differentiation matrices derived for both the 'local' and 'global' codes, a two-dimensional differentiation matrix can now be constructed which will allow the discretisation of the governing equation. Figure A.1 illustrates a simplified discretised domain.

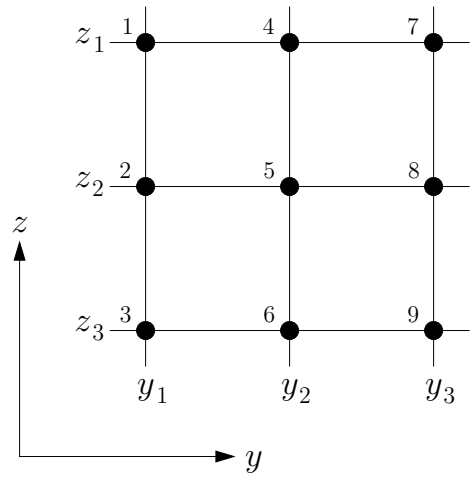

Figure A.1: Example of a small two-dimensional discretised domain

Suppose an appropriate differentiation matrix for the above domain in both the y and the z directions is;

$$D = \begin{bmatrix} a & 0 & 0 \\ 0 & b & 0 \\ 0 & 0 & c \end{bmatrix}.$$

It is convenient to order the values at each grid point as a vector of N_y block rows with each column containing N_z entries. The vector P will then be

$$P = \left[\begin{array}{c} 1 \\ 2 \\ 3 \\ \hline 4 \\ 5 \\ 6 \\ \hline 7 \\ 8 \\ 9 \end{array}\right].$$

In the one-dimensional case, the differentiation matrices act as follow

$$\begin{bmatrix} a & 0 & 0 \\ 0 & b & 0 \\ 0 & 0 & c \end{bmatrix} \begin{bmatrix} y_1 \\ y_2 \\ y_3 \end{bmatrix} \text{ and } \begin{bmatrix} a & 0 & 0 \\ 0 & b & 0 \\ 0 & 0 & c \end{bmatrix} \begin{bmatrix} z_1 \\ z_2 \\ z_3 \end{bmatrix}.$$

So, in the two-dimensional case, the one-dimensional differentiation matrix with respect to y is written as

$$D_y^{(2D)} = D_y \otimes I_z = \left[\begin{array}{ccc|ccc|ccc} a_y & & & & & & & & \\ & a_y & & & 0 & & & 0 & \\ & & a_y & & & & & & \\ \hline & & & b_y & & & & & \\ & 0 & & & b_y & & & 0 & \\ & & & & & b_y & & & \\ \hline & & & & & & c_y & & \\ & 0 & & & 0 & & & c_y & \\ & & & & & & & & c_y \end{array}\right] \left[\begin{array}{c} 1 \\ 2 \\ 3 \\ \hline 4 \\ 5 \\ 6 \\ \hline 7 \\ 8 \\ 9 \end{array}\right] \begin{array}{l} \left.\begin{array}{c} \\ \\ \\ \end{array}\right\} (y_1) \\ \left.\begin{array}{c} \\ \\ \\ \end{array}\right\} (y_2) \\ \left.\begin{array}{c} \\ \\ \\ \end{array}\right\} (y_3) \end{array}$$

and with respect to z

$$D_z^{(2D)} = I_y \otimes D_z = \left[\begin{array}{ccc|ccc|ccc} a_z & & & & & & & & \\ & b_z & & 0 & & & 0 & & \\ & & c_z & & & & & & \\ \hline & & & a_z & & & & & \\ 0 & & & & b_z & & 0 & & \\ & & & & & c_z & & & \\ \hline & & & & & & a_z & & \\ 0 & & & 0 & & & & b_z & \\ & & & & & & & & c_z \end{array}\right] \left[\begin{array}{c} 1 \\ 2 \\ 3 \\ \hline 4 \\ 5 \\ 6 \\ \hline 7 \\ 8 \\ 9 \end{array}\right] \begin{array}{l} (z_1) \\ (z_2) \\ (z_3) \\ (z_1) \\ (z_2) \\ (z_3) \\ (z_1) \\ (z_2) \\ (z_3) \end{array}$$

where $\otimes$ defines the Kronecker tensor product. Therefore, to construct our two-dimensional differentiation matrix we combine the directional two-dimensional matrices such that,

$$D^{(2D)} = D_y^{(2D)} + D_z^{(2D)} = (D_y \otimes I_z) + (I_y \otimes D_z),$$

and similarly for higher order derivatives.

Appendix B

B.1 Derivation of Two-parameter Viscous Eigenvalue Problem

B.1.1 Cartesian Co-ordinates

Starting with equations (2.2.26) – (2.2.29), the reduced governing equations in their complete form are

$$\mathrm{i}\alpha U_p + \frac{\partial V_p}{\partial y} + \frac{\partial W_p}{\partial z} = 0, \tag{B-1}$$

$$\begin{aligned} \mathrm{i}\alpha(U-c)U_p + V_p\frac{\partial U}{\partial y} &+ W_p\frac{\partial U}{\partial z} + V\frac{\partial U_p}{\partial y} + W\frac{\partial U_p}{\partial z} \\ &= -\mathrm{i}\alpha P_p + \frac{1}{Re}\left(-\alpha^2 U_p + \frac{\partial^2 U_p}{\partial y^2} + \frac{\partial U_p}{\partial z^2}\right), \end{aligned} \tag{B-2}$$

$$\begin{aligned} \mathrm{i}\alpha(U-c)V_p + V_p\frac{\partial V}{\partial y} &+ W_p\frac{\partial V}{\partial z} + V\frac{\partial V_p}{\partial y} + W\frac{\partial V_p}{\partial z} \\ &= -\frac{\partial P_p}{\partial y} + \frac{1}{Re}\left(-\alpha^2 V_p + \frac{\partial^2 V_p}{\partial y^2} + \frac{\partial V_p}{\partial z^2}\right), \end{aligned} \tag{B-3}$$

$$\begin{aligned} \mathrm{i}\alpha(U-c)W_p + V_p\frac{\partial W}{\partial y} &+ W_p\frac{\partial W}{\partial z} + V\frac{\partial W_p}{\partial y} + W\frac{\partial W_p}{\partial z} \\ &= -\frac{\partial P_p}{\partial z} + \frac{1}{Re}\left(-\alpha^2 W_p + \frac{\partial^2 W_p}{\partial y^2} + \frac{\partial W_p}{\partial z^2}\right). \end{aligned} \tag{B-4}$$

Differentiating (B-2) with respect to y yields

$$\begin{aligned} \mathrm{i}\alpha(U-c)\frac{\partial U_p}{\partial y} &+ \mathrm{i}\alpha\frac{\partial U}{\partial y}U_p + \frac{\partial U}{\partial y}\frac{\partial V_p}{\partial y} + \frac{\partial^2 U}{\partial y^2}V_p + \frac{\partial U}{\partial z}\frac{\partial W_p}{\partial y} + \frac{\partial^2 U}{\partial z\partial y}W_p \\ &+ \frac{\partial V}{\partial y}\frac{\partial U_p}{\partial y} + V\frac{\partial^2 U_p}{\partial y^2} + \frac{\partial W}{\partial y}\frac{\partial U_p}{\partial z} + W\frac{\partial^2 U_p}{\partial z\partial y} \\ &= -\mathrm{i}\alpha\frac{\partial P_p}{\partial y} + \frac{1}{Re}\left(-\alpha^2\frac{\partial}{\partial y} + \frac{\partial^3}{\partial y^3} + \frac{\partial^3}{\partial z^2\partial y}\right)U_p, \end{aligned} \tag{B-5}$$

and similarly differentiating (B-2) with respect to z gives

$$\begin{aligned} \mathrm{i}\alpha(U-c)\frac{\partial U_p}{\partial z} &+ \mathrm{i}\alpha\frac{\partial U}{\partial z}U_p + \frac{\partial U}{\partial y}\frac{\partial V_p}{\partial z} + \frac{\partial^2 U}{\partial y \partial z}V_p + \frac{\partial U}{\partial z}\frac{\partial W_p}{\partial z} + \frac{\partial^2 U}{\partial z^2}W_p \\ &+ \frac{\partial V}{\partial z}\frac{\partial U_p}{\partial y} + V\frac{\partial^2 U_p}{\partial y \partial z} + \frac{\partial W}{\partial z}\frac{\partial U_p}{\partial z} + W\frac{\partial^2 U_p}{\partial z^2} \\ &= -\mathrm{i}\alpha\frac{\partial P_p}{\partial z} + \frac{1}{Re}\left(-\alpha^2\frac{\partial}{\partial z} + \frac{\partial^3}{\partial y^2 \partial z} + \frac{\partial^3}{\partial z^3}\right)U_p. \end{aligned} \tag{B-6}$$

Multiplying (B-3) by $\mathrm{i}\alpha$ gives

$$\begin{aligned} -\alpha^2(U-c)V_p &+ \mathrm{i}\alpha\left(\frac{\partial V}{\partial y}V_p + \frac{\partial V}{\partial z}W_p + V\frac{\partial V_p}{\partial y} + W\frac{\partial V_p}{\partial z}\right) \\ &= -\mathrm{i}\alpha\frac{\partial P_p}{\partial y} + \frac{\mathrm{i}\alpha}{Re}\left(-\alpha^2 + \frac{\partial^2}{\partial y^2} + \frac{\partial^2}{\partial z^2}\right)V_p, \end{aligned} \tag{B-7}$$

and similarly multiplying (B-4) by $\mathrm{i}\alpha$ gives

$$\begin{aligned} -\alpha^2(U-c)W_p &+ \mathrm{i}\alpha\left(\frac{\partial W}{\partial y}V_p + \frac{\partial W}{\partial z}W_p + V\frac{\partial W_p}{\partial y} + W\frac{\partial W_p}{\partial z}\right) \\ &= -\mathrm{i}\alpha\frac{\partial P_p}{\partial z} + \frac{\mathrm{i}\alpha}{Re}\left(-\alpha^2 + \frac{\partial^2}{\partial y^2} + \frac{\partial^2}{\partial z^2}\right)W_p. \end{aligned} \tag{B-8}$$

Now, subtracting (B-7) from (B-5) yields

$$\begin{aligned} \mathrm{i}\alpha(U-c)\frac{\partial U_p}{\partial y} &+ \mathrm{i}\alpha\frac{\partial U}{\partial y}U_p + \frac{\partial U}{\partial y}\frac{\partial V_p}{\partial y} + \frac{\partial^2 U}{\partial y^2}V_p + \frac{\partial U}{\partial z}\frac{\partial W_p}{\partial y} + \frac{\partial^2 U}{\partial z \partial y}W_p \\ &+ \frac{\partial V}{\partial y}\frac{\partial U_p}{\partial y} + V\frac{\partial^2 U_p}{\partial y^2} + \frac{\partial W}{\partial y}\frac{\partial U_p}{\partial z} + W\frac{\partial^2 U_p}{\partial z \partial y} + \alpha^2(U-c)V_p \\ &- \mathrm{i}\alpha\left(\frac{\partial V}{\partial y}V_p + \frac{\partial V}{\partial z}W_p + V\frac{\partial V_p}{\partial y} + W\frac{\partial V_p}{\partial z}\right) = \frac{1}{Re}\left(-\alpha^2\frac{\partial}{\partial y}\right. \\ &\left. + \frac{\partial^3}{\partial y^3} + \frac{\partial^3}{\partial z^2 \partial y}\right)U_p - \frac{\mathrm{i}\alpha}{Re}\left(-\alpha^2 + \frac{\partial^2}{\partial y^2} + \frac{\partial^2}{\partial z^2}\right)V_p. \end{aligned} \tag{B-9}$$

From (B-1) we write

$$U_p = -\frac{1}{\mathrm{i}\alpha}\left(\frac{\partial V_p}{\partial y} + \frac{\partial W_p}{\partial z}\right), \tag{B-10}$$

from which we can obtain the following derivatives;

$$\frac{\partial U_p}{\partial y} = -\frac{1}{\mathrm{i}\alpha}\left(\frac{\partial^2 V_p}{\partial y^2} + \frac{\partial^2 W_p}{\partial z \partial y}\right), \tag{B-11}$$

$$\frac{\partial^2 U_p}{\partial y^2} = -\frac{1}{\mathrm{i}\alpha}\left(\frac{\partial^3 V_p}{\partial y^3} + \frac{\partial^3 W_p}{\partial z \partial y^2}\right), \tag{B-12}$$

$$\frac{\partial^3 U_p}{\partial y^3} = -\frac{1}{\mathrm{i}\alpha}\left(\frac{\partial^4 V_p}{\partial y^4} + \frac{\partial^4 W_p}{\partial z \partial y^3}\right), \tag{B-13}$$

$$\frac{\partial^2 U_p}{\partial z \partial y} = -\frac{1}{\mathrm{i}\alpha}\left(\frac{\partial^3 V_p}{\partial y^2 \partial z} + \frac{\partial^3 W_p}{\partial z^2 \partial y}\right), \tag{B-14}$$

$$\frac{\partial^3 U_p}{\partial z^2 \partial y} = -\frac{1}{\mathrm{i}\alpha}\left(\frac{\partial^4 V_p}{\partial y^2 \partial z^2} + \frac{\partial^4 W_p}{\partial z^3 \partial y}\right), \tag{B-15}$$

$$\frac{\partial U_p}{\partial z} = -\frac{1}{\mathrm{i}\alpha}\left(\frac{\partial^2 V_p}{\partial y \partial z} + \frac{\partial^2 W_p}{\partial z^2}\right), \tag{B-16}$$

$$\frac{\partial^2 U_p}{\partial z^2} = -\frac{1}{\mathrm{i}\alpha}\left(\frac{\partial^3 V_p}{\partial y \partial z^2} + \frac{\partial^3 W_p}{\partial z^3}\right), \tag{B-17}$$

$$\frac{\partial^3 U_p}{\partial z^3} = -\frac{1}{\mathrm{i}\alpha}\left(\frac{\partial^4 V_p}{\partial y \partial z^3} + \frac{\partial^4 W_p}{\partial z^4}\right), \tag{B-18}$$

$$\frac{\partial^3 U_p}{\partial y^2 \partial z} = -\frac{1}{\mathrm{i}\alpha}\left(\frac{\partial^4 V_p}{\partial y^3 \partial z} + \frac{\partial^4 W_p}{\partial z^2 \partial y^2}\right). \tag{B-19}$$

Substituting (B-10) – (B-19) into equation (B-9), expanding the $(U - c)$ term and separating the coefficients of V_p and W_p, we are left with the left hand side of the equation in the form

$$\begin{aligned} -U\Bigg(\frac{\partial^2}{\partial y^2} &- \alpha^2\Bigg) V_p + c\left(\frac{\partial^2}{\partial y^2} - \alpha^2\right) V_p + \Bigg\{\frac{\partial^2 U}{\partial y^2} \\ &+ \frac{1}{Re}\left[\frac{1}{\mathrm{i}\alpha}\left(-\alpha^2\frac{\partial^2}{\partial y^2} + \frac{\partial^4}{\partial y^4} + \frac{\partial^4}{\partial y^2 \partial z^2}\right) + \mathrm{i}\alpha\left(-\alpha^2\right.\right. \\ &+ \left.\left.\frac{\partial^2}{\partial y^2} + \frac{\partial^2}{\partial z^2}\right)\right] - \frac{1}{\mathrm{i}\alpha}\left[\frac{\partial V}{\partial y}\frac{\partial^2}{\partial y^2} + V\frac{\partial^3}{\partial y^3} + \frac{\partial W}{\partial y}\frac{\partial^2}{\partial y \partial z}\right. \\ &+ \left. W\frac{\partial^3}{\partial y^2 \partial z}\right] - \mathrm{i}\alpha\left[\frac{\partial V}{\partial y} + V\frac{\partial}{\partial y} + W\frac{\partial}{\partial z}\right]\Bigg\} V_p. \end{aligned} \tag{B-20}$$

Let,

$$A_2 = \left(\frac{\partial^2}{\partial y^2} - \alpha^2\right),$$
$$A_1 = -UA_2 + \{\cdots\}.$$

where $\{\cdots\}$ represents the portion of equation (B-20) that is found between the braces. The right hand side of the equation then becomes

$$\begin{aligned} U\frac{\partial^2 W_p}{\partial z \partial y} &- c\frac{\partial^2 W_p}{\partial z \partial y} + \left\{\frac{\partial U}{\partial y}\frac{\partial}{\partial z} - \frac{\partial U}{\partial z}\frac{\partial}{\partial y} - \frac{\partial^2 U}{\partial z \partial y} - \frac{1}{Re}\left[\frac{1}{\mathrm{i}\alpha}\left(-\alpha^2\frac{\partial^2}{\partial z \partial y}\right.\right.\right. \\ &+ \left.\left.\left.\frac{\partial^4}{\partial z \partial y^3} + \frac{\partial^4}{\partial z^3 \partial y}\right)\right] + \mathrm{i}\alpha\frac{\partial V}{\partial z} + \frac{1}{\mathrm{i}\alpha}\left[\frac{\partial V}{\partial y}\frac{\partial^2}{\partial z \partial y}\right. \\ &+ \left.\left. V\frac{\partial^3}{\partial z \partial y^2} + \frac{\partial W}{\partial y}\frac{\partial^2}{\partial z^2} + W\frac{\partial^3}{\partial z^2 \partial y}\right]\right\} W_p. \end{aligned} \tag{B-21}$$

Let,

$$B_2 = \frac{\partial^2}{\partial z \partial y},$$
$$B_1 = UB_2 + \{\cdots\}.$$

Therefore we can write the final equation as

$$-A_1 V_p + B_1 W_p = c(A_2 V_p + B_2 W_p). \tag{B-22}$$

Similarly subtracting equation (B-8) from (B-6) gives

$$\begin{aligned} \mathrm{i}\alpha(U-c)\frac{\partial U_p}{\partial z} \;+\; & \mathrm{i}\alpha U_p \frac{\partial U}{\partial z} + \frac{\partial V_p}{\partial z}\frac{\partial U}{\partial y} + V_p \frac{\partial^2 U}{\partial y \partial z} + \frac{\partial W_p}{\partial z}\frac{\partial U}{\partial z} + W_p \frac{\partial^2 U}{\partial z^2} \\ & + \frac{\partial V}{\partial z}\frac{\partial U_p}{\partial y} + V\frac{\partial^2 U_p}{\partial y \partial z} + \frac{\partial W}{\partial z}\frac{\partial U_p}{\partial z} + W\frac{\partial^2 U_p}{\partial z^2} + \alpha^2(U-c)W_p \\ & - \mathrm{i}\alpha\left(V_p\frac{\partial W}{\partial y} + W_p\frac{\partial W}{\partial z} + V\frac{\partial W_p}{\partial y} + W\frac{\partial W_p}{\partial z}\right) = \frac{1}{Re}\left(-\alpha^2\frac{\partial}{\partial z}\right. \\ & \left. + \frac{\partial^3}{\partial y^2 \partial z} + \frac{\partial^3}{\partial z^3}\right) U_p - \frac{\mathrm{i}\alpha}{Re}\left(-\alpha^2 + \frac{\partial^2}{\partial y^2} + \frac{\partial^2}{\partial z^2}\right) W_p, \end{aligned} \tag{B-23}$$

where we can substitute expressions for U_p (and the relevant derivatives) into equation (B-23), expanding the $(U-c)$ term and separating the coefficients of V_p and W_p, the left hand side of the equation becomes

$$\begin{aligned} -U\left(\frac{\partial^2}{\partial z^2} - \alpha^2\right) W_p \;+\; & c\left(\frac{\partial^2}{\partial z^2} - \alpha^2\right) W_p + \left\{\frac{\partial^2 U}{\partial z^2} + \frac{1}{Re}\left[\frac{1}{\mathrm{i}\alpha}\left(-\alpha^2\frac{\partial^2}{\partial z^2}\right.\right.\right. \\ & \left.\left.\left. + \frac{\partial^4}{\partial z^4} + \frac{\partial^4}{\partial z^2 \partial y^2}\right) + \mathrm{i}\alpha\left(-\alpha^2 + \frac{\partial^2}{\partial y^2} + \frac{\partial^2}{\partial z^2}\right)\right] \right. \\ & - \frac{1}{\mathrm{i}\alpha}\left[\frac{\partial V}{\partial z}\frac{\partial^2}{\partial z \partial y} + V\frac{\partial^3}{\partial z^2 \partial y} + \frac{\partial W}{\partial z}\frac{\partial^2}{\partial z^2} + W\frac{\partial^3}{\partial z^3}\right] \\ & \left. - \mathrm{i}\alpha\left[\frac{\partial W}{\partial z} + V\frac{\partial}{\partial y} + W\frac{\partial}{\partial z}\right]\right\} W_p. \end{aligned} \tag{B-24}$$

Let,

$$A_4 = \left(\frac{\partial^2}{\partial z^2} - \alpha^2\right),$$
$$A_3 = -UA_4 + \{\cdots\}.$$

and the right hand side,

$$\begin{aligned} U\frac{\partial^2 V_p}{\partial y \partial z} \;-\; & c\frac{\partial^2 V_p}{\partial y \partial z} + \left\{\frac{\partial U}{\partial z}\frac{\partial}{\partial y} - \frac{\partial U}{\partial y}\frac{\partial}{\partial z} - \frac{\partial^2 U}{\partial y \partial z} - \frac{1}{Re}\left[\frac{1}{\mathrm{i}\alpha}\left(-\alpha^2\frac{\partial^2}{\partial y \partial z}\right.\right.\right. \\ & \left.\left.\left. + \frac{\partial^4}{\partial y^3 \partial z} + \frac{\partial^4}{\partial y \partial z^3}\right)\right] + \mathrm{i}\alpha\frac{\partial W}{\partial y} + \frac{1}{\mathrm{i}\alpha}\left[\frac{\partial V}{\partial z}\frac{\partial^2}{\partial y^2}\right. \\ & \left.\left. + V\frac{\partial^3}{\partial y^2 \partial z} + \frac{\partial W}{\partial z}\frac{\partial^2}{\partial y \partial z} + W\frac{\partial^3}{\partial y \partial z^2}\right]\right\} V_p, . \end{aligned} \tag{B-25}$$

Let,

$$B_4 = \frac{\partial^2}{\partial y \partial z},$$
$$B_3 = UB_4 + \{\cdots\}.$$

Therefore we can write

$$A_3 W_p - B_3 V_p = c(-A_4 W_p - B_4 V_p). \tag{B-26}$$

Equations (B-22) and (B-26) can be arranged into a matrix equation to form a Generalised Eigenvalue Problem of the form $\mathbf{Ax} = c\mathbf{Bx}$. The eigenfunctions $\mathbf{x}$ (or $[V_p; W_p]$) can only exist if α and ω are constrained to satisfy the Dispersion Relation, $\mathbf{D}[\alpha, \omega; R] = 0$, where R is some system parameter, such as the Reynolds number. We write

$$\begin{bmatrix} -A_1 & B_1 \\ B_3 & -A_3 \end{bmatrix} \begin{bmatrix} V_p \\ W_p \end{bmatrix} = c \begin{bmatrix} A_2 & B_2 \\ B_4 & A_4 \end{bmatrix} \begin{bmatrix} V_p \\ W_p \end{bmatrix}. \tag{B-27}$$

If we write equations (B-22) and (B-26) in terms of their linear operators

$$(A_1 + cA_2)V_p = (B_1 - cB_2)W_p, \tag{B-28}$$
$$(A_3 + cA_4)W_p = (B_3 - cB_4)V_p, \tag{B-29}$$

our two equations (with the cross-flow components removed) take the form as used by Tatsumi and Yoshimura [61], which can be thought of as a two-dimensional extension of the one-dimensional Orr-Sommerfeld equation. Using the terminology of Tatsumi and Yoshimura [61] we write

$$\mathcal{E}(y, z)V_p = \mathcal{O}(y, z)W_p, \tag{B-30}$$
$$\mathcal{E}(z, y)W_p = \mathcal{O}(z, y)V_p. \tag{B-31}$$

where $\mathcal{E}$ and $\mathcal{O}$ are the linear operators derived previously which under closer examination, are equivalent with the spatial parameters y and z switched.

B.1.2 Cylindrical Polar Co-ordinates

Starting with equations (2.3.12) – (2.3.15) we first differentiate (2.3.15) with respect to r

$$\begin{aligned}\mathrm{i}\alpha(U-c)\frac{\partial U_p}{\partial r} &+ \mathrm{i}\alpha\frac{\partial U}{\partial r}U_p + \frac{1}{r}\frac{\partial W}{\partial r}\frac{\partial U_p}{\partial \theta} - \frac{W}{r^2}\frac{\partial U_p}{\partial \theta} + \frac{W}{r}\frac{\partial^2 U_p}{\partial\theta\partial r}\\ &+ \frac{\partial U}{\partial r}\frac{\partial V_p}{\partial r} + \frac{\partial^2 U}{\partial r^2}V_p + \frac{\partial U}{\partial\theta}\left(\frac{1}{r}\frac{\partial W_p}{\partial r} - \frac{W_p}{r^2}\right)\\ &+ \frac{1}{r}\frac{\partial^2 U}{\partial\theta\partial r}W_p = -\mathrm{i}\alpha\frac{\partial P_p}{\partial r} + \frac{1}{Re}\frac{\partial}{\partial r}\mathcal{Q}(U_p),\end{aligned} \tag{B-32}$$

and differentiate (2.3.15) with respect to θ

$$\begin{aligned}\mathrm{i}\alpha(U-c)\frac{\partial U_p}{\partial \theta} &+ \mathrm{i}\alpha\frac{\partial U}{\partial \theta}U_p + \frac{1}{r}\frac{\partial W}{\partial \theta}\frac{\partial U_p}{\partial \theta} + \frac{W}{r}\frac{\partial^2 U_p}{\partial\theta^2} + \frac{\partial U}{\partial r}\frac{\partial V_p}{\partial \theta}\\ &+ \frac{\partial^2 U}{\partial r\partial\theta}V_p + \frac{1}{r}\frac{\partial U}{\partial\theta}\frac{\partial W_p}{\partial\theta} + \frac{1}{r}\frac{\partial^2 U}{\partial\theta^2}W_p\\ &= -\mathrm{i}\alpha\frac{\partial P_p}{\partial\theta} + \frac{1}{Re}\frac{\partial}{\partial\theta}\mathcal{Q}(U_p).\end{aligned} \tag{B-33}$$

Multiplying (2.3.13) by $\mathrm{i}\alpha$ gives

$$-\alpha^2(U-c)V_p + \frac{\mathrm{i}\alpha W}{r}\frac{\partial V_p}{\partial\theta} = -\mathrm{i}\alpha\frac{\partial P_p}{\partial r} + \frac{\mathrm{i}\alpha}{Re}\mathcal{L}(V_p) - \frac{2\mathrm{i}\alpha}{r^2 Re}\frac{\partial W_p}{\partial\theta}, \tag{B-34}$$

and similarly multiplying (2.3.14) by $\mathrm{i}\alpha r$ gives

$$\begin{aligned}-\alpha^2 r(U-c)W_p &+ \mathrm{i}\alpha\left(W\frac{\partial W_p}{\partial\theta} + r\frac{\partial W}{\partial r}V_p + \frac{\partial W}{\partial\theta}W_p + WV_p\right)\\ &= -\mathrm{i}\alpha\frac{\partial P_p}{\partial\theta} + \frac{\mathrm{i}\alpha r}{Re}\mathcal{L}(W_p) - \frac{2\mathrm{i}\alpha}{rRe}\frac{\partial V_p}{\partial\theta}.\end{aligned} \tag{B-35}$$

Now, if we subtract equation (B-34) from (B-32) we obtain

$$\begin{aligned}\mathrm{i}\alpha(U-c)\frac{\partial U_p}{\partial r} &+ \mathrm{i}\alpha\frac{\partial U}{\partial r}U_p + \left(\frac{1}{r}\frac{\partial W}{\partial r} - \frac{W}{r^2}\right)\frac{\partial U_p}{\partial\theta} + \frac{W}{r}\frac{\partial^2 U_p}{\partial\theta\partial r}\\ &+ \frac{\partial U}{\partial r}\frac{\partial V_p}{\partial r} + \frac{\partial^2 U}{\partial r^2}V_p + \frac{1}{r}\frac{\partial U}{\partial\theta}\frac{\partial W_p}{\partial r} - \frac{1}{r^2}\frac{\partial U}{\partial\theta}W_p\\ &+ \frac{1}{r}\frac{\partial^2 U}{\partial\theta\partial r}W_p + \alpha^2(U-c)V_p - \frac{\mathrm{i}\alpha W}{r}\frac{\partial V_p}{\partial\theta} = \frac{1}{Re}\left[\frac{1}{r}\frac{\partial^2 U_p}{\partial r^2}\right.\\ &- \left.\frac{1}{r^2}\frac{\partial U_p}{\partial r} + \frac{\partial^3 U_p}{\partial r^3} - \frac{2}{r^3}\frac{\partial^2 U_p}{\partial\theta^2} + \frac{1}{r^2}\frac{\partial^3 U_p}{\partial\theta^2\partial r} - \alpha^2\frac{\partial U_p}{\partial r}\right]\\ &- \frac{\mathrm{i}\alpha}{Re}\mathcal{L}(V_p) + \frac{2\mathrm{i}\alpha}{r^2 Re}\frac{\partial W_p}{\partial\theta}.\end{aligned} \tag{B-36}$$

From equation (2.3.12) we write

$$U_p = -\frac{1}{\mathrm{i}\alpha}\left(\frac{V_p}{r} + \frac{\partial V_p}{\partial r} + \frac{1}{r}\frac{\partial W_p}{\partial\theta}\right), \tag{B-37}$$

from which we can obtain the following derivatives

$$\frac{\partial U_p}{\partial r} = -\frac{1}{\mathrm{i}\alpha}\left(\frac{1}{r}\frac{\partial V_p}{\partial r} - \frac{V_p}{r^2} + \frac{\partial^2 V_p}{\partial r^2} - \frac{1}{r^2}\frac{\partial W_p}{\partial \theta} + \frac{1}{r}\frac{\partial^2 W_p}{\partial \theta \partial r}\right), \tag{B-38}$$

$$\frac{\partial U_p}{\partial \theta} = -\frac{1}{\mathrm{i}\alpha}\left(\frac{1}{r}\frac{\partial V_p}{\partial \theta} + \frac{\partial^2 V_p}{\partial r \partial \theta} + \frac{1}{r}\frac{\partial^2 W_p}{\partial \theta^2}\right), \tag{B-39}$$

$$\begin{aligned}\frac{\partial^2 U_p}{\partial r^2} &= -\frac{1}{\mathrm{i}\alpha}\left(\frac{1}{r}\frac{\partial^2 V_p}{\partial r^2} - \frac{2}{r^2}\frac{\partial V_p}{\partial r} + \frac{2V_p}{r^3} + \frac{\partial^3 V_p}{\partial r^3} + \frac{2}{r^3}\frac{\partial W_p}{\partial \theta}\right.\\ &\qquad \left. - \frac{2}{r^2}\frac{\partial^2 W_p}{\partial \theta \partial r} + \frac{1}{r}\frac{\partial^3 W_p}{\partial \theta \partial r^2}\right),\end{aligned} \tag{B-40}$$

$$\frac{\partial^2 U_p}{\partial \theta^2} = -\frac{1}{\mathrm{i}\alpha}\left(\frac{1}{r}\frac{\partial^2 V_p}{\partial \theta^2} + \frac{\partial^3 V_p}{\partial r \partial \theta^2} + \frac{1}{r}\frac{\partial^3 W_p}{\partial \theta^3}\right), \tag{B-41}$$

$$\begin{aligned}\frac{\partial^3 U_p}{\partial r^3} &= -\frac{1}{\mathrm{i}\alpha}\left(\frac{1}{r}\frac{\partial^3 V_p}{\partial r^3} - \frac{3}{r^2}\frac{\partial^2 V_p}{\partial r^2} + \frac{6}{r^3}\frac{\partial V_p}{\partial r} + \frac{\partial^4 V_p}{\partial r^4} - \frac{6V_p}{r^4} - \frac{6}{r^4}\frac{\partial W_p}{\partial \theta}\right.\\ &\qquad \left. + \frac{6}{r^3}\frac{\partial^2 W_p}{\partial \theta \partial r} - \frac{3}{r^2}\frac{\partial^3 W_p}{\partial \theta \partial r^2} + \frac{1}{r}\frac{\partial^4 W_p}{\partial \theta \partial r^3}\right),\end{aligned} \tag{B-42}$$

$$\frac{\partial^3 U_p}{\partial \theta^2 \partial r} = -\frac{1}{\mathrm{i}\alpha}\left(\frac{1}{r}\frac{\partial^3 V_p}{\partial \theta^2 \partial r} - \frac{1}{r^2}\frac{\partial^2 V_p}{\partial \theta^2} + \frac{\partial^4 V_p}{\partial r^2 \partial \theta^2} + \frac{1}{r}\frac{\partial^4 W_p}{\partial \theta^3 \partial r} - \frac{1}{r^2}\frac{\partial^3 W_p}{\partial \theta^3}\right), \tag{B-43}$$

$$\frac{\partial^2 U_p}{\partial r \partial \theta} = -\frac{1}{\mathrm{i}\alpha}\left(\frac{1}{r}\frac{\partial^2 V_p}{\partial r \partial \theta} - \frac{1}{r^2}\frac{\partial V_p}{\partial \theta} + \frac{\partial^3 V_p}{\partial r^2 \partial \theta} - \frac{1}{r^2}\frac{\partial^2 W_p}{\partial \theta^2} + \frac{1}{r}\frac{\partial^3 W_p}{\partial \theta^2 \partial r}\right), \tag{B-44}$$

$$\begin{aligned}\frac{\partial^3 U_p}{\partial r^2 \partial \theta} &= -\frac{1}{\mathrm{i}\alpha}\left(\frac{1}{r}\frac{\partial^3 V_p}{\partial r^2 \partial \theta} - \frac{2}{r^2}\frac{\partial^2 V_p}{\partial r \partial \theta} + \frac{2}{r^3}\frac{\partial V_p}{\partial \theta} + \frac{\partial^4 V_p}{\partial r^3 \partial \theta} + \frac{2}{r^3}\frac{\partial^2 W_p}{\partial \theta^2}\right.\\ &\qquad \left. - \frac{2}{r^2}\frac{\partial^3 W_p}{\partial \theta^2 \partial r} + \frac{1}{r}\frac{\partial^4 W_p}{\partial \theta^2 \partial r^2}\right),\end{aligned} \tag{B-45}$$

$$\frac{\partial^3 U_p}{\partial \theta^3} = -\frac{1}{\mathrm{i}\alpha}\left(\frac{1}{r}\frac{\partial^3 V_p}{\partial \theta^3} + \frac{\partial^4 V_p}{\partial r \partial \theta^3} + \frac{1}{r}\frac{\partial^4 W_p}{\partial \theta^4}\right). \tag{B-46}$$

Substituting (B-37) – (B-46) into equation (B-36), expanding the $(U-c)$ term and separating the coefficients of V_p and W_p, we are left with the left hand side of the equation in the form

$$\begin{aligned}&U\left(-\frac{1}{r}\frac{\partial}{\partial r} + \frac{1}{r^2} - \frac{\partial^2}{\partial r^2} + \alpha^2\right)V_p \;-\; c\left(-\frac{1}{r}\frac{\partial}{\partial r} + \frac{1}{r^2} - \frac{\partial^2}{\partial r^2} + \alpha^2\right)V_p\\ &\quad + \left\{-\frac{1}{r}\frac{\partial U}{\partial r} + \frac{\partial^2 U}{\partial r^2} + \frac{\mathrm{i}\alpha}{r}\left[\left(\frac{\partial W}{\partial r} - \frac{W}{r}\right)\left(\frac{1}{r}\frac{\partial}{\partial \theta} + \frac{\partial^2}{\partial r \partial \theta}\right)\right.\right.\\ &\quad \left.\left. + W\left(\frac{1}{r}\frac{\partial^2}{\partial r \partial \theta} - \frac{1}{r^2}\frac{\partial}{\partial \theta} + \frac{\partial^3}{\partial r^2 \partial \theta} - \frac{\partial}{\partial \theta}\right)\right] - \frac{1}{\mathrm{i}\alpha Re}\left[\frac{1}{r^4}\left(-3 + 3\frac{\partial^2}{\partial \theta^2}\right)\right.\right.\\ &\quad \left.\left. + \frac{1}{r^3}\left(-3 + \frac{\partial^2}{\partial \theta^2}\right)\frac{\partial}{\partial r} + \frac{1}{r^2}\left(3 - \frac{\partial^2}{\partial \theta^2}\right)\frac{\partial^2}{\partial r^2} - \frac{2}{r}\frac{\partial^3}{\partial r^3} - \frac{\partial^4}{\partial r^4}\right]\right.\\ &\quad \left. - \frac{\alpha}{\mathrm{i}Re}\left(\frac{1}{r}\frac{\partial}{\partial r} - \frac{1}{r^2} + \frac{\partial^2}{\partial r^2}\right) + \frac{\mathrm{i}\alpha}{Re}\left(\frac{1}{r}\frac{\partial}{\partial r} + \frac{\partial^2}{\partial r^2}\right.\right.\\ &\quad \left.\left. - \frac{1}{r^2} + \frac{1}{r^2}\frac{\partial^2}{\partial \theta^2} - \alpha^2\right)\right\}V_p.\end{aligned} \tag{B-47}$$

Let,

$$A_2 = \left(-\frac{1}{r}\frac{\partial}{\partial r} + \frac{1}{r^2} - \frac{\partial^2}{\partial r^2} + \alpha^2\right),$$
$$A_1 = UA_2 + \{\cdots\}.$$

The right hand side becomes

$$\begin{aligned} U\left(-\frac{1}{r^2}\frac{\partial}{\partial\theta} + \frac{1}{r}\frac{\partial^2}{\partial\theta\partial r}\right)W_p \quad - \quad & c\left(-\frac{1}{r^2}\frac{\partial}{\partial\theta} + \frac{1}{r}\frac{\partial^2}{\partial\theta\partial r}\right)W_p \\ & + \left\{\frac{1}{r}\left(\frac{\partial U}{\partial r}\frac{\partial}{\partial\theta} - \frac{\partial U}{\partial\theta}\frac{\partial}{\partial r} - \frac{\partial^2 U}{\partial\theta\partial r}\right) + \frac{1}{r^2}\frac{\partial U}{\partial\theta} - \frac{\mathrm{i}\alpha}{r}\left[\left(\frac{1}{r}\frac{\partial W}{\partial r} - \frac{W}{r^2}\right)\right.\right. \\ & \left. + \frac{W}{r^2}\left(-1 + \frac{\partial}{\partial r}\right)\right]\frac{\partial}{\partial\theta^2} + \frac{1}{\mathrm{i}\alpha Re}\left[\frac{1}{r^4}\left(3\frac{\partial}{\partial\theta} + 3\frac{\partial^3}{\partial\theta^3}\right)\right. \\ & - \frac{1}{r^3}\left(3\frac{\partial}{\partial\theta} + \frac{\partial^3}{\partial\theta^3}\right)\frac{\partial}{\partial r} + \left(\frac{2}{r^2}\frac{\partial^2}{\partial r^2} - \frac{1}{r}\frac{\partial^3}{\partial r^3}\right)\frac{\partial}{\partial\theta}\Big] \\ & \left. - \frac{\alpha}{\mathrm{i}Re}\left(-\frac{1}{r^2} + \frac{1}{r}\frac{\partial}{\partial r}\right)\frac{\partial}{\partial\theta} + \frac{2i\alpha}{r^2 Re}\frac{\partial}{\partial\theta}\right\}W_p. \end{aligned} \tag{B-48}$$

Let,

$$B_2 = \left(-\frac{1}{r^2} + \frac{1}{r}\frac{\partial}{\partial r}\right)\frac{\partial}{\partial\theta},$$
$$B_1 = UB_2 + \{\cdots\}.$$

We can then write the full equation as

$$A_1 V_p - B_1 W_p = c(A_2 V_p - B_2 W_p). \tag{B-49}$$

Subtracting equation (B-35) from (B-33) gives

$$\begin{aligned} \mathrm{i}\alpha(U-c)\frac{\partial U_p}{\partial\theta} \quad + \quad & \mathrm{i}\alpha\frac{\partial U}{\partial\theta}U_p + \frac{1}{r}\frac{\partial W}{\partial\theta}\frac{\partial U_p}{\partial\theta} + \frac{W}{r}\frac{\partial^2 U_p}{\partial\theta^2} + \frac{\partial U}{\partial r}\frac{\partial V_p}{\partial\theta} + \frac{\partial^2 U}{\partial r\partial\theta}V_p \\ + \quad & \frac{1}{r}\frac{\partial U}{\partial\theta}\frac{\partial W_p}{\partial\theta} + \frac{1}{r}\frac{\partial^2 U}{\partial\theta^2}W_p + \alpha^2 r(U-c)W_p - \mathrm{i}\alpha\left(W\frac{\partial W_p}{\partial\theta}\right. \\ + \quad & \left. r\frac{\partial W}{\partial r}V_p + \frac{\partial W}{\partial\theta}W_p + WV_p\right) = \frac{1}{Re}\left[\frac{1}{r}\frac{\partial^2 U_p}{\partial r\partial\theta} + \frac{\partial^3 U_p}{\partial r^2\partial\theta}\right. \\ + \quad & \left.\frac{1}{r^2}\frac{\partial^3 U_p}{\partial\theta^3} - \alpha^2\frac{\partial U_p}{\partial\theta}\right] - \frac{\mathrm{i}\alpha r}{Re}\mathcal{L}(W_p) + \frac{2\mathrm{i}\alpha}{rRe}\frac{\partial V_p}{\partial\theta}, \end{aligned} \tag{B-50}$$

where we can substitute expressions for U_p (and derivatives thereof) into equation (B-50), expanding the $(U-c)$ term and separating the coefficients of V_p and W_p,

where once again we write the left hand side of the equation as

$$\begin{aligned} U\left(-\frac{1}{r}\frac{\partial}{\partial\theta}-\frac{\partial^2}{\partial r\partial\theta}\right)V_p \;-\; c\left(-\frac{1}{r}\frac{\partial}{\partial\theta}-\frac{\partial^2}{\partial r\partial\theta}\right)V_p+\left\{-\frac{\partial U}{\partial\theta}\left(\frac{1}{r}+\frac{\partial}{\partial r}\right)\right. \\ -\frac{\mathrm{i}\alpha}{r}\left[\frac{\partial W}{\partial\theta}\left(\frac{1}{r}\frac{\partial}{\partial\theta}+\frac{\partial^2}{\partial r\partial\theta}\right)+\frac{W}{r}\frac{\partial^2}{\partial\theta^2}+W\frac{\partial^3}{\partial r\partial\theta^2}\right] \\ +\frac{\partial U}{\partial r}\frac{\partial}{\partial\theta}+\frac{\partial^2 U}{\partial r\partial\theta}-\mathrm{i}\alpha\left(r\frac{\partial W}{\partial r}+W\right)+\frac{1}{\mathrm{i}\alpha Re}\left[\frac{1}{r^3}\left(\frac{\partial}{\partial\theta}+\frac{\partial^3}{\partial\theta^3}\right)\right. \\ +\frac{1}{r^2}\left(\frac{\partial^3}{\partial\theta^3}-\frac{\partial}{\partial\theta}\right)\frac{\partial}{\partial r}+\left(\frac{2}{r}\frac{\partial^2}{\partial r^2}+\frac{\partial^3}{\partial r^3}\right)\frac{\partial}{\partial\theta}\Big] \\ \left.-\frac{\alpha}{\mathrm{i}Re}\left(\frac{1}{r}+\frac{\partial}{\partial r}\right)\frac{\partial}{\partial\theta}-\frac{2\mathrm{i}\alpha}{rRe}\frac{\partial}{\partial\theta}\right\}V_p. \end{aligned} \tag{B-51}$$

Let,

$$\begin{aligned} A_4 &= \left(-\frac{1}{r}-\frac{\partial}{\partial r}\right)\frac{\partial}{\partial\theta}, \\ A_3 &= UA_4+\{\cdots\}. \end{aligned}$$

The right hand side is written in the form

$$\begin{aligned} U\left(\frac{1}{r}\frac{\partial^2}{\partial\theta^2}-\alpha^2 r\right)W_p \;-\; c\left(\frac{1}{r}\frac{\partial^2}{\partial\theta^2}-\alpha^2 r\right)W_p+\left\{-\frac{1}{r}\frac{\partial^2 U}{\partial\theta^2}+\mathrm{i}\alpha\frac{\partial W}{\partial\theta}\right. \\ -\frac{\mathrm{i}\alpha}{r}\left[\frac{\partial W}{\partial\theta}\frac{\partial^2}{\partial\theta^2}+W\frac{\partial^3}{\partial\theta^3}\right]-\frac{1}{\mathrm{i}\alpha Re}\left[\left(\frac{1}{r^3}-\frac{1}{r^2}\frac{\partial}{\partial r}+\frac{1}{r}\frac{\partial^2}{\partial r^2}\right)\frac{\partial^2}{\partial\theta^2}\right. \\ \left.+\frac{1}{r^3}\frac{\partial^4}{\partial\theta^4}\right]+\mathrm{i}\alpha W\frac{\partial}{\partial\theta}+\frac{\alpha}{\mathrm{i}rRe}\frac{\partial^2}{\partial\theta^2}-\frac{\mathrm{i}\alpha}{Re}\left(\frac{\partial}{\partial r}+r\frac{\partial^2}{\partial r^2}\right. \\ \left.\left.-\frac{1}{r}+\frac{1}{r}\frac{\partial^2}{\partial\theta^2}-\alpha^2 r\right)\right\}W_p. \end{aligned} \tag{B-52}$$

Let,

$$\begin{aligned} B_4 &= \left(\frac{1}{r}\frac{\partial^2}{\partial\theta^2}-\alpha^2 r\right), \\ B_3 &= UB_4+\{\cdots\}. \end{aligned}$$

We can then write the full equation as

$$A_3V_p-B_3W_p=c(A_4V_p-B_4W_p). \tag{B-53}$$

Equations (B-49) and (B-53) can be arranged into a matrix equation to form a Generalised Eigenvalue Problem of the form $\mathbf{Ax}=c\mathbf{Bx}$, subject to $\mathbf{D}[\alpha,\omega;R]=0$;

$$\begin{bmatrix} A_1 & -B_1 \\ A_3 & -B_3 \end{bmatrix}\begin{bmatrix} V_p \\ W_p \end{bmatrix}=c\begin{bmatrix} A_2 & B_2 \\ A_4 & -B_4 \end{bmatrix}\begin{bmatrix} V_p \\ W_p \end{bmatrix}. \tag{B-54}$$

Unlike the Cartesian form, the four linear operators are unable to be written in terms of an odd and even operator with the order of the differentiation terms reversed.

Appendix C

C.1 Numerical Convergence of Cartesian Pseudo-spectral code

Here we present a convergence study of the accuracy of the least stable eigenvalues recovered using the Cartesian based pseudo-spectral code.

C.1.1 Single Vortex Numerical Convergence

Figure C.1 is a plot of the smallest stable eigenvalues found by setting the ARPACK shift parameter $\sigma = 0 - 0\mathrm{i}$ (to find eigenvalues about the neutral axis) for $(N_y, N_z) = (51, 51); (55, 55); (61, 61); (65, 65)$ and $(s_y, s_z) = (0.975, 0.975)$, from which it can be seen that good convergence is reached at $(N_y, N_z) = (51, 51)$ for the first 10 or so modes. The values $\alpha = 0.418, q = 0.475$ and $Re = 100$ correspond to those used by Theofilis *et al.* [25] and are a useful visual comparison with the results presented herein. Increasing the spectral accuracy does improve the convergence for more stable modes but a significant increase in the number of grid points is required to resolve these further which in turn involves excessive run-times and significant memory overheads.

Looking at the eigenvalues for a range of (N_y, N_z), table C.1 shows that, for the two 'least-stable' modes, approximately 5 decimal place convergence is achievable with $(N_y, N_z) = (41, 41)$ and six decimal place accuracy with $(N_y, N_z) = (61, 61)$ in both the real and imaginary components using $(s_y, s_z) = (0.95, 0.95)$.

Table C.2 gives the convergence history of the same least-stable modes for a variation in the grid clustering rate from none, through to very heavy clustering

about the co-ordinate origin with $(N_y, N_z) = (61, 61)$. The results indicate that in both cases a high degree of convergence is seen at $(s_y, s_z) = (0.95, 0.95)$ but the eigenvalue appears to be relatively well resolved for lower degrees of clustering. At $(s_y, s_z) = (0.975, 0.975)$ the values appear to diverge, perhaps indicating that too few points are left in the outer regions with this much concentration.

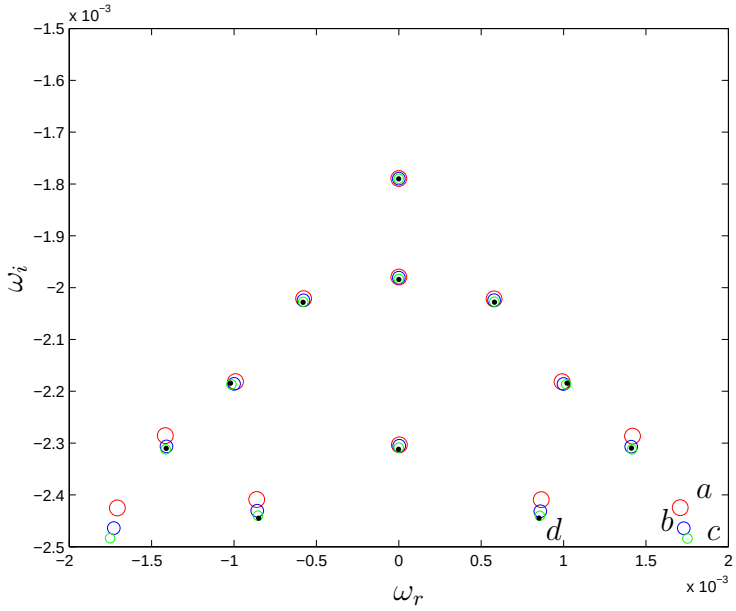

Figure C.1: Convergence of eigenvalues for the viscous stability of a single vortex. In descending size of marker, (N_y, N_z) = (a) $(51, 51)$, (b) $(55, 55)$, (c) $(61, 61)$ and (d) $(65, 65)$ - dots.

(N_y, N_z)	'Mode 1'	'Mode 2'
(41,41)	0.00000074 - 0.00178885i	0.00000379 - 0.00197827i
(45,45)	0.00000058 - 0.00178896i	0.00000296 - 0.00197937i
(51,51)	0.00000062 - 0.00178941i	0.00000078 - 0.00197953i
(55,55)	0.00000042 - 0.00178961i	0.00000037 - 0.00198069i
(61,61)	-0.00000002 - 0.00178987i	0.00000053 - 0.00198312i
(65,65)	-0.00000013 - 0.00179015i	0.00000015 - 0.00198436i

Table C.1: Convergence history of the two least-stable eigenvalues for a single vortex, varying (N_y, N_z).

s	'Mode 1'	'Mode 2'
0	-0.00000834 - 0.00179135i	-0.00002418 - 0.00198499i
0.5	-0.00000362 - 0.00179561i	-0.00001182 - 0.00198899i
0.6	-0.00000201 - 0.00179664i	-0.00000756 - 0.00200246i
0.7	-0.00000218 - 0.00179927i	-0.00000915 - 0.00201017i
0.8	-0.00114239 - 0.00179469i	-0.00000754 - 0.00180501i
0.9	-0.00001640 - 0.00179716i	-0.00005115 - 0.00200524i
0.95	-0.00000144 - 0.00179283i	-0.00000469 - 0.00199318i
0.975	-0.00000002 - 0.00178987i	-0.00000053 - 0.00199312i

Table C.2: Convergence history of the two least-stable eigenvalues for a single vortex, varying the clustering parameter, s.

To further illustrate the numerical convergence of the scheme for those values found closest to the neutral axis, convergence histories of the subsequent four modes are given below relative to an increase in spectral accuracy.

(N_y, N_z)	'Mode 3'	'Mode 4'
(41,41)	-0.00058215 - 0.00200927i	0.00058392 - 0.00201160i
(45,45)	-0.00057786 - 0.00201482i	0.00057878 - 0.00201597i
(51,51)	-0.00057746 - 0.00202132i	0.00057807 - 0.00202166i
(55,55)	-0.00057807 - 0.00202441i	0.00057851 - 0.00202436i
(61,61)	-0.00057957 - 0.00202735i	0.00057975 - 0.00202707i
(65,65)	-0.00058050 - 0.00202831i	0.00058059 - 0.00202803i

Table C.3: Convergence history of the third and fourth least-stable eigenvalues for a single vortex, varying (N_y, N_z).

C.1.2 Two-Vortex Numerical Convergence

Figure C.2 represents the spectra of least-stable values as found by setting the vortices at $(y, z) = (2.0, 0)$. As before we see good convergence near the point of neutral stability.

(N_y, N_z)	'Mode 5'	'Mode 6'
(41,41)	0.00090789 - 0.00216179i	-0.00090804 - 0.00216223i
(45,45)	0.00096037 - 0.00219336i	-0.00096085 - 0.00219333i
(51,51)	0.00099048 - 0.00218168i	-0.00099052 - 0.00218148i
(55,55)	0.00099987 - 0.00218591i	-0.00099984 - 0.00218576i
(61,61)	0.00101607 - 0.00218673i	-0.00101596 - 0.00218666i
(65,65)	0.00102145 - 0.00218436i	-0.00102136 - 0.00218437i

Table C.4: Convergence history of the fifth and sixth least-stable eigenvalue for a single vortex, varying (N_y, N_z).

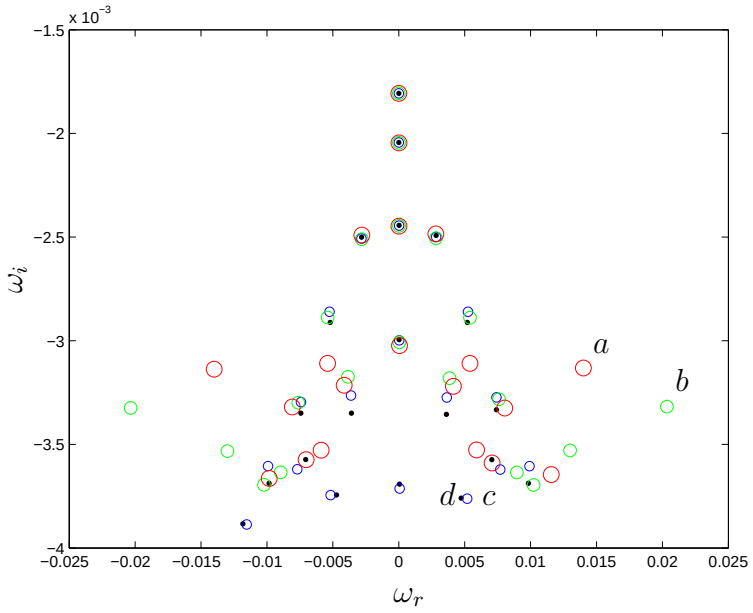

Figure C.2: Convergence of eigenvalues for the viscous stability of a two-vortex configuration. In descending size of marker, $(N_y, N_z) =$ (a) $(51, 51)$, (b) $(55, 55)$, (c) $(61, 61)$ and (d) $(65, 65)$ - dots.

Table C.5 gives the two least-stable eigenvalues for the same variation in (N_y, N_z) as was used earlier. The clustering for the two-vortex configuration is set at $(s_y, s_z) = (0.93, 0.95)$, $s_y = 0.93$ was chosen to slightly relax the clustering in the plane of two vortices as they sit away from the origin. It can be seen that again, five decimal place convergence is achieved at relatively low grid resolutions with six decimal place

convergence for a higher number of grid points.

(N_y, N_z)	'Mode 1'	'Mode 2'
(41,41)	0.00000472 - 0.00180671i	0.00000571 - 0.00204316i
(45,45)	0.00000480 - 0.00180707i	0.00000925 - 0.00204615i
(51,51)	0.00000319 - 0.00180664i	0.00001350 - 0.00204530i
(55,55)	0.00000317 - 0.00180643i	0.00001304 - 0.00204501i
(61,61)	0.00000399 - 0.00180659i	0.00000949 - 0.00204387i
(65,65)	0.00000380 - 0.00180647i	0.00000923 - 0.00204370i

Table C.5: Convergence history of the two least-stable eigenvalues for a two-vortex configuration, varying (N_y, N_z).

The convergence histories of four further modes are given below for comparison. It should be noted that for all the convergence histories proceeding and following, the mode numbers stated are purely arbitrary and assigned only by descending order of magnitude of the imaginary component of the eigenvalue as obtained from the initial resolution study.

(N_y, N_z)	'Mode 4'	'Mode 5'
(41,41)	-0.00287834 - 0.00252238i	0.00293804 - 0.00252701i
(45,45)	-0.00284181 - 0.00246741i	0.00285589 - 0.00245802i
(51,51)	-0.00280657 - 0.00249042i	0.00281019 - 0.00248474i
(55,55)	-0.00281453 - 0.00250991i	0.00281886 - 0.00250503i
(61,61)	-0.00283033 - 0.00250667i	0.00283611 - 0.00249923i
(65,65)	-0.00282734 - 0.00250058i	0.00283142 - 0.00249201i

Table C.6: Convergence history of the fourth and fifth least-stable eigenvalues for a two-vortex configuration, varying (N_y, N_z).

C.1.3 Four-Vortex Numerical Convergence

The vortices are at $(y_1, y_2) = (5, 0.7)$ with $a_2 = 0.5$ and $q_2 = -0.19$ corresponding to the ratios of Theofilis *et al.* [25], $\alpha = 0.3$ and $Re = 100$. The clustering param-

eters were left the same as for the two-vortex case and appear to be appropriate for the four-vortex configuration. Figure C.3 illustrates the region of convergence of the eigenvalues showing the now familiar convergence of least-stable values at manageable problem dimensions.

(N_y, N_z)	'Mode 3'	'Mode 8'
(41,41)	0.00003491 - 0.00246221i	-
(45,45)	0.00003245 - 0.00244688i	0.00005551 - 0.00313659i
(51,51)	0.00001937 - 0.00244734i	0.00005043 - 0.00302383i
(55,55)	0.00001908 - 0.00244570i	0.00004482 - 0.00300738i
(61,61)	0.00002536 - 0.00244479i	0.00003073 - 0.00299789i
(65,65)	0.00002396 - 0.00244321i	0.00002988 - 0.00299496i

Table C.7: Convergence history of the third and eighth least-stable eigenvalue for a two-vortex configuration, varying (N_y, N_z).

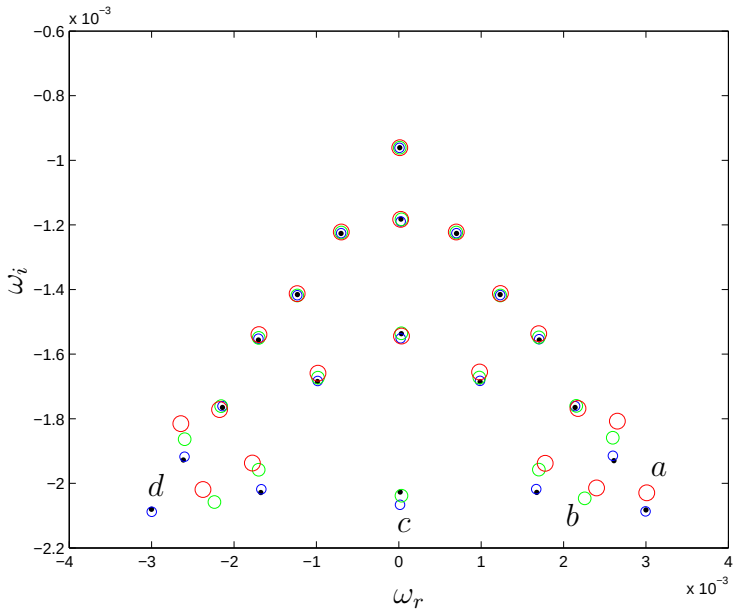

Figure C.3: Convergence of eigenvalues for the viscous stability of a four-vortex configuration. In descending size of marker, $(N_y, N_z) =$ (a) $(51, 51)$, (b) $(55, 55)$, (c) $(61, 61)$ and (d) $(65, 65)$ - dots.

In table C.8 we see a similar pattern of numerical convergence; approximately five decimal places at the starting resolution and approaching six decimal places as the resolution increases with some fluctuation in predominantly the real component.

(N_y, N_z)	'Mode 1'	'Mode 2'
(41,41)	0.00001289 - 0.00096099i	0.00004293 - 0.00117880i
(45,45)	0.00001981 - 0.00096266i	0.00003993 - 0.00118049i
(51,51)	0.00001213 - 0.00096111i	0.00002262 - 0.00118277i
(55,55)	0.00001203 - 0.00096110i	0.00003326 - 0.00118286i
(61,61)	0.00000940 - 0.00096149i	0.00002258 - 0.00118953i
(65,65)	0.00001193 - 0.00096115i	0.00002676 - 0.00118199i

Table C.8: Convergence history of the two least-stable eigenvalues for a four-vortex configuration, varying (N_y, N_z).

As before, we present convergence histories of some further eigenvalues to illustrate the convergence of the numerical scheme as $\omega_i \to 0$.

(N_y, N_z)	'Mode 3'	'Mode 4'
(41,41)	0.00069685 - 0.00121913i	-0.00069794 - 0.00122124i
(45,45)	0.00069716 - 0.00121982i	-0.00069701 - 0.00122069i
(51,51)	0.00069755 - 0.00122197i	-0.00069718 - 0.00122209i
(55,55)	0.00069834 - 0.00122365i	-0.00069807 - 0.00122374i
(61,61)	0.00070001 - 0.00122572i	-0.00069987 - 0.00122576i
(65,65)	0.00070102 - 0.00122651i	-0.00070097 - 0.00122670i

Table C.9: Convergence history of the third and fourth least-stable eigenvalues for a four-vortex configuration, varying (N_y, N_z).

(N_y, N_z)	'Mode 5'	'Mode 6'
(41,41)	0.00128230 - 0.00141518i	-0.00128216 - 0.00141588i
(45,45)	0.00125472 - 0.00139888i	-0.00125469 - 0.00139943i
(51,51)	0.00123321 - 0.00141259i	-0.00123317 - 0.00141294i
(55,55)	0.00123195 - 0.00141849i	-0.00123192 - 0.00141873i
(61,61)	0.00123173 - 0.00141741i	-0.00123166 - 0.00141754i
(65,65)	0.00123034 - 0.00141560i	-0.00123026 - 0.00141571i

Table C.10: Convergence history of the fifth and sixth least-stable eigenvalue for a four-vortex configuration, varying (N_y, N_z).

Appendix D

D.1 Further Detail of Viscous Code Verification

D.1.1 Axial flow in a Rectangular Duct

In figures D.1 and D.2, the eigenvalue spectra for flow in a duct recovered by the two-equation, fourth order derivative model using finite-difference discretisation and those eigenvalues recovered using the four-equation, second order derivative model implementing pseudo-spectral discretisation are shown respectively corresponding to the parameters outlined in section 3.7.3.

The results presented in figure D.1, although producing the 'primary' modes, suffer from a lack of grid resolution about the boundaries hence the lack of further modes in this figure. The results in figure D.2 demonstrate a more defined band of values about $\omega_r \approx 0.67$ consisting of multiple values relating to each of the four eigenfunctions.

D.1.2 Axial flow in a Circular Pipe

Figure D.3 shows the eigenvalue spectra recovered for Hagen-Poiseuille flow in a pipe by the two-equation pseudo-spectral code. The one-dimensional values of Schmid and Henningson [51] (and recovered by a one-dimensional, n-dependent code written for this study) are superimposed as circles.

D.1.3 A Single Batchelor Vortex Located at the Origin

To further test the validity of the numerical methods used for the analysis in this study, we computed eigenvalue spectra for a single Batchelor vortex from two dis-

tinctly different codes (namely the Cartesian and polar co-ordinate codes) and compared these for a set of determining parameters. It should also be remembered that due to the symmetry used in the discretisation of the polar domain, at an equivalent resolution, we would expect this scheme to produce more accurate results. Figure D.4 shows the spectra of figure 3.20 in section 3.7.3, from the polar code with the Cartesian spectra of the same parameters superimposed as circles. We can see that the least stable modes are in close agreement and that the entire structure of the spectra is consistent, the differences being due to the reduced accuracy of the Cartesian code.

In figure D.5 we present a comparison of the eigenvalue spectra produced using the one-dimensional code for a variety of azimuthal wave-numbers (circles) with those recovered using the two-dimensional 'global' code. We can see that for this set of parameters, $\alpha = 1, q = 0.8, Re = 1000$, good agreement is observed for the least-stable values where $\omega_i > -0.0014$. This is consistent with other parameter choices and gives us confidence that in the vicinity the neutral stability axis ($\omega_i = 0$), our results are correct.

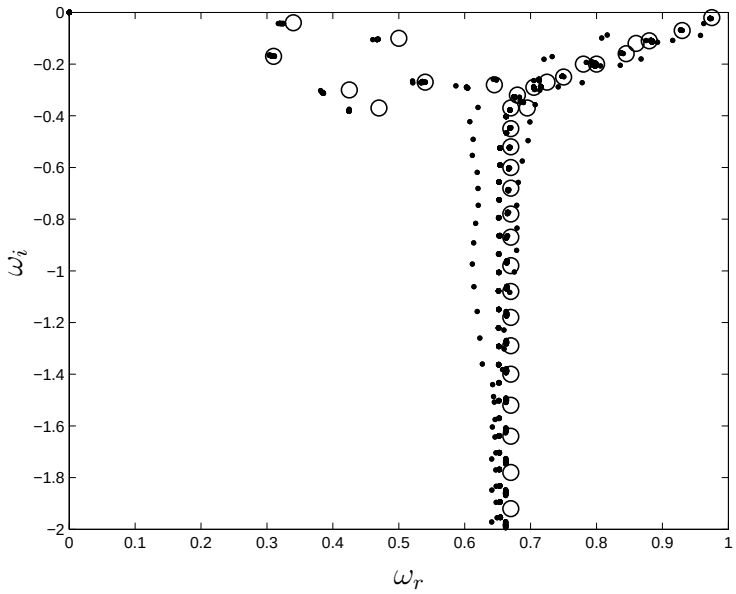

Figure D.1: Plane Poiseuille flow in a large aspect ratio duct using a finite-difference numerical scheme with dependent parameters $[V, W]$. Circles represent the results of Theofilis *et al.* [63].

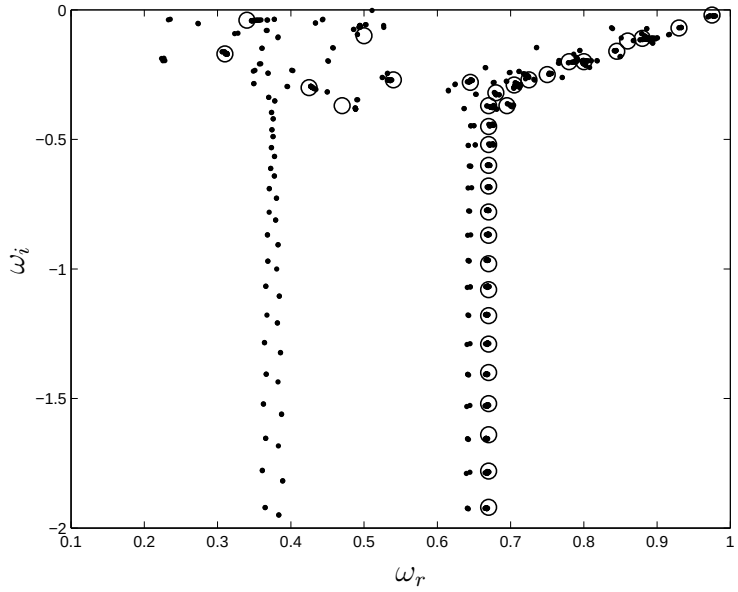

Figure D.2: Plane Poiseuille flow in a large aspect ratio duct using a pseudo-spectral numerical scheme with dependent parameters $[U, V, W, P]$. Circles represent the results of Theofilis *et al.* [63].

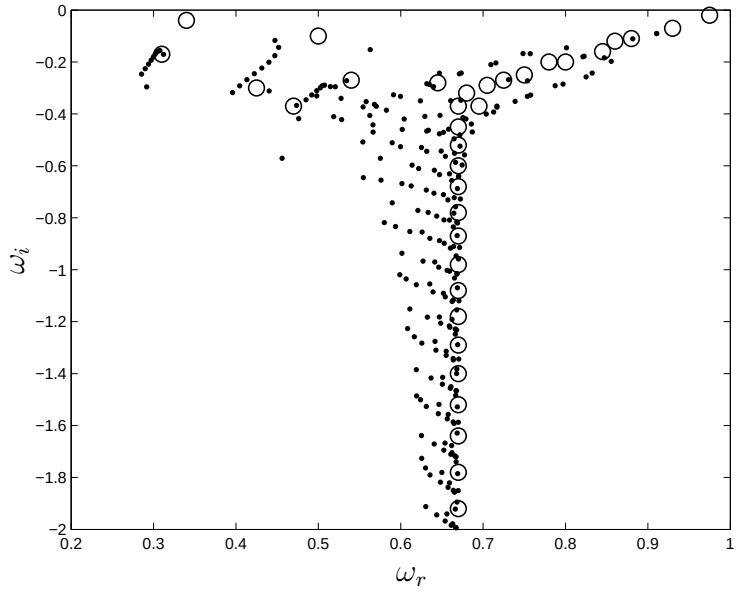

Figure D.3: Hagen-Poiseuille flow in a pipe of radius 1, found using a pseudo-spectral numerical scheme implementing the two-equation method. Circles represent the results of Schmid and Henningson [51].

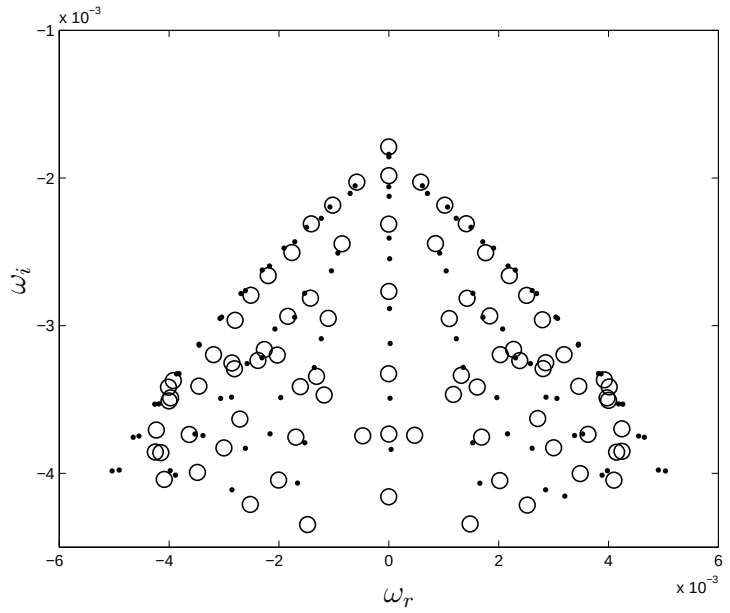

Figure D.4: A comparison of the eigenvalue spectra recovered by the polar codes (dots) and Cartesian code (circles) using parameters matching those of Hein and Theofilis [25] for a single Batchelor vortex.

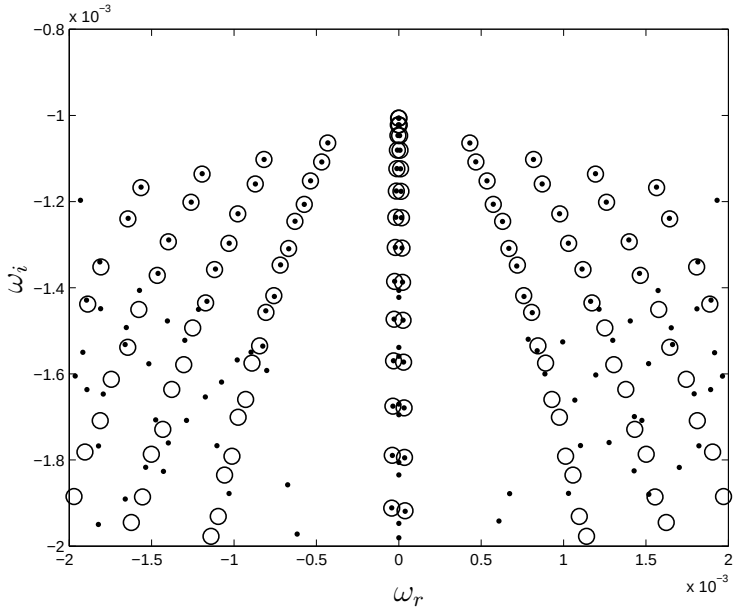

Figure D.5: A comparison of the eigenvalue spectra recovered by the polar 'global' code (dots) and one-dimensional, n-dependent code (circles) using parameters $\alpha = 1, q = 0.8, Re = 1000$, for a single Batchelor vortex.

Bibliography

[1] M. Abid and M.E. Brachet. Direct numerical simulations of the Batchelor trailing vortex by a spectral method. *Phys. Fluids*, 10(2):469–75, 1998.

[2] Civil Aviation Authority. *United Kingdom, Aeronautical Information Circular*. Aeronautical Information Service, Control Tower, London Heathrow Airport, Hounslow, Middlesex, TW6 1JJ, 1999.

[3] G. K. Batchelor. Axial flow in trailing line vortices. *J. Fluid Mech.*, 20:645–58, 1964.

[4] G. K. Batchelor and A.E. Gill. Analysis of the stability of axisymmetric jets. *J. Fluid Mech.*, 14:529–51, 1962.

[5] T. J. Bridges and P.J. Morris. Differential eigenvalue problems in which the parameter appears non-linearly. *J. Comp. Fluids*, 55:437–60, 1984.

[6] C.E. Brown. Aerodynamics of wake vortices. *AIAA Journal*, 11(4):531–6, 1973.

[7] P.M. Condit and P.W. Tracy. *Results of the Boeing Company wake turbulence test program, (in) Aircraft Wake Turbulence and its Detection. (ed) J. Olsen, A. Goldburg, M. Rogers.* Plennum, NY, 1971.

[8] J.D. Crouch. Instability and transient growth for two trailing-vortex pairs. *J. Fluid Mech.*, 350:311–30, 1997.

[9] J.D. Crouch. Airplane trailing vortices and their control. *C.R. Physique*, 6:487–99, 2005.

[10] S.C. Crow. Stability theory for a pair of trailing vortices. *AIAA Journal*, 8(12):2172–79, 1970.

[11] S.C. Crow. *Panel Discussion, (in) Aircraft Wake Turbulence and its Detection. (ed) J. Olsen, A. Goldburg, M. Rogers.* Plennum, NY, 1971.

[12] M. Czech, G. Miller, J. Crouch, and M. Strelets. Predicting the near-field evolution of airplane trailing vortices. *C.R. Physique*, 6:451–66, 2005.

[13] J.P. Denier and J.A.K. Stott. The dominant wave mode within a trailing line vortex. *Phys. Fluids*, 17(1):Art. 014101, 2005.

[14] W.J. Devonport, J.S. Zsoldos, and C.M. Vogel. The structure and development of a counter-rotating wing-tip vortex pair. *J. Fluid Mech.*, 332:71–104, 1997.

[15] P.W. Duck and M.R. Foster. The inviscid stability of a trailing line vortex. *J. App. Maths and Phys.*, 31, 1980.

[16] P.W. Duck and M.R. Khorrami. A note on the effects of viscosity on the stability of a trailing-line vortex. *J. Fluid Mech.*, 245:175–89, 1992.

[17] D. Fabre, C. Cossu, and L. Jacqiun. Spatio-temporal development of the long and short-wave vortex-pair instabilities. *Phys. Fluids*, 12(5):1247–50, 2000.

[18] D. Fabre and L. Jacqiun. Stability of a four-vortex aircraft wake model. *Phys. Fluids*, 12(10):2438–43, 2000.

[19] D. Fabre and L. Jacquin. Viscous instabilities in trailing vortices at large swirl numbers. *J. Fluid Mech.*, 500:239–262, 2004.

[20] D. Fabre, L. Jacquin, and A. Loof. Optimal perturbations in a four-vortex aircraft wake in counter-rotating configuration. *J. Fluid Mech.*, 451:319–28, 2002.

[21] T. Gerz and F. Holzäpfel. Wing-tip vortices, turbulence and the distribution of emissions. *AIAA Journal*, 37(10):1270–76, 1999.

[22] Sheldon I. Green. *Wing Tip Vortices, (in) Fluid Vortices. (ed) Sheldon I. Green.* Kluwer Academic Publishers, Dordrecht, 1995.

[23] P. Hall and N.J. Horseman. The linear inviscid secondary instability of longitudunal vortex structures in boundary layers. *J. Fluid Mech.*, 232:741–53, 1991.

[24] C.J. Heaton. Centre modes in inviscid swirling flows and their application to the stability of the Batchelor vortex. *J. Fluid Mech.*, 576:325–48, 2007.

[25] S. Hein and V. Theofilis. On stability characteristics of isolated vortices and models of trailing-vortex systems. *Computers & Fluids*, 33:741–53, 2004.

[26] L. Jacquin. Vortices in aerodynamics: a keynote. *Proc. 6th World Conference on Experimental Heat Transfer, Fluid Mechanics and Thermodynamics. Matsushima, Myagi, Japan. 17-21 April.*, pages 1–12, 2005.

[27] L. Jacquin, D. Fabre, D. Sipp, V. Theofilis, and H. Vollmers. Instability and unsteadiness of aircraft wake vortices. *Aerospace Science and Technology*, 7:577–93, 2003.

[28] L. Jacquin and C. Pantano. On the persistence of trailing vortices. *J. Fluid Mech.*, 471:159–68, 2002.

[29] J. Jimenez. Stability of a pair of co-rotating vortices. *Phys. Fluids*, 18(11):1580–1, 1975.

[30] M.R. Khorrami. On the viscous modes of instability of a trailing line vortex. *J. Fluid Mech.*, 225:197–212, 1991.

[31] M.R. Khorrami. Behaviour of asymmetric unstable modes of a trailing line vortex near the upper neutral curve. *Phys. Fluids*, 4(6):1310–13, 1992.

[32] M.R. Khorrami, M.R. Malik, and R.L. Ash. Application of spectral collocation techniques to the stability of swirling flows. *J. Comp. Fluids*, 81:206–29, 1989.

[33] F. Laporte and A. Corjon. Direct numerical simulations of the elliptic instability of a vortex pair. *Phys. Fluids*, 12(5):1016–31, 2000.

[34] S. Le Dizés and F. Laporte. Theoretical predictions for the elliptical instability in a two-vortex flow. *J. Fluid Mech.*, 471:169–201, 2002.

[35] R.B. Lehoucq, D.C. Sorensen, and C. Yang. *ARPACK user's guide: Solution of large scale eigenvalue problems with implicitly restarted Arnoldi methods.* Online, 1987.

[36] S Leibovich and K Stewartson. A sufficient condition for the instability of columnar vortices. *J. Fluid Mech.*, 126:335–56, 1983.

[37] M. Lessen and F. Paillet. The stability of a trailing line vortex. part 2. viscous theory. *J. Fluid Mech.*, 65(4):769–79, 1974.

[38] M. Lessen, J.P. Singh, and F. Paillet. The stability of a trailing line vortex. part 1. inviscid theory. *J. Fluid Mech.*, 63(4):753–63, 1974.

[39] D.C. Lewellen and W.S. Lewellen. Large-eddy simulations of the vortex-pair break-up in aircraft wakes. *AIAA Journal*, 34(11):2337–45, 1996.

[40] W.S. Luffsey. *Panel Discussion, (in) Aircraft Wake Turbulence and its Detection. (ed) J. Olsen, A. Goldburg, M. Rogers.* Plennum, NY, 1971.

[41] E.W. Mayer and K.G. Powell. Viscous and inviscid instabilities of a trailing vortex. *J. Fluid Mech.*, 245:91–114, 1991.

[42] J. Menkes and F.H. Abernathy. *Panel Discussion, (in) Aircraft Wake Turbulence and its Detection. (ed) J. Olsen, A. Goldburg, M. Rogers.* Plennum, NY, 1971.

[43] A. Meseguer and F. Mellibovsky. On a solenoidal Fourier-Chebyshev spectral method for stability analysis of the Hagen-Poiseuille flow. *Applied Numerical Mathematics*, 75:920–38, 2007.

[44] D.M. Nosenchuck, W.S. Flannery, and G.L. Brown. Control of wing-tip vortices. *Proc. FAA Wake Vortices Conf., Washington D.C. Oct 29-31*, 1991.

[45] Akira Ogawa. *Trailing Vortex (in) Vortex Flow.* CRC Press, Inc. Florida, USA, 1993.

[46] P. Orlandi, G.F. Carnevale, S.K. Lele, and K. Shariff. DNS study of stability of trailing vortices. *Centre for Turbulence Research, Proc. Summer Program*, pages 187–208, 1998.

[47] S.R. Otto and J.P. Denier. Numerical solution of a generalized elliptic partial differential eigenvalue problem. *J. Comp. Fluids*, 156:352–9, 1999.

[48] S.C. Rennich and S.K. Lele. Method for accelerating the destruction of aircraft wake vortices. *J. Aircraft*, 36(2):398–404, 1999.

[49] K. Ryan and G.J. Sheard. Non-linear growth of short-wave instabilities in a Batchelor vortex pair. *Proc. 16th Australasian Fluid Mechanics Conference. Gold Coast. Australia. 2-7 Dec.*, pages 1463–69, 2007.

[50] Ö. Savaş. Experimental investigations on wake vortices and their alleviation. *C.R. Physique*, 6:415–29, 2005.

[51] P.J. Schmid and D.S. Henningson. Optimal energy density growth in Hagen-Poiseuille flow. *J. Fluid Mech.*, 277:197–225, 1994.

[52] P.I. Singh and M.S. Uberoi. Experiments on vortex stability. *Phys. Fluids*, 19(12):1858–63, 1976.

[53] D. Sipp, F. Coppens, and L. Jacquin. Theoretical and numerical analysis of wake vortices. *ESAIM Proc*, 7:397–407, 1999.

[54] F.T. Smith and S.N. Brown. The inviscid instability of a Blasius boundary layer at large values of the mach number. *J. Fluid Mech.*, 219:499–518, 1990.

[55] P.R. Spalart. Airplane trailing vortices. *Annu. Rev. Fluid Mech.*, 30:107–38, 1998.

[56] K. Stewartson. The stability of swirling flows at large Reynolds number when subjected to disturbances with large azimuthal wave-number. *Phys. Fluids*, 25(11):1953–57, 1982.

[57] K Stewartson and S.N. Brown. Near-neutral centre-modes as inviscid perturbations to a trailing line vortex. *J. Fluid Mech.*, 156:387–99, 1985.

[58] K. Stewartson and K Capell. On the stability of ring modes in a trailing line vortex: the upper neutral points. *J. Fluid Mech.*, 156:369–86, 1985.

[59] J.A.K. Stott and P.W. Duck. The stability of a trailing-line vortex in compressible flow. *J. Fluid Mech.*, 269:323–51, 1994.

[60] J.A.K. Stott and P.W. Duck. The effects of viscosity on the stability of a trailing-line vortex in compressible flow. *Phys. Fluids*, 7(9):2265–70, 1995.

[61] T. Tatsumi and T. Yoshimura. Stability of the laminar flow in a rectangular duct. *J. Fluid Mech.*, 212:437–99, 1990.

[62] V Theofilis. Advances in global linear instability analysis of nonparallel and three-dimensional flows. *Progress in Aerospace Sciences*, 39:249–315, 2003.

[63] V. Theofilis, P.W Duck, and J. Owen. Linear stability analysis of rectangular duct and cavity flows. *J. Fluid Mech.*, 505:249–86, 2004.

[64] S.N. Timoshin and F.T. Smith. Singular modes in Rayleigh instability of three-dimensional streamwise-vortex flows. *J. Fluid Mech.*, 333:139–60, 1997.

[65] L. N. Trefethen. *Spectral Methods in Matlab.* SIAM. Philadelphia, PA., 2000.

[66] S.E. Widnall, D. Bliss, and A. Zalay. *Theoretical and experimental study of the stability of a vortex pair. (in) Aircraft Wake Turbulence and its Detection. (ed) J. Olsen, A. Goldburg, M. Rogers.* Plennum, NY, 1970.